

Measuring pilot control behavior in control tasks with haptic feedback

Mario Olivari

Measuring pilot control behavior in control tasks with haptic feedback

Dissertation

University of Pisa
Department of Information Engineering
and

Max Planck Institute for Biological Cybernetics
Department of Human Perception, Cognition, and Action

Engineering Ph.D. School “Leonardo da Vinci”
Ph.D. Program in Automation, Robotics,
Bioengineering

by

Mario OLIVARI

Date of examination:

5 July 2016

Supervisors:

Prof. dr. ir. L. Pollini

Dr. ir. F. M. Nieuwenhuizen

Ph.D. course chairman:

Prof. dr. ir. A. Caiti

Examination board:

Prof. dr. H. H. Bühlhoff

Prof. dr. ir. A. Landi

Prof. dr. ir. C. Colombo

Measuring pilot control behavior in control tasks with haptic feedback

Mario Olivari

External aids are required to increase safety and performance during the control of an aerial vehicle. Although automated systems commonly outperform human operators, they are inefficient when unpredicted changes happen in the external environment. Thus, the human operator is still important for monitoring and handling unexpected events. The presence of human operator gives rise to some issues related to human factors. For instance, when operator's rule is reduced in monitoring the automated system, human operators may lose their skills of manually controlling the aerial vehicle, and be late in recognizing and recovering from failures of the support system.

An alternative approach to automation consists of using systems that share the control authority with the human operator. Examples are input-mixing systems, which provide an additional control signal directly into the aerial vehicle to help the human operator perform a control task, while still leaving full control authority. However, since the human operator is not aware of the additional control signal, this

approach may lead to similar issues to those found for automated systems.

Haptic aids have been proposed as a powerful tool to overcome these issues. Haptic aids share the control authority with pilots similarly to input-mixing systems, but they show their control command through forces on the control device. Pilots continuously sense the haptic feedback and are always aware of the control strategy of haptic aid.

Despite the attention that haptic aids have been received in the last few years, many questions remain unanswered. Most studies tended to focus on theoretical advantages of haptic feedback over input-mixing systems. However, there is still a need for quantitative comparisons between the two support systems. Furthermore, haptic aids have been commonly tuned heuristically by testing different systems until satisfactory results were achieved. Recent studies argued that the tuning process could be improved and formalized by accounting for how pilots adapt their responses to generic haptic aids. However, adaptation of pilot's dynamic responses is only poorly understood.

The research goal of this thesis was **to increase the understanding of effects of haptic feedback on human's performance and control behavior**. Three main objectives were formulated towards this goal. The first objective was to evaluate effectiveness of haptic aids on improving human's performance in different control scenarios. Comparisons between haptic and input-mixing systems were of particular interest. The second objective was to investigate influence of haptic feedback on human's behavior. To achieve this, novel identification methods were developed for estimating human's dynamic responses during a steering task. These methods assumed a time-invariant behavior of human's responses. The third object was to extend the identification methods to account for time-varying behavior of human's responses.

To achieve the first objective, haptic and input-mixing systems were first compared in nominal conditions, i.e., without considering unexpected events like failures. Two haptic and input-mixing systems were designed for a compensatory tracking task. The two systems were designed to be equivalent, i.e., to provide same control

commands without human in-the-loop. Note that from the human operator's point of view, the net effect of the input-mixing system is to augment the dynamics of the controlled element, making them easier to control. On the other hand, the haptic feedback does not modify the dynamics of the controlled element, but only helps participants control the original dynamics by using a force feedback. The two systems were compared in a human in-the-loop experiment, and contrasted to a baseline condition without external aids. **Performance improved with haptic and input-mixing systems compared to the baseline condition. However, the input-mixing system helped participants achieve better performance than the haptic aid.** On the other hand, control effort was reduced by the haptic aid and the input-mixing system in a similar way. Taken together, these findings suggest that both the haptic aid and the input-mixing system made the control task less demanding, but participants found it easier controlling the augmented dynamics with the input-mixing system than controlling the original dynamics with the help of the force feedback.

Although the input-mixing system yielded better performance than the haptic aid in nominal conditions, it is not yet well established what happens when an unexpected event occurs, e.g., a failure of the support system. This aspect has received great attention in literature, but only very few experimental implementations have been reported. In this thesis, an experiment was performed to investigate effects that a failure of the support system may have on human's performance. In the experiment, failures of haptic and input-mixing systems were simulated as a total loss of support action. The results showed that **participants recovered better from failures of the haptic system than from failures of the input-mixing system.** Surprisingly, participants using haptic aid were able to re-gain levels of performance they had before the failure, which were better than performances obtained in tasks without external aids. This would appear to indicate that the haptic feedback helped participants learn a control strategy for performing the task.

In literature, inconclusive evidence was provided on effectiveness of haptic feedback for learning purposes. Thus, an experiment was conducted to gain an insight into this aspect. Two groups of

participants performed a compensatory tracking task. The first group performed a training phase with the support of a haptic aid, followed by an evaluation phase where the haptic aid was turned off (haptic group). The second group performed all experimental trials without haptic support (no-aid group). Results indicated that the haptic group learned quicker the control task, and their levels of performance did not worsen after the haptic feedback was turned off. On the other hand, the no-aid group needed several trials before achieving similar performance to the haptic group. Thus, **haptic feedback helped participants learn the compensatory tracking task.**

All these findings contributed to the first objective of the thesis. However, although haptic aids were shown to have beneficial effects on human's performance in different control scenarios, it remains unclear how human operators can realize these benefits. The second objective of the thesis aimed at obtaining a quantitative insight into how humans adapt their behaviour to exploit the haptic feedback. Such insight was obtained by identifying pilot's dynamic responses to the external cues.

In a compensatory tracking task with haptic feedback, the external cues are the visual tracking error and the haptic feedback, and pilot's responses to these cues are represented by the visual and the neuromuscular responses, respectively. A widely used method to identify pilot's visual and neuromuscular responses is based on cross-spectral analysis (CS method). However, this thesis presents a mathematical proof that this method is biased when a non-interference hypothesis is not fulfilled. This hypothesis may be difficult to be met during actual experimental designs.

To overcome this issue, we developed two novel methods that are unbiased even when the non-interference hypothesis is not fulfilled: the ARX and CS-ML methods. The ARX method is based on ARX models, while the CS-ML method combines cross-spectral analysis with block diagram algebra. The two novel methods were validated in different sets of Monte-Carlo simulations and contrasted to the CS method. The results confirmed that the CS method fails

when the non-interference hypothesis is not fulfilled. On the contrary, our proposed techniques gave reliable estimates of visual and neuromuscular responses even when the CS method fails.

The novel methods were then applied to experimental data. The ARX and CS-ML techniques gave comparable estimates of visual and neuromuscular responses, different from those obtained by the CS method. The differences matched those found with the simulations. Thus, **the two novel identification methods provided reliable estimates even in cases where the classical method failed.**

After validation, the novel methods were applied to estimate how humans adapt their dynamic responses to different haptic aids. Two haptic aids were designed according to different approaches, the Direct Haptic Aid (DHA) and the Indirect Haptic Aid (IHA) approaches. The DHA provides forces on the control device that suggest a right control action to the human operator, whereas the IHA provides forces opposite in sign with respect to the DHA. The two approaches are complementary, since they require a different response to the haptic stimulus: with DHA humans should be compliant with the haptic force, while with IHA humans should oppose to it in order to achieve the task. Experimental results showed that **participants significantly adapted their neuromuscular responses to fully exploit the haptic feedback.** They were more compliant with the DHA force, whereas they showed stiffer neuromuscular settings with the IHA feedback.

The CS, CS-ML, and ARX methods assume time-invariant behaviour of human's dynamic responses. Although this assumption can be met in experimental settings, humans are likely to change their responses in realistic control scenarios, due to human-related variables (e.g., fatigue, motivation, etc.) and to environmental factors (e.g., weather, ambient illumination, etc.). Consequently, the third objective of the thesis was to develop methods that can estimate time-varying human's responses.

At a first stage, this thesis focused on disturbance rejection tasks, which consist of adopting different neuromuscular responses while an external force disturbance is applied on the control device, and do not involve visual feedback. Human's behavior in these tasks

can be modelled by a single-input dynamic response, i.e., the neuromuscular response. A novel identification method was developed to identify time-varying neuromuscular response in the single-input disturbance-rejection tasks. The method approximates the neuromuscular response by a Finite Impulse Response (FIR) filter, and estimates FIR coefficients by using a Recursive Least Squares (RLS) algorithm. The method was validated by performing a set of Monte-Carlo simulations with increasing levels of external noise. Even with high level of external noise, the RLS-based method provided accurate estimates of the simulated time-varying neuromuscular response over a broad range of frequencies. However, estimates were not accurate at high frequencies. A second set of Monte-Carlo simulations was performed to find optimal values for the parameters of the RLS-based algorithm. By using these optimal values, RLS-based method was applied to data obtained in a human-in-the-loop experiment. Experimental results showed that **the RLS-based method was able to track time-varying neuromuscular dynamics in disturbance-rejection tasks. However, the estimates showed high variability at low and high frequencies**, indicating that the RLS-based method was very sensitive to relatively high levels of human remnant noise.

To improve robustness to noise, the RLS-based method was extended to include regularization methods. Specifically, two regularization methods were employed: the Truncated Singular Value Decomposition, and the Tikhonov regularization. **The mathematical framework for the two regularized RLS-based methods was developed, and recursive implementations were derived.**

Finally, a regularized RLS-based method was developed to estimate time-varying human's responses in a multi-loop compensatory tracking task. The method approximates neuromuscular and visual responses with FIR filters, and simultaneously estimates FIR coefficients by using a RLS algorithm with Tikhonov regularization. Simulation results showed that **the regularized RLS method was successful in estimating time-varying pilot's responses with low levels of remnant noise. However, estimates showed high variability with large levels of remnant noise.**

All findings of this thesis can be summarized in the following overall conclusions:

- Although haptic aids are outperformed by input-mixing systems, they allow human operators to remain in-the-loop and improve their skills in recovering from unexpected events like failures. Furthermore, haptic aids help the human operator learn quicker a compensatory tracking task.
- Human operators realize benefits of haptic aids by adapting their dynamic responses. The novel ARX and CS-ML methods are a powerful tool to obtain a quantitative insight into how humans adapt their responses to different haptic aids.
- The RLS-based methods provide accurate estimates of time-varying neuromuscular response in disturbance-rejection tasks. More research is required to optimize the parameters of RLS-based methods, to obtain accurate estimates in compensatory tracking tasks.

These findings suggest the following opportunities for future research:

- The further use of ARX and CS-ML methods should be encouraged to improve understanding of humans adaptation to different haptic aids.
- Further work needs to be carried out to improve robustness of RLS-based methods in estimating multi-loop human's responses.

Nomenclature

Acronyms

ACT	Neuronal activation dynamics
ADM	Admittance
ANOVA	Analysis of variance
ARMAX	Autoregressive moving average with exogenous inputs
ARX	Autoregressive with exogenous inputs
BJ	Box Jenkins
CC	Contractile components of neuromuscular hardware
CD	Control device dynamics
CE	Controlled element dynamics
CNS	Central nervous system
COMB	Combined dynamics of human admittance and control device
CON	Control dynamics of human and control device
CS	Cross spectra
CS-ML	Cross spectra multi-loop

DHA	Direct haptic aid
FIR	Finite impulse response
FRF	Frequency response function
FT	Force task
HA	Haptic aid
HUM	Human dynamic responses
HW	Neuromuscular hardware
I	Inertia of neuromuscular hardware
IHA	Indirect haptic aid
IM	Input-mixing
INT	Intrinsic arm dynamics
LTl	Linear time invariant
MSE	Mean square error
MSE_w	Windowed mean square error
NoA	No external aids
NoHA	No haptic aid
NPS	Neutral point shift
OL	Open loop
OOTL	Out of the loop
PEC	Muscle parallel elastic component of neuromuscular hardware
PFD	Primary flight display
PT	Position task
REFL	Reflexive dynamics
RLS	Recursive least squares

RT	Relax task
SEC	Muscle series elastic component of neuromuscular hardware
SKIN	Skin dynamics
SNR	Signal-to-noise ratio
SVD	Singular values decomposition
SW	Neuromuscular software
TI	Tikhonov regularization
TSVD	Truncated singular values decomposition
TVT	Time varying task
VAF	Variance accounted for
VIS	Visual response dynamics

Greek Symbols

δ_{cd}	Control device deflection	[rad or m]
δ_{li}	Internal neuromuscular representation of limb position	[rad or m]
δ_{nps}	Neutral point shift	[rad or m]
δ_t	Target trajectory for limb position	[rad or m]
ϵ	Prediction error	
Γ_{block}^2	Squared coherence function associated to BLOCK	[-]
λ	Forgetting factor	[-]
ω	Frequency	[rad/s]
ω_c	Crossover frequency	[rad/s]
ϕ_{ce}	Roll angle of the controlled element	[rad or deg]
ϕ_t	Target trajectory for the roll angle	[rad or deg]

ψ_k	Phase of the k^{th} sinusoidal component of a multisine	[-]
σ	Standard deviation	
σ^2	Variance	
τ_p	Pilot visual delay	[s]
θ_{ce}	Pitch angle of the controlled element	[rad or deg]
θ_t	Target trajectory for the pitch angle	[rad or deg]

Latin Symbols

A_k	Amplitude of the k^{th} sinusoidal component of a multisine	[-]
AM	Admittance mode	[-]
CM	Control mode	[-]
e	Tracking error	[rad or deg]
e_{cum}^2	Cumulative squared error	[rad ² or deg ²]
$E_{H_{block}}$	Relative error between estimated and simulated $H_{block}(f)$	[-]
$E_{h_{block}}$	Relative error between estimated and simulated h_{block}	[-]
f	Frequency	[Hz]
f_0	Base frequency	[Hz]
f_k	Frequency of the k^{th} sinusoidal component of a multisine	[Hz]
F_{adm}	Human force from neuromuscular system	[N or Nm]
f_c	Crossover frequency	[Hz]
F_{dha}	Force feedback of the direct haptic aid	[N or Nm]
F_d	Force disturbance	[N or Nm]
F_{ex}	Total external force	[N or Nm]

E_{ha}	Haptic force	[N or Nm]
E_{hum}	Human force	[N or Nm]
E_{iha}	Force feedback of the indirect haptic aid	[N or Nm]
F_{vis}	Human force from visual system	[N or Nm]
H_{block}	Transfer function of BLOCK	
h_{block}	Impulse response of BLOCK	
$H_{block}(f)$	Frequency Response Function of BLOCK	
H_{vw}	Transfer function between v and w	
h_{vw}	Impulse response between v and w	
$H_{vw}(f)$	Frequency Response Function between v and w	
j	Imaginary unit	[-]
K_{cd}	Control device gain	[-]
K_{ce}	Controlled element gain	[-]
K_{ha}	Haptic aid gain	[-]
K_{nps}	Gain of neutral point shift	[-]
K_N	Remnant gain	[-]
K_p	Pilot visual gain	[-]
K_{vis}	Gain of pilot visual response	[-]
M	Memory of impulse response	[-]
N	Human remnant signal	[N or Nm]
q	Activation signal for neuromuscular software	[-]
s	Laplace variable	[-]
S_{vv}	Spectrum of v	
S_{vw}	Cross-spectrum between v and w	
T	Sample time	[s]

t	Time	[s]
t_k	k^{th} time sample	[s]
T_L	Pilot lead time constant	[s]
T_l	Pilot lag time constant	[s]
u	Input for the controlled element	[rad or m]
u_{cns}	Cognitive actions from the central nervous system	[-]
u_{im}	Feedback signal of the input-mixing aid	[rad or m]
w	Gaussian noise with unitary variance	[-]

Subscripts

d	Force disturbance related
ms	Multisine related
N	Remnant related
pn	Pseudonoise related
t	Target trajectory related

Other

-	Averaged
^	Estimated

Contents

Summary	v
Nomenclature	xiii
1 Introduction	1
1.1 Issues of automation	1
1.2 Haptic aids	3
1.3 Human-centered design	5
1.3.1 Modelling pilot control behavior	5
1.3.2 Identifying neuromuscular response	6
1.4 Research motivation and goal	9
1.5 Thesis contents	10
1.6 Thesis scope	12
I Evaluating effectiveness of haptic feedback on human's performance	15
2 Input-mixing and haptic aids in nominal conditions	17
2.1 Introduction	19
2.2 Control task and human behavior	21
2.3 Design of haptic aid	21
2.4 Design of input-mixing control system	24

2.5	Experiment setup	26
2.5.1	Task and apparatus	26
2.5.2	Target trajectory	27
2.5.3	Participants and experiment procedure	28
2.5.4	Data collection and analysis	29
2.6	Results and discussion	31
2.6.1	Performance and control activity	31
2.6.2	Human's dynamic response	33
2.7	Conclusions	35
3	On effects of failures of input-mixing and haptic aids	37
3.1	Introduction	39
3.2	Design of external aids and simulated failure	40
3.2.1	Haptic aid design	41
3.2.2	Input-mixing aid design	42
3.2.3	Failure	43
3.3	Experiment setup	43
3.3.1	Apparatus and control task	43
3.3.2	Target trajectory	43
3.3.3	Participants and experimental procedure	45
3.3.4	Measures	46
3.3.5	Hypotheses	46
3.4	Results and discussion	47
3.4.1	No failure	47
3.4.2	Failure	47
3.5	Conclusions	52
4	Evaluation of haptic support system for training purposes	53
4.1	Introduction	55
4.2	Design of haptic aid for training	57
4.2.1	Compensatory tracking task	57
4.2.2	Haptic aid design	58
4.2.3	Preliminary evaluation of the haptic feedback	59
4.3	Experimental setup and results	60
4.3.1	Control task, target trajectory, and apparatus	60
4.3.2	Participants and experimental procedure	62
4.3.3	Measures	62

4.3.4	Hypotheses	65
4.3.5	Results	65
4.4	Conclusions	69
II	Identifying time-invariant neuromuscular response in multi-loop tasks	71
5	Methods for identifying time-invariant neuromuscular responses in multi-loop tasks	73
5.1	Introduction	75
5.2	Pilot model and control task description	77
5.3	Conventional identification technique	78
5.3.1	Forcing functions design	79
5.3.2	Cross-spectral density analysis	82
5.4	Novel identification techniques	84
5.4.1	AutoRegressive models with eXogenous inputs	85
5.4.2	Multi-loop cross-spectral densities	87
5.5	Off-line simulations	89
5.5.1	Simulations with reference parameter values .	89
5.5.2	Variation of the gain of the controlled element	92
5.5.3	Variation of the noise power of noise	95
5.6	Experimental evaluations	98
5.6.1	Method	98
5.6.2	Results	99
5.7	Conclusions	103
5.8	Appendix	105
6	Pilot adaptation to different classes of haptic aids	107
6.1	Introduction	109
6.2	Design of haptic aids for a tracking task	110
6.2.1	DHA approach	110
6.2.2	IHA approach	112
6.2.3	Comparison of DHA and IHA approaches . .	113
6.3	Modelling of human control behavior	114
6.4	Identification of human control behavior	116
6.5	Experiment design	121

6.5.1	Control task and apparatus	121
6.5.2	Controlled element and haptic aid dynamics	122
6.5.3	Forcing functions	123
6.5.4	Performance of haptic systems and influence of force disturbance	125
6.5.5	Independent variables	126
6.5.6	Participants and experimental procedure	126
6.5.7	Dependent measures	128
6.5.8	Hypotheses	129
6.6	Results	130
6.6.1	Tracking performance and control activity	130
6.6.2	Admittance	132
6.6.3	Pilot visual response	136
6.6.4	Control and open-loop transfer functions	137
6.7	Conclusions	140

III Identifying time-varying neuromuscular response 143

7	Methods for identifying time-varying neuromuscular re- sponse in single-loop tasks	145
7.1	Introduction	147
7.2	Control task	149
7.3	Estimating time-varying neuromuscular dynamics	150
7.3.1	Impulse response of COMB	151
7.3.2	RLS algorithm	152
7.3.3	Estimating admittance frequency response	152
7.3.4	Force disturbance design	153
7.4	Validation of the RLS-based method in simulation	155
7.4.1	Robustness to remnant noise	155
7.4.2	Influence of the forgetting factor λ	162
7.5	Experiment	167
7.5.1	Apparatus	167
7.5.2	Participants, experimental conditions and ex- perimental procedure	168
7.5.3	Identification of neuromuscular response and dependent measures	169

7.5.4	Hypotheses	170
7.5.5	Results	170
7.6	Conclusions	173
8	Identifying time-varying neuromuscular response: Regularized RLS algorithms	175
8.1	Introduction	177
8.2	Control task	178
8.3	Estimating the impulse response	179
8.4	Conventional RLS-based method	180
8.4.1	Issues of conventional RLS algorithm	182
8.4.2	Solution adopted by the conventional RLS-based method: adding a pseudonoise	183
8.5	Novel approaches: regularized RLS-based methods	185
8.5.1	RLS algorithm with Truncated Singular Value Decomposition	185
8.5.2	RLS algorithm with Tikhonov regularization	188
8.6	Conclusions	192
9	Methods for identifying time-varying neuromuscular response in multi-loop tasks	193
9.1	Introduction	195
9.2	Control task	196
9.3	Estimating time-varying human's responses	197
9.3.1	Impulse responses	198
9.3.2	Recursive Least Squares algorithm	199
9.4	A Monte-Carlo simulation study	202
9.4.1	Control task	202
9.4.2	Forcing functions	204
9.4.3	Independent variables and data analysis	206
9.4.4	Results	207
9.5	Conclusions	211
10	Conclusions and recommendations	213
10.1	Quantifying effects of haptic feedback on human's performance	214
10.2	Identifying time-invariant human's responses	216

10.3 Methods for identifying time-varying human's responses	218
10.4 Main contributions	220
10.5 Recommendations	221
Bibliography	223
Appendices	239
A Modelling of pilot's dynamic responses	241
A.1 Single-input pilot model for a compensatory tracking task	241
A.2 Multi-input pilot models for a compensatory tracking task	242
A.2.1 Non-parametric model with admittance and visual response	242
A.2.2 Non-parametric model with force and error feedtroughs	243
A.2.3 Parametric model - Schouten et al. [2008b] . .	244
A.2.4 Parametric model - van Paassen et al. [2004] .	246
List of my publications	249
Curriculum Vitae	253

Introduction

1.1 Issues of automation

MANUAL control of an aerial vehicle is a difficult task. Pilot loss of control is the primary cause of fatal accidents for general aviation vehicles, and this happens primarily during phases that require pilots to perform a large number of critical tasks (e.g., landing, maneuvering) [NTSB, 2012; Schutte et al., 2007]. To improve the safety of flying, pilots need to be supported with external aids that can facilitate the control task.

Automated systems have been introduced to assist human operator during the control task. These systems accomplish “(partially or fully) a function that was previously carried out (partially or fully) by a human operator” [Wickens et al., 1998]. By delegating complex tasks to automated systems, the control of the aerial vehicle can be simplified. Furthermore, performance of automated systems generally surpasses human pilots [Norman, 1990]. A common belief is that safety and performance would drastically increase with a fully automated aerial vehicle, where the automation is able to perform all control tasks without human interaction.

However, this is far from being realized. Automation is inefficient when unpredicted changes happen on the external environment, or when a novel decision must be taken [Billings, 1997]. Thus,

the presence of human operator is still crucial even with highly-automated systems.

The presence of human operators gives rise to several issues related to human factors that could happen with an improper design of automated systems. When automated systems take over the biggest part of a control task, operator's role may be reduced in monitoring the automated system. This could lead to a decreased ability of human operator in understanding the system state and the elements in the environment (loss of situational awareness) [Endsley, 1995; Wickens, 2008]. Furthermore, pilots may over-rely on automation, decrement their vigilance and loose their skills of manually controlling the aerial vehicle [Bainbridge, 1983; Endsley and Kiris, 1995; Kaber and Endsley, 2004]. Ignoring such issues could lead to severe problems. For example, pilots may require too much time to detect failures of the automation, and they may not be able to recover from these failures. These outcomes have been known as out-of-the-loop (OOTL) performance problems [Billings, 1991; Endsley and Kiris, 1995; Kaber and Endsley, 1997].

To maintain the pilot in-the-loop, previous studies have been put forward an alternative approach to automation: the *shared control* [Abbink and Mulder, 2010; Abbink et al., 2012; Flemisch et al., 2003]. In shared control, operator and external aid continuously share the control authority on the vehicle and work together to achieve the same task. The operator is always in control, while being supported by external aids.

Examples of shared-control systems are the input-mixing aids. These systems support pilots by providing an external feedback signal directly into the controlled element, while still leaving full control authority to pilots. A drawback of input-mixing systems is that the operator is not aware of the external feedback, but can only see the effect that the control signal has on the state variables of the controlled element. This may lead to similar issues as those with automated systems, i.e., loss of situation awareness, skills degradation in controlling the actual vehicle, and so on [Abbink and Mulder, 2010].

To minimize such issues of input-mixing systems, a main guideline has been put forward: pilots should always receive feedback

about the input-mixing system [Abbink et al., 2012; Norman, 1990]. These feedback would allow pilots to be always informed, detect possible errors and respond to them. The feedback should be designed to be intuitive and not too invasive for pilots, in order to “keep people well informed, on the top of the issues, but not annoyed and irritated” [Norman, 1990]. Most commonly used feedback are visual or auditory signals. However, these approaches suffer from a number of pitfalls, like overloading of information and presence of false alarms [Pritchett, 2001].

Recently, a novel approach has been proposed to provide the feedback signal in a shared-control system: to use a tactile feedback on the control device. Systems that use the tactile feedback are called *haptic aids*. Human operator can always sense the haptic feedback, is always informed about haptic aid state, and can easily detect possible errors of haptic aid and respond to them.

1.2 Haptic aids

Haptic aids have been widely employed in several contexts different from piloting an aerial vehicle. Many studies used the haptic feedback during teleoperations, where the *operator is separated from the operated object*. Examples are remote control of a robot arm with the master-slave paradigm [Hashtrudi-Zaad and Salcudean, 2002; Smisek et al., 2015], force feedback in servo-actuated systems [Parker et al., 1993], robotic assisted surgery [Rosen et al., 1999], and teleoperations of Uninhabited Aerial Vehicles [Alaimo et al., 2011b; Lam et al., 2006, 2009]. In these contexts the haptic channel is used to let the operator feel variations and/or discontinuities in the environment, like hitting or approaching an obstacle, encountering unexpected loads, or interacting with surfaces (i.e. tissues) with different softness. This knowledge eventually increases performance and situational awareness.

In recent years, there has been considerable interest in designing haptic aids as support systems for manned systems, i.e., systems where *operator and operated system are not separated*. These haptic systems are commonly designed to suggest a possible control action

to the operator. Many examples can be found in the field of car driving: a haptic gas pedal that assists the driver in car following [Abbink et al., 2008; Mulder et al., 2008a,b], a haptic steering wheel for lane-keeping [Brandt et al., 2007; Profumo et al., 2013], and a haptic steering wheel for obstacle avoidance [Katzourakis et al., 2011].

Only a few studies have investigated use of haptic aids as pilot support systems in manned aerial vehicles. Recently, researchers at NASA Langley developed a Haptic Flight Control System for aircraft (HFC) with the main goal of achieving easy-to-use Personal Air Vehicles [Goodrich et al., 2011]. The HFC continuously moved the stick by repositioning its neutral point in order to perform a desired maneuver. The pilot could either follow the HFC control signal or override it if he/she disagreed with its control action. The HFC was evaluated in a motion-based simulator, showing beneficial effects in terms of pilot workload and situational awareness [Goodrich et al., 2011].

In a different research project (ALLFlight), the Institute of Flight Systems Germany (DLR) developed a HFC for an EC135 helicopter [Abildgaard and von Grünhagen, 2008; Doehler et al., 2009]. Similar to the NASA's system, this HFC was designed to move the stick to a position corresponding to a desired trajectory of the helicopter. Evaluations in flight showed workload reductions and improved situational awareness when the HFC was activated [Abildgaard and von Grünhagen, 2008].

Despite the growing interest in haptic support systems for aerial vehicle, there are still some questions to be answered. For instance, it has not yet established whether haptic feedback can help pilots achieve similar performance to those obtained with input-mixing aids. Furthermore, as pointed out in the previous section, haptic aids may be a solution against the OOTL problems that input-mixing control is affected of. However, to the best of our knowledge, only theoretical considerations have been presented and these considerations are largely based on very limited data.

1.3 Human-centered design

Although a well designed guidance haptic feedback could result in improved performance at significantly reduced control effort, improper tuning of the haptic feedback may lead to a system that makes the control task more difficult instead of simplifying it. For instance, very strong haptic feedback could result in disagreement between haptic aid and the human operator [Lam et al., 2007]. Thus, a proper design of the haptic feedback is crucial for the effectiveness of the haptic aid.

Common practice is to design the haptic feedback heuristically by testing different haptic dynamics until satisfactory performance is achieved. Recently, many experts have argued that rather than using heuristic approaches it might be more useful to design the haptic aid based on how pilots adapt their behavior to the force feedback itself, see for instance Mulder et al. [2008b]. With this human-centered design, pilots would quickly get acquainted with the haptic feedback and learn how to exploit it to increase their performance.

A human-centered design requires a quantitative insight into how pilots adapt their control behavior to different haptic aids. This insight can be achieved by modelling and estimating of pilot control behavior.

1.3.1 Modelling pilot control behavior

Pilot control behaviour can be modelled by considering the dynamic responses to all relevant perceived cues. Initial work in this field primarily focused on compensatory tracking tasks, where pilots are asked to track a target roll (or pitch) angle by minimizing the tracking error shown on a visual display [McRuer; McRuer and Jex, 1967]. In this task, the only perceived cue is the visual error, and the pilot can be modelled by a single-input dynamic response to the visual error, combined with a remnant signal that accounts for unmodelled non-linearities. Such models are referred to as *quasi-linear models*.

More recently, quasi-linear models have been used to model pilot control behaviour in tasks with more external cues. For instance, quasi-linear models were developed for tracking tasks with a pursuit display that shows the current aircraft output and the target signal [Drop et al., 2013; Hess, 1981; McRuer and Jex, 1967]. The pursuit display provides three external cues to the pilot: the target signal, the aircraft output, and the tracking error. Thus, the pilot can be modelled by a multi-input linear system describing the dynamic responses to the three external cues, together with a remnant signal. Other works developed quasi-linear models for tracking tasks with physical motion feedback. In this case, the motion feedback was considered as an additional input to the pilot model [Nieuwenhuizen et al., 2008; Pool et al., 2011; Zaal et al., 2009].

When haptic aids are used, the haptic feedback needs to be modeled as an additional cue to the pilot. A pilot model that includes the haptic feedback as an additional input was previously developed by van Paassen [1994] and used in various scenarios, such as a tracking task without haptic aids [van Paassen, 1994] and car following with haptic aid [Abbink and Mulder, 2010]. The model describes the pilot's response to the haptic feedback by the limb's *neuromuscular dynamic response*, i.e., the dynamic relationship between a force applied to the limb and the resulting position.

Previous studies have shown that humans can adapt their neuromuscular response to respond differently to the haptic feedback. For instance, the neuromuscular settings can be adapted to be compliant and follow the haptic force, or to be stiff and oppose to it. It follows that an insight into the neuromuscular response is crucial for an effective design and evaluation of haptic aids. This insight can be achieved by using identification methods to estimate the neuromuscular response during a control task.

1.3.2 Identifying neuromuscular response

Identification methods are powerful tools that can be employed for estimating the neuromuscular response. Identification methods can be divided into two main categories: parametric and non-parametric methods. Parametric approaches represent systems dynamics with

parametric models, and provide estimates of the model parameters. In parametric methods, one must take care not to use too many parameters, as this may lead to inaccurate parameter estimation [Zaal and Sweet, 2012]. Unfortunately, multiple parameters are needed to describe neuromuscular dynamics [Schouten et al., 2008b]. Therefore, parametric methods may be not appropriate for identifying such dynamics.

On the other hand, non-parametric methods provide estimates of black-box descriptions of the system, without requiring any parametric description or a-priori knowledge of the system. These methods are suitable for identifying neuromuscular response and will be considered in this thesis.

There is a considerable amount of literature on non-parametric methods for identifying neuromuscular response. Early experiments focused on disturbance-rejection tasks, where human operator is asked to adopt different control strategies in response to a force disturbance applied to the control device [Lasschuit et al., 2008; Mugge et al., 2010; Schouten et al., 2008b]. Examples are the position task with the instruction to counteract the disturbance force, or the relax task with the instruction to relax the arm and passively follow the disturbance force. In these tasks, humans are provided with only one external cue, i.e. the disturbance force, and can be described by a single-input dynamic response, i.e. the neuromuscular response. To estimate neuromuscular response in disturbance-rejection tasks, a well-known and validated method is based on Cross-Spectra analysis (CS method) [Jenkins and Watts, 1969; Pintelon and Schoukens, 2012].

Identification of neuromuscular response becomes more involved in steering tasks, where multiple external cues are provided and multi-input models are needed to describe human behavior. Recent works extended the CS method to estimate neuromuscular response in multi-input tasks [Abbink et al., 2011; Damveld et al., 2009; Venrooij et al., 2014]. However, the CS method requires an additional force disturbance on the control device, and assumes that this force does not interfere with the visual feedback. Unfortunately, when this non-interference assumption is not verified, the CS method provides biased estimates.

Alternative methods have been proposed to estimate neuromuscular responses in multi-loop control tasks. For instance, polynomial models have been used to estimate driver behavior during a car following task [Abbink, 2006]. Specifically, the driver was modelled by single input dynamics representing the neuromuscular response to external forces, and the responses to other cues were treated as an external filtered Gaussian noise. Then, an ARMAX model was used to estimate the single input driver's response. Although this approach provided reliable neuromuscular estimates, it may fail when the response to the other external cues cannot be approximated as an external Gaussian noise.

Thus, current identification methods are inefficient in estimating neuromuscular response in multi-loop tasks. A second distinct defect of most of the current methods is that they assume that humans do not vary their neuromuscular response during the identification period. Although this assumption can be met in experimental settings, humans are likely to change their responses in realistic control scenarios due to human-related variables (e.g., fatigue, motivation, etc.) and to environmental factors (e.g., weather, ambient illumination, etc.) [McRuer]. Thus, methods are needed that can estimate time-varying neuromuscular responses.

Little research on human manual control has focused on identifying time-varying neuromuscular responses. Parametric methods have been proposed to estimate different pilot's responses (motion and visual responses) [Hess, 2011; Zaal and Sweet, 2012]. However, as already pointed out, parametric methods may be not appropriate for identifying neuromuscular response.

Recent studies have attempted to use non-parametric methods for estimating time-varying neuromuscular response. An example of non-parametric description of a dynamic system is the frequency response. Wavelet transforms were used to estimate frequency responses of time-varying visual, motion, and neuromuscular systems [Mulder et al., 2011b; Thompson et al., 2001]. However, wavelet transforms were shown to be very sensitive to human remnant noise and they produced inaccurate results when applied to human data.

A different non-parametric description of a dynamic system is the impulse response. Ensemble methods were used to estimate the

impulse response of a time-varying neuromuscular system [Kirsch and Kearney, 1997; Lortie and Kearney, 2001; Ludvig et al., 2011]. These methods require data from many experimental trials, in which the neuromuscular system is assumed to undergo identical time-varying behavior. Unfortunately, this requirement is difficult to be met in a control task where humans actively respond to an external force feedback.

1.4 Research motivation and goal

It is clear from the previous sections that there is still much uncertainty regarding the influence of haptic aids on pilot's performance and control behavior. As regards performance, most studies have only focused on comparing haptic aids to manual control without external aids. It is not yet known whether haptic aids can help humans achieve similar performance to that achieved with different support systems like input-mixing aids. Furthermore, there is still a need for quantitative evaluations of haptic aids in control situations that could generate OOTL problems, like a sudden failure of the support system.

Next to the performance analysis, an insight into pilot's control behaviour is crucial for understanding how pilots can realize eventual benefits of haptic aids. To achieve this insight, identification methods are needed that can estimate neuromuscular dynamics in multi-loop steering tasks. Although previous research has developed methods for identifying neuromuscular dynamics in multi-loop tasks, these methods rely on restrictive assumptions that may not be verified in an experimental setup. Furthermore, apart from experimental settings, humans are likely to vary their neuromuscular dynamics in realistic control scenarios. However, most identification methods assume a time-invariant behavior of neuromuscular response.

The goal of the research presented in this thesis was:

Research goal

Increase the understanding of influence of haptic aids on pilot's performance and control behavior.

To achieve this research goal, three objectives were formulated:

- The effectiveness of haptic feedback on pilot's performance needs to be assessed in different control scenarios. By comparing haptic aids to input-mixing systems in nominal and unexpected control situations like system failures, it will be possible to evaluate whether the transparency of haptic feedback yields positive outcomes in terms of performance and OOTL problems.
- Novel methods need to be developed that can estimate neuromuscular responses in multi-loop control tasks without relying on restrictive assumptions. By applying these methods, it will be possible to gain an insight into how pilots adapt their dynamic responses to different haptic aids.
- Methods need to be developed that can estimate time-varying neuromuscular responses. This will provide a powerful tool to investigate how pilots adapt their responses in more realistic control scenarios.

1.5 Thesis contents

The chapters of this thesis are based on published work. Specifically, the research underlying this thesis was published in 12 conference papers, 2 journal papers, and 3 posters. Of these, 8 conference papers and 2 journal papers were collected in this thesis. The contents of each paper were rephrased to improve readability of the thesis as a whole. At the same time, some concepts were repeated along different chapters, to ensure their independent readability.

The thesis is split into three main different parts. The *first part* presents quantitative evaluations of haptic aids in different control

scenarios. The *second part* presents novel methods for identifying neuromuscular response in multi-loop tasks with haptic aids. In the *third part*, novel methods for identifying time-varying neuromuscular response are described. Finally, conclusions are drawn.

Part I: Evaluating effectiveness of haptic feedback on human's performance

Chapter 2 presents an experimental comparison between haptic and input-mixing systems in a compensatory tracking task. The haptic feedback is designed to provide a force feedback on the control device that suggests a possible right control action. The input-mixing system is designed to provide an "equivalent" control signal directly into the aerial vehicle dynamics. Human performances are compared between the two aids, and contrasted to a baseline condition without external aids.

Chapter 3 describes an experiment performed to investigate effects of failures of input-mixing or haptic aids on human performance. Failures of the support systems are simulated as sudden loss of support action. Human performances are evaluated before and after failures of haptic and input-mixing aids, to assess whether the transparency of the haptic feedback can help participants recover from the failure.

Chapter 4 evaluates effectiveness of haptic feedback for learning purposes. An experiment is presented where two groups of participants learn a compensatory tracking task either with or without haptic feedback. Then, both groups perform a following phase without haptic feedback. Performances are compared between the two groups, to assess effect of haptic feedback on learning a compensatory tracking task.

Part II: Identifying time-invariant neuromuscular response in multi-loop tasks

Chapter 5 presents the development of two novel methods to estimate neuromuscular response in multi-loop control tasks. The novel methods are based on ARX models (ARX method) and on

cross-spectral analysis (CS-ML method). ARX and CS-ML methods are first validated in Monte-Carlo simulations, then applied to experimental data.

In *Chapter 6*, the ARX and CS-ML methods are applied to estimate human neuromuscular response with two different haptic aids: a Direct Haptic Aid (DHA) and an Indirect Haptic Aid (IHA). The DHA and IHA aids require the human operator to adopt different control strategies to fully exploit the haptic feedback. The two haptic aids are evaluated in a human in-the-loop experiment, and human's adaptation to the two haptic aids is estimated.

Part III: Identifying time-varying neuromuscular response

Chapter 7 presents a method to identify time-varying neuromuscular responses in single-input disturbance-rejection tasks. The method approximates the neuromuscular impulse response with a Finite Impulse Response (FIR) filter, and uses a RLS algorithm to estimate the filter coefficients. The method is first validated by using Monte-Carlo simulations, then applied to experimental data.

Chapter 8 combines the RLS-based method with regularization methods to improve robustness to external noise. Specifically, two regularization methods are considered: the Truncated Singular Value Decomposition, and the Tikhonov regularization. The mathematical framework for the regularized RLS-based methods is developed, and recursive implementations are derived.

Chapter 9 extends the RLS-based methods to identify time-varying neuromuscular response in multi-input compensatory tracking tasks. Only the RLS-based method with Tikhonov regularization allows for extension to multi-input control tasks. The method is validated using data from Monte-Carlo simulations.

1.6 Thesis scope

The work presented in this thesis was limited by the following factors:

- All participants recruited during the experiments were Ph.D. students at the Max Planck Institute. None of them had previous flight experience.
- In all the control tasks considered in this thesis, the external cues were restricted to visual or/and haptic feedback. Influence of other cues (e.g., motion) on human behavior was out of the scope of this thesis.
- Care was paid in setting the parameters of the control tasks to minimize nonlinearities in human dynamic responses. For instance, the parameters in the compensatory tracking task were set such that participants could perform the task by generating small stick deflections, since large stick deflections would induce non-linearities in the neuromuscular response.

Part I

Evaluating effectiveness of haptic feedback on human's performance

Input-mixing and haptic aids in nominal conditions

Despite the theoretical advantages of haptic aids compared to input-mixing system, it is not yet known whether the transparency of the haptic control action worsen performance compared to an input-mixing system. This chapter presents a quantitative comparison between haptic and input-mixing systems in nominal conditions, i.e., without considering unexpected events like failures. The haptic and the input-mixing aids were designed for a compensatory tracking task to be equivalent when the human operator was out-of-the-loop, i.e., to provide the same control command. The two aids were tested in a human in-the-loop experiment and contrasted to a baseline condition without external aids. The haptic system allowed participants to improve performance compared to the baseline condition. However, input-mixing aid outperformed the other two conditions. Participants control effort was reduced by haptic and input-mixing aids in a similar way. In addition, the human open-loop response was estimated with a non-parametric estimation method. Changes in the human response were observed in terms of increased crossover frequency with the input-mixing system, and decreased neuromuscular peak with the haptic aid.

The contents of this chapter are based on:

- Paper title** An experimental comparison of haptic and automated pilot support systems
- Authors** Olivari, M., Nieuwenhuizen, F. M., Bühlhoff, H. H., and Pollini, L.
- Published in** Proceedings of the AIAA Modeling and Simulation Technologies Conference, AIAA SciTech, January 2014

2.1 Introduction

MANUAL control of an aerial vehicle is a difficult task that is prone to human errors. Conventional solutions are to partially or fully delegate the control task to automated systems. However, this approach suffers from a number of pitfalls related to human's factors. For instance, human operators could over-rely on automation, loose their skills of manually controlling the aerial vehicle, and be unprepared to detect and recover from failures [Bainbridge, 1983; Endsley and Kiris, 1995; Kaber and Endsley, 2004].

In recent years an alternative approach has been put forward: the *shared control* [Abbink and Mulder, 2010; Abbink et al., 2012; Flemisch et al., 2003]. In shared control, operator and external aid continuously share the control of the vehicle, allowing the human operator to be always in-the-loop. Two main categories of shared control have been investigated by previous works: input-mixing and haptic shared control.

Input-mixing aids provide an external feedback directly into the controlled element. The external feedback helps humans perform the task, while still leaving full control authority. However, although the human operator is always in control, the control signal is not transparent to the human operator. This may lead to similar issues of automated systems, i.e., loss of situation awareness, skills degradation in controlling the actual vehicle, and so on [Abbink and Mulder, 2010].

Haptic systems provide the additional signal as a tactile feedback on the control device. The human operator always aware of the haptic aid control strategy, and can always decide either to be compliant or to override it if they disagree with the system. Examples are haptic feedback for helicopters [Goodrich et al., 2008], haptic gas pedal to support car following [Abbink et al., 2008; Mulder et al., 2008b], or haptic steering wheel for lane keeping [Griffiths and Gillespie, 2005; Mulder et al., 2012].

Although the transparency of the haptic feedback allows the human operator to be always aware of the control signal, it introduces some drawbacks. The haptic feedback is first processed by

the human operator before being fed into the controlled element, resulting in some delay before the haptic control action is actually applied to the controlled element. Furthermore, interaction of the haptic feedback with the human operator puts some constraints on the feedback force. The question arises as to how much these drawbacks influence performance compared to an input-mixing system that interfaces directly to the aircraft.

Most studies tended to compare haptics with baseline conditions without any external aids. In these cases, haptic aids led to better performance and reduced control effort [Abbink et al., 2011; Mulder et al., 2008b]. In a more recent work dealing with car driving, a haptic pedal was compared to a full automated system during a curve negotiation task [Mulder et al., 2012]. The haptic aid improved performance compared with the manual control (measured through the peak of lateral error), but it reached lower performance than automation (the peak was larger with haptic aid than with automation). To the best of our knowledge, in literature there are no analogous works comparing haptic and input-mixing aids.

The goal of this chapter is to obtain a quantitative comparison between input-mixing and haptic aids in a compensatory tracking task [McRuer]. The haptic system was designed to suggest a possible control strategy to the human operator. The input-mixing aid was designed to be “equivalent” to the haptic system, in the sense that it gave the same performance *without human in-the-loop*. The input-mixing and haptic systems were tested in an experimental setup *with human in-the-loop*. Performance and control behavior were evaluated and compared to those obtained in a baseline condition without external aids.

The structure of this chapter is as follows. Section 2.2 introduces the compensatory tracking task. Section 2.3 and Section 2.4 present the design of the haptic aid and the input-mixing system, respectively. In Section 2.5 the experiment design is described, and in Section 2.6 results are presented. Finally, conclusions are drawn in Section 2.7.

2.2 Control task and human behavior

This chapter focuses on a compensatory tracking task in the roll axis, see Figure 2.1. The task consists of tracking a target roll trajectory ϕ_t with the controlled element CE. Only the tracking error e between the target trajectory and the actual roll angle ϕ_{ce} is shown to the human operator HO on a compensatory display.

External aids are used to help the human operator during the control task. The haptic aid HA generates forces F_{ha} on the stick, see Figure 2.1a, while the input mixing system IM provides an additional command u_{im} directly into the controlled element, see Figure 2.1b. Note that, in this model, the human operator can feel the haptic forces through the variations that they cause on the stick deflection δ_{cd} .

Human behavior in a compensatory tracking task has been extensively investigated in literature. McRuer provided quantitative models that describe the human response to the tracking error for different controlled elements [McRuer; McRuer and Jex, 1967; McRuer and Weir, 1969]. These models assess that humans adapt their response such that the open-loop transfer function between the tracking error e and the roll angle of the aircraft ϕ_{ce} resembles integrator-like dynamics at frequencies around the crossover frequency ω_c :

$$H_{con}H_{ce} = \frac{\omega_c e^{-s\tau_p}}{s} \quad 2.1$$

Here, H_{block} represents the transfer function of BLOCK. Specifically, H_{con} is the human control response from the tracking error e to the stick deflection δ_{cd} , and includes dynamics of the human operator and the control device CD, see Figure 2.1. The parameters ω_c and τ_p represent the crossover frequency and the human visual delay, respectively. Note that Equation (2.1) is only valid around the crossover frequency ω_c .

2.3 Design of haptic aid

A haptic aid was designed according to the Direct Haptic Aid approach (DHA) [Alaimo et al., 2011b]. The DHA system continuously

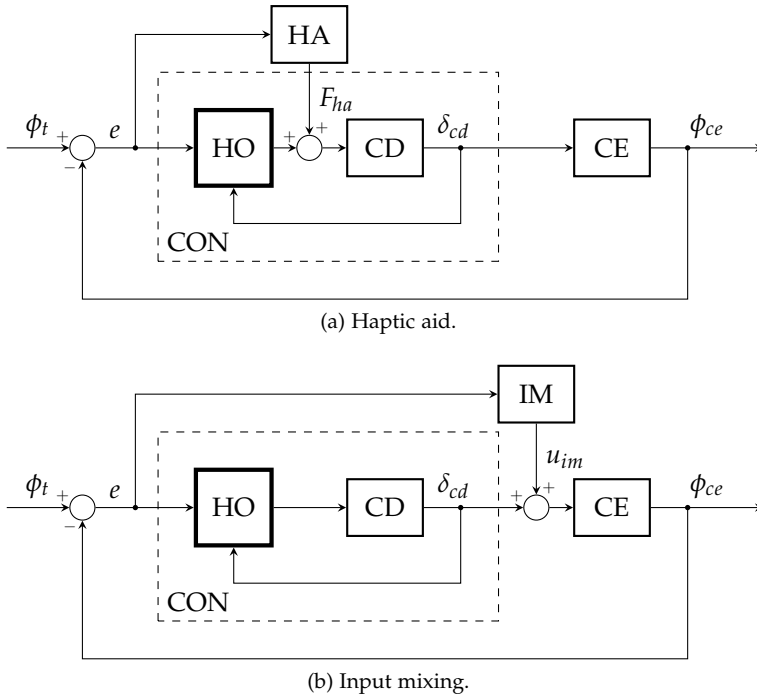


Figure 2.1: Compensatory tracking task with external aids.

generates forces on the stick that aim to reduce the roll tracking error. Although several techniques could be used to design a haptic controller that reduces the tracking error, the interaction of the human operator with the haptic feedback imposes some requirements on the haptic control signal [Abbink et al., 2008]. The haptic feedback should be large enough to be felt by the human operator, but at the same time it should leave full authority to the human operator to take a different control action. Furthermore, the haptic feedback should induce the human operator to adopt a force task, i.e. to be compliant with the forces. If this does not happen, the haptic aid may even make the control task more difficult, instead of simplifying it.

To meet these requirements, a common approach is to mimic the human behavior: the haptic aid is designed to yield an open-loop transfer function similar to those given by the human operator during the tracking task without haptic aids [Mulder, 2007]. In the compensatory tracking task in Figure 2.1, the haptic open-loop transfer function is given by $H_{ha}H_{cd}H_{ce}$, while the human open-loop transfer function is $H_{con}H_{ce}$. Thus, a haptic aid that mimics the human behavior is given by:

$$H_{ha}H_{cd}H_{ce} = H_{con}H_{ce} \Rightarrow H_{ha} = \frac{H_{con}}{H_{cd}} \quad 2.2$$

In our experimental setup, the dynamics H_{ce} were chosen as a double integrator (as detailed in Section 2.5):

$$H_{ce} = \frac{K_{ce}}{s^2} \quad 2.3$$

where K_{ce} represents the gain of the controlled element. According to McRuer's theories, the human response to these dynamics is given by [McRuer and Weir, 1969]:

$$H_{con} = K_p(T_L s + 1)e^{-\tau_p s} \quad 2.4$$

where K_p , T_L , and τ_p are the human gain, the lead time constant and the visual time delay, respectively. The parameters K_p and T_L usually assume values such that Equation (2.1) holds around the crossover frequency ω_c . Based on Equation (2.2) and Equation (2.4), the dynamics of the haptic aid were chosen as:

$$H_{ha} = \frac{K_p(T_L s + 1)e^{-\tau_p s}}{H_{cd}} \quad 2.5$$

The values for the parameters in Equation (2.5) were chosen according to the following criteria. The parameter T_L approximated the lead time that humans assume for a double-integrator control. The value for T_L reported in previous works was 5 s [McRuer]. The visual delay τ_p was set to zero, to obtain a haptic response slightly faster than the human response (a typical value for human's visual delay is $\tau_p = 0.3$ s). The dynamics H_{cd} were approximated as a

static gain, since H_{cd} behaves like a gain at frequencies around ω_c where the model in Equation (2.4) is valid. The gain K_p was tuned such that the haptic force could be felt by the human operator, but at the same time could leave full authority to the human operator. The chosen value was $K_p = 2$.

Note that the chosen haptic dynamics provided low performance without the human operator in-the-loop. Thus, the human control action was still needed to perform the task.

2.4 Design of input-mixing control system

The haptic aid was compared to an “equivalent” input-mixing system IM. Specifically, the input-mixing system was designed to provide the same control action u as the haptic system considering the human operator *out-of-the-loop*. With this mind, H_{im} was obtained as:

$$H_{im} = H_{ha}H_{cd} = K_p(T_L s + 1) \quad 2.6$$

A further analysis is required to investigate what is the net effect of using the input-mixing system from the human’s point of view. The human operator is not aware of the control command from the input-mixing control, since it is provided directly to the controlled element. Furthermore, the effect of the input-mixing control on the roll angle ϕ_{ce} can not be deduced from the compensatory display, since the display does not show the roll angle but only the tracking error. Thus, the input-mixing system is obscured from the human operator.

By using block diagram algebra, the control task in Figure 2.1b can be rearranged as shown in Figure 2.2. Note that the block dynamics have been replaced by the corresponding transfer functions. The control task with the input-mixing system is equivalent to a control task where:

- the target trajectory ϕ_t is prefiltered with the filter H_t

$$H_t = \frac{1}{1 + H_{ce}H_{im}} \quad 2.7$$

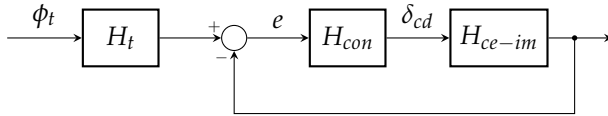


Figure 2.2: Prefilter H_t and equivalent dynamics H_{ce-im} for tracking task with the input-mixing system.

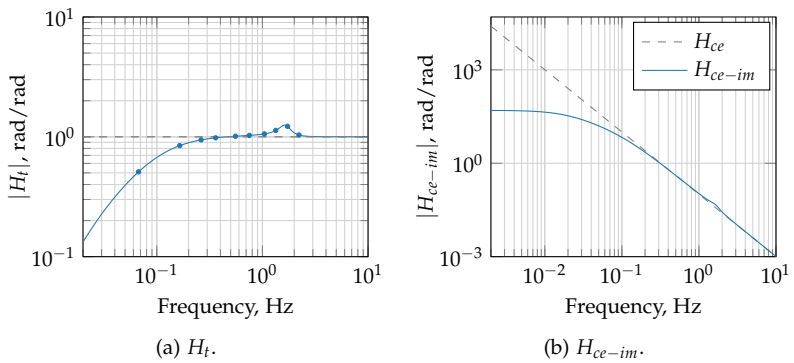


Figure 2.3: Prefilter H_t and equivalent dynamics H_{ce-im} for the tracking task with the input-mixing system.

- the controlled element has modified dynamics H_{ce-im} :

$$H_{ce-im} = \frac{H_{ce}}{1 + H_{ce}H_{im}}$$

2.8

Figure 2.3a and Figure 2.3b show magnitude of H_t and H_{ce-im} , respectively. Magnitude of H_t is lower than 1 at low frequencies, whereas it becomes slightly larger at frequencies around 1.5 Hz. Since most of the power of ϕ_t is concentrated at low frequencies (see Figure 2.5), the filtered trajectory becomes less demanding for the human operator. The modified dynamics H_{ce-im} is stable and behaves like a gain at low frequencies. The control of these dynamics is much easier compared to the double integrator in Equation (2.3). Thus, from the human's point of view, use of the input-mixing aid

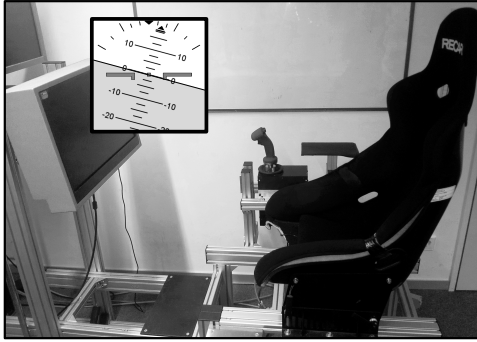


Figure 2.4: Apparatus.

drastically reduces the complexity of the compensatory tracking task.

2.5 Experiment setup

A human-in-the-loop experiment was performed to compare haptic and input-mixing aids. The experiment resembled control of an aircraft during a tracking task. This section details the experimental design.

2.5.1 Task and apparatus

The experimental task involved the tracking of a target trajectory of a roll angle. The tracking error e was presented on a high-resolution display from VPixx Technologies Inc., Canada, see Figure 2.4. The resolution of the display is 1920(H) x 1200(V) pixels, the refresh rate is 120 Hz. The error e was shown as the angular difference between the moving horizontal line and the fixed aircraft symbol. The vertical offset between the horizontal line and the aircraft symbol was kept to zero.

Participants controlled the roll angle of the aircraft with a control-loading sidestick from Wittenstein Aerospace & Simulation GmbH,

Germany. The dynamics of the sidestick resembled a mass-spring-damper system. The stiffness of the stick was set to 1.1 N/deg in accordance with previous works dealing with similar control tasks [Pool et al., 2008, 2011]. The mass and the damping parameters were set to the minimum available values. The resulting sidestick dynamics were:

$$H_{cd} = \frac{1}{0.0151 s^2 + 0.0616 s + 1.1} \quad [\text{deg/N}] \quad 2.9$$

Since the pitch axis of the sidestick was not used during the experiment, it was fixed in the zero position. An armrest was positioned close to the sidestick.

The aircraft roll attitude dynamics were chosen as:

$$H_{ce} = \frac{4}{s^2} \quad [\text{deg/deg}] \quad 2.10$$

The double integrator resembles the dynamics of a simplified roll attitude control of an aircraft [McRuer and Krendel]. The gain of H_{ce} was chosen to give optimal control authority on the roll angle.

A real-time computer running xPC Target (MathWorks, Inc.) was used to interface the flight display and the sidestick with the simulated aircraft dynamics. The update frequency of the real-time computer was 500 Hz.

2.5.2 Target trajectory

The target trajectory ϕ_t was selected as a multisine signal:

$$\phi_t(t) = \sum_{k=1}^{N_t} A_k \sin(2\pi f_k t + \psi_k) \quad 2.11$$

where A_k , f_k , and ψ_k are the amplitude, the frequency and the phase of the k^{th} sinusoidal component of the signal ϕ_t . The amplitudes A_k were distributed according to the absolute value of the following filter [Zaal et al., 2008]:

$$A_k = \left| \frac{(j2\pi f_k T_1 + 1)^2}{(j2\pi f_k T_2 + 2)^2} \right| \quad 2.12$$

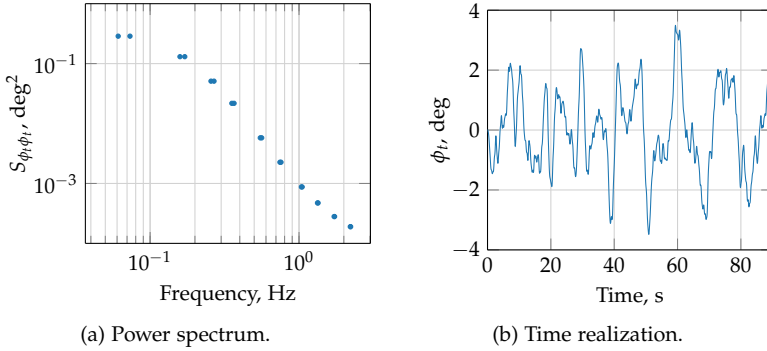


Figure 2.5: Target trajectory ϕ_t .

where $T_1 = 0.1$ s and $T_2 = 0.8$ s. The frequencies f_k were logarithmically spaced in the range $[0.05 - 3]$ Hz, which is sufficiently large to capture the dynamical properties of human response. Specifically, they were chosen as integer multiples of a base frequency f_0 , i.e. $f_k = k \cdot f_0$. To generate an integer number of periods in the measurement time, the base frequency f_0 was chosen as the inverse of the measurement time $T = 81.92$ s. The phases ψ_k were selected from a random set to yield an approximately Gaussian distribution of the values of ϕ_t [Zaal et al., 2008]. Finally, the time realization was scaled to have a power of 2 deg^2 . Figure 2.5 shows time realization and power spectrum of the resulting target trajectory.

2.5.3 Participants and experiment procedure

Six male participants between the age of 25 and 32 years were recruited for the experiment. All participants were affiliated with Max Planck Institute for Biological Cybernetics, three of them had previous experience with compensatory control tasks.

Before starting the experiment, participants were instructed to minimize the error shown in the compensatory display. They were informed about the possible presence of haptic forces on the control device, but no specific instructions were given on how to exploit

the haptic feedback. All participants performed three tracking conditions: tracking task without aids (NoA), with Haptic Aid (HA), and with Input-Mixing system (IM). The order of the conditions was randomized between participants according to a Latin Square Matrix. For each condition, participants performed some training trials until they reached a consistent level of performance. Then, four more trials were performed to collect measurement data. Each trial lasted 90 s, with regular breaks in between the trials. The whole experiment lasted around three hours.

2.5.4 Data collection and analysis

Time realizations of different signals were logged at 100 Hz during the experiment. These included the aircraft roll angle ϕ_{ce} , the human force F_{ho} , and the deflection of the stick δ_{cd} . To remove transients at the beginning of the trials, only the last 81.92 s of the measurements were considered for data analysis.

Several measures were calculated to investigate influence of haptic and input-mixing aids on human performance and control behavior. Human performances were evaluated by the variance of the tracking error $\sigma^2(e)$:

$$\sigma^2(e) = \frac{\sum_{k=1}^N [e(t_k) - \bar{e}]^2}{N}$$

2.13

where N indicates the number of time samples within an experimental trial, t_k is the k -th time sample, and \bar{e} is the mean value of e . Variances of the stick deflection δ_{cd} and of the human force F_{ho} were calculated as measures of human control activity.

To test statistical differences between variances in the three tracking conditions, a one-way repeated measurement ANalysis Of VAriance (ANOVA) was used. Post-hoc tests with Bonferroni correction were employed to perform pairwise comparisons. Values of $p < 0.050$ were considered highly significant, whereas values in the range $0.050 \leq p < 0.100$ were considered marginally significant.

Human control behavior was evaluated by estimating the open-loop dynamics of human operator and controlled element. Estimates

of human's open-loop responses were calculated by using a cross-spectra based method (CS method) [Pintelon and Schoukens, 2012]. The method estimates the human open-loop transfer response as:

$$\hat{H}_{ol}(f) = \frac{\hat{S}_{\phi_t \phi_{ce}}(f)}{\hat{S}_{\phi_{te}}(f)}, \quad f \in \{f_t\}. \quad 2.14$$

Here, \hat{S}_{vw} represents an estimate of the cross-spectra between the generic signals v and w , obtained as:

$$\hat{S}_{vw}(f) = V^*(f)W(f) \quad 2.15$$

where V, W are the Discrete Fourier Transform of v and w , respectively, and V^* is the complex conjugate of v . The coherence functions Γ^2 was used as a reliability indicator of the estimate [Pintelon and Schoukens, 2012]:

$$\Gamma^2(f) = \frac{|\hat{S}_{\phi_{te}}(f)|^2}{\hat{S}_{\phi_t \phi_t}(f) \hat{S}_{ee}(f)}, \quad f \in \{f_t\}. \quad 2.16$$

The coherence can assume values between 0.0 and 1.0. The maximum value 1.0 indicates that the measurements of e and ϕ_{ce} are linearly related and without noise, whereas smaller values indicate the presence of nonlinearities and noise. To reduce variance of the estimates, the time signals were averaged over the four trials and the resulting estimates over two adjacent frequency points [Wellstead, 1981].

Finally, crossover frequency f_c and neuromuscular peak of open-loop responses were calculated and statistically compared with ANOVA and post-hoc tests with Bonferroni correction. The crossover frequency f_c represents the bandwidth of the human response. High values of f_c imply a fast dynamic response and a higher ability to follow the tracking signal. On the other hand, high neuromuscular peaks represent stiff settings of the neuromuscular system and may induce unstable oscillations on the aircraft [Johnston and McRuer, 1987].

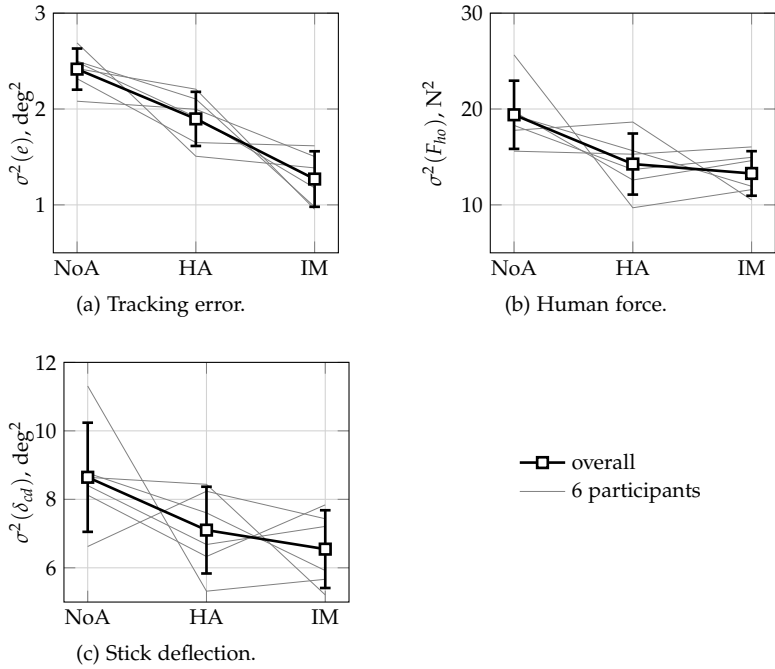


Figure 2.6: Mean and 95 % confidence intervals of $\sigma^2(\cdot)$ over all participants.

2.6 Results and discussion

This section presents results of the experimental comparison between haptic and input-sharing aids. Performance and control activity are contrasted between the three experimental tracking conditions. Furthermore, differences in the participants open-loop responses are investigated.

2.6.1 Performance and control activity

Participants performances were evaluated using the variance of the tracking error $\sigma^2(e)$. Figure 2.6a shows results of each participant (thin lines), together with means and 95 % confidence intervals

Table 2.1: Results of post-hoc tests with Bonferroni correction for $\sigma^2(\cdot)$ data.

Independent variables	Dependent measures					
	$\sigma^2(e)$		$\sigma^2(F_{ho})$		$\sigma^2(\delta_{cd})$	
Factor	p	Sig. ^a	p	Sig.	p	Sig.
NoA vs. HA	0.067	*	0.098	*	0.582	–
NoA vs. IM	0.003	**	0.078	*	0.239	–
HA vs. IM	0.086	*	1.000	–	1.000	–

a. **: highly significant ($p < 0.050$) * : marginally significant ($0.050 \leq p < 0.100$)
 –: not significant ($p \geq 0.100$)

(error bars). Results of ANOVA ($F(2, 10) = 10.627$, $p < 0.05$) and post-hoc tests with Bonferroni correction (Table 2.1) indicated that the differences between all conditions were statistically significant. Performance improved with haptic and input-mixing aids compared to the baseline condition without aids. However, the haptic did not yield same performance as the input mixing control, which reduced $\sigma^2(e)$ with almost 50% compared to NoA.

Variances of human force F_{ho} and stick deflection δ_{cd} were calculated as measures of participants control effort. Figure 2.6b and Figure 2.6c depict means and 95 % confidence intervals of $\sigma^2(F_{ho})$ and $\sigma^2(\delta_{cd})$, respectively. Human force was affected by the external aids ($F(2, 10) = 5.064$, $p < 0.05$). Post-hoc test with Bonferroni correction revealed a statistically significant difference between NoA and the other two tracking conditions (Table 2.1). This indicates that the aids allowed participants to significantly reduce the forces needed to control the controlled element. Furthermore, participants applied similar forces with HA and IM. The variance of the stick deflection was slightly lower for IM and HA conditions compared to NoA. However, no statistically significant difference was found between the three conditions ($F(2, 10) = 2.876$, $p = 0.103$).

Taken together, these findings indicate that both HA and IM aids helped participants perform the control task with reduced control effort. However, participants found it easier to control the augmented stable dynamics H_{ce-aut} , rather than the original unstable dynamics H_{ce} combined with the haptic forces.

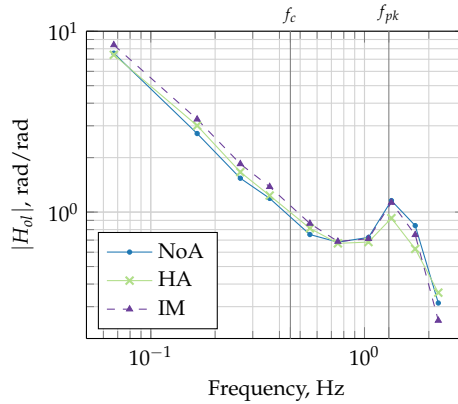


Figure 2.7: Estimated H_{ol} for participant 4.

2.6.2 Human's dynamic response

An analysis was made to look for influence of haptic and input-mixing aids on human open-loop responses. Figure 2.7 shows open-loop responses of participant 4. High coherence values indicated reliability of the estimates ($\Gamma^2(f) > 0.8$ for all $f \in \{f_i\}$). Note that these responses are representative for all participants.

All estimates closely followed integrator-like dynamics at frequencies close to the crossover frequencies f_c where $|H_{ol}(f_c)| = 1$. This is consistent with McRuer theories, indicating that McRuer theories can still be applied when haptics or automation are employed in the control loop.

The crossover frequency f_c was found to be influenced by the presence of external aids ($F(2,10) = 5.122$, $p = 0.029$), see Figure 2.8a. Post-hoc tests with Bonferroni correction revealed that IM was statistically different from the other two conditions. This is in complete agreement with the higher performance found for the IM system.

Figure 2.8b shows that neuromuscular peaks $H_{ol}(f_{pk})$ decreased with HA, where f_{pk} indicates the frequencies where the peaks occur. Although the ANOVA test revealed a marginally significant effect

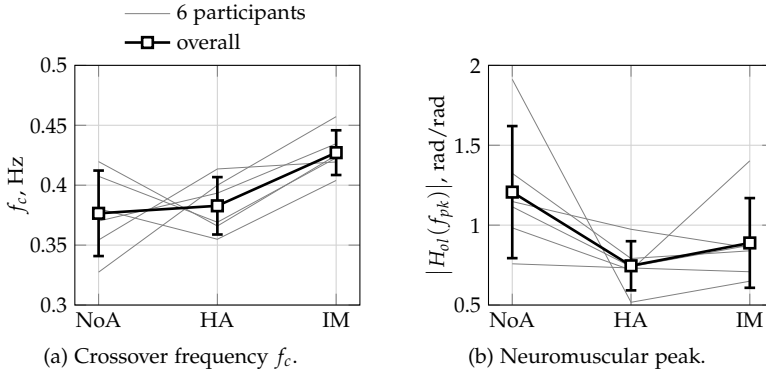


Figure 2.8: Mean and 95 % confidence intervals of f_c and neuromuscular peak $H_{ol}(f_{pk})$ over all participants.

Table 2.2: Results of post-hoc tests with Bonferroni correction for f_c and $|H_{ol}(f_{pk})|$.

Independent variables	Dependent measures			
	f_c		$ H_{ol}(f_{pk}) $	
Factor	p	Sig. ^b	p	Sig.
NoA vs. HA	1.000	—	0.207	—
NoA vs. IM	0.131	—	0.659	—
HA vs. IM	0.008	**	0.807	—

b.** : highly significant ($p < 0.050$) * : marginally significant ($0.050 \leq p < 0.100$)
 — : not significant ($p \geq 0.100$)

($F(2, 10) = 3.198, p = 0.084$), post-hoc tests for pairwise comparisons did not result in statistically significant differences between the conditions due to the large variance in the NoA and IM conditions.

2.7 Conclusions

To investigate the effects of haptic and input-mixing aids on performances and control behavior, two equivalent haptic and input-mixing systems were designed and tested in a compensatory tracking task. Performance, control effort, and humans control behavior were evaluated and compared to a baseline condition without external aids.

Participants significantly improved their performance with the haptic and input-mixing aids compared to the baseline condition. However, the input-mixing system outperformed the other two conditions. Both external aids allowed participants to perform the task by applying lower forces, indicating decreased control effort.

Participants realized the benefits of input-mixing and haptic systems by adapting their open-loop responses in different ways. The input-mixing aid led to an increased crossover frequency, whereas the haptic system reduced the peak of the neuromuscular system.

On effects of failures of input-mixing and haptic aids

Although input-mixing systems may yield better performance compared to haptic aids, it is not very well understood what happens in the event of a failure of the support systems. This chapter investigates how failures of haptic and input-mixing systems influence human's performance. An experiment was conducted in which participants performed a compensatory tracking task with haptic and input-mixing aids. Half of experimental trials were affected by a failure of the support system, which corresponded to a complete removal of the support action. Results showed that after failures of both support systems, participants experienced a sudden decrease of performances. However, loss of performance was much larger with the input-mixing aid. Surprisingly, participants with haptic aid were able to approximately return to performance levels they had just before the failure. Instead, participants with the input-mixing aid could not re-gain pre-failure levels of performance.

The contents of this chapter are based on:

- Paper title** On effects of failures in haptic and automated pilot support systems
- Authors** Maimeri, M., Olivari, M., Bühlhoff, H. H., and Pollini, L.
- Published in** Proceedings of the AIAA Modeling and Simulation Technologies Conference, AIAA SciTech, January 2016

3.1 Introduction

INPUT-MIXING aids help the human operator perform a specific control task by providing a feedback signal directly into the controlled element. Although input-mixing aids generally help the human operator improve performance, they have some disadvantages due to the fact that the human operator is not aware of the feedback signal [Abbink and Mulder, 2010]. For instance, the human operator may not recognize failures of the input-mixing aid, or may not be able to recover before an accident would occur. These outcomes have been known as Out-Of-The-Loop (OOTL) performance problems [Endsley and Kiris, 1995; Kaber and Endsley, 1997].

Haptic aids have been put forth as an appropriate solution to OOTL problems [Abbink et al., 2008, 2012; Goodrich et al., 2011; de Stigter et al., 2007]. Such aids communicate their control action by exerting tactile feedback on the control device. Human operators are always aware of haptic control action and always remain in-the-loop. So far, however, only theoretical considerations have been presented regarding effectiveness of using haptic aids for overcoming OOTL problems.

The goal of this chapter is to experimentally investigate whether the transparency of haptic feedback can be useful for overcoming OOTL problems. Specifically, this chapter focuses on OOTL problems that may occur after a *failure* of the pilot support system. The considered failure is a total loss of support action, due for instance to a broken sensor, a broken actuator, etc. To achieve the goal, an experiment was conducted where participants performed a compensatory tracking task with haptic and input-mixing aids. Sudden failures of haptic and input-mixing aids were simulated, and control performances were evaluated before and after the failures occurred.

The chapter is structured as follows. Section 3.2 presents the design of the haptic aid and of the input-mixing system for a compensatory tracking task. Section 3.3 describes the experiment, followed by the experimental results in Section 3.4. Finally, conclusions are drawn.

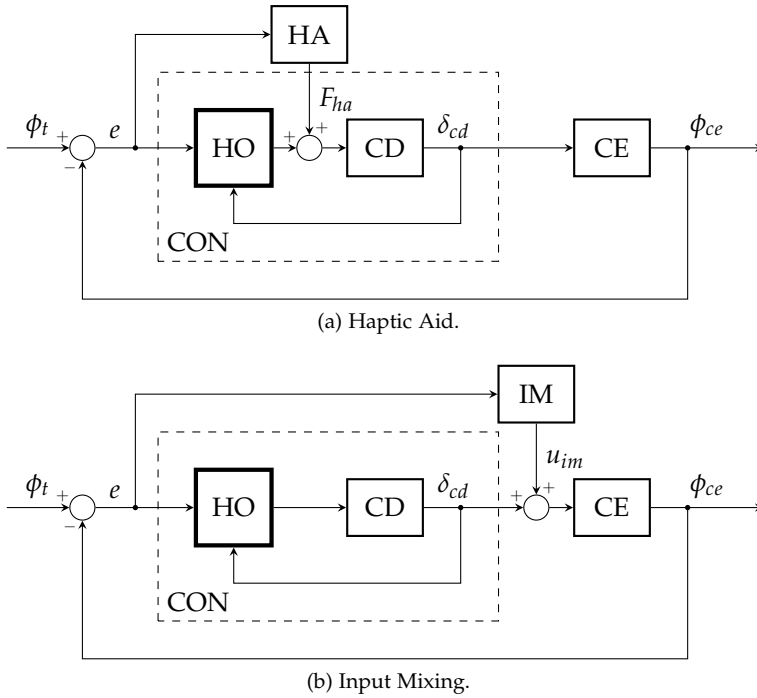


Figure 3.1: Compensatory tracking task with external aids.

3.2 Design of external aids and simulated failure

This chapter focuses on the design of aids for a compensatory tracking task in the roll axis, as depicted in Figure 3.1. The task is to track the target signal ϕ_t by minimizing the tracking error e between ϕ_t and the roll angle ϕ_{ce} of the controlled element CE. The roll angle ϕ_{ce} is controlled by the lateral deflection δ_{cd} of the control device CD. The tracking error is presented on a compensatory display.

When using the haptic aid HA, the force feedback F_{ha} guides the human operator according to a possible control strategy, see Figure 3.1a. Note that the human operator HO can feel the haptic forces through the variations that they cause on the stick deflection δ_{cd} .

When using the input-mixing aid IM instead, the additional command u_{im} is directly provided into the controlled element, see Figure 3.1b. The human operator is not aware of the command u_{im} and can only see the effects it has on the controlled element. As explained in Section 2.4, the input-mixing aid has the net result of augmenting the closed-loop dynamics of CE, resulting in easier to control dynamics.

3.2.1 Haptic aid design

The haptic aid was designed to generate forces on the stick that suggest a possible control strategy [Alaimo et al., 2010]. A commonly used approach for designing such haptic feedback is to mimic the human behavior: the haptic forces are designed to be similar to those given by the human operator during the tracking task without haptic aids [Mulder, 2007].

Pilot behavior in a compensatory tracking task has been extensively investigated in literature. McRuer provided quantitative models that describe the human response to the tracking error for different controlled elements [McRuer; McRuer and Weir, 1969]. These models assess that humans adapt their response such that the open-loop transfer function between the tracking error e and the roll angle ϕ_{ce} resembles an integrator-like dynamics at frequencies around the crossover frequency ω_c :

$$H_{con}H_{ce} = \frac{\omega_c e^{-s\tau_p}}{s} \quad 3.1$$

Here, the parameter τ_p represents the human visual delay and H_{block} represents the transfer function of BLOCK. Specifically, H_{con} is the human control response from the tracking error e to the stick deflection δ_{cd} . Note that H_{con} includes both dynamics of the human operator and of the control device, see Figure 3.1.

According to Equation (3.1), the control dynamics H_{con} change based on the dynamics of the controlled element H_{ce} . In our experimental setup, H_{ce} was chosen as:

$$H_{ce} = \frac{K_{ce}}{s(s+1)} \quad 3.2$$

where K_{ce} represents the gain of the controlled element. The control response to these dynamics is given by [McRuer and Weir, 1969]:

$$H_{con} = \frac{\omega_c}{K_{ce}}(s+1)e^{-\tau_p s} = K_p(s+1)e^{-\tau_p s} \quad 3.3$$

where K_p is the human static gain. Large values of K_p correspond to large crossover frequencies ω_c , resulting in a faster human response.

To obtain similar open-loop dynamics as in Equation (3.3), the haptic aid was chosen as follows:

$$H_{ha}H_{cd} = H_{con} \quad \Rightarrow \quad H_{ha} = \frac{K_p(s+1)e^{-\tau_p s}}{H_{cd}} \quad 3.4$$

The values for the parameters in Equation (3.4) were chosen slightly different from those typically estimated for humans in a tracking task. The visual delay τ_p was set to zero, to obtain a haptic response slightly faster than the human response (typical values for humans are $\tau_p = 0.3$ s). The gain K_p was tuned experimentally such that the haptic force could be felt by the human operator, but at the same time could leave them full control authority. The control device H_{cd} was approximated by its static gain, since H_{cd} behaves like a gain at frequencies around ω_c where the model in Equation (3.3) is valid.

3.2.2 Input-mixing aid design

The input-mixing aid was designed to provide an “equivalent” level of support as the haptic aid, i.e., to provide the same control action as the haptic aid when the human operator was *out-of-the-loop*. With this mind, the dynamics of input-mixing aid were chosen as:

$$H_{im} = H_{ha}H_{cd} = K_p(s+1) \quad 3.5$$

As mentioned in Section 2.4, the control task with the input-mixing system is equivalent to a control task where the dynamics of the controlled element are:

$$H_{ce-im} = \frac{H_{ce}}{1 + H_{ce}H_{im}} \quad 3.6$$

The resulting dynamics H_{ce-im} are significantly different and much easier to control than the original dynamics H_{ce} .

3.2.3 Failure

Failures of haptic and input-mixing aids are considered as sudden disengages of the systems. For the haptic aid, the failure is simulated by setting the haptic feedback F_{ha} to zero. After the failure, the human operator is not anymore provided with haptic feedback and has to manually control the aircraft.

For the input-mixing aid, the failure is simulated by setting the feedback signal u_{im} to zero. After the failure, the human operator switches from controlling the augmented dynamics H_{ce-im} to manually controlling the un-augmented aircraft dynamics H_{ce} .

3.3 Experiment setup

A human-in-the-loop experiment was designed to investigate how failures of haptic and input-mixing aids affect human performance.

3.3.1 Apparatus and control task

In the experiment, participants performed a compensatory tracking task in the roll axis. The tracking error was shown as the roll angle of the Primary Flight Display (PFD) in Figure 3.2. All other indicators of the PFD were kept fixed to zero.

A control-loaded sidestick developed at University of Pisa was used to control the simulated roll dynamics, see Figure 3.2. The longitudinal axis of the sidestick was fixed at the centered position, whereas the lateral axis was free to move with dynamics H_{cd} . More technical details about the sidestick can be found in Pollini et al. [2016]. A soft armrest was positioned close to the sidestick.

3.3.2 Target trajectory

The target trajectory ϕ_t was chosen as a multisine signal:

$$\phi_t(t) = \sum_{k=1}^{N_t} A_k \sin(2\pi f_k t + \psi_k)$$



Figure 3.2: Apparatus.

where A_k , f_k , and ψ_k are the amplitude, the frequency and the phase of the k^{th} sinusoidal component. The amplitudes A_k were chosen as follows [Zaal et al., 2008]:

$$A_k = \left| \frac{(j2\pi f_k T_1 + 1)^2}{(j2\pi f_k T_2 + 2)^2} \right| \quad 3.8$$

where $T_1 = 0.1$ s and $T_2 = 0.8$ s. The frequencies f_k were multiples of a base frequency $f_0 = 1/81.92$ Hz, chosen to be logarithmically spaced between 0.06 Hz and 3 Hz. The phases ψ_k were selected from a random set to yield an approximately Gaussian distribution of the values of ϕ_t [Zaal et al., 2008]. The resulting time realization was scaled to have a power of 0.04 rad^2 . Figure 3.3 shows the time realization and the power spectrum of the resulting signal.

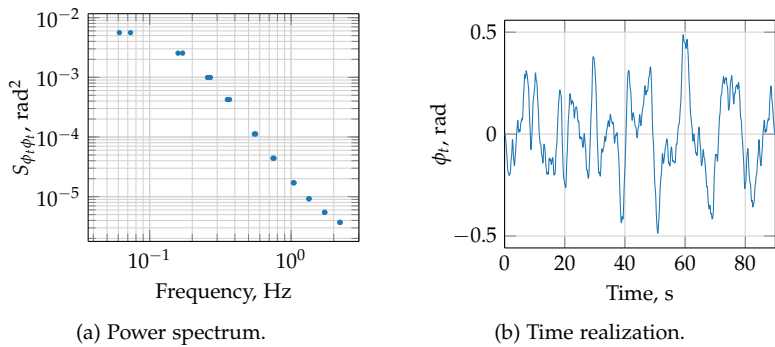


Figure 3.3: Target trajectory ϕ_t .

3.3.3 Participants and experimental procedure

Ten participants (9 males, 1 female) between the age of 25 and 27 years were recruited for the experiment. All participants were affiliated with University of Pisa, none of them had previous experience with compensatory control tasks. Before starting the experiment, participants were instructed to minimize the error shown in the compensatory display. They were informed about the possible presence of haptic forces on the control device, but no specific instructions were given on how to exploit the haptic force.

All participants performed three tracking conditions: tracking task without aids (NoA), with the haptic aid (HA), and with the input-mixing system (IM). The order of the conditions was randomized between participants according to a Latin Square Matrix. For each condition, participants performed some training trials until they reached a consistent level of performance. Then, 10 more trials were performed to collect measurement data. Each trial lasted 90 s, and regular breaks were taken in between the trials.

In 5 of the 10 trials of IM and HA conditions, sudden failures of the external aid were simulated. The failures happened at random time instants between 25 s and 55 s. To minimize differences between trials with different failure times, the target trajectory ϕ_t

was translated such that the failure happened exactly at the same position of ϕ_t for all trials.

3.3.4 Measures

Time realizations of the tracking error e were logged with a sample frequency $f_s = 100$ Hz. Then, the cumulative squared error e_{cum}^2 was calculated:

$$e_{cum}^2(t_{k_0}, t_{k_f}) = \frac{\sum_{k=k_0}^{k_f} e^2(t_k)}{f_s} \quad 3.9$$

where t_{k_0} and t_{k_f} indicate initial and final time samples.

In addition, human's performance was evaluated by using the windowed Mean Square Error (MSE_w):

$$MSE_w = \frac{\sum_{k=k_w}^{k_w+N_w} e^2(t_k)}{N_w} \quad 3.10$$

where t_{k_w} is the first time sample of the window, and N_w is the number of time samples within the window. The MSE_w was calculated for three different time windows: 20 s before the fault (*steady condition*), first 10 s after the fault (*recovery phase*), and successive 10 seconds (*new steady condition*).

Note that MSE_w can be written as:

$$MSE_w = \frac{e_{cum}^2(t_{k_w}, t_{k_w+N_w}) f_s}{N_w} = \frac{e_{cum}^2(t_{k_w}, t_{k_w+N_w})}{\Delta t_w} \quad 3.11$$

where Δt_w represents the time length of the window. Thus, MSE_w corresponds to the average slope of the cumulative error over the time window.

3.3.5 Hypotheses

In trials without failures, IM and HA aids are expected to yield better performance compared to the condition without aids. Furthermore, participants are expected to perform better with IM than with HA.

In trials with failure, the MSE_w is expected to suddenly increase after the failure of both IM and HA systems, i.e., during the recovery

phase. However, participants are expected to recover quicker after the failure of the HA system than of the IM system. Thus, during the new steady condition phase, MSE_w is hypothesized to be smaller for the HA condition than for the IM condition.

3.4 Results and discussion

This section presents results of the human-in-the-loop experiment. First, the section illustrates results obtained in the trials without failure, to investigate capability of the designed aids to actually support participants in performing the task. Successively, effects of failures on human performances are investigated.

3.4.1 No failure

Figure 3.4 shows the cumulative squared error e_{cum}^2 of a sample participant in the conditions without aid (NoA), with haptic aid (HA) and with input-mixing system (IM). The errors were averaged over the different trials without failure (5 for HA and IM, 10 for NoA). As expected, HA and IM aids helped the participant achieve better performance compared to the condition without external aids. Furthermore, performance with IM was better than with HA.

3.4.2 Failure

Figure 3.5 and Figure 3.6 show the cumulative errors in cases where the input-mixing system and the haptic aid failed, respectively. Failure times are shown as vertical dashed lines. In addition, dashed lines indicate the averaged e_{cum}^2 obtained in the trials without failure. After the failure of IM system, the change in the slope of e_{cum}^2 is evident. On the other hand, e_{cum}^2 did not present an evident change in slope after the failure of HA.

To obtain a general overview of e_{cum}^2 trends across different trials, the traces of e_{cum}^2 were translated so that the failure instant happened at time $t = 0$ for all trials. Then, two 20 s windows were considered before and after the failure, and error traces were averaged over trials. The cumulative errors were virtually reset at $t = -20$ and

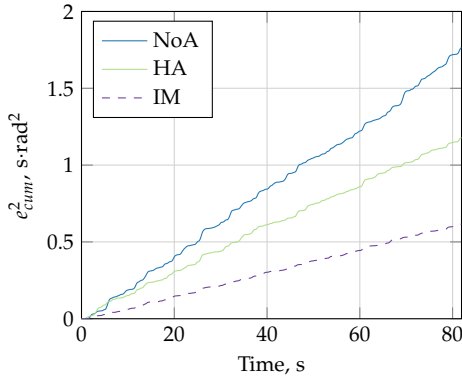


Figure 3.4: Cumulative squared errors e_{cum}^2 , averaged over runs without failures.

$t = 0$ to facilitate slope comparisons. Figure 3.7 shows the resulting e_{cum}^2 curves for a sample participant. The IM condition presented a net increase of error slope after the failure. This yielded to a final cumulative error even larger than in the NoA condition. On the other hand, the HA condition did not present a noticeable change of slope after the failure.

To investigate whether the results obtained for the sample participant stand for all other participants, windowed MSE_w were calculated for all participants before failures, soon after failures, and long after failures. Figure 3.8 shows the MSE_w obtained for each participant (marks), together with means across different participants (thick lines). In the first time window, both IM and HA systems allowed participants to achieve smaller MSE_w compared to the NoA condition. Specifically, MSE_w was smaller with the IM system than with the HA. Note that MSE_w presented a lower dispersion in the IM condition, indicating that pilots performed similarly well when using the IM system. This may be due to a limited contribution of the pilot in performing the control task.

In the second time window, the failures of IM and HA systems caused an evident increase of the MSE_w . This sudden decrease of

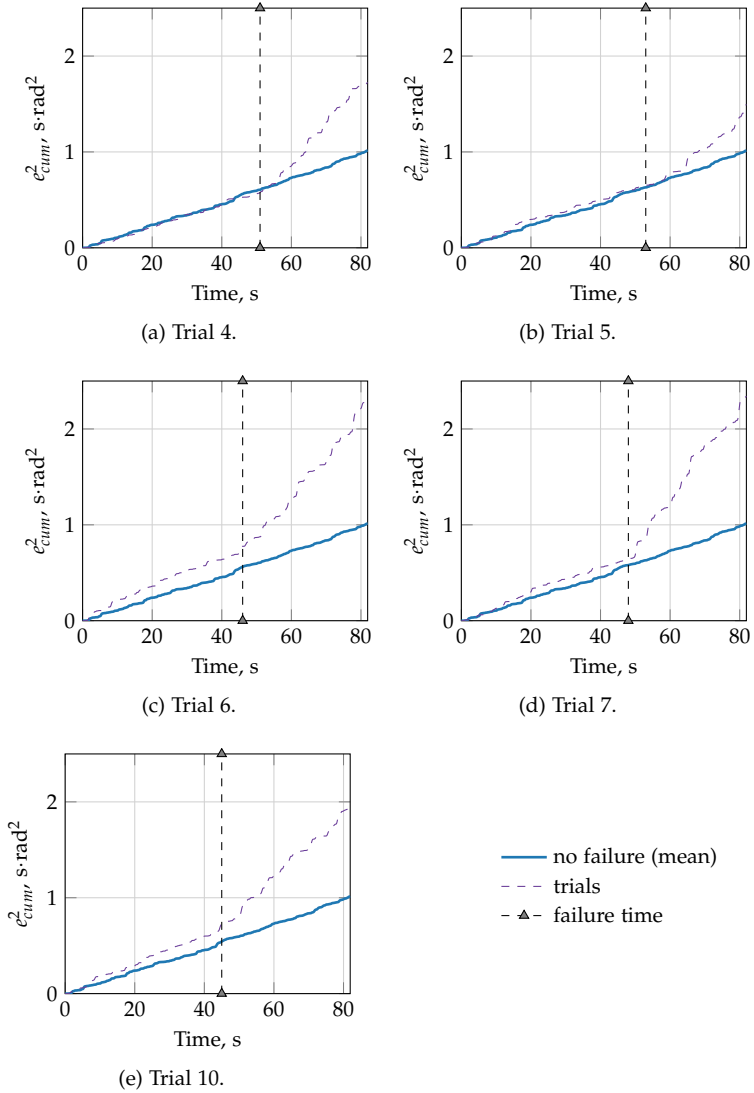


Figure 3.5: Cumulative squared error e_{cum}^2 for a sample participant during IM condition.

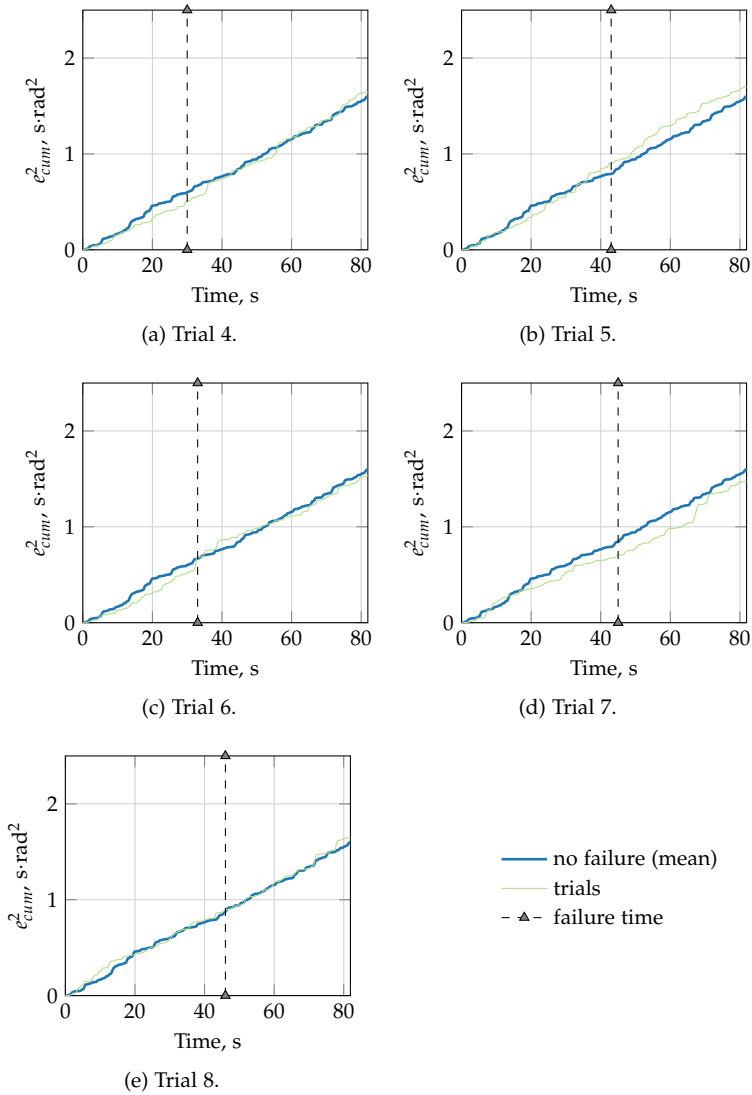


Figure 3.6: Cumulative squared error e_{cum}^2 for a sample participant during HA condition.

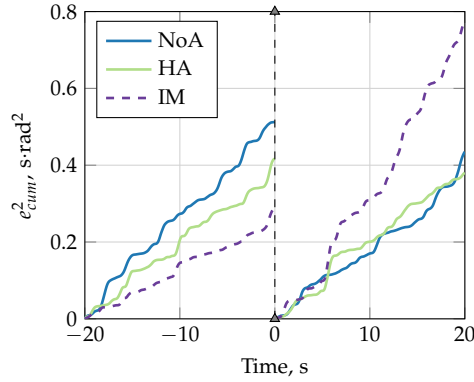


Figure 3.7: Cumulative squared error for a sample participant before and after failures, averaged over trials. Note that the e^2_{cum} curves were translated over time, such that failures happened at $t = 0$ for all trials.

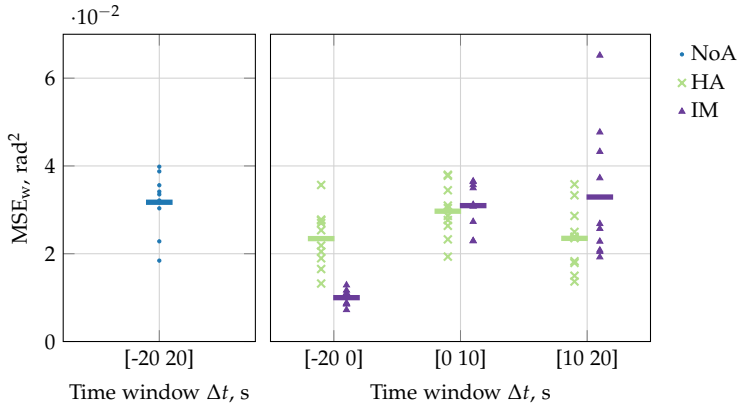


Figure 3.8: Windowed Mean Square Errors MSE_w before, soon after and after the fault. Each marker represents the mean slope of a single subject over different trials. Thick lines are the average slopes amongst all participants.

performance was expected, since participants needed some time to notice the failure and to react to it.

In the third time window, participants that were using the IM system were not able to recover similar levels of performance they had before the failure. Furthermore, although the mean of MSE_w was similar to the NoA condition, the dispersion was larger. This indicates that many participants were not able to adapt their control strategy to the new dynamics of the controlled element. On the other hand, pilots that were using the HA were able to recover similar levels of performance they had before the failure. These levels of performance were on average better than those obtained in the NoA case. Presumably a training effect may be responsible for this result: participants may have learnt from the haptic aid how to control the controlled element, so that they were able to maintain similar levels of performance as before the HA failure.

3.5 Conclusions

This chapter has presented a study on the effect of failures of haptic (HA) and input-mixing (IM) support systems. Ten participants performed a compensatory tracking task without external aids, with HA or with IM system. Failures of the external aids were simulated as total loss of the external feedback signal. Experimental results indicated that participants better recovered from HA failure than from failure of the IM system. Surprisingly, participants using HA were able to recover similar levels of performance they had before the failure. This may mean that haptic feedback helped participants learn the control task. However, this possibility requires further investigation.

Evaluation of haptic support system for training purposes

This chapter investigates whether haptic feedback can be used to help humans learn a specific control task. An experiment was performed where participants performed a compensatory tracking task. Participants were divided into two groups: the haptic group and the no-aid group. The haptic group performed a first training phase with haptic feedback and a second evaluation phase without haptic feedback. The no-aid group performed the whole experiment without haptic feedback. Results indicated that haptic group achieved better performance than the no aid group during the training phase. Furthermore, performance of haptic group did not worsen in the evaluation phase when the haptic feedback was turned off. On the other hand, the no-aid group needed more experimental trials to achieve similar performance to the haptic group. These findings indicate that haptic feedback helped participants learn the task quicker.

The contents of this chapter are based on:

- Paper title** Evaluation of haptic support system for training purposes in a tracking task
- Authors** D’Intino, G., Olivari, M., Geluardi, S., Venrooij, J., Innocenti, M., Bülthoff, H. H., and Pollini, L.
- Submitted to** Proceedings of the IEEE International Conference on Systems, Man and Cybernetics, Budapest, Hungary, October 2016

4.1 Introduction

Haptic aids are attracting increasing interest as pilot support systems in steering tasks. Such aids provide a tactile feedback on the control device that suggests a possible right control action to the human operator [Alaimo et al., 2010]. Benefits of haptic aids were shown in terms of improved performance and reduced control effort compared to unaided manual control [Abbink et al., 2011; Mulder et al., 2008b].

Recent works have attempted to use haptic feedback to help the human operator learn a specific control task. The rationale is that haptic feedback may facilitate learning the control task by directly showing a correct control strategy. However, inconclusive evidence was provided by previous studies on the advantages of haptic feedback on training.

In studies on motor learning, haptic feedback was found to enhance training effectiveness. For instance, Feygin et al. [2002] investigated use of haptic aids for learning a complex 3D motion. A haptic feedback was designed to guide participants through an ideal 3D motion. The designed haptic aid was tested in a human-in-the-loop experiment, where participants learned the 3D motion under three different training conditions: visual, haptic and haptic plus visual. Haptic feedback was found to help participants reproduce 3D motion. In a different study, a haptic feedback was used for learning a task that required recalling of a sequence of forces [Morris et al., 2007]. Participants were guided along a predefined trajectory and were asked to recall a sequence of force along the trajectory. Three training modalities were tested: visual, haptic and visual plus haptic training. The visuohaptic training produced more accurate force recall than the other two training conditions.

Differently, a null effect of haptic training was shown in a number of studies on manipulation of virtual objects. Yokokohji et al. [1996] evaluated use of haptic feedback to support human operators in learning the manipulation of a cube in a virtual environment. First, an expert operator performed a cube manipulation in a virtual environment, and the applied forces and cube positions/velocities were recorded. Then, the recorded measurements were used to train

a second non-expert human operator to replicate the cube motion. Training with the haptic feedback did not improve replication of cube motion. The authors suggested that this may be due to the simplicity of the task. In a different study, a target-hitting task was considered [O' Malley et al., 2006]. Participants used a joystick to control a virtual mass and hit fixed targets, and the haptic feedback was used to actively demonstrate a desired motion. Results indicated that haptic support was not beneficial for enhancing training effectiveness, probably due to the relatively low complexity of the task.

Recently, haptic aids have been employed to train humans in controlling specific dynamic systems. In Honing et al. [2014], the control of an excavator in a pursuit task was considered. An experiment was performed where participants learned to control the excavator either with or without haptic aid during training. Then, performances were evaluated during an evaluation phase without haptic aid. Performances of both groups were similar, indicating that the haptic feedback did not enhance training effectiveness. The authors of the study suggested this was probably due to the simplicity of excavator dynamics. In a different work, a haptic feedback was designed with the aim of improving driver's skill in backward parking [Tada and Wada, 2015]. Experimental results indicated that the haptic feedback helped the drivers achieve better parking performances.

The aim of this chapter is to investigate the influence of a haptic support system on training of a human operator on a compensatory tracking task [McRuer]. A human-in-the-loop experiment was conducted where participants performed a compensatory tracking task. Participants were split into two groups. The first group performed a training phase with haptic feedback, and an evaluation phase without external aids. The second group performed the whole experiment without external supports. Performance were compared between the two groups, to investigate whether the haptic aid helped participants to learn the task.

This chapter is structured as follows. Section 4.2 outlines the design and a preliminary evaluation of the haptic feedback. Section 4.3 presents the experimental setup and results. The chapter ends with discussions and conclusions.

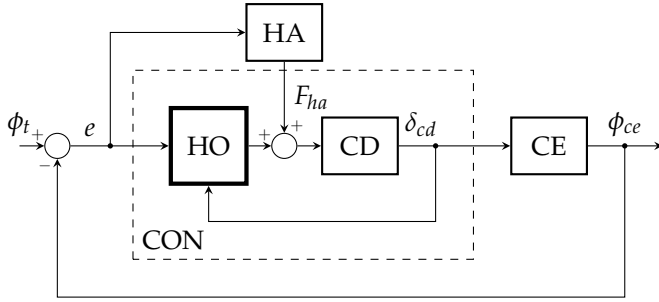


Figure 4.1: Compensatory tracking task with haptic aid.

4.2 Design of haptic aid for training

This section presents the design of a haptic support system for a compensatory tracking task. Great care is taken in tuning some parameters to obtain a control task and a haptic support system suitable for training purposes.

4.2.1 Compensatory tracking task

A compensatory tracking task was used to investigate the possibility of using a haptic support system for training. Figure 4.1 shows a model of the compensatory tracking task. The task is to minimize the tracking error e between the target trajectory ϕ_t and the roll angle ϕ_{ce} of the controlled element CE. The human operator HO can control CE by manipulating the deflection δ_{cd} of the control device CD. Only the tracking error is shown on a compensatory display. Throughout this chapter, the transfer function of each BLOCK is referred to as H_{block} .

The dynamics of the controlled element determine the difficulty of the control task. Too difficult dynamics would require a long training before participants could actually perform the control task. On the other hand, too easy dynamics would not highlight possible benefits of the haptic aid on training [O' Malley et al., 2006; Yokokohji et al., 1996]. In this paper, the dynamics of H_{ce} were chosen easy enough to allow participants to learn the task after a

small number of trials, but difficult enough to highlight differences between training with and without the haptic aid. According to previous studies, dynamics that satisfy these requirements can be obtained as [McRuer]:

$$H_{ce} = \frac{K_{ce}}{s(s+1)} \quad 4.1$$

4.2.2 Haptic aid design

The haptic aid was designed to suggest a possible control strategy to the human operator. A common design approach is to mimic pilot dynamic response [Mulder, 2007]. According to McRuer's theories, pilots adapt their response such that the open-loop transfer function between the tracking error e and the aircraft roll angle ϕ_{ce} resembles an integrator-like dynamics around the crossover frequency ω_c [McRuer].

$$H_{con}H_{ce} = \frac{w_c e^{-s\tau_p}}{s} \quad 4.2$$

where τ_p is the visual time delay, and H_{con} represents the pilot control response between the tracking error e and the control device deflection δ_{cd} . Note that H_{con} includes pilot responses and dynamics of the control device H_{cd} , see Figure 4.1.

The haptic aid transfer function was chosen to yield open-loop dynamics that resemble the crossover model in Equation (4.2):

$$H_{ha}H_{cd}H_{ce} = \frac{w_c e^{-s\tau_p}}{s} \quad 4.3$$

Substituting Equation (4.1) into Equation (4.3), we obtain:

$$H_{ha} = \frac{K_{ha}w_c}{K_{ce}} \frac{(s+1)e^{-s\tau_p}}{H_{cd}} = \bar{K}_{ha} \frac{(s+1)e^{-s\tau_p}}{H_{cd}} \quad 4.4$$

where K_{ha} is an additional gain used to scale the force feedback, and \bar{K}_{ha} is the resulting static gain of H_{ha} . The parameters τ_p and \bar{K}_{ha} were tuned as follows. The time delay τ_p was set to 0 to yield a haptic response slightly faster than the human response. The

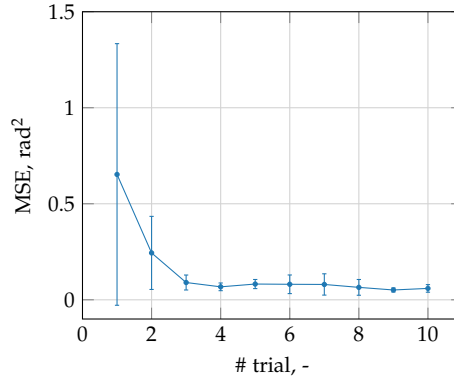


Figure 4.2: Evolution of the Mean Squared Errors in following trials. Markers and errorbars indicate means and standard deviations over different participants, respectively.

gain \bar{K}_{ha} was set large enough to generate forces that can be felt by the human operator, while still leaving full-control authority to the human operator. Based on these considerations and on preliminary studies, the gain \bar{K}_{ha} was set equal to 2.

4.2.3 Preliminary evaluation of the haptic feedback

A preliminary experiment was performed to evaluate the number of trials needed to achieve steady performance in the compensatory tracking task with the haptic aid. Five participants performed 10 trials of the compensatory tracking task. The target roll trajectory was chosen as a multisine, see Figure 4.3, while haptic and controlled element dynamics were chosen as in Equation (4.4) and Equation (4.1), respectively. Performance was evaluated by using the Mean Squared Error (MSE):

$$\text{MSE} = \frac{\sum_{k=1}^N e^2(t_k)}{N}$$

4.5

where N is the number of time samples.

Figure 4.2 shows MSEs obtained for different trials, averaged over participants. Means and standard deviations decreased during

the first 3 trials, indicating that participants were still learning the control task. After the fourth trial, means and standard deviations of MSE achieved steady values. Thus, participants needed 4 trials to learn the compensatory tracking task with haptic feedback.

4.3 Experimental setup and results

An experiment was performed to evaluate the effect of using the designed haptic feedback for learning purposes. This section presents experimental setup and results.

4.3.1 Control task, target trajectory, and apparatus

Participants performed a compensatory tracking task in the roll axis. The target roll angle ϕ_t was chosen as a multisine signal:

$$\phi_t(t) = \sum_{k=1}^{N_t} A_k \sin(2\pi f_k t + \psi_k) \quad 4.6$$

The amplitudes A_k were distributed according the following filter [Zaal et al., 2008]:

$$A_k = \left| \frac{(j2\pi f_k 0.1 + 1)^2}{(j2\pi f_k 0.8 + 2)^2} \right| \quad 4.7$$

The frequencies f_k were chosen as integer multiples of a base frequency $f_0 = 1/81.92$ Hz and were logarithmically spaced in the range between 0.06 Hz and 3 Hz. The phases ψ_k were selected from a random set to yield an approximately Gaussian distribution of the values of ϕ_t [Zaal et al., 2008]. Figure 4.3 shows the time realization and the power spectrum of the resulting signal.

When performing the task, participants were seated on a chair in front of a display with refresh rate of 100 Hz. The display showed the artificial horizon in Figure 4.4. Only the roll axis of the artificial horizon was free to move, showing the roll tracking error. A sidestick developed at University of Pisa was used to control the roll dynamics of the controlled element. The longitudinal axis of the sidestick was fixed at the center position, whereas the lateral axis was free to move.

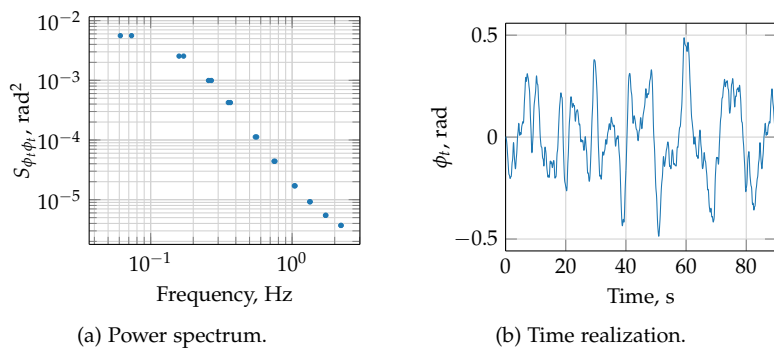


Figure 4.3: Target trajectory ϕ_t .



Figure 4.4: Apparatus.

Participants held the sidestick using the right hand and positioning their elbow on a soft armrest, see Figure 4.4.

4.3.2 Participants and experimental procedure

Twenty participants (17 males, 3 females) performed the experiment. All participants were affiliated with University of Pisa, none of them had previous experience with compensatory tracking tasks. Before starting the experiment, participants were informed about the experimental goal.

Participants were split into two groups of 10 participants. The first group performed 9 runs of the compensatory tracking task without support. The second group performed a first training phase using the haptic aid and a following evaluation phase without support. The number of trials for the training phase was set to 4 based on the preliminary evaluation of the haptic feedback, see Figure 4.2. The number of trials for the evaluation phase was set to 5.

4.3.3 Measures

A number of measures were considered for evaluating participants' performances. A first measure was obtained by calculating the MSE in Equation (4.5). To highlight how MSE correlates with the evolution of the squared tracking error e^2 , Figure 4.5a shows a typical trend of e^2 together with the corresponding MSE. Although the error e^2 oscillates around the MSE, the dispersion of e^2 is small and the MSE can be considered representative of e^2 along the whole trial. However, in our experiment performance is evaluated during a training phase where participants are learning the control task. During the training phase, participants are more prone to generate wrong control commands, which would result in sudden increases of e^2 in a small amount of time, see Figure 4.5b. The MSE is largely influenced by these sudden increases of e^2 , and it deviates from the actual trend that the error e^2 has in time intervals when participants do not generate wrong control commands.

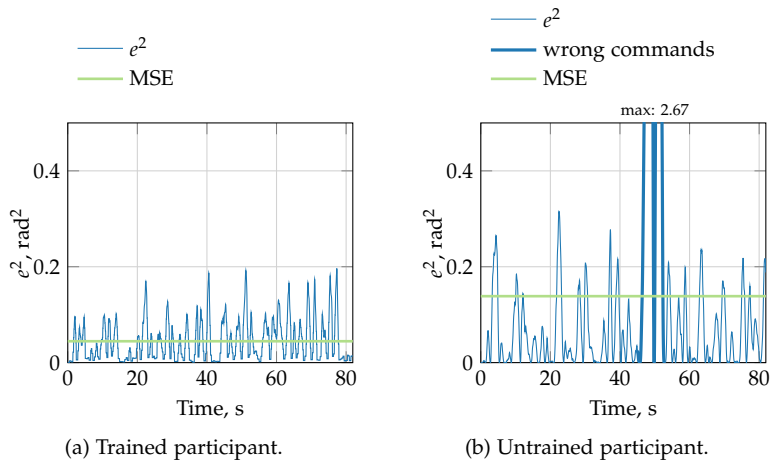


Figure 4.5: Typical trends of the squared cumulative error e^2 .

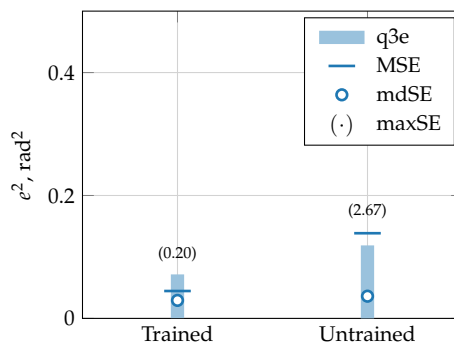


Figure 4.6: Distributions of the values of the squared error e^2 for trained and untrained participants.

To better describe the trend of the error e^2 , we considered additional performance measures:

- the median of e^2 (mdSE). The median is lightly influenced by outliers that correspond to sudden increases of e^2 . Thus, the

median can be considered as a measure for the actual trend of e^2 .

- the third quartile of e^2 (q3SE). The third quartile represents the data point at the 75th percentile. This means that about 75% of the data lie below q3SE. Small values of q3SE indicate that 75% of e^2 values were close to the median mdSE along the whole experimental trail.
- the maximum value of e^2 (maxSE). The maximum value maxSE accounts for the sudden increases of e^2 due the wrong commands during the trials.

Figure 4.6 shows means MSE, medians mdSE, third quartiles q3SE, and maximum values maxSE for the distributions of e^2 values shown in Figure 4.5. The medians mdSE and the third quartiles q3SE are similar for untrained and trained participants, indicating that they are not influenced by wrong control commands given by the untrained participant. On the other hand, the mean MSE and the maximum value maxSE are larger for the untrained participant, indicating that they account for the large increases of e^2 due to wrong control commands.

The measures MSE, mdSE, q3SE and maxSE were calculated for each participant. To obtain a general analysis for all participants, median and percentiles were calculated for all the considered measures across all participants. First, the between-participants variability was removed by correcting the data such that average over different trials was the same for all participants of each group [Cousineau, 2005]. Then, the following overall measures were calculated for the corrected MSE, mdSE, q3SE and maxSE: the median, the first and third quartiles (Q1 and Q3, respectively), and the interquartile range $IQR=Q3-Q1$. In the following figures, these overall measures are represented by box-whiskers plots. On each box, the circle indicates the median over different participants, the bottom and the top edges of the box indicate first and third quartiles, the top and the bottom ends of the whisker indicate the highest and the lowest datum still

within 1.5 of the interquartile range. All the data not included between the whiskers are considered as outliers and plotted as circle markers.

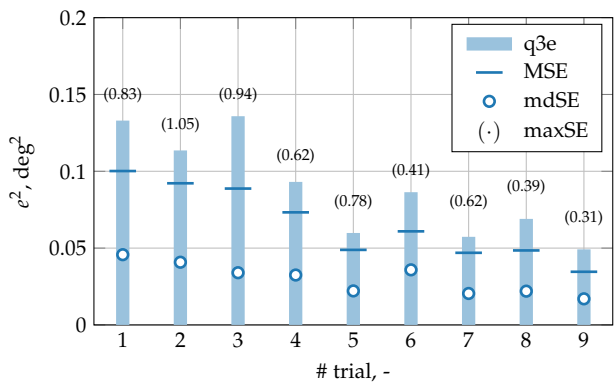
4.3.4 Hypotheses

All participants are hypothesized to need some trials to learn the task. Thus, performance measures are expected to improve with successive trials for both groups of participants. However, haptic feedback is expected to help participants learn the task quicker. This means that the haptic group (HA) is expected to achieve steady performances faster than the group without haptic feedback (NoHA group).

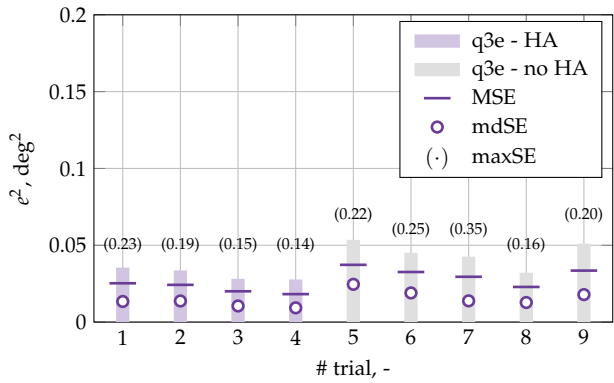
4.3.5 Results

Figure 4.7a and Figure 4.7b show the distributions of e^2 values obtained by two sample participants belonging to NoHA and HA groups, respectively. The NoHA participant performed the control task without external aids, while the HA participant performed the first 4 trials with haptic feedback and the following 5 trials without external aids. For the NoHA participant, all performance measures (MSE, mdSE, q3SE, and maxSE) progressively decreased with successive trials, before achieving approximately steady values after the 7th trial. This indicates that the participant required almost all experimental trials to learn the control task. On the other hand, the HA participants already achieved approximately steady performance in the training phase. Furthermore, the HA participant did not show a large performance deterioration after the haptic feedback was turned off.

Figure 4.8 shows boxplots for the mean squared errors MSE over all participants. The NoHA participants progressively improved their MSE with successive trials (smaller median values), before achieving approximately constant performance in the last three trials. High values of MSE in trials 4 and 6 may indicate that some participants generated wrong control commands. On the other hand, the HA participants achieved approximately constant MSE already



(a) Sample participant of the NoHA group.



(b) Sample participant of the HA group.

Figure 4.7: Evolutions of the distributions of e^2 values.

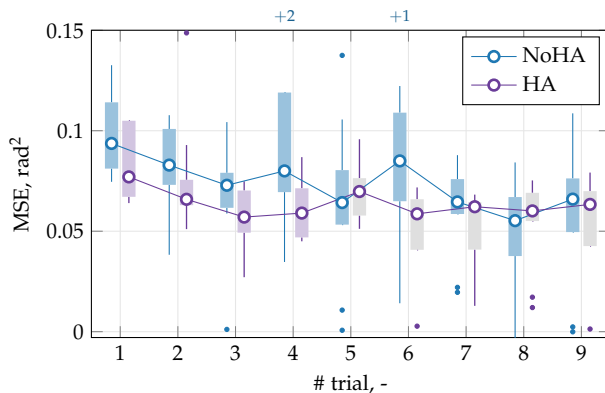


Figure 4.8: Evolutions of the mean MSE for all participants.

after the third trial. Although the MSE slightly increased in trial 5 when the haptic feedback was turned off, HA participants were able to recover same levels of MSE already in trial 6.

In the first 4 trials, the median of the MSE for the NoHA group was larger than the top of the boxes for the HA group. This indicates that 75% of HA participants were able to obtain better performance than 50% of NoHA participants. Thus, haptic feedback helped participants perform the control task. When the haptic feedback was turned off in trial 4, the MSE of the HA group increased to similar levels to the NoHA group. However, already in trial 6, HA participants were able to recover and to maintain similar performance achieved in the first four trials. On the other hand, participants of NoHA group needed 7 trials to achieve similar performances to the HA group.

As highlighted in the previous section, the MSE is largely influenced by sudden increases of the error e^2 caused by wrong control commands. For this reason, the MSE may not give a useful description of the actual trend of e^2 during the experimental trial. This not the case for the median mdSE and the third quartile q3SE, which are more robust to sudden increases of e^2 . Figure 4.9 and Figure 4.10 show boxplots of mdSE and q3SE over all participants. Trends of

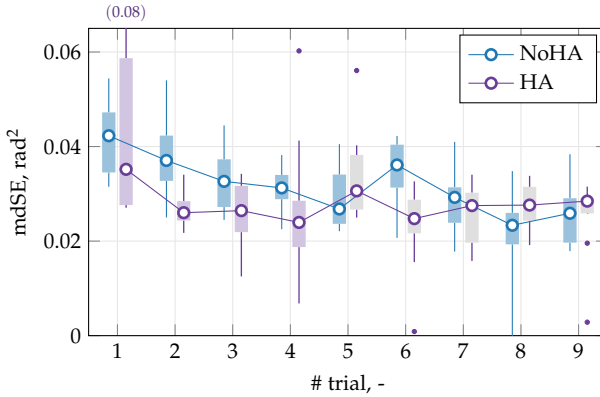


Figure 4.9: Evolution of the median mdSE for all participants.

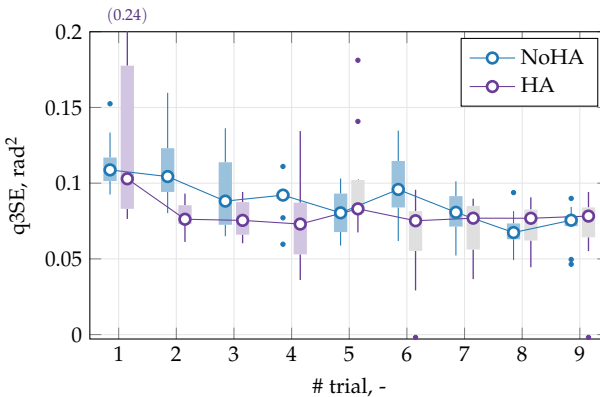


Figure 4.10: Evolution of the third quartile q3SE for all participants.

mdSE and q3SE resembled the trends obtained for the MSE. The haptic feedback helped participants obtain small values of e^2 in the first 4 trials. Although performance of HA degraded when the haptic aid was turned off, the HA group was able to recover previous levels of performance already in the trial 6. On the other hand, NoHA participants needed 7 trials to achieve similar mdSE and

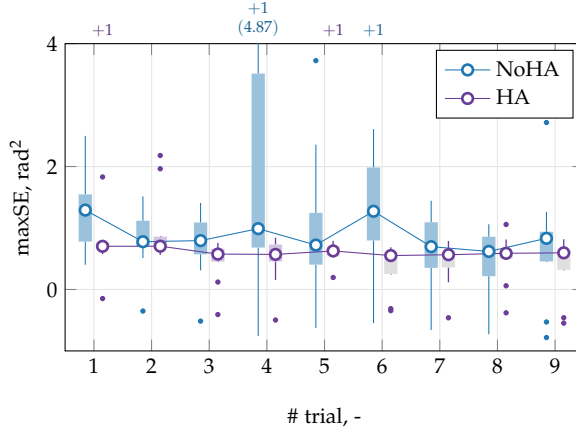


Figure 4.11: Evolution of the maximum value maxSE for all participants.

q3SE as the HA group. It is worth noting that, contrary to the MSE, mdSE and q3SE did not largely increase in the trial 4 as the MSE. This indicates that the large MSE in trial 4 was caused by sudden increases of e^2 generated by some participants.

To highlight the presence of sudden increases of e^2 , the maximum values maxSE were calculated. In all trials, the medians of maxSE were larger for the NoHA group than for the HA group. Furthermore, the boxes (first and third quartiles) and the whiskers ($1.5 \times \text{IQR}$) were large for the NoHA group, indicating a large variability between participants. Thus, several participants of the NoHA group were prone to generate wrong control commands. On the other hand, the HA group showed small boxes and whiskers. This means that most participants of the HA group were able not to generate sudden increases of the tracking error.

4.4 Conclusions

This chapter investigated effects of using haptic feedback for learning a compensatory tracking task. Two groups of subjects performed a compensatory tracking task. The first group performed the task

with a haptic feedback during the training phase and without haptic feedback during the evaluation phase. The second group was not supported by any haptic aid.

Participants that were trained with haptic feedback were less likely to exhibit wrong control commands during the control task compared to participants that were not supported by the haptic aid during the training phase. Haptic feedback helped the HA group learn faster the control strategy and to achieve stable performance earlier. Furthermore, performance of HA group did not worsen when the haptic feedback was turned off.

Part II

Identifying time-invariant neuromuscular response in multi-loop tasks

Methods for identifying time-invariant neuromuscular responses in multi-loop tasks

A quantitative insight into human's dynamic responses is required for a human-centered design of haptic feedback. This chapter proposes identification methods to estimate the neuromuscular and visual responses of a multi-loop model of the human operator. A conventional and widely used technique for simultaneous identification of the neuromuscular and visual systems makes use of cross-spectral density estimates. This chapter shows that this technique provides biased estimates when a specific non-interference hypothesis is not fulfilled. Furthermore, two methods are proposed that do not have the same limitation. The first method is based on ARX models, whereas the second one combines cross-spectral estimators with interpolation in the frequency domain. Offline simulations confirmed that classic method fails when the non-interference hypothesis is not fulfilled, whereas the two proposed techniques give reliable estimates. Finally, the three identification methods were applied to experimental data with human-in-the-loop. The two proposed techniques gave comparable estimates, different from those obtained by the classic method. The differences matched those found with the simulations.

The contents of this chapter are based on:

- | | |
|---------------------|---|
| Paper title | Methods for multi-loop identification of visual and neuromuscular pilot responses |
| Authors | Olivari, M., Nieuwenhuizen, F. M., Venrooij, J., Bülthoff, H. H., and Pollini, L. |
| Published in | IEEE Transactions on Cybernetics, Vol. 45, No. 12, December 2015 |

5.1 Introduction

DESIGN of haptic feedback is a critical issue, since it determines its effectiveness on improving human's performance and reducing control effort. Although many approaches were different in nature, human operators were able to quickly get acquainted with haptic feedback, learn how to exploit it to increase their performance, and adapt their responses to the specific type of haptic aid [Abbink et al., 2011; Profumo et al., 2013]. Since humans can adapt their responses over a large range, an effective design of haptic aid requires accurate knowledge of human adaptation to the provided continuous haptic feedback. This chapter seeks to address how to model and estimate the human responses in control tasks with continuous haptic feedback.

Quasi-linear models are commonly used to describe human behavior in various control tasks [Hess, 1981; McRuer; McRuer and Jex, 1967]. These models represent human behavior with linear describing functions combined with a remnant signal to account for non-linearities. When haptic aids are used and tactile information is provided in addition to presenting visual information, the tactile perception channel needs to be modeled as an additional input to the human operator. A multi-loop quasi-linear model that meets this requirement was developed by van Paassen et al. [2004]. This model is characterized by two control loops, one describing the visual perception channel and one describing the tactile information processed by the neuromuscular system. Identifying the neuromuscular and visual responses would provide quantitative insights into the human adaptation to the haptic feedback.

To identify human visual and neuromuscular responses, identification techniques are needed that account for the multi-loop nature of the task. A commonly used technique is based on Cross Spectral (CS) analysis [Pintelon and Schoukens, 2012]. This technique has been initially applied to neuromuscular system estimation for tasks in which human visual feedback is not involved and the human operator is essentially a single-input single-output system [Abbink, 2007].

Recently, Abbink et al. [2011] and Damveld et al. [2009] applied the method to estimate neuromuscular system in control tasks with visual feedback. Two mutually uncorrelated forcing functions, a visual reference trajectory and a force disturbance, were inserted in the feedback loop to estimate the neuromuscular and visual dynamics. The contribution of force disturbance in the visual error was implicitly assumed to be negligible, i.e., the force disturbance used for identification was assumed not to interfere with the visual feedback. Unfortunately, this *non-interference* assumption is not always verified. As a sufficiently high Signal-to-Noise Ratio (SNR) is required for the identification procedure, the power of the force disturbance cannot be decreased such that its effect on the visual feedback is not actually perceived by the human operator.

This chapter shows that the commonly used CS method may provide biased estimates when the non-interference assumption is not fulfilled. Two novel identification methods are presented, which also produce reliable estimates when the force disturbance influences the visual error. In the first method (*ARX method*), a multi-loop Auto-Regressive model with eXogenous inputs (ARX) is used to fit the measured data in the time domain. A similar identification procedure was successfully applied for a different control task [Nieuwenhuizen et al., 2008]. The second method (*CS-ML method*) makes use of the Cross Spectral density analysis like the conventional method, but does not require the non-interference assumption. Numerical simulations and human in-the-loop experiment are performed to provide supportive evidence of the reliability of the two novel methods.

The chapter is structured as follows. Section 5.2 presents a model that describes the human operator in a tracking task with haptic aids. Section 5.3 and Section 5.4 illustrate the theoretical basis of the three adopted identification methods, followed by a set of off-line Monte Carlo simulations in Section 5.5. Subsequently, Section 5.6 shows an experimental validation of the proposed identification methods. Finally, conclusions are drawn.

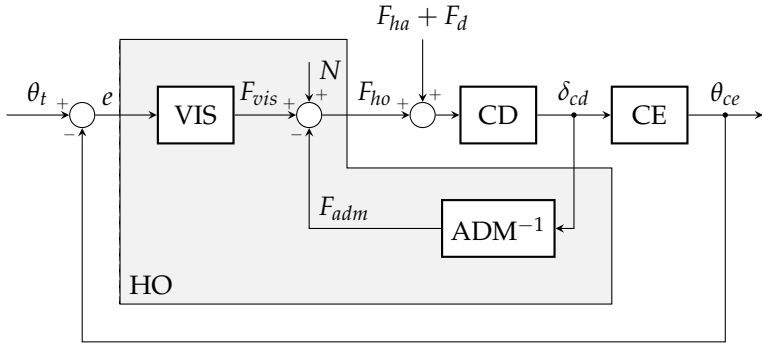


Figure 5.1: Compensatory tracking task, in which a human operator controls the controlled element CE through a control device CD. The human operator HO is described with a visual (VIS) and a neuromuscular response (the inverse of the admittance ADM), combined with the remnant signal N .

5.2 Pilot model and control task description

This paper focuses on a compensatory tracking task in the pitch axis. In such task, the human operator is asked to follow a reference pitch signal θ_t by compensating for the tracking error e . When haptic aids are used, additional tactile information is provided to the human operator for achieving the control task. To assess the influence of this second input on the human operator, the visual and tactile perception channels need to be modelled separately.

A multi-loop model that meets these requirements was developed by van Paassen et al. [2004], see Figure 5.1. The human operator HO is described by two control loops, the outer describing the visual response, whereas the inner loop describes the neuromuscular response. The neuromuscular response is represented by the inverse of the arm admittance ADM, defined as the dynamic relationship between the force acting on the arm and the position of the arm [Abbink et al., 2011]. The visual system VIS and the neuromuscular response ADM both contribute to the total human force F_{ho} . The visual and the neuromuscular responses are assumed to be linear and time-invariant., and nonlinearities in human's responses are

accounted for by the remnant signal N [McRuer and Jex, 1967]. In the rest of the chapter, the notation H_{block} is used to indicate the transfer function of BLOCK.

The haptic force F_{ha} represents any additional force feedback provided by the haptic aid. In the field of guidance haptic aids, the haptic system is generally designed as a standard compensator, which continuously provides forces that aim at achieving a certain control task [Mulder et al., 2011a]. Referring to the compensatory tracking task shown in Figure 5.1, the haptic compensator is commonly designed to regulate the tracking error e to zero. Throughout this paper, we will consider the dynamics of the haptic compensator equal to zero for the purposes of developing the identification techniques. This simplification does not affect the generality of the developed identification methods, since they are easily extensible to the case of non-zero haptic aid dynamics.

5.3 Conventional identification technique

This section describes the identification technique, based on cross-spectral analysis, that is commonly used to estimate the human responses of the model shown in Figure 5.1. To simultaneously estimate the admittance and the visual response, two deterministic forcing functions need to be inserted into the loop: the target pitch angle θ_t , which represents the reference trajectory that the human operator has to track, and the force disturbance F_d , which represents a continuous force disturbance that the human operator can feel on the control device.

Great care must be paid on tuning of the forcing functions, as the presence of human in the control loop poses constraints on their power content. The amount of power and the bandwidth should not be too high, to prevent changes in the human control strategy. At the same time, they should not be too low in order to ensure an accurate estimate. To satisfy both conflicting constraints simultaneously, a trade-off has to be found.

5.3.1 Forcing functions design

The two forcing functions θ_t and F_d were designed as multisine signals [Schouten et al., 2008a]:

$$\theta_t(t) = \sum_{k=1}^{N_t} A_{t,k} \sin(2\pi f_{t,k}t + \psi_{t,k}) \quad 5.1$$

$$F_d(t) = \sum_{k=1}^{N_d} A_{d,k} \sin(2\pi f_{d,k}t + \psi_{d,k}) \quad 5.2$$

Each frequency $f_{d,k}$ and $f_{t,k}$ was chosen as an integer multiple of the base frequency, which is defined as the inverse of the measurement time of the forcing function. In this case, all measurements lasted 81.92 s, corresponding to a base frequency of 0.0122 Hz.

Simultaneously applying two forcing functions requires a method that allows distinguishing their contribution in the measurements. A well-documented method consists of assigning different sets of discrete points in the available frequency range to F_d and θ_t [Abbink, 2006]. Figure 5.2a shows the frequency separation of the two forcing signals used in this research. Each set of frequency points is composed of a cluster of two adjacent frequencies to allow for frequency averaging during estimation.

For both forcing functions, the phases ψ_k were chosen randomly to obtain unpredictable behavior. A cresting technique was applied to avoid peaks in the time domain [Pintelon and Schoukens, 2012]. This technique minimizes the cresting factor, which is defined as the maximum amplitude of the signal divided by the Root Mean Square of the signal. By minimizing the cresting factor, the power of the signal can be higher without increasing the signal amplitude. The increased signal power generally results in better Signal-to-Noise Ratios, and, consequently, in better estimates.

The choice of signal amplitudes must account for human limitations. For the target position θ_t , the sinusoidal amplitudes at high frequencies should not be too large, since the pilot must be able to follow them. The amplitude distribution was chosen to match the

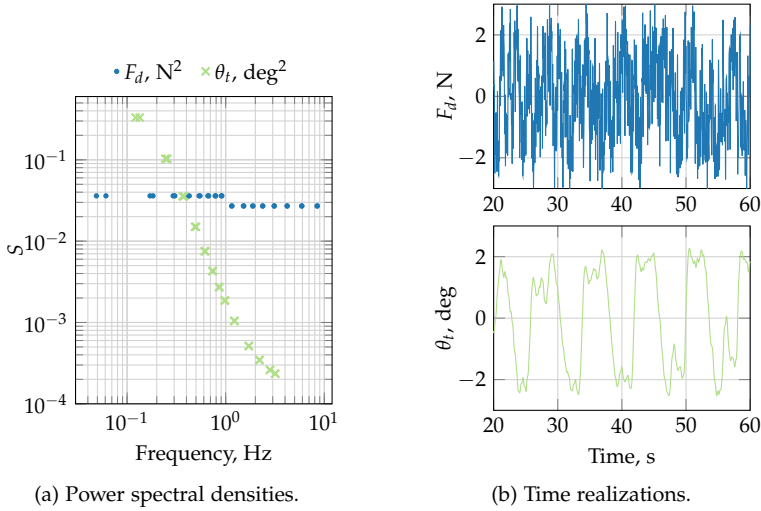


Figure 5.2: Forcing signals θ_t and F_d .

frequency response of the following filter [Zaal et al., 2008]:

$$A_{t,k} = \left| \frac{(j2\pi f_{t,k}T_1 + 1)^2}{(j2\pi f_{t,k}T_2 + 2)^2} \right| \quad 5.3$$

where $T_1 = 0.1$ s and $T_2 = 0.8$ s.

The amplitudes for F_d were tuned to reach a trade-off between two conflicting objectives: they have to be low enough not to disturb the human operator during the tracking task, but still allow distinguishing their contribution in the measurements. Furthermore, the “Reduced Power Method” was used [Mugge et al., 2007], see Figure 5.2a. The principle of this method is to apply a reduced power level at higher frequencies, to allow estimation in a wide range of frequencies without influencing the control behavior of the human operator.

The multisine time signals were obtained from their spectra using the inverse Fourier Transform. Table 5.1 lists the base-frequency multiple k , the actual frequency f_k , the amplitude A_k and the phase

Table 5.1: Frequencies, amplitudes, and phases defining the disturbance and target forcing functions.

Disturbance F_d				Target θ_t			
k	$f_{d,k}$	$A_{d,k}$	$\phi_{d,k}$	k	$f_{t,k}$	$A_{t,k}$	$\phi_{t,k}$
(-)	(Hz)	(N)	(rad)	(-)	(Hz)	(rad)	(rad)
4	0.0488	0.3810	1.3875	10	0.1221	0.0198	-0.7003
5	0.0610	0.3810	2.5511	11	0.1343	0.0198	2.2216
14	0.1709	0.3810	2.7917	20	0.2441	0.0111	4.5432
15	0.1831	0.3810	-0.4228	21	0.2563	0.0111	4.3424
24	0.2930	0.3810	-2.9281	30	0.3662	0.0065	4.5408
25	0.3052	0.3810	-1.8836	31	0.3784	0.0065	6.6869
34	0.4150	0.3810	-3.6960	40	0.4883	0.0042	4.6231
35	0.4272	0.3810	-4.1771	41	0.5005	0.0042	5.8999
44	0.5371	0.3810	-2.6694	50	0.6104	0.0030	8.3374
45	0.5493	0.3810	-3.5128	51	0.6226	0.0030	7.1502
54	0.6592	0.3810	-2.6805	60	0.7324	0.0023	7.4114
55	0.6714	0.3810	-0.1215	61	0.7446	0.0023	5.1712
64	0.7813	0.3810	2.9424	70	0.8545	0.0018	8.4636
65	0.7935	0.3810	2.8250	71	0.8667	0.0018	9.6620
74	0.9033	0.3810	-0.0129	80	0.9766	0.0015	8.6567
75	0.9155	0.3810	-1.2966	81	0.9888	0.0015	9.8456
94	1.1475	0.3302	2.2066	100	1.2207	0.0011	8.1844
95	1.1597	0.3302	2.0687	101	1.2329	0.0011	8.1368
124	1.5137	0.3302	0.1803	140	1.7090	0.0008	5.7817
125	1.5259	0.3302	0.4412	141	1.7212	0.0008	6.0687
154	1.8799	0.3302	3.8712	180	2.1973	0.0006	9.5528
155	1.8921	0.3302	3.7964	181	2.2095	0.0006	10.5519
194	2.3682	0.3302	0.4953	230	2.8076	0.0006	7.6383
195	2.3804	0.3302	1.6589	231	2.8198	0.0006	8.0429
254	3.1006	0.3302	2.1529	260	3.1738	0.0005	7.0004
255	3.1128	0.3302	-0.8407	261	3.1860	0.0005	6.3912
344	4.1992	0.3302	-0.2912				
345	4.2114	0.3302	2.0218				
484	5.9082	0.3302	4.7341				
485	5.9204	0.3302	8.1897				
694	8.4717	0.3302	5.8242				
695	8.4839	0.3302	9.2787				

ϕ_k of each of the sine in the forcing functions, and Figure 5.2b shows sample realizations of F_d and θ_t .

5.3.2 Cross-spectral density analysis

A common method for identification of control behavior is based on Cross-Spectra analysis (*CS method*). This approach has previously been used for pilots in a pitch tracking task [Damveld et al., 2010, 2009] and for car drivers in a car following task [Abbink, 2006].

In a closed multi-loop system like in Figure 5.1, the best linear approximation of the human admittance can be calculated as [Pintelon and Schoukens, 2012]:

$$\hat{H}_{adm}(f) = \frac{\hat{S}_{F_d \delta_{cd}}(f)}{\hat{S}_{F_d F_{adm}}(f)}, \quad f \in \{f_d\} \quad 5.4$$

where $\{f_d\}$ is the set of frequencies in which F_d has power, $\hat{S}_{F_d \delta_{cd}}$ and $\hat{S}_{F_d F_{adm}}$ are the estimated cross-spectral densities between F_d and δ_{cd} and between F_d and F_{adm} , respectively.

The CS method assumes linearity of the human admittance. The validity of this assumption can be checked with the squared coherence function defined as [Pintelon and Schoukens, 2012]:

$$\hat{\Gamma}^2(f) = \frac{|\hat{S}_{F_d \delta_{cd}}(f)|^2}{\hat{S}_{F_d F_d}(f) \hat{S}_{\delta_{cd} \delta_{cd}}(f)}, \quad f \in \{f_d\} \quad 5.5$$

The coherence function $\hat{\Gamma}$ equals 1.0 when the system is linear and there is no noise, and approaches 0.0 when no linear relation is found.

To estimate the cross-spectral density $\hat{S}_{F_d F_{adm}}$ in Equation (5.4), the time realization of the force F_{adm} must be known. Unfortunately, only the total human force F_{ho} on the control device can be measured, which is given by the sum of F_{adm} and F_{vis} (and the remnant noise N). To overcome this issue, if it is assumed that the visual response F_{vis} does not contain power at frequencies in $\{f_d\}$, the force F_{adm} at frequencies $\{f_d\}$ can be approximated with the human force F_{ho} measured at frequencies $\{f_d\}$. In this case, the admittance at frequencies $\{f_d\}$ can be estimated given measurements of δ_{cd} , F_d and F_{ho} as:

$$\hat{H}_{adm}(f) = \frac{\hat{S}_{F_d \delta_{cd}}(f)}{\hat{S}_{F_d F_{adm}}(f)} \approx \frac{\hat{S}_{F_d \delta_{cd}}(f)}{\hat{S}_{F_d F_{ho}}(f)}, \quad f \in \{f_d\} \quad 5.6$$

Note that only if the power of the tracking error e is zero for all frequencies $\{f_d\}$ does F_{vis} not contain power at frequencies in $\{f_d\}$. This is because the visual response H_{vis} in Figure 5.1 is considered linear. Therefore, to apply the common identification method, it must be assumed that the power of the tracking error e must be zero for all frequencies $\{f_d\}$: the *non-interference* assumption.

When the non-interference assumption is not fulfilled and F_{adm} cannot be approximated with F_{ho} , the estimator in Equation (5.6) actually estimates a transfer function different from the admittance. The estimated Frequency Response Function (FRF) can be written as:

$$\begin{aligned}\hat{H}_{adm}(f) &= \frac{\hat{S}_{F_d\delta_{cd}}(f)}{\hat{S}_{F_dF_{ho}}(f)} = \frac{\hat{S}_{F_d\delta_{cd}}(f) / \hat{S}_{F_dF_d}(f)}{\hat{S}_{F_dF_{ho}}(f) / \hat{S}_{F_dF_d}(f)} \\ &= \frac{\hat{H}_{F_d\delta_{cd}}(f)}{\hat{H}_{F_dF_{ho}}(f)}, \quad f \in \{f_d\}\end{aligned}\tag{5.7}$$

where $\hat{H}_{F_d\delta_{cd}}$ is the FRF from F_d to δ_{cd} , and $\hat{H}_{F_dF_{ho}}$ is the FRF from F_d to F_{ho} . Note that the transfer function $\hat{H}_{F_d\delta_{cd}}$ is generally referred to as the force disturbance feedthrough [Venrooij et al., 2013]. Rearranging the model of the compensatory tracking task in Figure 5.1, an analytical expression of $H_{F_dF_{ho}}$ is obtained as a function of the transfer functions H_{adm} , H_{vis} , H_{ce} , and H_{cd} , i.e.:

$$\begin{aligned}H_{F_dF_{ho}} &= \frac{-H_{cd}H_{ce}H_{vis} + H_{adm}^{-1}}{1 + H_{cd}(H_{ce}H_{vis} + H_{adm}^{-1})} \\ &= -\frac{H_{cd}H_{ce}H_{vis}H_{adm} + H_{cd}}{H_{adm} + H_{cd}H_{ce}H_{vis}H_{adm} + H_{cd}}\end{aligned}\tag{5.8}$$

Similar steps are applied to find an analytical expression for the transfer function $H_{F_d\delta_{cd}}$:

$$H_{F_d\delta_{cd}} = \frac{\frac{H_{cd}H_{adm}}{H_{adm} + H_{cd}}}{1 + \frac{H_{cd}H_{adm}}{H_{adm} + H_{cd}}H_{vis}H_{ce}} = \frac{H_{cd}H_{adm}}{H_{adm} + H_{cd} + H_{cd}H_{adm}H_{vis}H_{ce}}\tag{5.9}$$

More details on obtaining the previous expressions are given in the Appendix. Dividing Equation (5.9) by Equation (5.8), an analytical expression of the estimated admittance is found:

$$\begin{aligned}\hat{H}_{adm} &= \frac{H_{Fd}\delta_{cd}}{H_{Fd}F_{ho}} = \frac{H_{cd}H_{adm}}{H_{cd}H_{ce}H_{vis}H_{adm} + H_{cd}} \\ &= \frac{H_{adm}}{1 + H_{ce}H_{vis}H_{adm}}\end{aligned}\quad 5.10$$

It is clear that Equation (5.10) represents a biased estimate of the admittance. The estimate \hat{H}_{adm} approaches the real admittance H_{adm} only at those frequencies where the product of H_{vis} , H_{ce} , and H_{adm} is small compared to 1 ($H_{ce}H_{vis}H_{adm} \ll 1$). Therefore, if the non-interference assumption is violated, the estimated admittance may become unreliable.

Another drawback of the CS method is that the human visual response H_{vis} can not be obtained directly, because the force F_{vis} can not be measured. On the contrary, the transfer function between the visual error e and the position of the controlled element θ_{ce} , i.e., the open-loop transfer function, can be estimated using cross-spectra estimates. In this case, the target forcing function θ_t is considered as the external deterministic input uncorrelated with the remnant noise. The human open-loop FRF can be estimated as:

$$\hat{H}_{ol}(f) = \frac{\hat{S}_{\theta_t\theta_{ce}}(f)}{\hat{S}_{\theta_t e}(f)}, \quad f \in \{f_t\} \quad 5.11$$

where $\{f_t\}$ is the set of frequencies in which θ_t has power. The corresponding coherence function is given by:

$$\hat{\Gamma}_{OL}^2(f) = \frac{|\hat{S}_{\theta_t\theta_{ce}}(f)|^2}{\hat{S}_{\theta_t\theta_t}(f)\hat{S}_{\theta_{ce}\theta_{ce}}(f)}, \quad f \in \{f_t\} \quad 5.12$$

5.4 Novel identification techniques

Two novel identification techniques are presented that address the limitations of the conventional identification method described in

the previous section. The first method operates in the time-domain and uses an AutoRegressive model with eXogenous inputs (ARX) to fit measured data. The second identification method operates in the frequency domain and uses cross-spectral density estimates similarly to the conventional technique. However, it does not require the non-interference assumption.

5.4.1 AutoRegressive models with eXogenous inputs

Linear Time-Invariant (LTI) polynomial models, such as the ARX, ARMAX, and Box-Jenkins (BJ) models, are commonly used for the identification of a large variety of dynamic systems [Ljung]. These models describe the relationship between the system inputs, the noise and the system outputs with parametric rational transfer functions. Based on time measurements of input and output signals of a generic dynamic system, an optimization procedure is used to find the LTI polynomial model that fits the time signals best.

Polynomial models were previously used to estimate human admittance during a car following task [Abbink, 2006]. The driver model consisted of neuromuscular and visual responses as shown in Figure 5.1. To identify the neuromuscular response, the response to the visual error e was treated as an external filtered Gaussian noise. Single-input BJ models were then used to estimate the neuromuscular response. Although this approach provided reliable neuromuscular estimate, it may fail when the response to the visual error e cannot be approximated as an external Gaussian noise.

The ARX method described in our paper explicitly accounts for the response to the visual error e by using a multi-input ARX method. The stick deflection δ_{cd} can be considered as the output of a linear system that has the visual error e and the disturbance force F_d as inputs, and that is perturbed by the remnant noise N (Figure 5.1). A multi-input ARX model is then used to describe this dynamic system [Ljung]:

$$\delta_{cd}(t) = H_e(q)e(t_k) + H_F(q)F_d(t_k) + H_n(q)N(t_k) =$$

$$\frac{B_e(q)}{A(q)}e(t_k) + \frac{B_f(q)}{A(q)}F_d(t_k) + \frac{1}{A(q)}w(t_k)$$

with:

$$A(q) = 1 + a_1 q^{-1} + \dots + a_{n_a} q^{-n_a} \quad 5.14$$

$$B_{e,f}(q) = b_{0_{e,f}} + b_{1_{e,f}} q^{-1} + \dots + b_{n_{be,bf}} q^{-n_{be,bf}} \quad 5.15$$

Here, t_k are the time samples, H_e and H_F represent the transfer functions from e and F_d to δ_{cd} , respectively, which are related to the visual response H_{vis} and the admittance H_{adm} . The transfer function H_n models the effect of the remnant noise N on stick deflection. In the ARX model, this effect is represented by the white noise signal $w(t)$ filtered by the transfer function $\frac{1}{A(q)}$. The terms n_a , n_{be} , and n_{bf} are the order of the corresponding polynomials. It should be noted that all the transfer functions of the system have the same set of poles. Although this coupling may be unrealistic, simulations and experimental results in Section 5.5 and Section 5.6 will show that this does not affect identification accuracy.

Given the measurements of δ_{cd} , F_d , and e , the polynomial orders and the parameter values of the ARX model are estimated as the optimal solution of a suitable cost function. In this paper, the Akaike final prediction error was used as the cost function [Ljung]. The optimal least-squares solution comes in closed form as a linear regression, and does not suffer from local minima.

Note that the ARX method does not require frequency separation between the inputs signals e and F_d [Nieuwenhuizen et al., 2008]. Thus, contrary to the CS method, the ARX method does not require any assumption about possible interference of the feedback from F_d with the visual error e .

The arm admittance, visual response and open loop transfer functions are obtained from H_e , H_F using block diagram algebra:

$$\hat{H}_{adm} = \frac{H_{cd} H_F}{H_{cd} - H_F} \quad 5.16$$

$$\hat{H}_{vis} = \frac{H_e}{H_F} \quad 5.17$$

$$\hat{H}_{ol} = H_e H_{ce} \quad 5.18$$

Validity of ARX estimates is assessed by the Variance Accounted For (VAF), which shows how well the model can predict the measured

output signal [Nieuwenhuizen et al., 2008]. The VAF is defined as:

$$VAF = \left[1 - \frac{\sum_{k=1}^N |\delta_{cd}(t_k) - \hat{\delta}_{cd,ARX}(t_k)|^2}{\sum_{k=1}^N |\delta_{cd}(t_k)|^2} \right] \times 100\% \quad 5.19$$

where $\delta_{cd}(t_k)$ and $\hat{\delta}_{cd,ARX}(t_k)$ represent measured and predicted stick deflections, respectively, and k indexes the time samples. VAF varies between 0% and 100%, where 100% indicates that the ARX model completely describes the measured system response. Lower values indicate a worse model fit due to noise, nonlinearities, or unmodeled system dynamics.

5.4.2 Multi-loop cross-spectral densities

This section presents a second novel identification method based on cross-spectral analysis, which explicitly accounts for the multi-loop nature of the considered control task. This method, referred to as the CS-ML method, does not require the non-interference hypothesis and does not assume a rigid predefined model structure as the ARX approach.

The CS-ML method uses the cross-spectral analysis to estimate the following auxiliary FRFs:

- the FRF of the transfer function $H_{\theta_t \delta_{cd}}$ from the target trajectory θ_t to the stick deflection δ_{cd} , i.e.:

$$\hat{H}_{\theta_t \delta_{cd}}(f) = \frac{\hat{S}_{\theta_t \delta_{cd}}(f)}{\hat{S}_{\theta_t \theta_t}(f)}, \quad f \in \{f_t\} \quad 5.20$$

- the FRF of the transfer function $H_{F_d \delta_{cd}}$ from the force disturbance F_d to the stick deflection δ_{cd} , i.e., the so-called force disturbance feedthrough [Venrooij et al., 2013, 2014]:

$$\hat{H}_{F_d \delta_{cd}}(f) = \frac{\hat{S}_{F_d \delta_{cd}}(f)}{\hat{S}_{F_d F_d}(f)}, \quad f \in \{f_d\} \quad 5.21$$

$\hat{H}_{\theta_t\delta_{cd}}$ and $\hat{H}_{F_d\delta_{cd}}$ represent closed-loop dynamics from θ_t and F_d to δ_{cd} , respectively. Therefore they include dynamics of admittance H_{adm} , visual response H_{vis} , controlled element H_{ce} , and control device H_{cd} , see Figure 5.1. The feedback loop from F_d to the visual error e is explicitly accounted for in the closed-loop dynamics. Thus, the presence of any frequency content originating from F_d in the visual error is explicitly accounted for.

The admittance \hat{H}_{adm} and visual response \hat{H}_{vis} are computed from $\hat{H}_{\theta_t\delta_{cd}}$ and $\hat{H}_{F_d\delta_{cd}}$ using block diagram algebra. This procedure requires that $\hat{H}_{\theta_t\delta_{cd}}$ and $\hat{H}_{F_d\delta_{cd}}$ must be known for a common set of frequencies $\{\tilde{f}\}$ over which they can be combined. Unfortunately, $\hat{H}_{\theta_t\delta_{cd}}$ and $\hat{H}_{F_d\delta_{cd}}$ are known only for the sets $\{f_t\}$ and $\{f_d\}$ respectively, which do not have frequency points in common. However, it is reasonable to assume a “smooth” behavior of the frequency response functions $\hat{H}_{\theta_t\delta_{cd}}$ and $\hat{H}_{F_d\delta_{cd}}$. Thus, a linear interpolation between neighbouring frequencies can be applied to obtain $\hat{H}_{\theta_t\delta_{cd}}$ and $\hat{H}_{F_d\delta_{cd}}$ on frequencies at which they are not known. The CS-ML method uses interpolation to estimate $\hat{H}_{\theta_t\delta_{cd}}$ in the set $\{f_d\}$ and $\hat{H}_{F_d\delta_{cd}}$ in the set $\{f_t\}$. A similar interpolation approach was used in [Venrooij et al., 2013].

As shown in Figure 5.2, the frequency range of $\{f_d\}$ (0.05 Hz - 10 Hz) is larger than the frequency range of $\{f_t\}$ (0.1 Hz - 3 Hz). Since an interpolation of $\hat{H}_{\theta_t\delta_{cd}}$ outside the range of $\{f_t\}$ would produce unreliable estimates, the interpolation procedure can only be applied to the frequencies of $\{f_d\}$ in the range 0.1 Hz - 3 Hz. The resulting set $\{\tilde{f}\}$ contained all frequencies in $\{f_d\}$ and $\{f_t\}$ in the range 0.1 Hz - 3 Hz, in which both $\hat{H}_{\theta_t\delta_{cd}}$ and $\hat{H}_{F_d\delta_{cd}}$ could be estimated.

Analytical expressions for $H_{F_d\delta_{cd}}$ and $H_{\theta_t\delta_{cd}}$ can be given as functions of different transfer functions, see Equation (5.9) and Equation (5.22):

$$H_{\theta_t\delta_{cd}} = \frac{H_{vis} \frac{H_{cd}H_{adm}}{H_{adm}+H_{cd}}}{1 + \frac{H_{cd}H_{adm}}{H_{adm}+H_{cd}} H_{vis} H_{ce}} \quad 5.22$$

The derivation of these expressions is detailed in the Appendix. The FRFs of human admittance and visual response are estimated from

Equation (5.9) and Equation (5.22) by using the estimated $\hat{H}_{\theta_t \delta_{cd}}$ and $\hat{H}_{F_d \delta_{cd}}$:

$$\hat{H}_{vis}(f) = \frac{\hat{H}_{\theta_t \delta_{cd}}(f)}{\hat{H}_{F_d \delta_{cd}}(f)} \quad 5.23$$

$$\hat{H}_{adm}(f) = \frac{\hat{H}_{F_d \delta_{cd}}(f) H_{cd}(f)}{H_{cd}(f) - H_{cd}(f) \hat{H}_{\theta_t \delta_{cd}}(f) H_{ce}(f) - \hat{H}_{F_d \delta_{cd}}(f)} \quad 5.24$$

Each FRF is calculated at the set of frequency points $\{\bar{f}\}$ resulting from the interpolation. In addition, the open-loop FRF \hat{H}_{ol} from the visual error e to the pitch angle θ_{ce} is calculated as:

$$\hat{H}_{ol}(f) = H_{ce}(f) \frac{\hat{H}_{\theta_t \delta_{cd}}(f)}{1 - \hat{H}_{\theta_t \delta_{cd}}(f) H_{ce}(f)}, \quad f \in \{\bar{f}\}. \quad 5.25$$

5.5 Off-line simulations

This section presents a comparison of the three identification techniques introduced in Section 5.3 and Section 5.4. The identification methods were validated by using a Monte-Carlo simulation with a fixed remnant power. In addition, the effect of the controlled element gain on the accuracy of admittance estimation was assessed. Finally, the identification methods were tested with increasing levels of the remnant power in order to analyse their robustness to external noise.

5.5.1 Simulations with reference parameter values

Method

The model in Figure 5.1 was simulated with 100 different realizations of the remnant noise N , obtained as a Gaussian white noise filtered by a third-order low-pass filter H_n [Zaal et al., 2009]:

$$H_n(s) = K_N \frac{12.7^3}{(s + 12.7)(s^2 + 2 \cdot 0.26 \cdot 12.7s + 12.7^2)} \quad [-] \quad 5.26$$

The value of the gain K_N was set to 2.12, in order to obtain a ratio of 0.5 between the remnant power and the power of the linear part of the human response: $F_{vis} - F_{adm}$.

All blocks in Figure 5.1 were simulated with fixed dynamics for all simulations. The controlled element H_{ce} was modelled similar to a previous study [Hess, 1995]:

$$H_{ce}(s) = \frac{18}{s(s+3)} \quad [\text{rad/rad}] \quad 5.27$$

Dynamics of the control device H_{cd} were based on the identified response of a collective stick from Wittenstein Aerospace & Simulation GmbH, Germany:

$$H_{cd}(s) = \frac{1}{1.522s^2 + 8.832s + 86.469} \quad [\text{rad/N}] \quad 5.28$$

The parameters for the model of the human operator were derived from Damveld et al. [2010] and slightly adapted to better match our experimental evaluations (Section 5.6). The visual response was modelled by a gain, a lead-lag filter and a time delay:

$$H_{vis}(s) = K_{vis} \frac{1 + sT_L}{1 + sT_l} e^{-s\tau_v} \quad [\text{N/rad}] \quad 5.29$$

where $K_p = 20$ N/rad, $T_L = 0.3$ s, $T_l = 0.04$ s, and $\tau_v = 0.2701$ s. The model of the arm admittance was determined heuristically to fit the non-parametric estimation shown by Damveld et al. [2010]. The resulting transfer function is given by:

$$H_{adm}(s) = \frac{4.566 \cdot 10^{-6}s^3 + 0.0046s^2 + 1.333s + 97.52}{s^3 + 82s^2 + 712.2s + 1.167 \cdot 10^{-4}} \quad [\text{rad/N}] \quad 5.30$$

Results

Figure 5.3 shows a typical power spectrum of the simulated visual error e . The power of e is not negligible at frequencies $\{f_t\}$ and $\{f_d\}$ where θ_t and F_d have power, respectively. This means that the force disturbance F_d produces a large interference on the visual error e

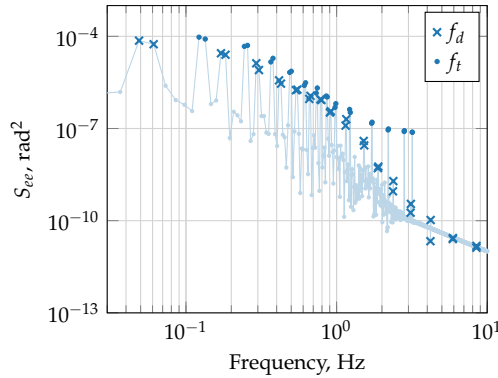


Figure 5.3: A typical power spectral density plot of the simulated visual error e .

and the non-interference hypothesis is not fulfilled. Therefore, the CS method is expected to provide biased estimates of neuromuscular response. In contrast, ARX and CS-ML methods are expected to provide reliable estimates.

The admittance estimates given by the three identification methods are shown in Figure 5.4. The CS approach does not give correct estimates of the admittance at low frequencies, where the power level of e at frequencies in $\{f_d\}$ is comparable to the power level at frequencies in $\{f_t\}$ (see Figure 5.3). On the contrary, both ARX and CS-ML methods give good results. Note that CS-ML provides admittance estimate on a relatively small frequency range due to interpolation.

The human visual response can only be directly estimated with the ARX and CS-ML methods. Figure 5.5 shows that both methods give reliable estimates. Finally, estimated open-loop transfer function fits the simulated response well for all identification methods, see Figure 5.6.

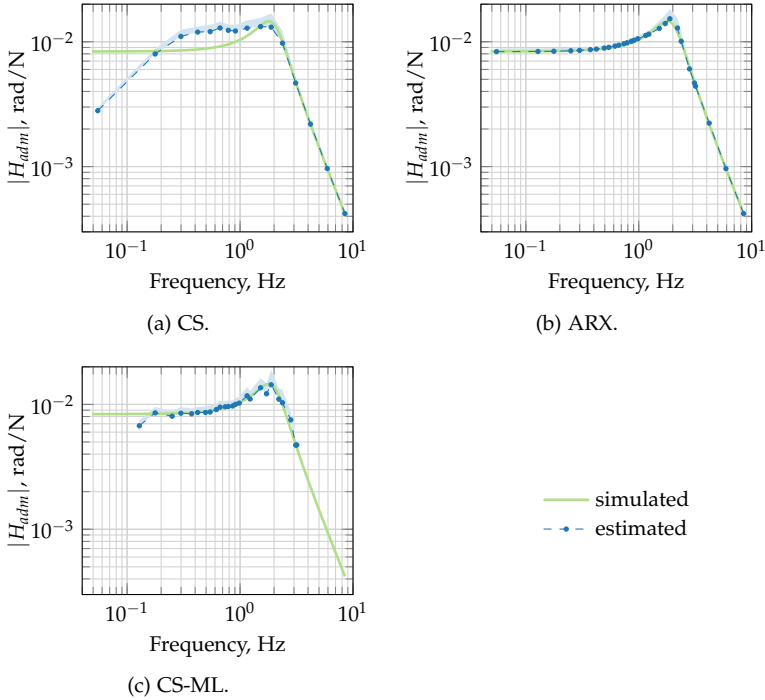


Figure 5.4: Comparison between admittance estimates given by the three identification methods. The estimates are averaged over all the simulations, and the shaded areas show the (positive) standard deviation (mean + SD).

5.5.2 Variation of the gain of the controlled element

Method

Admittance identified with the CS method can be influenced to a large extent by the power content of the visual error e . High power content in the visual error signal e at frequencies $\{f_d\}$ results in a biased estimate. As shown in Equation (5.10), the CS method produces reliable estimates only at frequencies where $H_{ce}H_{vis}H_{adm} \ll 1$. To investigate this aspect, multiple simulations were performed with

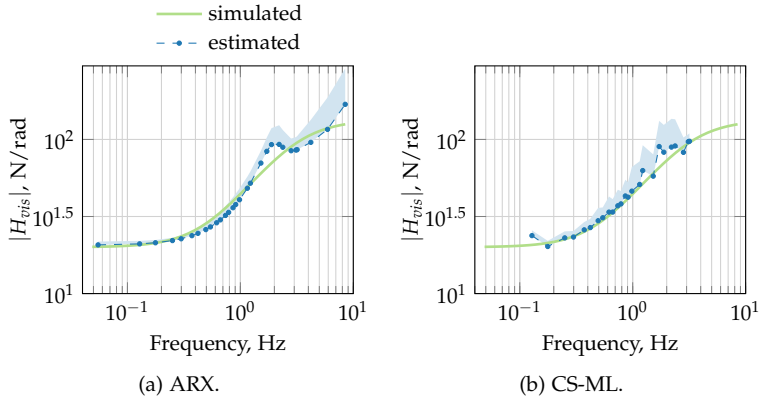


Figure 5.5: Comparison between visual response estimates given by ARX and CS-ML methods. The estimates are averaged over all the simulations, and the shaded areas show the (positive) standard deviation (mean + SD).

different values of the gain of the controlled element. It was hypothesized that the CS method would perform better with small gains of H_{ce} , whereas higher gains would result in a biased estimate of the admittance.

The dynamics for H_{cd} , H_{adm} , H_{vis} were the same as in Section 5.5.1. The H_{ce} dynamics were modelled as:

$$H_{ce} = K_{ce} \frac{3}{s(s+3)} \quad [\text{rad/rad}] \quad 5.31$$

Five different values of K_{ce} were tested: 0, 3, 6, 9, 12. The condition $K_{ce} = 0$ represents an open-loop situation, where the non-interference hypothesis is completely fulfilled. No additional noise was inserted into the loop, as this effect will be tested explicitly in the next section.

Results

Figure 5.7 shows the admittance estimated by the three methods. As expected, the performance of the CS method deteriorates with

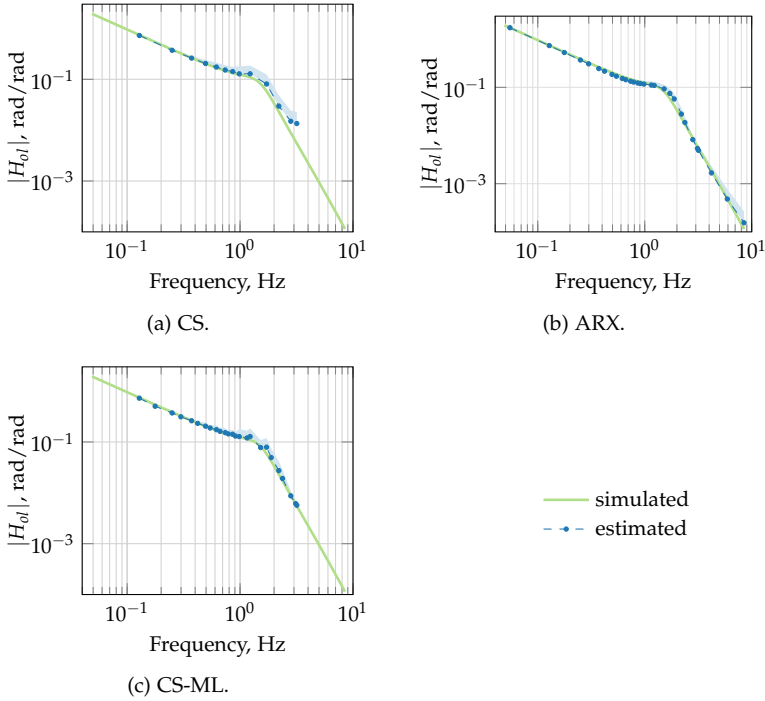


Figure 5.6: Comparison between open-loop transfer function estimates given by the three identification methods. The estimates are averaged over all the simulations, and the shaded areas show the (positive) standard deviation (mean + SD).

increasing values of K_{ce} . In contrast ARX and CS-ML methods are not influenced by changes in the K_{ce} value.

It should be noted that, in a realistic scenario, the human operator would adapt his/her behavior to the controlled element [McRuer and Weir, 1969]. However, this section aimed to highlight the influence of non-interference hypothesis on the admittance estimation, and this effect becomes more clear when the human operator is considered invariant.

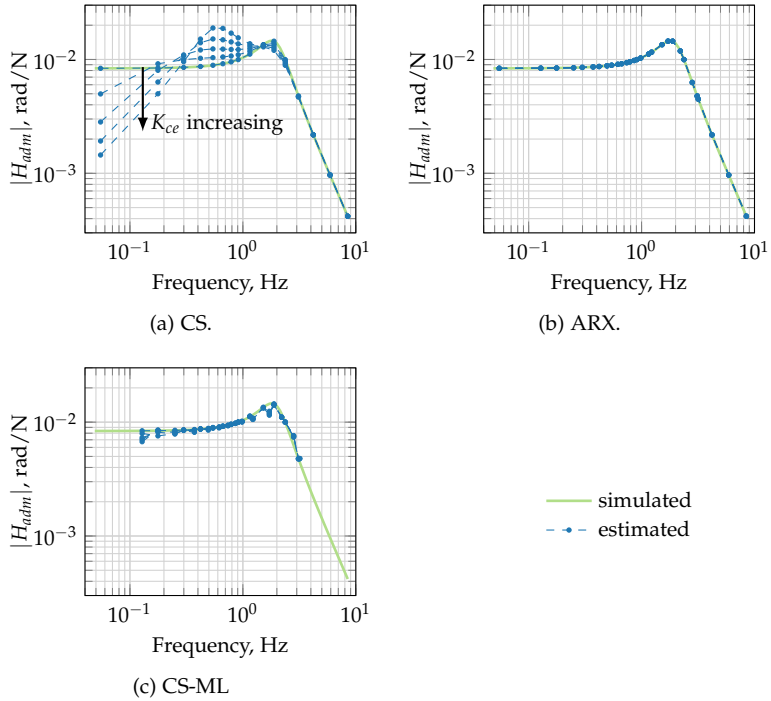


Figure 5.7: Admittances estimated for different values of K_{ce} ($K_{ce} = 0, 3, 6, 9, 12$). The ARX and CS-ML methods provide similar estimates for all values of K_{ce} .

5.5.3 Variation of the noise power of noise

Method

The robustness of the three identification methods to increasing levels of human remnant was investigated by simulating increasing levels of remnant noise power. The remnant gain K_N in Equation (5.26) was gradually increased, resulting in 7 ratios between remnant power σ_N^2 and signal power σ_F^2 , see Table 5.2. For each remnant level, 100 simulations were performed with different noise

Table 5.2: Simulated power ratios.

K_N	σ_N^2/σ_F^2
0	0
2.21	0.5
3.5	1
4.6	1.5
6	2
7.6	2.5
10	3

realizations. The analytical dynamics for H_{ce} , H_{cd} , H_{adm} , H_{vis} were chosen as in Section 5.5.1.

The admittance, the visual response and the open-loop transfer function were estimated by applying the three identification methods. To compare the performance of the methods, a cost function J was calculated, representing the logarithmic mean squared error between the estimated FRF (\hat{H}) and analytical FRF (H) [Pintelon et al., 1994]:

$$J = \frac{1}{N} \sum_{k=1}^N \left| \log \left(\frac{\hat{H}(f_k)}{H(f_k)} \right) \right|^2 \quad 5.32$$

This cost function accounts for both relative errors in the magnitude, and absolute errors in the phase. To obtain meaningful values, J was calculated considering the frequencies f_k that are common to the three identification methods, i.e., the frequencies in $\{f_d\}$ between 0.1 Hz and 3 Hz for admittance estimates, and the frequencies in $\{f_t\}$ for estimates of visual and open loop transfer functions.

Results

Figure 5.8 shows how the cost function J varies with respect to the power ratio σ_N^2/σ_F^2 . For all the estimates, J increases with increasing values of the remnant power, implying a growing discrepancy

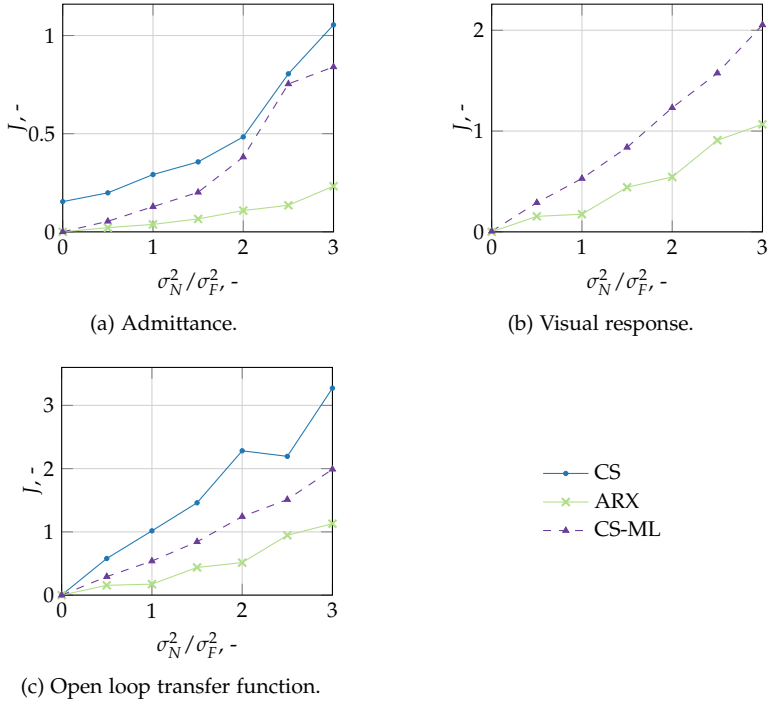


Figure 5.8: Averaged values of the cost function J for different remnant levels.

between analytical and estimated FRFs. The ARX method appears to be the most robust with respect to noise. This is due to the fact that the ARX method explicitly accounts for the remnant noise in the estimation procedure.

Considering the admittance estimates, the CS method shows a non-zero value of J when the remnant noise has zero power, i.e., $\sigma_N^2/\sigma_F^2 = 0$ in Figure 5.8a. This indicates that the CS method provides a biased admittance estimate even without remnant noise. On the other hand, CS-ML and ARX methods are unbiased.

Considering the visual response estimates, CS-ML and ARX methods show a similar degradation of accuracy. Also for the open-loop transfer function estimates, the three methods show comparable degradation trends.

5.6 Experimental evaluations

5.6.1 Method

The three identifications methods were applied to data obtained from an experimental compensatory tracking task. The experiment was performed using a control-loaded cyclic stick from Wittenstein Aerospace & Simulation GmbH, Germany. The lateral axis of the stick was fixed, whereas the dynamics of the longitudinal axis were set as in Equation (5.28).

Eight participants took part in the experiment, seven male and one female. All participants were recruited at Max Planck Institute for Biological Cybernetics, some had general experience with flight simulators. Before starting the experiment, participants received an overview about the scope of the experiment, and were instructed to minimize the tracking error shown on a primary flight display. The control device was continuously perturbed by a disturbance force. Both the reference signal and the disturbance force were designed as described in Section 5.3.1.

After a training phase, participants performed 8 experimental trials. Data were logged at 100 Hz and the last 2^{13} samples (= 81.92 s) of each trial of 90 s were used for identification purposes. The identification methods described in Section 5.3 and Section 5.4 were then applied to the measured data. Before identification, the data of the 8 trials of each participant were averaged in the time domain to reduce the effect of remnant noise.

It was hypothesized that the CS method would be influenced by the non-interference assumption, leading to estimates of admittance that differ from the ones obtained with the ARX and the CS-ML methods. Furthermore, it was expected that the ARX and the CS-ML would provide similar admittance estimates.

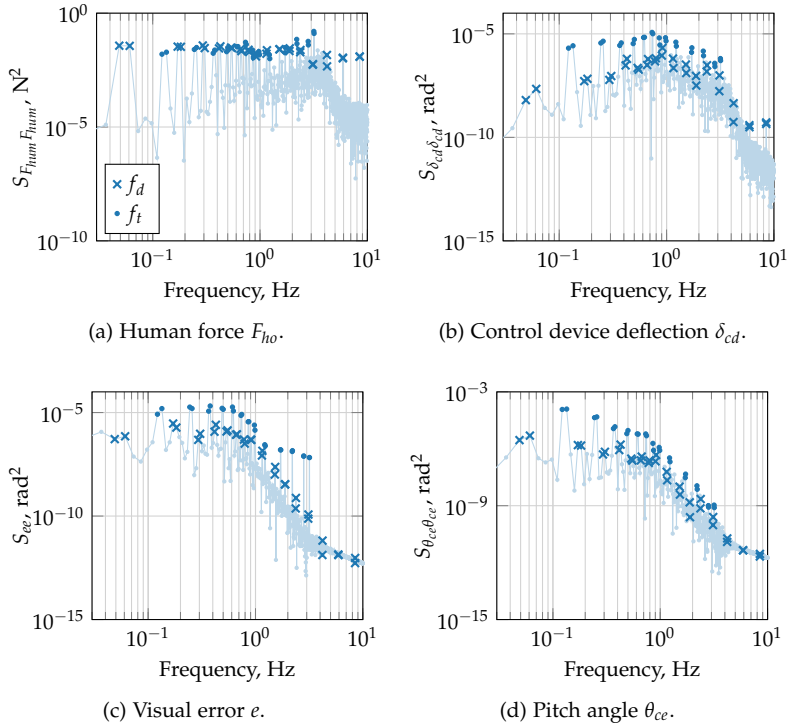


Figure 5.9: Power spectral densities. The crosses and the points represent the disturbance force and target position frequencies, respectively.

5.6.2 Results

Figure 5.9 illustrates the power spectra of the error signal e , the human force F_{ho} , the control signal δ_{cd} , and the pitch angle θ_{ce} for a single participant. The Signal-to-Noise Ratios were high for most of the input frequencies of ϕ_t and F_d . The power of e contained large peaks at frequencies $\{f_d\}$ where the force disturbance F_d had power, especially at low frequencies. This indicates that F_d had a large influence on the visual error e and the non-interference assumption of the CS method was not fulfilled.

Figure 5.10 shows the admittance identified by the three identification methods. The CS method gives the admittance FRFs for all frequencies of $\{f_d\}$, while the CS-ML method only provides admittance estimates for the frequency set $\{f_t\}$ as discussed in Section 5.4.2. On the other hand, the ARX method provides a mathematical expression for the admittance transfer function, and the FRFs can be calculated for all the desired frequency points ($\{f_d\} \cup \{f_t\}$ in Figure 5.10). Reliability of ARX estimates was indicated by high VAF values (the mean value of the VAF was 87%). Regarding CS estimates, high squared coherence values were found at all frequencies ($\Gamma^2 > 0.8$). However, great care must be paid in interpreting this result. In fact, the coherence function only indicates that the relation between the measured human force F_{ho} and the position of the control device δ_{cd} can be approximated as linear, but does not give information about the correspondence between the actual and the estimated admittance.

As shown in Figure 5.10, the ARX and CS-ML methods provided similar admittance estimates. On the other hand, CS method provided different estimates than ARX and CS-ML methods, especially at low frequencies. The admittance estimated by the CS showed the same bias as found in simulations, see Section 5.5.1. At low frequencies ($f < 0.2$ Hz), the magnitude of the admittance estimated by CS technique was lower than the magnitude given by the other two methods; the opposite occurred at medium frequencies ($0.2 \text{ Hz} < f < 2 \text{ Hz}$); at higher frequencies the differences between methods disappeared.

As shown in Equation (5.10), the bias in the CS method results from the admittance estimate including the dynamics of the visual response H_{vis} and the controlled element H_{ce} . The bias is negligible only at those frequencies where $H_{den} = 1 - H_{vis}H_{ce}H_{adm}$ is close to 1, whereas it becomes larger when H_{den} diverges from 1. H_{den} can thus be used as a measure of the bias of the CS estimate. To evaluate H_{den} , the actual dynamics of admittance H_{adm} and visual responses H_{vis} are required. Since these dynamics are not known a priori, the estimates provided by ARX and CS-ML methods can be used. Figure 5.11a shows that the resulting H_{den} . The magnitude of H_{den} is close to 1 at frequencies above 1 Hz, whereas it diverges from 1 at

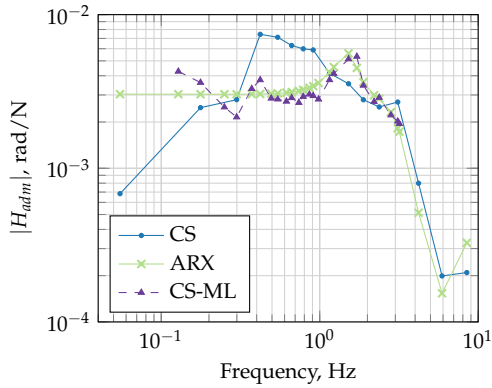


Figure 5.10: Admittance frequency response functions for the three identification methods. The estimates are averaged over all participants.

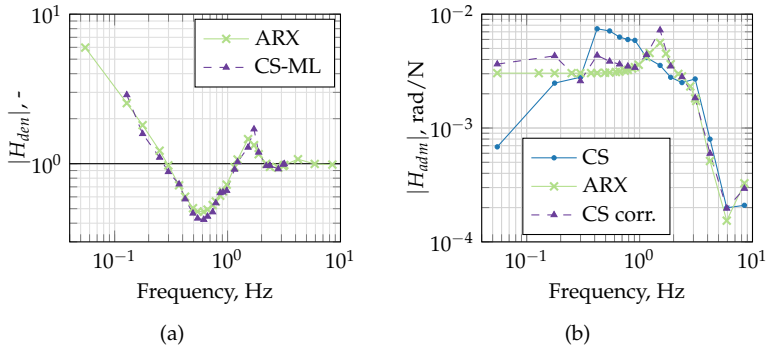


Figure 5.11: (a) Bias H_{den} of the admittance estimate by the CS method. The bias is calculated using the FRFs estimated by the ARX and the CS-ML methods. (b) Comparison between the admittance estimates by the CS and the ARX methods, and CS estimate corrected with H_{den} .

low frequencies. This is in complete agreement with results shown in Figure 5.10.

The bias measure H_{den} can be used to correct the biased admittance given by the CS method. The corrected admittance is obtained

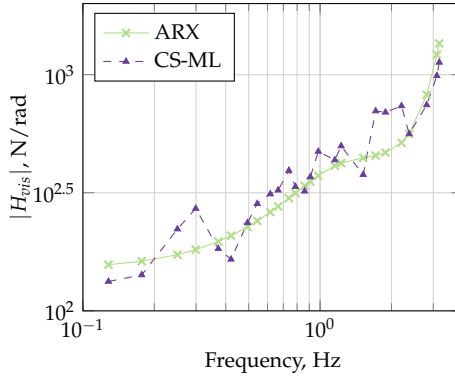


Figure 5.12: Comparison between visual responses given by ARX and CS-ML methods.

by multiplying the biased admittance by H_{den} , see Equation (5.10). Figure 5.11b shows the biased admittance given by CS method, together with the corrected admittance and the ARX estimate. As the admittance estimate from the CS-ML method was similar to the ARX estimate, it is not shown. As expected the corrected admittance is similar to the ARX estimate, confirming the validity of our analysis of the bias in the CS method.

The human visual response can be computed directly only with ARX and CS-ML methods. Figure 5.12 shows that the estimates were comparable. The shape of the visual response resembled a gain at low frequencies and a differentiator at higher frequencies. The three identification methods gave comparable estimates also for the open-loop transfer function H_{ol} (Figure 5.13). The open-loop responses resembled the dynamics of a single integrator at frequencies below 1 Hz. This correlates fairly well with McRuer's theories, which assess that human operators adapt their responses to yield integrator-like dynamics of the open-loop transfer function around the crossover frequency where $H_{ol} = 10^0$ rad/rad [McRuer]. The peak of the open-loop response at higher frequencies is related to the neuromuscular dynamics.

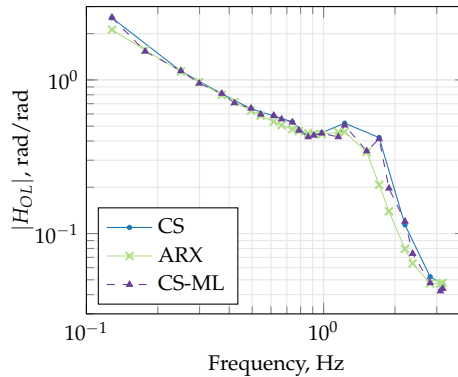


Figure 5.13: Comparison between open-loop transfer function estimates given by the three identification methods.

5.7 Conclusions

Three techniques for simultaneous identification of human neuromuscular and visual responses have been investigated. We showed that the identification method commonly used in literature (CS method) may give biased estimates of admittance in cases when a so-called *non-interference* assumption is not fulfilled. Furthermore, we have derived an analytic expression for the bias in the CS admittance estimate.

We presented two different procedures, one based on ARX models and one on cross-spectral analysis, which allow overcoming this limitation. The results of offline simulations confirmed that both the ARX and the CS-ML methods give reliable estimates also in the case when the *non-interference* assumption is not satisfied.

The three identification methods were validated experimentally. The ARX and the CS-ML methods showed estimates that were similar to each other, whereas the CS method gave a biased estimate of admittance. Similar results were also found in simulation. The biased estimate of admittance from the CS method could be corrected with experimental data, which corroborates our theoretical analysis of the CS method.

Taken together, these results suggest that the admittance estimated by the CS method cannot be considered to be reliable when the disturbance forcing function always has an influence on the visual error. On the contrary, the ARX and the CS-ML methods are not influenced by the power content of the visual error.

The two novel methods have clearly some limitations. The most important limitation of the ARX method lies in the fact that it assumes a rigid model structure that could be unrealistic. Despite this, the experimental results suggest that the ARX-model structure can describe our experimental data well. A potential limitation of the CS-ML method is that it provides admittance estimates in a reduced set of frequencies (at low frequencies in our case). Nevertheless, this method is a powerful tool for obtaining an accurate admittance estimate at low frequencies without assuming a rigid model structure.

5.8 Appendix

In a closed-loop linear system as in Figure 5.14a, the closed-loop transfer function H_{cl} between the input signal u and the output signal y is given by:

$$H_{cl} = \frac{H}{1 + H \cdot G} \quad 5.33$$

where H and G represent the transfer functions of the system dynamics in the forward and feedback path, respectively.

The closed-loop dynamics between two generic signals of the compensatory tracking task in Figure 5.1 can be obtained by rearranging the model to have a similar configuration as the system in Figure 5.14a. Figure 5.14b illustrates the rearranged model to obtain the dynamics between the disturbance force F_d and the human force F_{ho} . The forward and feedback transfer functions are given by:

$$H = H_{cd}(-H_{ce}H_{vis} - H_{adm}^{-1}), \quad G = -1 \quad 5.34$$

Figure 5.14c shows the rearranged model to calculate the dynamics from θ_t and F_d to δ_{cd} . The forward and feedback transfer functions for the input signals θ_t and F_d are:

$$\theta_t : \quad H = H_{vis} \frac{H_{cd}H_{adm}}{H_{adm} + H_{cd}}, \quad G = H_{ce} \quad 5.35$$

$$F_d : \quad H = \frac{H_{cd}H_{adm}}{H_{adm} + H_{cd}}, \quad G = H_{ce}H_{vis} \quad 5.36$$

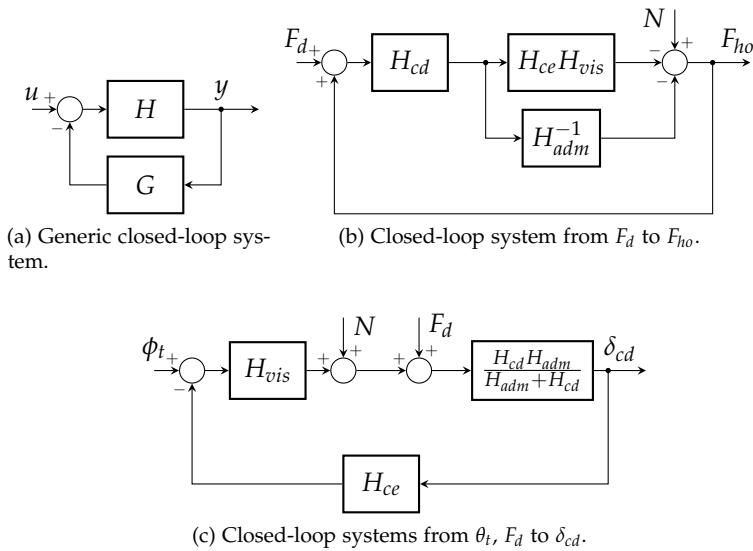


Figure 5.14: Rearranged models of the compensatory tracking task in Figure 5.1

Pilot adaptation to different classes of haptic aids

In this chapter, the two novel ARX and CS methods are applied to estimate human's dynamic responses with different haptic aids. Two different haptic aids were designed for a target tracking task: a Direct Haptic Aid (DHA) and an Indirect Haptic Aid (IHA). The DHA provides forces on the control device that suggest the right control action to the pilot, whereas the IHA provides forces opposite in sign with respect to the DHA. The DHA and the IHA were tested in an experimental setup with non-pilot participants and compared to a condition without haptic support. It was found that participants significantly adapted their admittance and visual response to fully exploit the haptic aids. They were more compliant with the DHA force, whereas they showed stiffer neuromuscular settings with the IHA as this approach required opposing the haptic forces.

The contents of this chapter are based on:

- | | |
|---------------------|--|
| Paper title | Pilot adaptation to different classes of haptic aids in tracking tasks |
| Authors | Olivari, M., Nieuwenhuizen, F. M., Bühlhoff, H. H., and Pollini, L. |
| Published in | AIAA Journal of Guidance, Control, and Dynamics, Vol. 37, No. 6, December 2014 |

6.1 Introduction

AN INSIGHT into how humans adapt their control behavior to different haptic aids becomes crucial for an effective design of the haptic feedback. In a control task with haptic and visual cues, control behavior can be analysed by looking at human's visual and neuromuscular dynamic responses [Abbink et al., 2011]. The question arises as to how humans adapt their visual and neuromuscular responses in relation to different haptic aids.

Adaptation of human's visual response has been widely investigated in literature. McRuer's theories highlight that humans modify their visual response depending on external conditions such as the dynamics of the controlled element [McRuer and Jex, 1967]. However, these theories do not consider the use of haptic cues, and, to the best of our knowledge, nobody has studied whether these rules are still valid when humans are supported with haptic systems.

There is also a vast amount of literature on the human capabilities to adapt the neuromuscular response to the performed task. Research has focused on neuromuscular adaptation during disturbance-rejection tasks that require humans to adopt different neuromuscular settings in response to force disturbances on the control device [van der Helm et al., 2002; Mugge et al., 2010; Schouten et al., 2008b]. More recent work focused on an aircraft tracking task and showed that the neuromuscular response is highly variable with different dynamics of the control device [Damveld et al., 2010, 2009]. Other studies indicated that the ankle-foot neuromuscular response of car drivers changes when a haptic aid is employed during a car-following task [Abbink et al., 2011]. Thus, humans adapt their neuromuscular response depending on the task they have to perform, and that haptic cues influence their neuromuscular response. However, it is not yet known how the neuromuscular response changes in relation to different types of haptic aid.

The goal of this chapter is to estimate pilot's dynamic responses in a compensatory tracking task with different haptic aids. First, our novel identification methods ARX and CS-ML were extended to account for the presence of haptic aids in the compensatory

tracking task. Then, two haptic systems were designed according to different approaches: the Direct Haptic Aid (DHA) approach and the Indirect Haptic Aid (IHA) approach. The two approaches provide haptic information in opposite ways and require humans to adopt different control strategies. Finally, the extended ARX and CS-ML methods were applied to data collected in a human in-the-loop experiment. This will shed new light on how participants adapt their neuromuscular and visual responses to DHA and IHA systems.

The chapter is structured as follows: Section 6.2 outlines the design of the two haptic aids. Section 6.3 presents a model that can be used to describe human control behavior during a tracking task with a haptic aid. Identification methods suitable for this model are then detailed in Section 6.4. The experimental procedure and setup are discussed in Section 6.5, followed by the experimental results in Section 6.6. Finally, conclusions are drawn in Section 6.7.

6.2 Design of haptic aids for a tracking task

Haptic cues can be used as pilot support systems, with the main objective of increasing the level of safety and performance in a particular task. This chapter focuses on a compensatory pitch tracking task, which involves the minimization of a tracking error e between a target trajectory and the pitch angle of the controlled element, i.e., the aircraft. Two different approaches were taken to design the haptic cue for the compensatory tracking task: the *Direct Haptic Aid* (DHA) and the *Indirect Haptic Aid* (IHA) approaches [Alaimo et al., 2010]. Note that the haptic aids in the previous chapters have been designed according to the DHA approach.

6.2.1 DHA approach

The DHA approach consists of producing kinaesthetic sensations that suggest the right control action to the human operator. In a compensatory tracking task, this can be achieved by designing the DHA force generation system as a standard compensator, which provides forces that reduce or regulate the tracking error to zero.

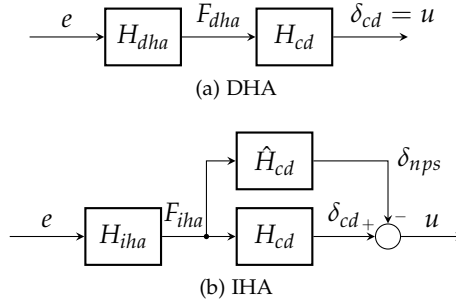


Figure 6.1: Haptic aids.

Figure 6.1a shows the implementation of DHA system. Based on the tracking error e , the DHA provides a force F_{dha} that generates a control signal δ_{cd} to reduce the tracking error.

Although several techniques can be used to design a compensator, experience shows that many of these may lead to a haptic “controller” that generates stick motion differently from what the human operator would do to minimize the tracking error [Alaimo et al., 2011a]. In such a case, the human operator may oppose the haptic cues instead of following them, which would result in degraded closed-loop performance. To overcome this issue, our approach was to design a DHA that “mimics” the human control strategy. As detailed in Section 2.3, this approach leads to the following dynamics for the DHA:

$$H_{dha} = \frac{H_{con}}{H_{cd}} \quad 6.1$$

$$F_{dha} = H_{dha}e \quad 6.2$$

where H_{cd} is the transfer function of the control device, and H_{con} represents the human control response as a transfer function between the tracking error e and the control signal δ_{cd} . Note that H_{con} includes the dynamics of both human operator and control device.

According to this design, the DHA can perform the tracking task without human in-the-loop. When the human operator is in-the-loop, haptic aid and human operator share the control of

the aircraft. The human operator could either be as compliant as possible and follow the haptic aid, or try to amplify the forces to improve performance. In addition, the human operator could always override the haptic control strategy in case of discordance.

6.2.2 IHA approach

Contrary to the DHA approach, the IHA is designed to inform humans and increase situational awareness indirectly, and not to suggest control actions. This approach has been adopted in different control tasks with the aim of exploiting the natural tendency of humans to counteract external forces presented on the control device. For instance, in some works dealing with wind gust rejection in teleoperation, a tactile disturbance was generated on the control device based on the effect of the wind gust on the controlled element [Alaimo et al., 2010]. By opposing the disturbance on the control device, human operators were able to reject the wind gust and control the trajectory of the controlled element. In other cases dealing with obstacle avoidance or with trajectory tracking, IHA systems were derived from a DHA system designed for the same goal by simply reversing the sign of the generated force [Alaimo et al., 2011a,b; Profumo et al., 2013]. The operator had to oppose the forces given by IHA to perform the task.

In our study, the IHA was designed to provide a force opposite in sign with respect to the DHA:

$$H_{iha} = -H_{dha} \quad 6.3$$

$$F_{iha} = H_{iha}e \quad 6.4$$

Unfortunately, this design presents a considerable drawback: if the human operator is not in the loop, the IHA force would generate a control action that would lead the controlled element to fly away from the target trajectory. It is clearly unwise to insert a possibly destabilizing component in the control loop.

To overcome this issue, the neutral point of the control device was shifted according to the current force provided by the IHA system, so that the actual control command to the aircraft is zero

when the human operator does not interact with the control device [Alaimo et al., 2011b; de Stigter et al., 2007]. This allows the IHA system to provide sensations to the human operator (via the stick motion) without having an effect on the actual command given to the aircraft.

The neutral point shift is implemented by using the compensation scheme shown in Figure 6.1b. The IHA generates a force F_{iha} based on the tracking error e . The deflection induced by F_{iha} must become the new neutral point δ_{nps} . To achieve this, the effect of F_{iha} on the control device is simulated by using a model of the control device \hat{H}_{cd} and subtracted from the actual position of the stick. This difference becomes the actual input u for the controlled element:

$$u = \delta_{cd} - \delta_{nps} = \delta_{cd} - \hat{H}_{cd}F_{iha} \quad 6.5$$

Note that, according to this design, the human operator can follow the target trajectory by simply holding the stick in the center. However, experimental evidence has shown that a human operator can improve the performance by actively responding to the resulting visual error.

6.2.3 Comparison of DHA and IHA approaches

It is now possible to compare a general DHA with a general IHA with neutral point shift. Let us consider the behavior of the DHA and IHA in two different conditions: a human operator showing infinite compliance with a DHA system, and a human operator showing infinite stiffness with a IHA system. These conditions represent extreme situations in which humans do not actively respond to the visual feedback, but only adopt a passive behavior that allows to take advantage of the two haptic aids. In the first case, the haptic force F_{dha} is the only force applied to the control device, thus the resulting control signal u is given by:

$$u_{dha} = H_{cd}F_{dha} \quad 6.6$$

On the other hand, with IHA and an infinitely rigid human operator, the control device is constantly held in the centre ($\delta_{cd} = 0$). The

resulting IHA control signal is only caused by the neutral point shift:

$$u_{iha} = \delta_{cd} - \delta_{nps} = 0 - \delta_{nps} = -\hat{H}_{cd}F_{iha} \quad 6.7$$

Under the hypothesis of an exact model of the control device ($H_{cd} = \hat{H}_{cd}$) and if the IHA force is generated according to the same dynamics as the DHA but opposite in sign (i.e, $F_{iha} = -F_{dha}$), the two approaches result in the same control signal for the aircraft: $u_{iha} = u_{dha}$.

6.3 Modelling of human control behavior

In previous studies, the use of haptic cues based on DHA and IHA has shown beneficial effects in terms of human performance [Abbink and Mulder, 2009; Alaimo et al., 2011b]. The question arises as to how humans can take advantage of two haptic aids that actually feed forces opposite in sign into the control loop. This can be explained by the human capability of modifying the control strategy to handle different external conditions [McRuer and Weir, 1969]. To gain a quantitative insight into how haptic cues influence human control strategy, a model of human control behavior is needed that can highlight the effects of haptic cues on the human's dynamic responses.

In a compensatory tracking task with haptic aids, two dynamic responses define the human control behavior: the visual response and the neuromuscular response [van Paassen, 1994]. The visual response describes how the human operator generates a control action based on the tracking error shown in the visual display. The neuromuscular response represents the dynamic settings of human's arm. By varying these settings, humans can oppose, or be compliant with, the haptic feedback. Thus, the neuromuscular response provides an indication of how the human operator interacts with the haptic feedback.

A model of human control behavior that includes both visual and neuromuscular responses has been illustrated in Section 5.2. Figure 6.2 shows the model adapted to include the haptic aid. The human operator HO is described with two describing functions: the

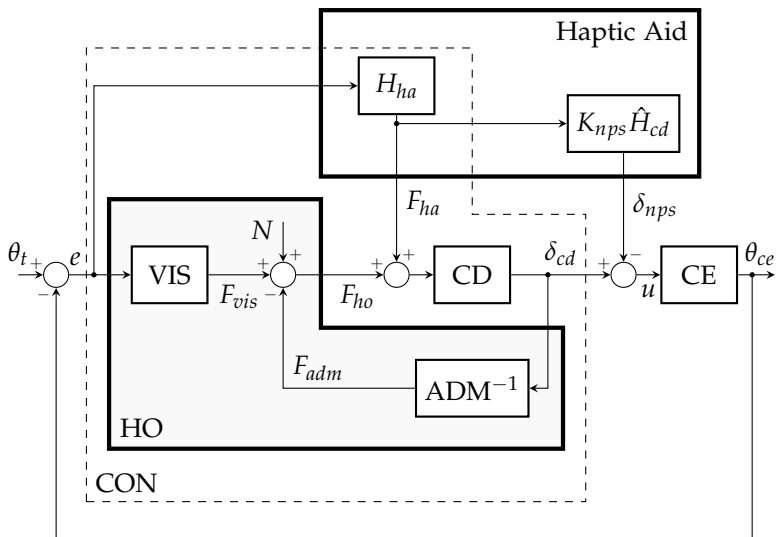


Figure 6.2: Model of human control behavior in a compensatory tracking task with haptic aids.

visual response VIS and the inverse of admittance ADM. For the purposes of this study, the two blocks VIS and ADM are assumed to be linear, and can be described by the corresponding transfer functions H_{vis} and H_{adm} . Noise and non-linear contributions to the human force F_{ho} are accounted for by the remnant signal N [McRuer and Jex, 1967].

Note that in literature, the term visual response often denominates the response from e to the stick deflection δ_{cd} , i.e., the system CON in Figure 6.2 [Damveld et al., 2010; McRuer]. However, in a control task with haptic aids, CON includes the dynamics H_{ha} of the haptic aid. Defining the visual response as the transfer function from e to F_{vis} allows us to separate the haptic system from the human responses.

The block H_{ha} represents the force generation dynamics of the haptic aid ($H_{ha} = H_{dha}$ and $H_{ha} = H_{iha}$ for DHA and IHA, respectively). Both the DHA and IHA generate a force F_{ha} on the control device based on the dynamics of the visual error e . The force generated by the haptic aid is sensed by pilots through its effect on the deflection of the control device δ_{cd} . The signal δ_{nps} represents the neutral point shift used in the IHA approach. As explained in Section 6.2, the dynamics of δ_{nps} are calculated by simulating the effect of the haptic force F_{ha} on the identified dynamics \hat{H}_{cd} of the control device CD. In the DHA approach $K_{nps} = 0$, whereas in the IHA approach $K_{nps} = 1$.

6.4 Identification of human control behavior

Identification of the human responses in Figure 6.2 allows for an evaluation of how haptic cues influence a human control behavior. Since two dynamic responses need to be estimated, i.e., the admittance and the visual response, identification methods require two external forcing functions to be inserted into the control loop [van Lunteren, 1979]. The target trajectory θ_t and an additional disturbance force on the control device F_d can be used for this purpose. Figure 6.3 shows power spectral densities and time realizations of the two forcing functions adopted in our experiment. Their design will be detailed in Section 6.5. For now, we would indicate that F_d and θ_t are chosen to have power at different sets of frequency points, $\{f_d\}$ and $\{f_t\}$ respectively.

The pilot's responses are identified by using three identification techniques: the CS method, the ARX method, and the CS-ML method. In Chapter 5, these three methods were applied to a compensatory tracking task without haptic aids. This chapter extends their applicability to the presence of a haptic aid.

The CS method is exactly as described in Section 5.3.2. The Frequency Response Function (FRF) of the admittance at frequencies in $\{f_d\}$ is estimated by using sample cross-spectral densities:

$$\hat{H}_{adm}(f) = \frac{\hat{S}_{F_d\delta_{cd}}(f)}{\hat{S}_{F_dF_{ho}}(f)}, \quad f \in \{f_d\}$$

6.8

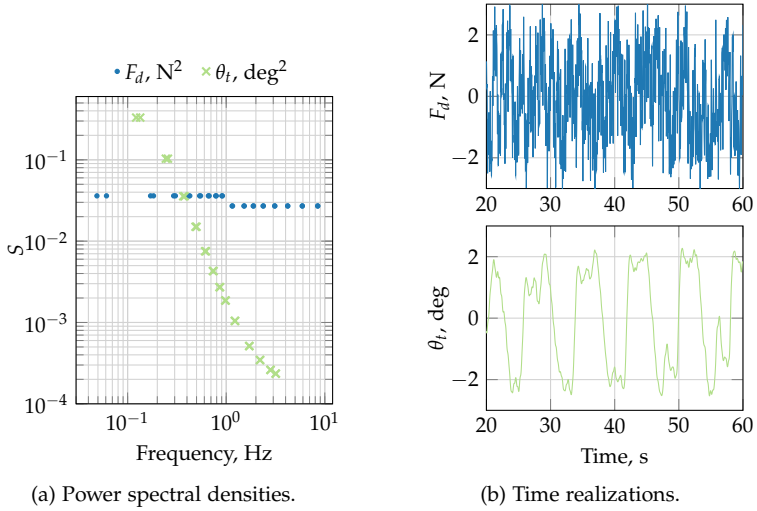


Figure 6.3: Forcing signals θ_t and F_d .

where \hat{S}_{vw} indicates the sample cross-spectral density between the generic signals v and w . The squared coherence function $\hat{\Gamma}^2$ is usually used to evaluate the reliability of the estimate:

$$\hat{\Gamma}_{adm}^2(f) = \frac{|\hat{S}_{F_d \delta_{cd}}(f)|^2}{\hat{S}_{F_d F_d}(f) \hat{S}_{\delta_{cd} \delta_{cd}}(f)}, \quad f \in \{f_d\} \quad 6.9$$

The coherence $\hat{\Gamma}^2$ is a measure of how much an output signal is linearly related to an the input signal. It assumes values between 0 and 1 and decreases with noise and non-linearities.

The FRF of the human visual response can not be estimated directly with the CS method. On the other hand, the FRF of the control transfer function H_{con} between the visual error e and the deflection of the control device δ_{cd} can be estimated at the frequencies $\{f_t\}$ according to:

$$\hat{H}_{con}(f) = \frac{\hat{S}_{\theta_t \delta_{cd}}(f)}{\hat{S}_{\theta_t e}(f)}, \quad f \in \{f_t\} \quad 6.10$$

The squared coherence function corresponding to \hat{H}_{con} is given by:

$$\hat{\Gamma}_{con}^2(f) = \frac{|\hat{S}_{\theta_t \delta_{cd}}(f)|^2}{\hat{S}_{\theta_t \theta_t}(f) \hat{S}_{\delta_{cd} \delta_{cd}}(f)}, \quad f \in \{f_t\} \quad 6.11$$

Similarly, the open-loop transfer function between the visual error e and the position of the controlled element θ_{ce} and the corresponding squared coherence function are estimated as:

$$\hat{H}_{ol}(f) = \frac{\hat{S}_{\theta_t \theta_{ce}}(f)}{\hat{S}_{\theta_t e}(f)}, \quad f \in \{f_t\} \quad \hat{\Gamma}_{ol}^2(f) = \frac{|\hat{S}_{\theta_t \theta_{ce}}(f)|^2}{\hat{S}_{\theta_t \theta_t}(f) \hat{S}_{\theta_{ce} \theta_{ce}}(f)}, \quad f \in \{f_t\} \quad 6.12$$

As proved in Section 5.3.2, the CS method requires that the contribution of the disturbance force F_d in the visual error is negligible (*non-interference hypothesis*). If the non-interference hypothesis is not fulfilled, the CS method provides biased estimate of the admittance. In such cases, the ARX and CS-ML methods can be employed. These methods do not require any non-interference hypothesis, since they explicitly account for the possible presence of the contribution of F_d in the visual error.

The ARX method operates in the time domain. The method considers the stick deflection δ_{cd} as the output of a linear system with inputs e and F_d , see Figure 6.2:

$$\delta_{cd}(t) = H_e e(t_k) + H_F F_d(t_k) + H_n N(t_k) \quad 6.13$$

where t_k represent the time samples, H_e , H_F and H_n are the transfer functions between e and δ_{cd} , between F_d and δ_{cd} , and between N and δ_{cd} , respectively. Note that H_e , H_F and H_n depend on the values of the transfer functions H_{adm} , H_{vis} , H_{cd} , and H_{ha} .

The linear system in Equation (6.13) is fitted with a multi-input linear ARX model, which provides estimates of H_e and H_F as polynomial transfer functions [Ljung]. The human admittance H_{adm} , the visual response H_{vis} , the control transfer function H_{con} , and the open-loop transfer function H_{ol} are then calculated from the estimates \hat{H}_e , \hat{H}_F and from the known transfer functions H_{cd} , H_{ha} ,

H_{nps} , and H_{ce} by using block diagram algebra:

$$H_{adm} = \frac{H_{cd}\hat{H}_F}{H_{cd} - \hat{H}_F} \quad 6.14$$

$$H_{vis} = \frac{\hat{H}_e - H_{ha}\hat{H}_F}{\hat{H}_F} \quad 6.15$$

$$H_{con} = \hat{H}_e \quad 6.16$$

$$H_{ol} = (\hat{H}_e - H_{nps})H_{ce} \quad 6.17$$

Differently from the estimate obtained in Section 5.4, estimates in Equation (6.14) accounts for H_{ha} and H_{nps} dynamics.

To test how well the estimated ARX model predicts the measured output signal, the Variance Accounted For (VAF) index can be calculated [Nieuwenhuizen et al., 2008]. The VAF is defined as:

$$VAF = \left[1 - \frac{\sum_{k=1}^N |\delta_{cd}(t_k) - \hat{\delta}_{cd,ARX}(t_k)|^2}{\sum_{k=1}^N |\delta_{cd}(t_k)|^2} \right] \times 100\% \quad 6.18$$

where δ_{cd} and $\hat{\delta}_{cd,ARX}$ are the measured and predicted deflection of the control device, respectively. The value of the VAF varies between 0% and 100%, with 100% indicating that the ARX model perfectly models the measured output signal.

The CS-ML method operates in the frequency domain. This method first uses estimates of cross-spectral densities to calculate the frequency response function $\hat{H}_{\theta_t\delta_{cd}}$ between θ_t and δ_{cd} , and the frequency response function $\hat{H}_{F_d\delta_{cd}}$ between F_d and δ_{cd} :

$$\hat{H}_{\theta_t\delta_{cd}}(f) = \frac{\hat{S}_{\theta_t\delta_{cd}}(f)}{\hat{S}_{\theta_t\theta_t}(f)} \quad 6.19$$

$$\hat{H}_{F_d\delta_{cd}}(f) = \frac{\hat{S}_{F_d\delta_{cd}}(f)}{\hat{S}_{F_dF_d}(f)} \quad 6.20$$

In our experiment, the forcing functions F_d and θ_t were designed to have power at different sets of frequencies, $\{f_d\}$ and $\{f_t\}$, respectively (see Figure 6.3). This implies that $\hat{H}_{F_d\delta_{cd}}$ can only be estimated on frequencies $\{f_d\}$, and $\hat{H}_{\theta_t\delta_{cd}}$ on frequencies $\{f_t\}$.

To obtain estimates of $\hat{H}_{\theta_t\delta_{cd}}$ and $\hat{H}_{F_d\delta_{cd}}$ on a common set of frequencies, the CS-ML method applies an interpolation procedure. More precisely, the values $\hat{H}_{F_d\delta_{cd}}(f_d)$ are interpolated to estimate $\hat{H}_{F_d\delta_{cd}}$ at frequencies in $\{f_t\}$, and the values $\hat{H}_{\theta_t\delta_{cd}}(f_t)$ are interpolated to estimate $\hat{H}_{\theta_t\delta_{cd}}$ at frequencies in $\{f_d\}$. Note that the range of $\{f_t\}$ is smaller than the range of $\{f_d\}$. Since extrapolation of the values $\hat{H}_{\theta_t\delta_{cd}}(f_t)$ at frequencies outside the range of $\{f_t\}$ would give unreliable estimates, $\hat{H}_{\theta_t\delta_{cd}}$ can not be estimated on all the frequencies $\{f_d\}$, but only on those frequencies of $\{f_d\}$ that are within the range of $\{f_t\}$. These frequencies together with the frequencies in $\{f_t\}$ constitute the set \tilde{f} in which both $\hat{H}_{F_d\delta_{cd}}$ and $\hat{H}_{\theta_t\delta_{cd}}$ can be calculated:

$$f_{min} = \max(\min\{f_t\}, \min\{f_d\}) \quad 6.21$$

$$f_{max} = \min(\max\{f_t\}, \max\{f_d\}) \quad 6.22$$

$$\tilde{f} = \{f \mid f \in (\{f_t\} \cup \{f_d\}) \text{ and } f_{min} \leq f \leq f_{max}\} \quad 6.23$$

After $\hat{H}_{\theta_t\delta_{cd}}$ and $\hat{H}_{F_d\delta_{cd}}$ have been estimated for the common set of frequencies \tilde{f} , they are combined using block diagram algebra to obtain estimates of the admittance \hat{H}_{adm} , the visual response \hat{H}_{vis} , the control transfer function \hat{H}_{con} and the open-loop transfer function \hat{H}_{ol} . Expressions for \hat{H}_{adm} , \hat{H}_{vis} , \hat{H}_{con} , and \hat{H}_{ol} are given as follows:

$$\hat{H}_{adm}(f) = \frac{\hat{H}_{F_d\delta_{cd}}(f)H_{cd}(f)}{H_{cd}(f) - H_{cd}(f)\hat{H}_{\theta_t\delta_{cd}}(f)H_{ce}(f) - \hat{H}_{F_d\delta_{cd}}(f)} \quad 6.24$$

$$\hat{H}_{vis}(f) = -H_{ha}(f) + \frac{\hat{H}_{\theta_t\delta_{cd}}(f)}{\hat{H}_{F_d\delta_{cd}}(f)}(1 - H_{nps}(f)H_{ce}(f)) \quad 6.25$$

$$\hat{H}_{con}(f) = \frac{\hat{H}_{\theta_t\delta_{cd}}(f) - H_{nps}(f)}{1 - \hat{H}_{\theta_t\delta_{cd}}(f)H_{ce}(f)} + H_{nps}(f) \quad 6.26$$

$$\hat{H}_{ol}(f) = H_{ce}(f) \frac{\hat{H}_{\theta_t\delta_{cd}}(f) - H_{nps}(f)}{1 - \hat{H}_{\theta_t\delta_{cd}}(f)H_{ce}(f)}, \quad f \in \{\tilde{f}\} \quad 6.27$$



Figure 6.4: Apparatus.

These expressions are essentially the same as those found in Section 5.4, but include the influence of the Direct and Indirect Haptic Aids.

6.5 Experiment design

An experiment was conducted to investigate the effects of different haptic aids on human behavior in a pitch tracking task. This section describes the experiment design.

6.5.1 Control task and apparatus

The experiment was designed to evaluate human behavior in a compensatory pitch tracking task with haptic aids as described in Section 6.2. The experimental setup is shown in Figure 6.4. Participants had to minimize the error between the target signal θ_t and the pitch attitude of the controlled element θ_{ce} . Only the tracking error was shown on the visual display. During the tracking task, participants were provided with continuous haptic information as additional forces on the control device. In addition to the haptic aid, the control device was perturbed by the disturbance force F_d introduced to allow identification of the neuromuscular admittance.

The control device was a control-loading cyclic stick from Wittenstein Aerospace & Simulation GmbH, Germany, which can provide force-feedback to participants. The stick dynamics were estimated and are given by:

$$H_{cd}(s) = \frac{1}{1.522s^2 + 8.832s + 86.469} \quad [\text{rad/N}] \quad 6.28$$

During the experiment, the lateral axis of the stick was fixed, leaving the longitudinal axis free for performing the control task. No armrest was present for the arm that controlled the stick and subjects were asked not to use their legs as support. All the components were driven by a real-time computer running xPC Target (MathWorks, Inc.) and data were logged at 100 Hz.

6.5.2 Controlled element and haptic aid dynamics

The controlled element was simulated using the following dynamics:

$$H_{ce} = \frac{6}{s(\frac{1}{3}s + 1)} \quad [\text{rad/rad}] \quad 6.29$$

These dynamics, although idealized and not representative of a wide range of aircrafts, have been commonly used to investigate pilot behavior in tracking tasks [Hess, 1995; McRuer and Krendel]. At higher frequencies, the selected dynamics are similar to a double integrator, which are difficult to control for a participant. These dynamics are expected to accentuate the differences in human performance between different experimental conditions.

The design of the DHA and IHA was extensively explained in Section 6.2. The DHA was designed to mimic the human control behavior. According to McRuer theories, pilot response to H_{ce} dynamics in Equation (6.29) is given by:

$$H_{con} = K_p \left(\frac{1}{3}s + 1 \right) e^{-\tau_p s} \quad 6.30$$

To make sure that the haptic aid is designed such that it behaves similarly to the human, values for the human gain K_p and the equivalent

time delay τ_p were estimated during a preliminary design phase. The preliminary study used the same apparatus, controlled element, and target signal as the real experiment, but did not employed any haptic feedback. The resulting values were $K_p = 0.33$ and $\tau_p = 0.16$ s, which correspond to a crossover frequency $\omega_c \approx 2$ rad/s. These values were comparable with values found in a previous study with similar experimental conditions [McRuer and Krendel].

The dynamics of the DHA were then chosen as in Equation (6.2). However, a number of small modifications were introduced. First, the delay τ_p in Equation (6.2) was set to 0 s instead of the value estimated in the preliminary design phase, so that the haptic response was slightly faster than the human response. This was expected to improve the help provided by the haptic aid. Second, the dynamics of the control device H_{cd} were approximated by its static gain $K_{cd} = H_{cd}|_{s=0}$. This approximation is reasonable since H_{cd} behaves like a gain at frequencies around ω_c where the crossover model provides reliable estimates for the human behavior. Finally, an additional pole was placed at high frequency to ensure causality of H_{dha} . The resulting dynamics H_{dha} were given by:

$$H_{dha} = \frac{\omega_c}{sK_{cd}H_{ce}} \cdot \frac{1}{0.05s + 1} \approx 10 \frac{s + 3}{0.05s + 1} \quad [\text{N/rad}] \quad 6.31$$

As detailed in Section 6.2, the IHA force was generated with the same dynamics of the DHA force but opposite in sign. Thus, the dynamics of the IHA were given as:

$$H_{iha} = -H_{dha} \quad 6.32$$

6.5.3 Forcing functions

The two forcing functions F_d and θ_t were designed as multisine signals:

$$\theta_t(t) = \sum_{k=1}^{N_t} A_{t,k} \sin(2\pi f_{t,k}t + \psi_{t,k}) \quad 6.33$$

$$F_d(t) = \sum_{k=1}^{N_d} A_{d,k} \sin(2\pi f_{d,k}t + \psi_{d,k}) \quad 6.34$$

Each frequency $f_{t,k}$ and $f_{d,k}$ was chosen as an integer multiple of the experimental base frequency $f_0 = 1/T$, where T is the measurement time. The measurement time of an individual trial was $T = 81.92$ s, yielding a base frequency $f_0 = 0.0122$ Hz.

To distinguish the contribution of each forcing function to the measurements, different sets of frequency points were assigned to F_d and θ_t [Venrooij et al., 2014], see Figure 6.3a. The two sets consisted of clusters of two adjacent frequency points to allow for frequency averaging.

The force disturbance F_d contained power from 0.01 Hz up to 10 Hz, to allow for estimation of admittance on a large range of frequencies. The power level at low frequencies, from 0.01 Hz up to 1 Hz, was set to 1.2 N^2 and distributed among linearly spaced frequencies. At high frequencies, from 1 Hz up to 10 Hz, the power level was set to 0.8 N^2 and distributed among logarithmically spaced frequencies according to the Reduced Power Method [Mugge et al., 2007]. This method applies reduced power at high frequencies to enable estimation of the admittance without influencing low-frequency behavior.

The target signal θ_t contained power from 0.1 Hz up to 3 Hz. To avoid crossover regression, the distribution of the amplitudes $A_{t,k}$ was shaped according to the following filter [Zaal et al., 2009]:

$$A_{t,k} = \left| \frac{(j2\pi f_{t,k} T_1 + 1)^2}{(j2\pi f_{t,k} T_2 + 2)^2} \right| \quad 6.35$$

where $T_1 = 0.1$ s and $T_2 = 0.8$ s.

For both θ_t and F_d , the phases were chosen randomly to obtain unpredictable behavior. A cresting technique was applied to avoid amplitude peaks in time realizations [Pintelon and Schoukens, 2012]. Figure 6.3b shows the time realizations of F_d and θ_t . Note that both forcing signals were smoothed in the first and in the last 2 s of the experimental time interval to avoid transient effects.

Table 6.1: Measures for haptic aids with passive human operator.

	<i>no F_d</i>		<i>with F_d</i>	
	DHA	IHA	DHA	IHA
$\sigma^2(F_{ha}), N^2$	0.72	0.70	2.35	0.70
$\sigma^2(\delta_{cd}), deg^2$	0.45	0	2.18	0
$\sigma^2(\delta_{nps}), deg^2$	0	0.44	0	0.44
$\sigma^2(e), deg^2$	0.55	0.54	2.00	0.54

6.5.4 Performance of haptic systems and influence of force disturbance

According to our design of haptic aids, participants could perform the task by adopting a passive behavior, i.e., by being as compliant as possible with DHA, and by holding the stick in the center with IHA. In these cases, the control input to the aircraft is essentially provided by the haptic aid. Analysis of performance and control activity in these extreme situations is crucial to understand how much participants add to the haptic control action during the real experiment. It is also important to test these situations with and without injecting the force disturbance F_d .

Table 6.1 shows the variances of the force F_{ha} , the stick deflection δ_{cd} , the neutral point shift δ_{nps} , and the tracking error e , obtained in the two extreme situations: human showing infinite compliance with DHA, and human holding the stick in the center with IHA. The first two columns show the results without F_d . It is possible to note that:

- $\sigma^2(F_{dha}) \approx \sigma^2(F_{iha})$
- $\sigma^2(\delta_{cd}^{dha}) \approx \sigma^2(\delta_{nps}^{iha})$
- $\sigma^2(e^{dha}) \approx \sigma^2(e^{iha})$

These equalities are in complete agreement with the haptic aid design concepts explained in Section 6.5.2.

The last two columns of Table 6.1 show the variances obtained with F_d . The IHA is not influenced by the disturbance force. This is because the stick is clamped in the center with an infinitely stiff human operator, and F_d does not result in any disturbance to the aircraft. On the other hand, the values of DHA variances change when F_d is chosen as in Equation (6.33). This is because the force disturbance F_d actually deflects the control device, thus becomes a disturbance input for the aircraft.

6.5.5 Independent variables

The independent variable was the approach used to design the haptic aid. The DHA and IHA systems were tested and compared to a baseline tracking condition without haptic aid. This resulted in three experimental conditions.

6.5.6 Participants and experimental procedure

Eight participants took part in the experiment, seven male and one female. All participants were Ph.D. students at the Max Planck Institute for Biological Cybernetics, some had general experience with flight simulators and closed-loop control tasks. A financial compensation was offered for their participation. Before starting the experiment, participants received instructions about the objective of the experiment and the control tasks they would perform.

The experiment was split into two parts. The first part consisted of measuring admittance during disturbance-rejection tasks, the so-called “classical tasks”. Participants were asked to adopt three different control behaviors in response to a disturbance force applied to the control device [Abbink and Mulder, 2010]:

- Relax Task (RT): participants relaxed their arm and adopted a passive behavior. The display was turned off to prevent any distraction.
- Position Task (PT): participants minimized the stick deflection by resisting the disturbance force. The display showed the stick deviation to help participants perform the task.

- Force Task (FT): participants were compliant with the disturbance force and minimized the force applied to the stick. During the first trials, the display showed the force applied to the stick. After some training, the display was switched off.

During PT trials participants must adopt maximum stiffness (low admittance), whereas during FT trials participants must adopt minimum stiffness (high admittance). Identification of admittance in these two tasks thus gives an indication of the range over which admittance changes. On the other hand, the RT trials allow for an evaluation of the inertial properties of the arm.

The disturbance force for the classical tasks was designed as a multi-sine signal similar to F_d used in tracking tasks, but with different power at low frequencies. The power at low frequencies was varied between the three tasks to obtain the same standard deviation of the stick deflection for all classical tasks. In this way, non-linearities of the neuromuscular system due to large stick deflections were negligible. The power at low frequencies for FT, RT, and PT was approximately chosen 1, 1.5, and 6.5 times larger than in the tracking task, respectively.

To avoid learning effects, the three classical tasks were presented in a counterbalanced order between participants using a Latin square matrix [Franklin et al., 1992]. Participants were trained on each task until a stable performance was achieved. The performance was evaluated using the variance of the stick deflection for the PT and RT, and the variance of the human force applied by participants for the FT. After the training phase, three 90-s runs of each task were performed for averaging purposes.

In the second part of the experiment, participants performed the compensatory tracking task. Participants were instructed to minimize the tracking error shown on the compensatory display. Three different tracking conditions were investigated, i.e. tracking without haptic aid (NoHA), tracking with DHA and tracking with IHA. In each condition, participants were informed on the possible presence of haptic aids, but they were not informed on how to exploit the haptic feedback. This was done to reduce the possibility that participants would have focused only on following or opposing

the force generated by the haptic aid, instead of actively performing the tracking task.

The conditions were presented in counterbalanced order between participants using a Latin square matrix. For each condition, participants performed a training phase and a measurement phase. During the training phase, a number of runs were executed until participants achieved a stable performance evaluated using the variance of the tracking error. After the training phase, eight repetitions of each condition were executed and measurement data were recorded. Participants took regular breaks during the experiment. The whole experiment lasted approximately 3 h.

6.5.7 Dependent measures

During the experiment, the force F_{ho} , the stick deflection δ_{cd} , and the visual error e were logged at 100 Hz. The time of each experimental repetition was 90 s, of which 81.92 s were considered for data analysis. To reduce the noise, the measured signals were averaged in the time domain over all repetitions of each experimental condition.

A number of dependent measures was calculated from the recorded data. The variance of the tracking error e was calculated as a measure of tracking performance:

$$\sigma^2(e) = \frac{\sum_{k=1}^N (e(t_k) - \bar{e})^2}{N} \quad 6.36$$

where N represents the number of time samples and \bar{e} is the mean value of the visual error. Lower values of $\sigma^2(e)$ indicate better tracking performance. The control activity was evaluated using the variance of control signal δ_{cd} . The variance of the force F_{ho} was calculated as an indication of the amount of force needed by participants to perform the tracking task.

A one-way repeated measures analysis of variance (ANOVA) was used to investigate the statistical effect of the haptic aid on the variance metrics. For each ANOVA, the hypothesis of sphericity was tested by Mauchly's test. If data violated the sphericity hypothesis,

the Greenhouse-Geisser correction was applied [Field, 2013]. Post-hoc tests using the Bonferroni correction were performed to allow for pairwise comparisons between the three tracking conditions.

In addition, human's dynamic responses were estimated. The identification methods detailed in Section 6.4 were used to estimate the admittance, the visual response and the open-loop transfer function. To reduce noise, the CS and CS-ML estimates were averaged over each cluster of frequency points [Jenkins and Watts, 1969]. For the classical tasks, admittance was estimated according the CS method shown in Equation (6.8). In these tasks the method provides unbiased estimates.

6.5.8 Hypotheses

Both DHA and IHA systems are expected to yield better tracking performance compared to the tracking task without a haptic aid, since they are designed to help humans achieve their task.

Furthermore, it is hypothesized that participants would adapt their admittance depending on the haptic aid. Participants are expected to be more compliant in the DHA condition, resulting in higher admittance values. With IHA instead, participants are expected to show a stiffer neuromuscular setting, resulting in lower admittance values. During the tracking task without haptic aids, the admittance is expected to lay in the middle of the two previous cases.

Finally, it is hypothesized that the haptic aid would also influence the participants visual response. Since the DHA provides a portion of the control action needed to track the target, a smaller control action is needed from the participants. The visual response is therefore expected to have a lower gain in DHA than in the other two conditions.

6.6 Results

This section presents the experimental results of the eight participants. Tracking performance and control effort are compared between the tracking conditions with and without haptic aids. The difference in human's dynamic responses are investigated.

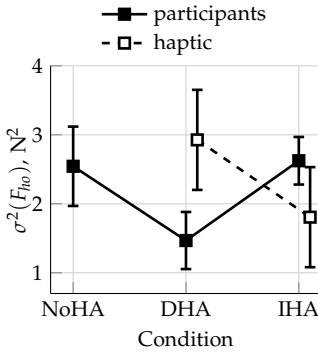
6.6.1 Tracking performance and control activity

To evaluate control effort, variance of force $\sigma^2(F_{ho})$ and control device deflection $\sigma^2(\delta_{cd})$ were calculated for the three experimental conditions: tracking task without haptic aid (NoHA), tracking task with DHA, and tracking task with IHA.

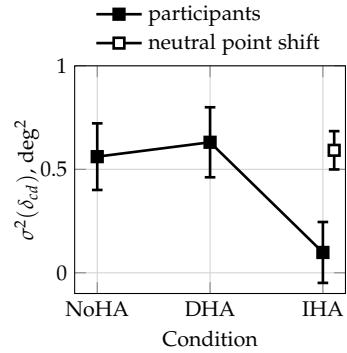
Figure 6.5a depicts the mean values and 95% confidence intervals of $\sigma^2(F_{ho})$ over all participants, together with the values for the variances $\sigma^2(F_{ha})$ of the force provided by the haptic aids. The effect of haptic aid on $\sigma^2(F_{ho})$ was found to be statistically significant ($F(2, 14) = 7.508$ and $p < 0.05$). Post-hoc tests with Bonferroni correction revealed that the DHA condition was statistically significantly different from the other two conditions (Table 6.2). Participants applied smaller forces with DHA to achieve the control task. This was because DHA provided part of the force needed for the tracking task, making the task less tiring for participants. The force provided by DHA had a variance $\sigma^2(F_{ha})$ approximately twice the variance of the force applied by participants (see Figure 6.5a). This indicates a large contribution of the DHA to the tracking task.

The variance of control device deflection $\sigma^2(\delta_{cd})$ was clearly reduced with the IHA (Figure 6.5b). The ANOVA test and post-hoc tests using Bonferroni correction showed that the differences between IHA and the other two cases were statistically significant ($F(2, 14) = 12.300$, $p < 0.05$, and Table 6.2). Participants slightly moved the stick from the center position in the IHA condition. This behavior, combined with the large shift of the neutral point shown in Figure 6.5b, allowed participants to keep the tracking error close to zero.

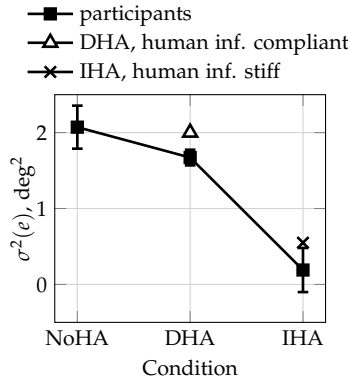
Pilot performance was evaluated by comparing the variance of the tracking error $\sigma^2(e)$ between the three tracking conditions.



(a) Pilot and haptic forces.



(b) Control device deflection and neutral point shift.



(c) Tracking error.

Figure 6.5: Means and 95% confidence intervals of measured variances over all participants.

Both the DHA and IHA led to a lower variance compared to the NoHA condition (Figure 6.5c). The ANOVA test showed that the effect of the haptic aid on $\sigma^2(e)$ was statistically significant ($F(1.2, 8.4) = 62.671$, $p < 0.05$). Post-hoc tests using the Bonferroni correction revealed that the differences between all the conditions

Table 6.2: Results of post-hoc tests with Bonferroni correction for $\sigma^2(\cdot)$ data.

Independent variables	Dependent measures					
	$\sigma^2(F_{ho})$		$\sigma^2(\delta_{cd})$		$\sigma^2(e)$	
Factor	p	Sig. ^a	p	Sig.	p	Sig.
DHA <i>vs.</i> NoHA	0.091	*	1.000	–	0.057	*
IHA <i>vs.</i> NoHA	1.000	–	0.011	**	0.000	**
IHA <i>vs.</i> DHA	0.003	**	0.007	**	0.000	**

a. **: highly significant ($p < 0.050$) * : marginally significant ($0.050 \leq p < 0.100$)
 –: not significant ($p \geq 0.100$)

were statistically significant (Table 6.2). Thus, both the DHA and IHA helped participants in increasing performance. While performance differed only slightly between DHA and NoHA, the variance in the IHA condition was approximately 80% lower than the other two conditions.

Figure 6.5c also shows the performance of DHA and IHA with an infinitely compliant and an infinitely stiff human, respectively. As explained in Section 6.5.4, the difference between the two values is due to the influence of the force disturbance F_d . It can be noted that in both DHA and IHA conditions, participants improved the performance that they would have obtained by assuming a passive behavior (i.e., infinitely compliant or infinitely stiff). This shows that a human operator who contributes actively to controlling the aircraft can achieve better performance with respect to the passive behavior described in the two extreme conditions.

6.6.2 Admittance

Figure 6.6 shows the admittance estimated with the three identification methods in conditions NoHA, DHA, and IHA, averaged over all participants. High VAF and coherence values $\hat{\Gamma}_{adm}^2$ were found for the ARX and the CS estimates, respectively (see Figure 6.7). Note that the coherence function only indicates that the relation between the measured human force F_{ho} and the position of the control device δ_{cd} can be approximated as linear, but does not give information

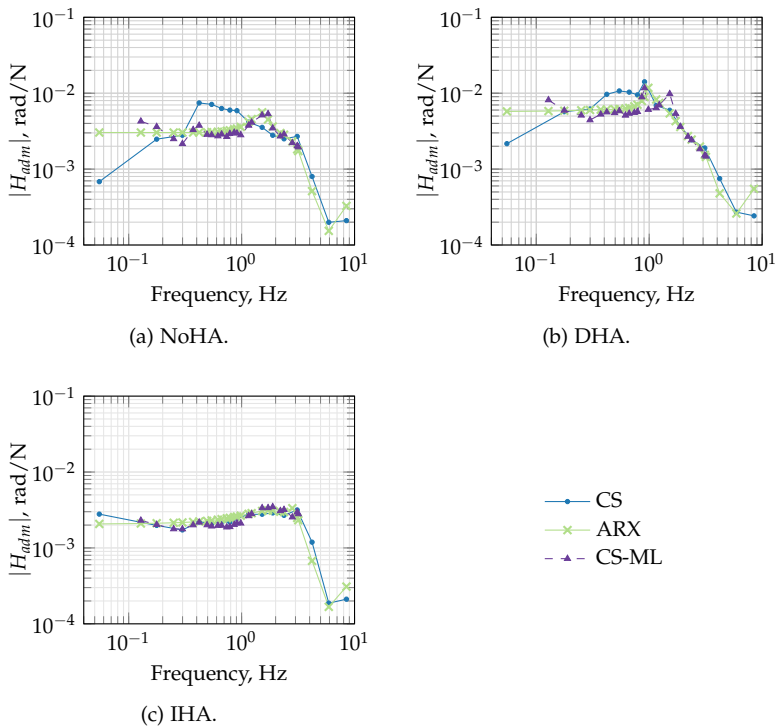


Figure 6.6: Admittance estimates for NoHA, DHA, and IHA conditions, averaged over all participants.

about the correspondence between the actual and the estimated admittance.

In the NoHA and DHA conditions, the CS method produced estimates that differed largely from those obtained with ARX and CS-ML methods at frequencies below 1 Hz. On the contrary, the admittance estimated by the ARX and CS-ML methods were similar. Only in the IHA case, the three methods gave similar results. As shown in Chapter 5, these differences could be due to a bias that characterizes the CS estimates when the so-called non-interference hypothesis is not fulfilled, i.e. when the power content of the visual

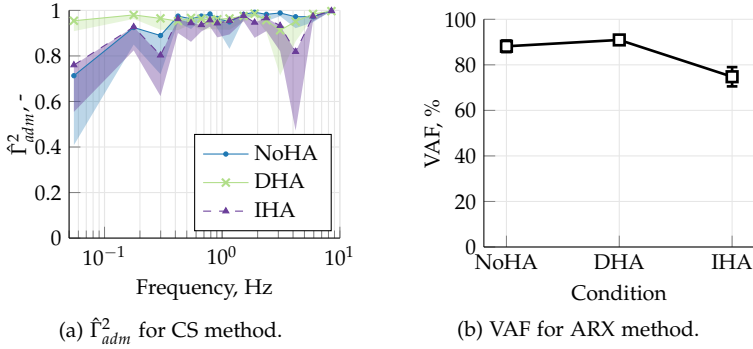


Figure 6.7: Means and standard deviations of reliability measures for neuromuscular estimates, over all participants.

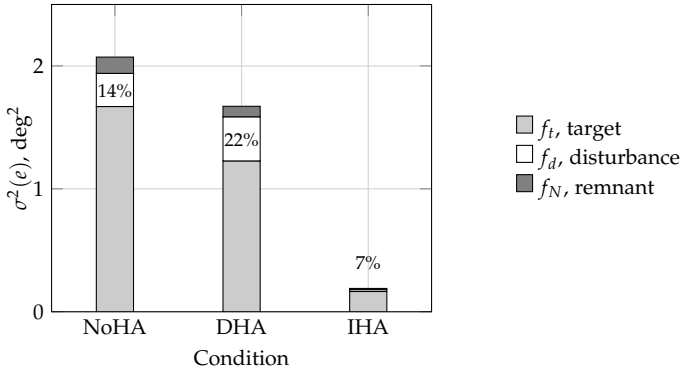


Figure 6.8: Decomposition of the variance of the visual error and percentages at frequencies $\{f_d\}$.

error e is not negligible at frequencies $\{f_d\}$ where the disturbance force F_d has power.

To verify if the non-interference hypothesis was fulfilled during our tracking conditions, Figure 6.8 shows the power content of e at frequencies $\{f_d\}$ (where the disturbance force F_d has power), $\{f_t\}$ (where the target trajectory θ_t has power), and $\{f_N\}$ (where both forcing functions have no power). The power content of e

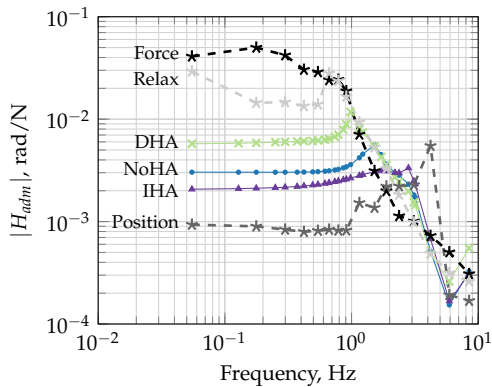


Figure 6.9: Admittances for classical and tracking tasks obtained with CS and ARX methods, respectively.

at frequencies $\{f_d\}$ is clearly not negligible for NoHA and DHA conditions (14% and 22% of the total power, respectively), whereas it is lower in the IHA case (7%). This explains the bias at low frequencies in the CS estimates for the NoHA and DHA cases.

To better highlight differences between NoHA, DHA, and IHA, the admittance estimated in the three conditions are shown together in Figure 6.9 (solid lines). Only estimates from the ARX method are provided, since they are similar but smoother than those obtained with the CS-ML method. The CS estimates are not considered as these estimates clearly contain a bias. In addition, Figure 6.9 shows average admittance estimated during the “classical tasks” (dashed lines). Admittance varied mostly at frequencies below 1 Hz. Higher admittance values were found in the DHA condition with respect to the NoHA condition. This indicates that participants were more compliant with the DHA to follow the control action suggested by the DHA force. On the other hand, admittance was lower in the IHA condition. Thus, participants adopted a stiffer setting of their arm, which allowed them to oppose the IHA force.

Compared to the classical tasks, participants varied their admittance over a smaller range during the tracking tasks. More precisely,

the admittance in the Position Task (i.e., adopt maximum stiffness) was smaller than in the tracking tasks, whereas admittance in Relax Task (i.e., relax the arm) and Force Task (i.e., adopt maximum compliance) were higher than in the tracking tasks. Thus, participants did not adopt maximum compliance during the DHA condition, or maximum stiffness during the IHA condition. We hypothesize that participants would only be able to reach maximum and minimum admittances if they would rely solely on forces provided by the haptic aids, without trying to actively minimize the tracking error.

At frequencies above 1 Hz, the admittance of all tracking conditions and classical tasks converged to similar values. The admittance shapes had a slope of approximately $100 \frac{rad}{dec}/N$ ($= 40 \frac{dB}{dec}$), which corresponds to the slope of the dynamics of a mass subjected to forces. This indicates that the admittance at high frequencies was mainly determined by inertial properties of the arm. The peak in the admittance of Position Task at frequencies around 4 Hz is probably due to activation of the Golgi Tendon Organ [Schouten et al., 2008b].

6.6.3 Pilot visual response

The visual response H_{vis} describes how participants generate a force F_{ho} on the control device based on the error e presented on the display. Note that in literature, the visual response often refers to the transfer function between the visual error to the stick control deflection δ_{cd} [McRuer]. As explained in Section 6.4, we adopted a different definition of H_{vis} not to include the haptic system in the visual response.

Only ARX and CS-ML methods can estimate H_{vis} directly. Results of the two methods are shown in Figure 6.10, averaged over all participants. Despite the fact that ARX method provided smoother estimates, both methods gave consistent results.

The general shape of the visual response estimates was very similar for NoHA and DHA conditions. The estimates resembled a gain at low frequencies and a differentiator at higher frequencies, i.e., the participants generated lead. The only relevant difference between NoHA and DHA was that the magnitude of the visual

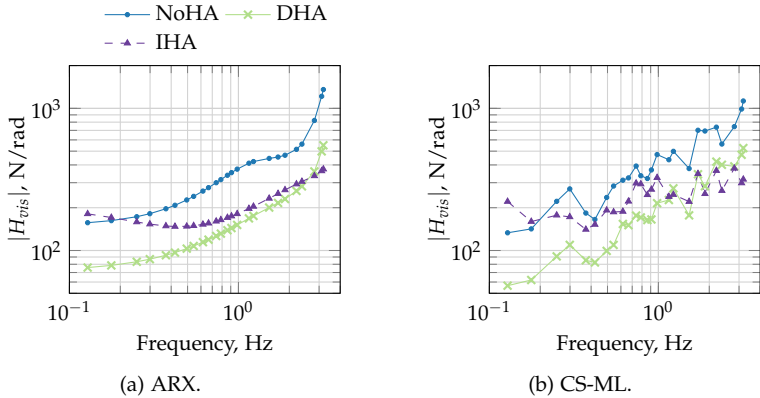


Figure 6.10: Pilot visual responses estimated with ARX and CS-ML methods, averaged over all participants.

response was lower at all frequencies for the DHA case. This indicates that participants applied lower forces on the control device in response to the visual tracking error. The IHA response was similar to the DHA response at higher frequencies, but resembled a gain at frequencies below 0.7 Hz. Participants started to generate lead at higher frequencies than in the NoHA and DHA conditions.

6.6.4 Control and open-loop transfer functions

The control transfer function H_{con} represents the transfer function from the visual error e to the deflection of the control device δ_{cd} . Note that in a compensatory tracking task without haptic aids, H_{con} includes the human visual response H_{vis} , the admittance H_{adm} , the control device H_{cd} , and the haptic aid H_{ha} , see Figure 6.2. Figure 6.11 depicts the control transfer functions estimated by CS, CS-ML, and ARX methods for all experimental conditions NoHA, DHA, and IHA. For all conditions, the coherence Γ_{con}^2 associated to the CS method was higher than 0.95, indicating accuracy of the estimates.

The three identification methods provided similar estimates of \hat{H}_{con} . The magnitude of \hat{H}_{con} changed slightly between the conditions NoHA, DHA, and IHA, but the general shape was similar. The

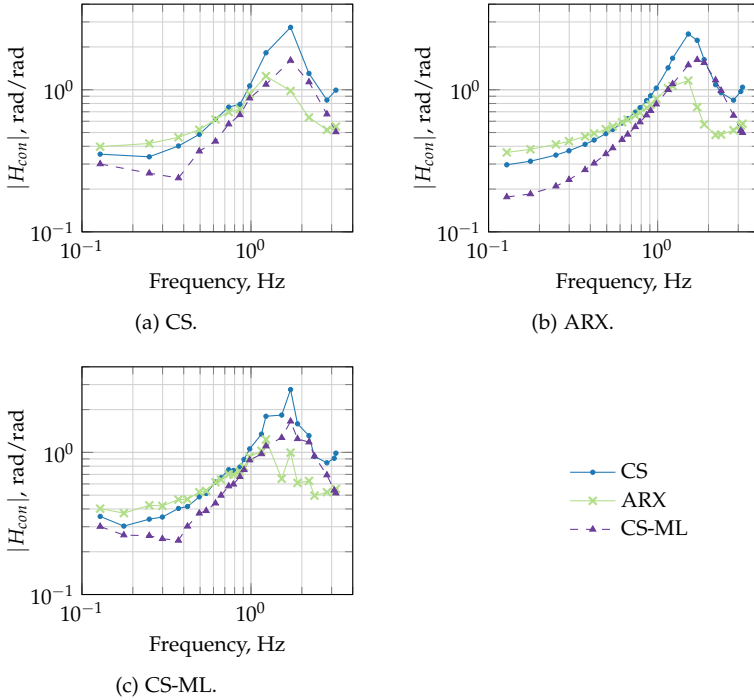


Figure 6.11: Responses H_{con} estimated with the three identification methods, averaged over all participants.

estimates resembled a gain at low frequencies and a differentiator at medium frequencies, as would be expected from the dynamics of the controlled element [McRuer]. The peak at high frequency is due to the combined dynamics of the control device and the neuromuscular system. The effect of DHA and IHA was to decrease the magnitude of this peak, which would result in improved closed-loop stability and better performance [Pool et al., 2008].

The open-loop transfer function H_{ol} represents the transfer function from the visual error e to the position of the controlled element θ_{ce} . In the control task shown in Figure 6.2, it includes the control response H_{con} , the dynamics of the neutral point shift (only for IHA),

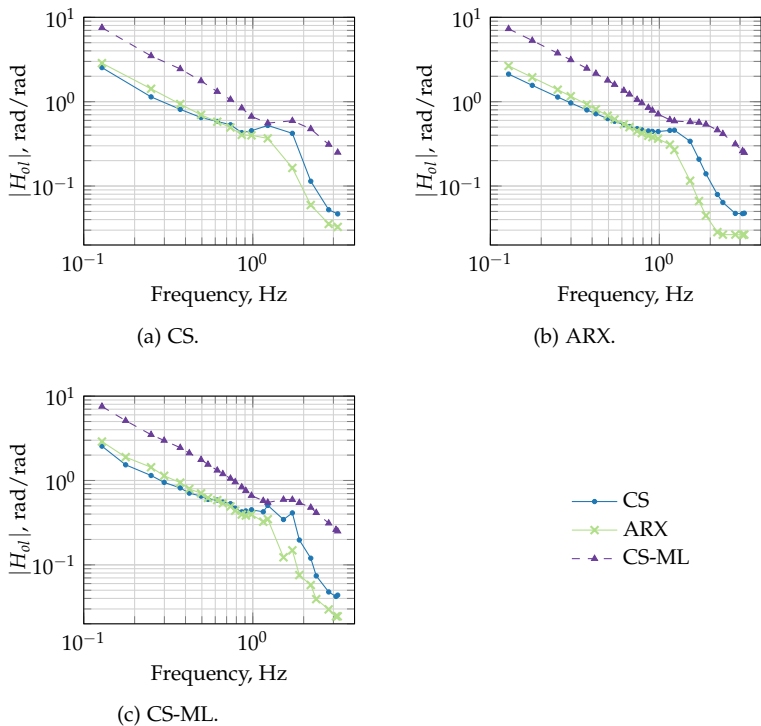


Figure 6.12: Open-loop responses estimated with the three identification methods, averaged over all participants.

and the controlled element H_{ce} . Figure 6.12 shows the estimates of H_{ol} given by the CS, CS-ML, and ARX methods for all experimental conditions. High coherence values Γ_{ol}^2 were found for the CS estimates ($\Gamma_{ol}^2 > 0.95$ at all frequencies), indicating reliability of the estimates.

The three identification methods gave similar estimates. At frequencies below 1 Hz, the open-loop transfer functions resembled integrator-like dynamics for all NoHA, DHA, and IHA conditions. These findings correlate favourably with McRuer's theories [McRuer], which assess that pilots adapt their responses to yield

a combined pilot-aircraft dynamics similar to a single integrator. Although these theories were developed for tracking tasks without haptic aids, our results lend support to their validity also when haptic aids are used. The crossover frequency ω_c was about 0.3 Hz for NoHA and DHA cases, while it significantly increased to about 0.8 Hz with IHA. A larger crossover frequency indicates that the system has a faster dynamic response and an improved ability to track the signal. This is in complete agreement with high performance found for IHA tracking condition, see Figure 6.8.

6.7 Conclusions

This chapter considered two different approaches for designing haptic aid systems: the DHA and IHA. A DHA and a IHA system were evaluated in a compensatory tracking task and compared to a baseline condition without haptic support. Both approaches allowed participants to increase performance. In particular, the IHA outperformed the DHA and the baseline condition. On the other hand, the physical effort was significantly reduced by the DHA. This was shown by a decreased variance of the force that participants applied on the control device to perform the task.

Pilot control behavior was estimated with three identification methods: the commonly used CS method and the two novel ARX and CS-ML methods. The ARX and the CS-ML method gave similar estimates, whereas the admittance estimated by the CS method contained a bias caused by non-compliance to the so-called *non-interference* hypothesis.

Participants adapted their admittance to fully exploit the haptic aids. They adopted a lower admittance (stiffer neuromuscular dynamics) to oppose the IHA force, whereas they adopted a higher admittance (more compliant neuromuscular dynamics) to better follow the control action suggested by the DHA force. Furthermore, participants adapted their visual response to yield an open-loop transfer function similar to a single integrator in all the tracking conditions. These findings suggest that McRuer's theories are still applicable when haptic aids are used, although this needs to be

confirmed with different control dynamics than those used in this study.

These results shed light on human adaptation to different designs of haptic aid. However, the current study has only considered non-pilot participants. It remains to be further investigated how real pilots would interact with DHA and IHA aids.

Part III

Identifying time-varying neuromuscular response

Methods for identifying time-varying neuromuscular response in single-loop tasks

In previous chapters, pilot's dynamic responses have been assumed to be time-invariant. Although this assumption can be met in experimental settings, humans are likely to change their responses in realistic control scenarios. Thus, methods are needed that account for time-varying behavior. This chapter presents a method that estimates online time-varying neuromuscular dynamics during disturbance-rejection tasks. This method is based on a Recursive Least Squares (RLS) algorithm and assumes that the neuromuscular response can be approximated by a Finite Impulse Response filter. The novel RLS-based method was first validated with sets of Monte-Carlo simulations, then applied to experimental data. The results indicated that RLS-based method is a valid tool for estimating online time-varying neuromuscular response.

The contents of this chapter are based on:

Paper title Identifying time-varying neuromuscular system with a Recursive Least-Squares algorithm: a Monte-Carlo simulation study

Authors Olivari, M., Nieuwenhuizen, F. M., Bühlhoff, H. H., and Pollini, L.

Published in Proceedings of the IEEE International Conference on Systems, Man and Cybernetics, San Diego, CA, October 2014, 3573-3578

- and -

Paper title Identifying time-varying neuromuscular response: experimental evaluation of a RLS-based algorithm

Authors Olivari, M., Nieuwenhuizen, F. M., Bühlhoff, H. H., and Pollini, L.

Published in Proceedings of the AIAA Modeling and Simulation Technologies Conference, Kissimmee, FL, January 2015, 1-15

7.1 Introduction

To assess whether haptic forces have a positive effect on the human operator performing the task, an insight is required into the control behavior of the human operator. The dynamics of the neuromuscular system play an important role when trying to investigate the effect of haptic aids on human behavior [Abbink et al., 2011]. Previous works have investigated methods to estimate the neuromuscular system during disturbance-rejection tasks [Schouten et al., 2008b] or more complex control tasks [Abbink et al., 2011; van Paassen et al., 2004]. However, a key limitation with much of the literature is that the estimation methods assume a time-invariant neuromuscular response. In realistic control scenarios, the neuromuscular response is likely to be time-variant, since humans change their behavior depending on environmental variables, fatigue, etc. [Mulder et al., 2011b]. Thus, there is a need for identification methods that can be used to assess the time-varying nature of the neuromuscular response.

Parametric identification methods have been used to estimate different time-varying human responses, like visual and vestibular responses [Hess, 2011; Zaal and Sweet, 2011, 2012]. These methods represent the dynamic responses by using a set of parametric equations, and provide estimates of the model parameters. However, parameter estimates may be unreliable if many parameters are used in the model or if the model is inaccurate [Zaal and Sweet, 2012]. Unfortunately, models of neuromuscular system require many parameters to describe the neuromuscular dynamics in different conditions [van Paassen et al., 2004; Schouten et al., 2008a]. Thus, using parametric approaches for estimating neuromuscular dynamics may lead to inaccurate estimates.

As opposed to parametric methods, non-parametric methods do not employ parametric models, but instead use non-parametric representations of the system [Wellstead, 1981]. An example of non-parametric representation is the Frequency Response Function (FRF). A number of attempts have been made to estimate the FRF of a time-varying neuromuscular system. Katzourakis et al. [2014] used

the windowed Fourier Transform to estimate the neuromuscular FRF on a sliding time window. By moving the sliding window over time, time-varying behavior of the neuromuscular FRF was identified. However, as others have highlighted, the windowed Fourier Transform has the drawback that it uses the same time window length for estimating the FRF on the whole frequency range [Balderas Silva, 2009; Mulder et al., 2011b; Thompson et al., 2004]. This reduces the ability of identifying fast changes at high frequencies.

A wavelet-based identification method was proposed to overcome this drawback. The wavelet transform gives the possibility of using different windows lengths for different frequencies, allowing for a rapid identification at high frequencies. Although the wavelet-based method provided reliable neuromuscular estimates at high frequencies, the accuracy of the estimates decreased at low frequencies [Mulder et al., 2011b].

Different studies focused on estimating the impulse response instead of the FRF. Ensemble methods have been successfully employed to estimate the impulse response of a time-varying neuromuscular system [Lortie and Kearney, 2001; Ludvig and Perreault, 2012; MacNeil et al., 1992]. These methods estimate the impulse response by using data from different experimental repetitions (ensembles). However, ensemble methods require that the neuromuscular response presents the same time-varying behavior in all the ensembles [MacNeil et al., 1992]. This requirement is difficult to be met during realistic control scenarios.

This chapter presents a novel method that estimates the impulse response of a time-varying neuromuscular system without requiring ensembles with the same time-varying behavior. The method is developed for disturbance-rejection tasks, and it will be extended for compensatory tracking tasks in Chapter 9. The method approximates the neuromuscular impulse response by a Finite Impulse Response (FIR) filter and uses a Recursive Least Squares (RLS) algorithm to estimate the parameters of the FIR filter itself. The reliability and the robustness of the method were analysed by using sets of Monte-Carlo simulations. Then, the method was applied to experimental data.

The chapter is organized as follows. Section 7.2 provides a model of the disturbance-rejection tasks. Section 7.3 gives a brief overview of the RLS-based method. In Section 7.4, Monte-Carlo simulations are presented to assess the accuracy of the RLS-based method. Then, the RLS-based method is applied to experimental data in Section 7.5. Conclusions are drawn in the final section.

7.2 Control task

In general, the human operator uses several degrees of freedom to interact with a control stick. However, the interaction can be simplified when considering some assumptions [van Paassen, 1994]. Firstly, we consider a control stick that possesses one degree of freedom (lateral axis). Secondly, an arm rest is employed to keep the elbow at a fixed position (point P in Figure 7.1a). In this situation, the human operator tends to move the control device by immobilizing the wrist and by rotating the lower arm (hand and ulna) around an axis normal to the armrest passing through P. Thus, the movement of the arm can be described with only one degree of freedom, which is the rotation α of the lower arm around the axis.

In the one-degree of freedom situation, the interaction of the human arm with the control stick can be modelled as shown in Figure 7.1b. The human operator HO generates a force F_{ho} to control the lateral deflection δ_{cd} of the control device CD. At the same time, proprioceptive sensors of the arm neuromuscular system sense the deflection δ_{cd} and its velocity (feedback path in Figure 7.1b) [Schouten et al., 2008a]. The dynamics of neuromuscular system are described by the inverse of the admittance ADM, which is defined as the causal relationship between the force acting on the arm and the position of the arm. All the elements of Figure 7.1b are assumed to be linear, and the remnant noise N accounts for all the unmodeled nonlinearities. The signal u_{cns} represents all cognitive actions that are communicated from the Central Nervous System, e.g., the human response to external visual cues.

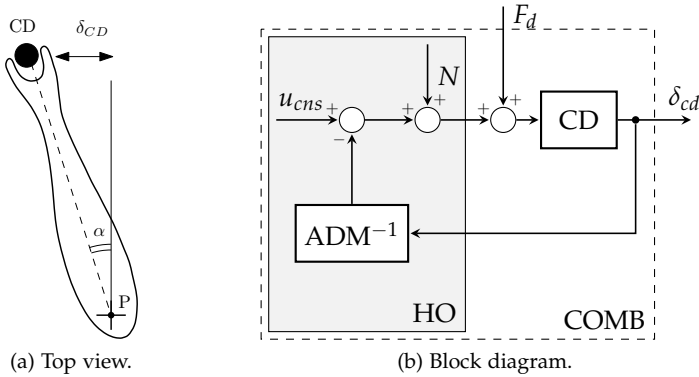


Figure 7.1: Interaction of a pilot with the control device.

This chapter focuses on disturbance-rejection tasks, where the human operator is asked to adopt different control strategies in response to a force disturbance applied on the control device. In these tasks, the contribution u_{cns} due to external cues can be considered negligible.

7.3 Estimating time-varying neuromuscular dynamics

Humans are able to adapt the neuromuscular dynamics to the task they perform. For instance, humans adopt a lower admittance (i.e., stiffer arm) when they want to oppose to external forces, or a higher admittance to be more compliant with the force. In realistic control situations, e.g., during postural control or driving tasks, humans vary their admittance continuously depending on the external environment [Mulder et al., 2011b].

This section presents a method that can be applied to estimate time-varying admittance. First, the method approximates the impulse response of the combined system COMB of admittance and control device by using a Finite Impulse Response (FIR) filter. Then, the filter coefficients are estimated by employing a Recursive Least

Squares algorithm. Finally, the admittance Frequency Response Function is calculated from the estimated impulse response by using Fourier analysis and block diagram algebra.

7.3.1 Impulse response of COMB

The impulse response $h_{comb}(t_n, t_m)$ is defined as the response of the system COMB at time $t_n = n \cdot T$ to an impulse applied at time $t_m = m \cdot T$ [Shmaliy, 2007]. The output δ_{cd} given a generic input signal F_d can be expressed as the convolution between the input and the impulse response:

$$\delta_{cd}(t_n) = T \sum_{k=-\infty}^{\infty} h_{comb}(t_n, t_k) F_d(t_k) \quad 7.1$$

Equation (7.1) has an infinite number of terms. However, it can be simplified by considering some properties of physical systems. First, physical systems are causal, i.e., their output does not depend on future inputs [Shmaliy, 2007]. For these systems, the impulse response must be 0 for all $t_n < t_m$. Furthermore, many physical systems (such as the neuromuscular system) have an approximately finite impulse response, i.e., $h_{comb}(t_n, t_m)$ becomes approximately zero after M time samples. After combining the assumptions of causality and finite memory, the response y of the system can be written as:

$$\begin{aligned} \delta_{cd}(t_n) &= T \sum_{k=n-M}^n h_{comb}(t_n, t_k) F_d(t_k) \\ &= \begin{bmatrix} T F_d(t_n) & \cdots & T F_d(t_{n-M+1}) \end{bmatrix} \begin{bmatrix} h_{comb}(t_n, t_n) \\ \vdots \\ h_{comb}(t_n, t_{n-M+1}) \end{bmatrix} \\ &= \mathbf{F}_d^T(t_n) \mathbf{h}_{comb}(t_n) \end{aligned} \quad 7.2$$

where $\mathbf{F}_d, \mathbf{h}_{comb} \in \mathbb{R}^M$.

Our aim is to estimate the impulse response vector \mathbf{h}_{comb} at each time step t_n given the measurements of $u(t_k)$, $y(t_k)$ at previous and

current time steps ($t_k \leq t_n$). To do this, a Recursive Least Squares (RLS) algorithm can be applied [Diniz, 2008].

7.3.2 RLS algorithm

The RLS algorithm calculates an estimate \hat{h}_{comb} of the impulse response vector by minimizing the following cost function:

$$\begin{aligned}\hat{h}_{comb}(t_n) &= \arg \min_{h \in \mathbb{R}^M} \sum_{k=n_0}^n \lambda^{n-k} \left[F_d^T(t_k) h - \delta_{cd}(t_k) \right]^2 \\ &= \min_h \sum_{k=n_0}^n \lambda^{n-k} \epsilon^2(t_k)\end{aligned}\tag{7.3}$$

where n_0 is the first time sample, ϵ represents the prediction error between predicted and the measured output, and λ is a forgetting factor that gives smaller weight to errors occurred further in the past ($0 \ll \lambda < 1$) [Diniz, 2008]. For the sake of clarity and without loss of generality, the initial time sample is assumed to be $n_0 = 1$.

The minimum solution \hat{h}_{comb} of Equation (7.3) is:

$$\begin{aligned}\hat{h}_{comb}(t_n) &= \left[\sum_{k=1}^n \lambda^{n-k} F_d(t_k) F_d^T(t_k) \right]^{-1} \sum_{k=1}^n \lambda^{n-k} F_d(t_k) \delta_{cd}(t_k) \\ &= R^{-1}(t_n) p(t_n)\end{aligned}\tag{7.4}$$

where the matrix R is assumed to be nonsingular. The algorithm, written as in Equation (7.4), requires computation of the inverse of R at each time step. However, this computation can be avoided by using the matrix inversion lemma [Diniz, 2008], which allows for calculating the inverse of the matrix $R(t_n)$ by using the inverse $R^{-1}(t_{n-1})$ calculated at the previous time step. Table 7.1 shows the resulting RLS-based algorithm ($S = R^{-1}$).

7.3.3 Estimating admittance frequency response

The estimated impulse response vector \hat{h}_{comb} is used to estimate the Frequency Response Function (FRF) of H_{comb} [Lataire et al., 2012;

Table 7.1: RLS algorithm

INITIALIZE	$S(0) = S_0$ $\hat{\mathbf{h}}_{comb}(0) = \mathbf{0}$
FOR $n \geq 0$ DO	$e(t_n) = \delta_{cd}(t_n) - \mathbf{F}_d^T(t_n) \hat{\mathbf{h}}_{comb}(t_{n-1})$ $\boldsymbol{\psi}(t_n) = \mathbf{S}(t_{n-1})\mathbf{F}_d(t_n)$ $\mathbf{S}(t_n) = \frac{1}{\lambda} \left[\mathbf{S}(t_{n-1}) - \frac{\boldsymbol{\psi}(t_n)\boldsymbol{\psi}^T(t_n)}{\lambda + \boldsymbol{\psi}^T(t_n)\mathbf{F}_d(t_n)} \right]$ $\hat{\mathbf{h}}_{comb}(t_n) = \hat{\mathbf{h}}_{comb}(t_{n-1}) + e(t_n)\mathbf{S}(t_n)\mathbf{F}_d(t_n)$

Shmaliy, 2007]:

$$\hat{H}_{comb}(f, t_n) = T \hat{\mathbf{h}}_{comb}^T(t_n) \begin{bmatrix} 1 \\ e^{-j2\pi f} \\ \vdots \\ e^{-j2\pi f N_{mem}} \end{bmatrix} \quad 7.5$$

where f indicates the frequency.

Then, the FRF of ADM is estimated from \hat{H}_{comb} by using block diagram algebra:

$$\hat{H}_{adm}(f, t_n) = \frac{H_{cd}(f) \hat{H}_{comb}(f, t_n)}{H_{cd}(f) - \hat{H}_{comb}(f, t_n)} \quad 7.6$$

where $H_{cd}(f)$ is the known FRF of the control device.

7.3.4 Force disturbance design

In the literature on admittance identification, the force disturbance F_d is commonly designed as a multisine signal [Abbink et al., 2011; Schouten et al., 2008a]:

$$F_{d,ms}(t_n) = \sum_{k=1}^{N_d} A_k \sin(2\pi f_k t_n + \psi_k) \quad 7.7$$

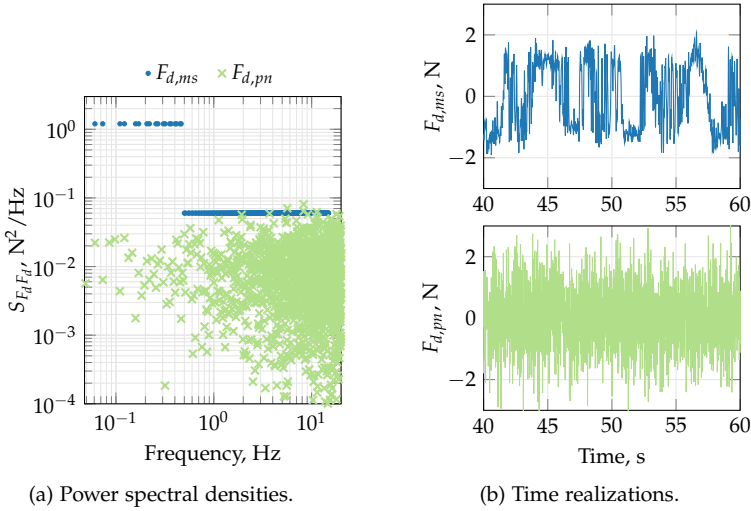


Figure 7.2: Multisine $F_{d,ms}$ and pseudonoise $F_{d,pn}$ components of the force disturbance.

where A_k , f_k and ψ_k are amplitudes, frequencies, and phases, respectively, and N_d are the number of sinusoids. The values of f_k , A_k , and ψ_k are usually chosen to capture relevant dynamics of the neuromuscular system without inducing suppression of reflexive activity [Abbink et al., 2011; Mugge et al., 2007]. Figure 7.2 shows typical time realizations and power spectral densities of $F_{d,ms}$.

To estimate \hat{h}_{comb} , the RLS-based algorithm requires computing the inverse of the matrix \mathbf{R} that only depends on values of the force disturbance F_d , see Equation (7.4). Thus, F_d must be designed such that \mathbf{R} is invertible, i.e., F_d must be *persistently exciting*. Unfortunately, it can be shown that the commonly used multisine signal is not persistently exciting and cannot be employed with the RLS algorithm.

To obtain an invertible \mathbf{R} matrix, a pseudonoise $F_{d,pn}$ was added to the multisine signal, see Figure 7.2. The resulting force disturbance F_d was chosen as:

$$F_d(t_n) = k_{ms}F_{d,ms}(t_n) + k_{pn}F_{d,pn}(t_n) \quad 7.8$$

where $F_{d,ms}$ and $F_{d,pn}$ were scaled to have variances equal to 1 N^2 , and the gains k_{ms} , k_{pn} were used to set final desired variances. The gain k_{pn} was chosen to be low enough to avoid suppression of reflexive activity [Mugge et al., 2007], while still generating an invertible and well-conditioned \mathbf{R} matrix. The gain k_{ms} was tuned to obtain a desired variance of the total force disturbance F_d .

7.4 Validation of the RLS-based method in simulation

The RLS-based method was validated by performing two sets of Monte-Carlo simulations. The first set investigated robustness of the RLS-based method to external noise. The second set focused on the influence of the forgetting factor λ on RLS-based estimates.

7.4.1 Robustness to remnant noise

Method

A Monte-Carlo simulation was performed to investigate the robustness of the RLS-based method to different levels of remnant noise N . To do this, the control task in Figure 7.1 was numerically simulated in Matlab/Simulink.

The admittance dynamics were simulated by using a parametric model detailed in Section A.2.3. The parameters were simulated to vary between stiff and relax settings. The parameters for the relax admittance and for the stiff admittance were chosen as estimated in a previous study, see Table 7.2 [Schouten et al., 2008b]. The time evolution of each parameter was chosen similarly to a previous work [Mulder et al., 2011b]:

$$p_i(t_n) = AM(t_n)p_i^s + (1 - AM(t_n))p_i^r \quad 7.9$$

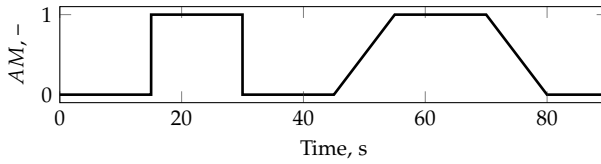


Figure 7.3: Time evolution of the parameter AM , which determines the evolution of the neuromuscular dynamics. Values 0 and 1 correspond to relax and stiff admittance, respectively.

Table 7.2: Admittance parameters (C-Compliant, S-Stiff)

	m_{int}	b_{int}	k_{int}	b_{skin}	k_{skin}	k_a	k_v	k_p	τ	ω_0	β
	kg	$\frac{Ns}{m}$	$\frac{N}{m}$	$\frac{Ns}{m}$	$\frac{kN}{m}$	$\frac{Ns^2}{m}$	$\frac{Ns}{m}$	$\frac{N}{m}$	ms	$\frac{rad}{s}$	-
C	2.02	32.5	382	228	11.7	2.3	37.4	91	28.4	13.63	0.74
S	2.02	14.4	169	44	2.6	0	0	0	0	13.63	0.74

where p_i^r , p_i^s represent the generic i -th parameter for relax and stiff admittance, respectively, and the parameter AM (Admittance Mode) varies between 0 and 1 as shown in Figure 7.3. The value $AM = 0$ corresponds to relax settings of the admittance, whereas $AM = 1$ indicates stiff settings. Figure 7.4 depicts the resulting time evolution of the admittance Frequency Response Function.

The dynamics of the control device CD were chosen as in Schouten et al. [2008b]:

$$H_{cd} = \frac{1}{s^2 + 50} \quad [m/N] \quad 7.10$$

The disturbance force F_d was designed as a linear combination of a multisine $F_{d,ms}$ and a pseudonoise $F_{d,pn}$ as shown in Equation (7.8). The gains k_{pn} and k_{ms} were tuned such that the variance of $F_{d,pn}$ was the 5% of the total variance, which was set to 3 N^2 .

The pseudonoise $F_{d,pn}$ was chosen as a realization of Gaussian noise, see Figure 7.2. The multisine $F_{d,ms}$ was chosen based on previous works on admittance estimation [Abbink et al., 2011; Schouten et al., 2008a]. Specifically, the multisine frequencies f_k were chosen

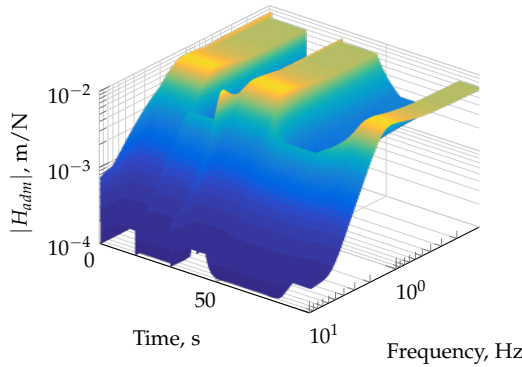


Figure 7.4: Time evolution of the simulated admittance H_{adm} .

as multiples of the base frequency $f_0 = 0.0122$ Hz, resulting in a periodic signal with a period of 81.92 s. To completely capture the neuromuscular dynamics, the frequencies f_k were selected in the range $[0.061 \text{ Hz} - 15 \text{ Hz}]$. The phases ψ_k were chosen to minimize the crest factor, in order to inject more power into the system without increasing peak values of $F_{d,ms}$ [Pintelon and Schoukens, 2012]. The multisine amplitudes A_k were chosen according to the Reduced Power Method [Mugge et al., 2007]. This method allows identification of neuromuscular response on a large frequency range without suppression of reflexive activity. The multisine $F_{d,ms}$ was generated offline in the frequency domain, and the Inverse Fourier Transform was applied to yield a 90 s time realization. Figure 7.2 shows the resulting time realization and the power spectral density of $F_{d,ms}$.

The remnant signal N was generated as a Gaussian noise w with variance $\sigma_w^2 = 1 \text{ N}^2$, filtered by a third-order low pass filter H_N [Zaal et al., 2009]:

$$H_N(s) = K_N \frac{\omega_N^3}{(s + \omega_N)(s^2 + 2\epsilon_N \omega_N s + \omega_N^2)} \quad [-] \quad 7.11$$

where $\epsilon_N = 0.26$ and $\omega_N = 12.7 \text{ rad/s}$. The value of K_N was gradually increased, to obtain three different ratios between remnant

standard deviation σ_N and signal standard deviation $\sigma_{F_{ho}}$ (0, 0.2 and 0.5). For each value of K_N , 100 simulations were performed with different realizations of the remnant noise.

The RLS-based method was applied to the simulated data corresponding to each noise realization. Since the simulated impulse response was almost zero after $t_M = 2$ s, the memory of the estimated impulse response \hat{h}_{comb} was set to $M = F_s \cdot t_M = 200$. The forgetting factor was set to $\lambda = 0.995$, to obtain a trade-off between noise rejection and capability of tracking the time-varying response [Vahidi et al., 2005].

To evaluate the reliability of the estimates given by the RLS-based algorithm, the relative error between estimated and simulated h_{comb} was calculated:

$$E_{h_{comb}}(t_n) = \frac{\|\hat{h}_{comb}(t_n) - h_{comb}(t_n)\|}{\|h_{comb}(t_n)\|} \quad 7.12$$

where $\|\cdot\|$ indicates the Euclidean norm. As an indicator for the reliability of the admittance estimate, the relative error between the estimated and the simulated FRFs was calculated:

$$E_{H_{adm}}(f, t_n) = \frac{|\hat{H}_{adm}(f, t_n) - H_{adm}(f, t_n)|^2}{|H_{adm}(f, t_n)|^2} \quad 7.13$$

Results

Figure 7.5 shows time evolutions of $E_{h_{comb}}$ for different values of $\sigma_N/\sigma_{F_{ho}}$. The time evolutions of $E_{h_{comb}}$ were similar for all the different values of $\sigma_N/\sigma_{F_{ho}}$. When the admittance parameters are constant or when they change slowly, the error was small ($E_{h_{comb}} < 0.3$), indicating that the estimates matched the simulated dynamics with high accuracy. The value of $E_{h_{comb}}$ increased to 1.2 when the neuromuscular response instantaneously varied from compliant to stiff settings ($t = 15$ s).

Figure 7.6 shows the estimated \hat{h}_{comb} at $t_1 = 14$ s, $t_2 = 17$ s, $t_3 = 20$ s, $t_4 = 23$ s, and $t_5 = 26$ s. The RLS algorithm needed almost 8 s to converge to an accurate estimate after the simulated h_{comb} changes instantaneously from h_{comb}^c to h_{comb}^s at $t = 15$ s.

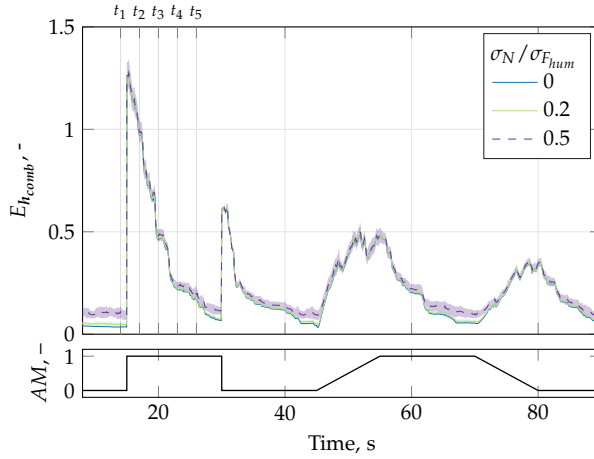


Figure 7.5: Evolution of the relative error $E_{h_{comb}}$ between the simulated and the estimated impulse responses \hat{h}_{comb} . The $E_{h_{comb}}$ is shown for different ratios $\sigma_N / \sigma_{F_{ho}}$ between remnant and signal standard deviation. Lines and shades indicate means and standard deviations over 100 different realizations of remnant noise.

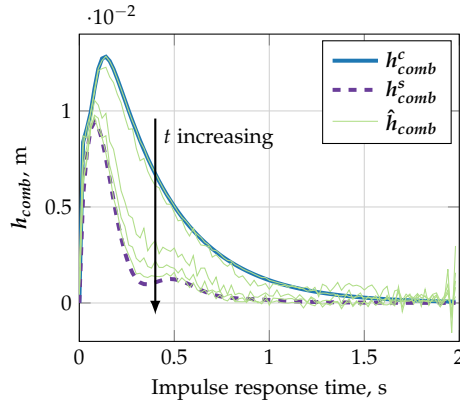


Figure 7.6: Estimates \hat{h}_{comb} at times t_1, t_2, t_3, t_4 , and t_5 . The estimates correspond to $\sigma_N / \sigma_{F_{ho}} = 0.2$.

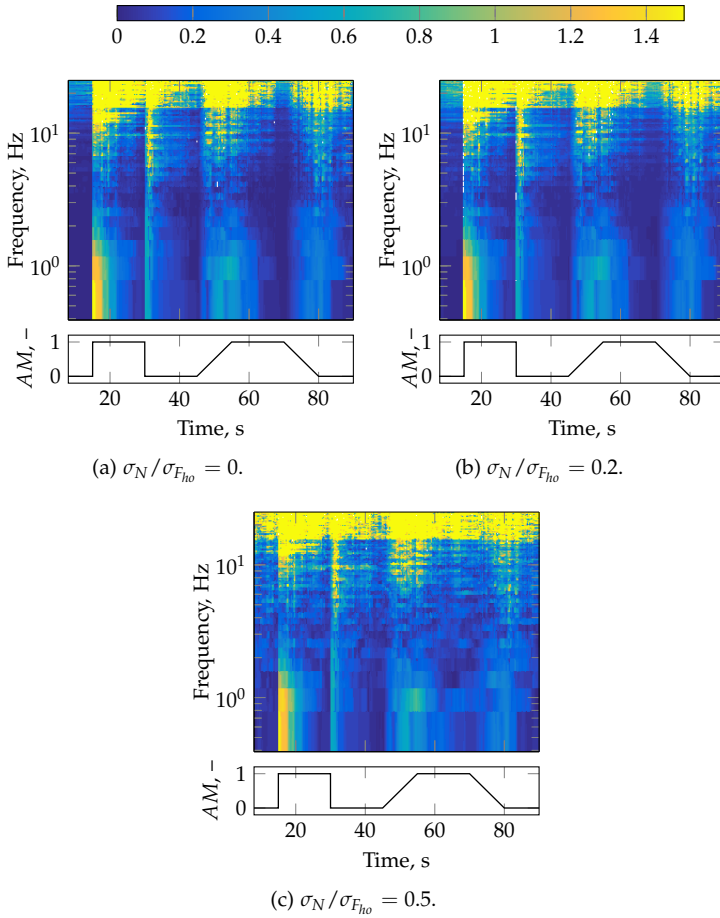


Figure 7.7: Relative error between estimated and simulated admittance frequency responses.

The frequency response of the admittance was estimated by using Equation (7.6). Figure 7.7 shows the relative error $E_{H_{adm}}$ between the simulated and the estimated frequency responses for different values of $\sigma_N / \sigma_{F_{ho}}$. At low and medium frequencies, the relative errors were small when the parameter were constant or changed gradually (blue

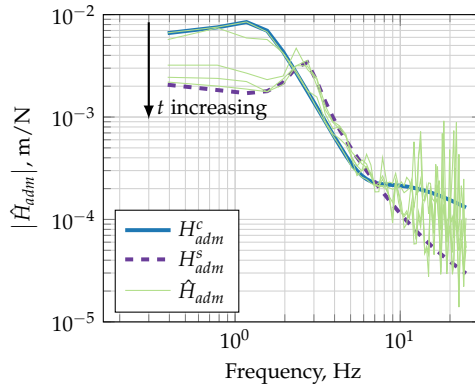


Figure 7.8: Estimates \hat{H}_{adm} at times t_1, t_2, t_3, t_4 , and t_5 . The estimates correspond to $\sigma_N/\sigma_{F_{ho}} = 0.2$.

color in Figure 7.7). When the admittance parameters changed instantaneously ($t = 15$ s), the estimated admittance needed some time to converge to the simulated admittance (yellow color). At very high frequencies, the relative errors were large, indicating that the admittance estimates were not accurate.

Figure 7.8 shows the admittances estimated during the time interval around $t = 15$ s for $\sigma_N/\sigma_{F_{ho}} = 0.2$. Similarly to \hat{h}_{comb} , the estimated admittance needed almost 8 s to converge to an accurate estimate after the simulated admittance changed instantaneously from H_{adm}^c to H_{adm}^s .

Conclusions

The main goal of the first set of Monte-Carlo simulations was to evaluate the robustness of the RLS-based method to different levels of remnant noise. Also with high levels of remnant noise, the RLS-based method was able to track slow changes in admittance dynamics at low and medium frequencies. When the admittance changed instantaneously, the RLS-based method needed about 8 s to provide reliable estimates.

The slow convergence time in case of instantaneous changes is related to the chosen value for the forgetting factor λ . As shown in a previous work [Diniz, 2008], the convergence time of a RLS algorithm is inversely proportional to $(1 - \lambda)$. Therefore, choosing lower values of λ would reduce the convergence time. However, lower values of λ affect the robustness of the RLS-based algorithm to the remnant noise and could lead to instability problems [Paleologu et al., 2008]. Therefore, the value of λ should be chosen to be a compromise between convergence time and robustness to the remnant noise. The next section presents a Monte-Carlo simulation study to find the value of λ that best compromises between convergence time and robustness to noise.

7.4.2 Influence of the forgetting factor λ

Method

The second set of Monte-Carlo simulations investigated the influence of the forgetting factor λ on accuracy of RLS-based estimates. The disturbance-rejection task in Figure 7.1b was simulated using Simulink (The MathWorks, Inc.). All parameters were set as in Section 7.4.1, except from the dynamics of the control device and the gain K_N of the remnant noise.

The dynamics of the control device H_{cd} were modelled as the identified dynamics of a sidestick from Wittenstein Aerospace & Simulation GmbH, Germany:

$$H_{cd}(s) = \frac{1}{0.864s^2 + 3.53s + 96.92} \quad [\text{rad/N}] \quad 7.14$$

The remnant noise N was simulated as a Gaussian noise filtered by a third-order filter, see Equation (7.11). The gain K_N was varied to obtain desired ratios between the variance of the remnant noise σ_N^2 and the variance of the human force $\sigma_{F_{ho}}^2$. The ratios used in these Monte-Carlo simulations were different from those used in Section 7.4.1:

$$\sigma_N^2 / \sigma_{F_{ho}}^2 \in \{0, 0.05, 0.1, 0.15, 0.20\} \quad 7.15$$

For each ratio, 100 different realizations of the remnant noise were generated and used to simulate the control task in Figure 7.1b.

The RLS-based method was applied to the simulated data corresponding to each noise realization. To assess the effect of the forgetting factor λ on the neuromuscular estimate, the RLS-based method was executed with different values of the forgetting factor λ :

$$\lambda \in \{0.80 + k \cdot 0.01, \quad k = 0, \dots, 19\} \cup \{0.995, 0.999\} \quad 7.16$$

A number of dependent measures were calculated to evaluate the quality of RLS-based estimates. The ability of the RLS-based method to predict the output signal was evaluated by calculating the Variance Accounted For (VAF) between the measured stick deflection δ_{cd} and the predicted stick deflection $\hat{\delta}_{cd} = \mathbf{F}_d^T \hat{\mathbf{h}}_{comb}$ [Lortie and Kearney, 2001]:

$$\text{VAF} = \left[1 - \frac{\sigma^2(\delta_{cd} - \hat{\delta}_{cd})}{\sigma^2(\delta_{cd})} \right] \times 100\% \quad 7.17$$

The VAF is maximum (100%) when $\hat{\delta}_{cd}$ equals δ_{cd} at each time step, and decreases with errors in the prediction.

The reliability of impulse response estimates $\hat{\mathbf{h}}_{comb}$ and admittance estimates \hat{H}_{adm} were evaluated by using the relative errors in Equation (7.12) and Equation (7.13), respectively.

Results

Figure 7.9 shows values of VAF for different forgetting factors λ (horizontal axis) and remnant levels $\sigma_N^2 / \sigma_{F_{ho}}^2$ (different lines). The values of VAF are not shown for λ between 0.80 and 0.89, since the RLS-based algorithm was unstable and resulted in very small VAF. The RLS-based estimates predicted the measured stick deflection very well for all values $\lambda \geq 0.90$ (VAF > 80%). The VAF increased with increasing values of λ and reached its maximum value for $\lambda = 0.99$. For higher values of λ , VAF decreased. This indicates that the best prediction of the stick deflection was obtained with $\lambda = 0.99$.

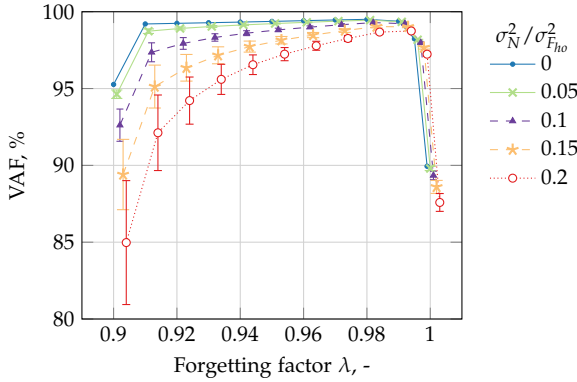


Figure 7.9: Means (lines) and standard deviations (error bars) of VAF between simulated and predicted stick deflection δ_{cd} .

The relative error $E_{h_{comb}}$ between estimated and simulated impulse responses h_{comb} is shown in Figure 7.10. Each subfigure corresponds to different values of λ , whereas different lines indicate different levels of remnant noise. In addition, each subfigure highlights the convergence time that the estimate \hat{h}_{comb} needed to converge to the simulated h_{comb} after the instantaneous change at time $t = 15$ s. The convergence time was evaluated as the first time sample after $t = 15$ s, at which $E_{h_{comb}} = 0.5$ in the simulations without remnant noise ($\sigma_N^2/\sigma_{Fho}^2 = 0$).

For all the values of λ , the error $E_{h_{comb}}$ increased when admittance parameters varied, especially when admittance changed instantaneously from relax to stiff settings at $t = 15$ s. After the instantaneous change at $t = 15$ s, the value $\lambda = 0.90$ resulted in the fastest convergence time without remnant noise, see Figure 7.10a. However, this value of λ did not result in accurate estimates when the remnant noise was added. By contrast, the estimates obtained with $\lambda = 0.999$ were almost not influenced by high levels of remnant noise, but their convergence time was large (see Figure 7.10c). The value $\lambda = 0.99$ gave the best compromise between robustness to the noise and converging rate, as shown in Figure 7.10b. In this case,

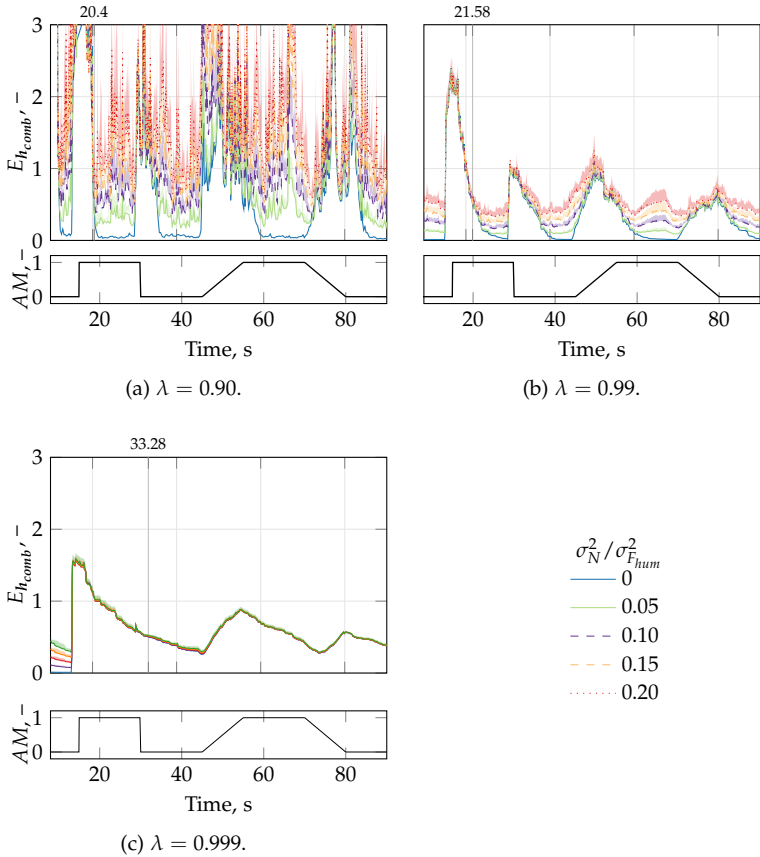


Figure 7.10: Means (lines) and standard deviations (shades) of the relative error $E_{h_{comb}}$ between simulated and estimated impulse responses h_{comb} .

the impulse response estimates were reliable for all levels of noise when admittance dynamics were constant or changed gradually ($E_{h_{comb}} < 1$). When admittance dynamics changed instantaneously from relax to stiff dynamics at $t = 15$ s, the RLS-based method needed approximately 6.5 s to provide reliable estimates.

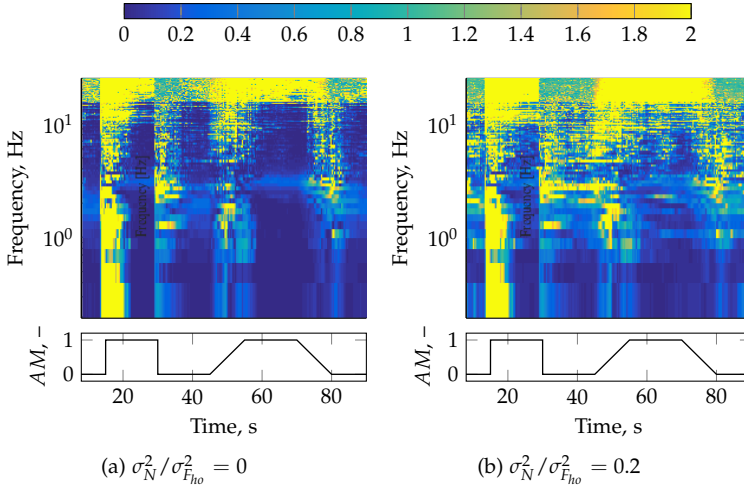


Figure 7.11: Mean values of the relative error $E_{H_{adm}}$ between simulated and estimated admittance frequency responses.

Figure 7.11 shows the relative errors $E_{H_{adm}}$ between the frequency responses of the estimated and simulated admittance. The figure only shows results for $\lambda = 0.99$ and for two levels of remnant noise: no noise ($\sigma_N^2 / \sigma_{F_{ho}}^2 = 0$) and maximum noise ($\sigma_N^2 / \sigma_{F_{ho}}^2 = 0.20$). At low and medium frequencies (< 10 Hz), the errors $E_{H_{adm}}$ were small when admittance parameters were constant or changed slowly, and increased when the parameters varied instantaneously at time $t = 15$ s. These results are in line with those obtained for the errors between simulated and estimated h_{comb} . At higher frequencies, admittance estimates were not accurate.

These findings indicate that the RLS-based method provides reliable estimates on a broad range of frequencies. Next section presents application of the RLS-based method to data obtained in a human in-the-loop experiment.

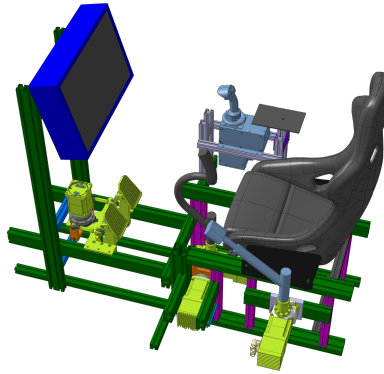


Figure 7.12: Apparatus.

7.5 Experiment

An human in-the-loop study was performed to test the accuracy of the RLS-based method with experimental data.

7.5.1 Apparatus

The experiment was performed in the Control Loading Lab at the Max Planck Institute for Biological Cybernetics, see Figure 7.12. A control device was located together with an armrest on the right side of the chair where participants were seated during the experiment. The control device was a control-loading sidestick from Wittenstein Aerospace & Simulation GmbH. During the experiment, the longitudinal axis of the sidestick was fixed to the center position, whereas the lateral axis was free to move. The lateral dynamics of the sidestick were previously estimated, see Equation (7.14). A high-resolution display from VPixx Technologies Inc., Canada (1920x1200

pixels, 120 Hz refresh rate) was positioned in front of the participants.

7.5.2 Participants, experimental conditions and experimental procedure

Four participants (age 26-32) took part in the experiment, and a financial compensation was offered for their participation. Before starting the experiment, participants were informed about the objective of the experiment and the experimental procedure.

During the experiment, participants were seated in front of the monitor and held the sidestick with the right hand. Their right elbow rested on the armrest to limit movements of the upper part of the arm. Participants were asked to adopt different control strategies in response to a disturbance force F_d applied on the control device. The following experimental conditions were investigated:

- Relax Task (RT): participants were instructed to relax their arm and adopt a passive behavior.
- Position Task (PT): participants were instructed to resist the disturbance force and to keep the stick in the center position, i.e., to be stiff.
- Time Varying Task (TVT): participants were instructed to relax the arm until 30 s, be stiff from 30 s to 60 s, and relax the arm until the end of the experimental condition (90 s).

The force disturbance F_d was designed as explained in Section 7.4.1. To avoid drift, the sidestick deflection was shown on the display as the lateral distance of a point from a center line.

The three conditions were presented to participants in a randomized order. For each experimental condition, several training runs were performed to allow participants to familiarize themselves with the control task. After the training phase, five repetitions of the experimental condition were executed to collect the measurement data.

7.5.3 Identification of neuromuscular response and dependent measures

During the experiment, measurements of stick deflection δ_{cd} and disturbance force F_d were logged at 100 Hz. The time records of δ_{cd} and F_d were used by the RLS-based method to estimate admittances \hat{H}_{adm}^{rls} for each repetitions of the experimental conditions. Note that no averaging was conducted among repetitions of the same experimental condition.

In the time-invariant conditions, admittance dynamics were also estimated by applying the CS method [Abbink et al., 2011; Schouten et al., 2008b]. This method is commonly used to estimate time-invariant admittance, and serves as a comparison for RLS-based estimates. The CS method estimates admittance dynamics by using cross-spectral analysis:

$$\hat{H}_{adm}^{cs}(f) = \frac{\hat{S}_{F_d \delta_{cd}}(f)}{\hat{S}_{F_d F_{ho}}(f)}, \quad f \in \{f_k\} \quad 7.18$$

where $\hat{S}_{u y}$ represents an estimate of the cross-spectrum between u and y , and $\{f_k\}$ is the set of frequency points where the multisine component $F_{d,ms}$ has power. To reduce noise, estimates of cross-spectra are averaged over different repetitions of each experimental condition [Pintelon and Schoukens, 2012]. Note that the estimate \hat{H}_{adm}^{cs} does not depend on the time sample t_n , since the CS method provides a time-invariant estimate.

The reliability of the CS estimate was evaluated by using the coherence function $\hat{\Gamma}^2$ [Abbink et al., 2011]:

$$\hat{\Gamma}^2(f) = \frac{|\hat{S}_{F_d \delta_{cd}}(f)|^2}{\hat{S}_{F_d F_d}(f) \hat{S}_{\delta_{cd} \delta_{cd}}(f)}, \quad f \in \{f_k\} \quad 7.19$$

The coherence function $\hat{\Gamma}^2$ is 1 if the estimated system can be described by a linear time-invariant system, and decreases to 0 with noise and nonlinearities [Pintelon and Schoukens, 2012].

To evaluate reliability of the RLS-based method, the RLS-based estimates were compared to the CS estimates by evaluating the

relative error $E_{H_{adm}}$:

$$E_{H_{adm}}(f, t_n) = \frac{|\hat{H}_{adm}^{cs}(f) - \hat{H}_{adm}^{rls}(f, t_n)|^2}{|\hat{H}_{adm}^{cs}(f)|^2} \quad 7.20$$

In the time-invariant conditions RT and PT, the RLS-based estimates were compared to the corresponding CS estimates. In the time-varying task (TVT), the RLS-based estimate was compared to the CS estimates obtained for RT and PT. Two different errors were calculated: $E_{H_{adm}-RT}$ between the RLS-based estimate in TVT and the CS estimate in RT, and $E_{H_{adm}-PT}$ between the RLS-based estimate in TVT and the CS estimate in PT. This allowed us to investigate whether the RLS-based estimate resembled stiff or relaxed admittance dynamics during the TVT condition.

7.5.4 Hypotheses

In the time-invariant tasks, the RLS-based method is expected to provide similar estimates to the CS method. Thus, the error $E_{H_{adm}}$ is expected to be small. In the time-varying task TVT, the RLS-based method is expected to provide similar estimates to RT when the instruction is to relax, and similar estimates to PT when the instruction is to be stiff. Thus, the error $E_{H_{adm}-RT}$ is expected to be small when the instruction is to be relaxed, and the error $E_{H_{adm}-PT}$ is expected to be small when the instruction is to be stiff.

7.5.5 Results

Figure 7.13 shows estimates of admittance \hat{H}_{adm} and corresponding coherence functions $\hat{\Gamma}^2$ provided by the CS method in the time-invariant tasks PT and RT. Values of $\hat{\Gamma}^2$ close to 1 indicated reliability of admittance estimates. The admittance magnitude was low in PT, indicating that participants were stiff to oppose to the force disturbance. On the other hand, participants adopted a large admittance in RT to be compliant with the force disturbance. This is in complete agreement with previous findings in the literature [Abbink et al., 2011; Venrooij et al., 2011].

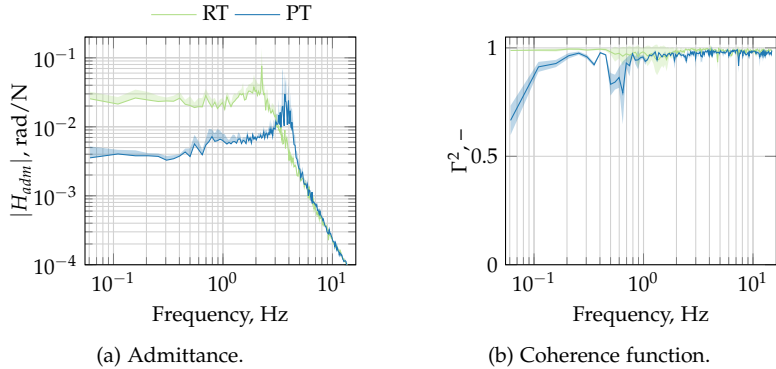


Figure 7.13: Admittance $|\hat{H}_{adm}|$ and coherence function \hat{r}^2 estimated by CS method for the time-invariant tasks (PT and RT). Lines and shades represent means and standard deviations among participants, respectively.

The normalized error $E_{H_{adm}}$ between RLS-based and CS estimates in the time-invariant tasks is shown in Figure 7.14. The errors were averaged among different repetitions of the experimental conditions and among participants. At the beginning of the conditions, $E_{H_{adm}}$ was large for approximately 8 s (yellow colour), indicating that the RLS-based method needed almost 8 s to converge to a reliable estimate. After this initial transient, $E_{H_{adm}}$ was small (blue color) over a broad range of frequencies (between 0.5 Hz and 10 Hz), indicating that the RLS-based estimates resembled the CS estimates.

Figure 7.15 shows the errors $E_{H_{adm}-RT}$ and $E_{H_{adm}-PT}$ obtained in the time-varying task TVT. The errors were averaged among different repetitions of TVT and among participants. In the first 30 s and in the last 30 s, $E_{H_{adm}-RT}$ was smaller than 0.5 at frequencies < 10 Hz, see Figure 7.15a. This indicates that the RLS-based estimates resembled the CS estimates obtained in RT when the instruction was to be relaxed. Between 30 s and 60 s, the error $E_{H_{adm}-RT}$ increased, whereas the error $E_{H_{adm}-PT}$ became small at frequencies between 0.5 Hz and 10 Hz, see Figure 7.15b. This indicates that RLS-based estimates were comparable to the CS estimates in PT when participants were asked to be stiff.

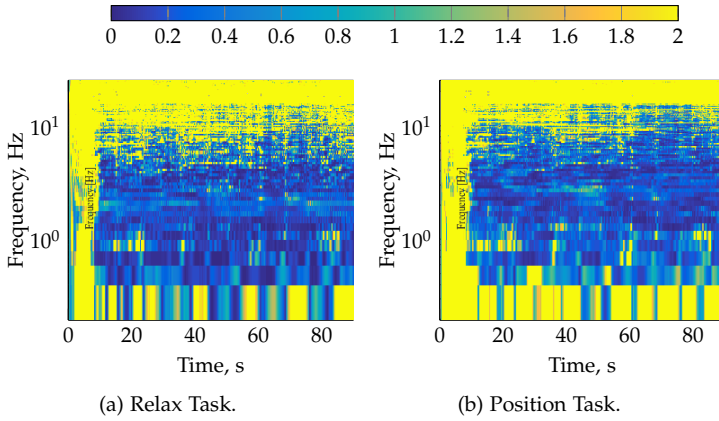


Figure 7.14: Errors $E_{H_{adm}}$ between RLS-based and CS estimates in the time-invariant tasks.

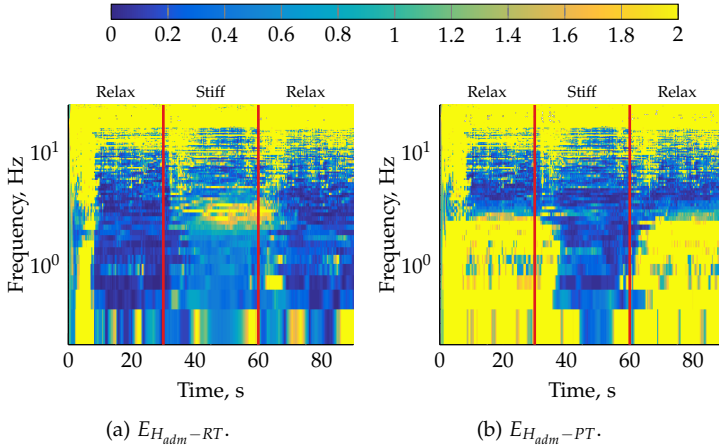


Figure 7.15: Errors $E_{H_{adm}}$ between RLS-based estimates in the time-varying task TVT and CS estimates in the time-invariant tasks.

These results offer evidence for the reliability of RLS-based method in estimating time-varying neuromuscular dynamics over a broad range of frequencies. However, RLS-based estimates were not accurate at low and high frequencies.

7.6 Conclusions

This chapter has presented a method to estimate a time-varying neuromuscular response. The method approximates the neuromuscular response with a Finite Impulse Response (FIR) filter and estimates FIR coefficients by using a Recursive Least Square (RLS) algorithm.

The method was validated in two sets of Monte-Carlo simulations. The first simulation set investigated robustness of the RLS-based method to increasing levels of remnant noise. When the neuromuscular response was constant or changed gradually, the method provided accurate estimates over a broad range of frequencies even with high-levels of remnant noise. Only at high frequencies the estimates were not accurate. In case of instantaneous admittance changes, the method needed almost 8 s to converge to the new admittance dynamics.

The second set of Monte-Carlo simulations investigated influence of the forgetting factor λ on RLS-based estimates. Results provided a value of λ that gave the best compromise between robustness to noise and converging rate of the estimates.

The RLS-based method was then applied to experimental data. The RLS-based method tracked time-varying dynamics of the neuromuscular response over a broad range of frequencies. However, RLS-based estimates were very sensitive to external noise at low and high frequencies. The next chapter will focus on improving the robustness of RLS-based estimates to external noise.

Identifying time-varying neuromuscular response: Regularized RLS algorithms

As seen in the previous chapter, the conventional RLS-based method requires an additional pseudonoise to be added to the multi-sine force disturbance. However, this may be the cause of the poor robustness of the RLS-based method when applied to experimental data. In this chapter, two novel methods are developed that can be used with multi-sine signals. The novel methods combine the classical RLS algorithm with regularization methods. Specifically, two different regularization methods are investigated: the Truncated Singular Value Decomposition and the Tikhonov regularization. The mathematical framework for the two regularized RLS-based methods is presented, and recursive implementations are derived.

The contents of this chapter are based on:

Paper title	Identifying time-varying neuromuscular response: Regularized Recursive Least-Squares algorithms
Authors	Olivari, M., Geluardi, S., Venrooij, J., Nieuwenhuizen, F. M., Pollini, L., and Bühlhoff, H. H.
In preparation	IEEE Transactions on Cybernetics

8.1 Introduction

In the previous chapter, a RLS-based method was developed to estimate the impulse response of a time-varying neuromuscular system. The method estimates recursively the impulse response as the least squares solution of a given cost function by using a conventional Recursive Least Squares (RLS). The method was applied in disturbance-rejection tasks, where the human operator is asked to oppose or to be compliant with a force provided on a control device.

The major disadvantage of the RLS-based method is that it imposes a constraint on the force disturbance: the so-called “deterministic correlation matrix” associated with the force disturbance must be nonsingular and well-conditioned, i.e., the force disturbance must be persistently exciting [Diniz, 2008]. This is because the RLS-based method requires inverting the deterministic correlation matrix to estimate the least squares solution. In experiments for neuromuscular identification, the force disturbance is commonly designed as a multisine signal, since multisine properties can be controlled to obtain a better Signal-to-Noise Ratio and improved robustness to noise [Schouten et al., 2008a]. Unfortunately, multisines signals have been shown not to be persistently exciting for the RLS-based method.

To overcome this issue, an additional pseudonoise was added to the multisine signal. The resulting signal generated a well-conditioned deterministic correlation matrix, thus the RLS-based method could be applied. However, this approach led to poor robustness to noise of the RLS-based method when applied to experimental data. This was because the power of the pseudonoise is spread over more frequencies than the multisine signal, resulting in a smaller Signal-to-Noise ratio [Schouten et al., 2008a].

Regularization is a typical technique used to calculate solutions of least squares problems with ill-conditioned matrices, i.e., discrete ill-posed problems [Hansen, 1994]. To calculate a meaningful solution of ill-posed problems, regularization methods incorporate additional information about the desired solution in the least-squares problem. Unfortunately, regularized solutions are difficult to update in a recursive way. Calculating a regularized solution at each time

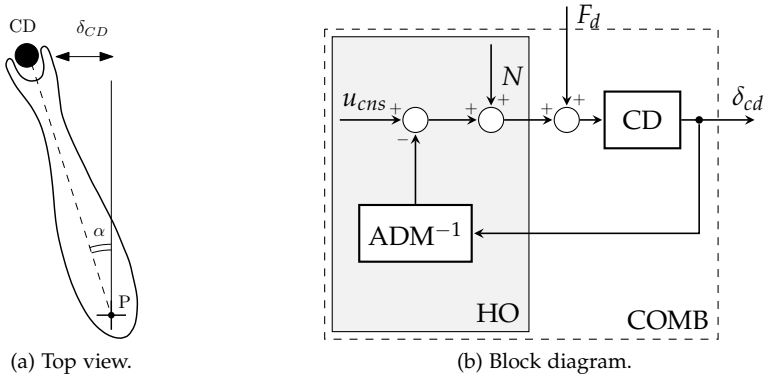


Figure 8.1: Human interaction with a control device.

step would be computationally expensive and hard to be done in applications with real-time constraints.

This chapter presents the mathematical framework for incorporating regularization methods into the conventional RLS algorithm. Specifically, two different regularization methods are considered: the Truncated Singular Values Decomposition and the Tikhonov Regularization. Recursive implementations of the two regularized methods are derived. The resulting regularized RLS-based methods that can be used with multisine signals without requiring an additional pseudonoise.

This chapter is structured as follows. Section 8.2 introduces the control task considered in this chapter. Next, Section 8.3 presents the mathematical foundations of the conventional and the regularized RLS-based approaches. Finally, conclusions are drawn.

8.2 Control task

Figure 8.1a shows the interaction of an human arm with a control device. The control device is assumed to only move in the lateral direction with deflection δ_{cd} , and humans are assumed to keep their elbow at a fixed position P on an armrest. Under these assumptions,

human arm can be considered as a joint with one degree of freedom (the angle α in Figure 8.1a) and can be modelled as in Figure 8.1b [van Paassen et al., 2004]. The block CD represents the control device dynamics, while the neuromuscular dynamics of human's arm are described by the inverse of the admittance ADM^{-1} [Abbink et al., 2011]. All the blocks are assumed linear, and the remnant signal N accounts for noise and unmodeled nonlinearities. The signal u_{cns} represents the response of the central nervous system to all external cues, e.g., visual or vestibular cues.

This chapter focuses on disturbance-rejection tasks [Abbink et al., 2011; Schouten et al., 2008b]. In these tasks, humans are asked to oppose or to be compliant with a force disturbance F_d presented on the control device. Since no external cues are provided to the humans, the signal u_{cns} can be considered negligible.

8.3 Estimating the impulse response

The dynamics of the combined COMB of admittance and control device can be described by the impulse response h_{comb} . The impulse response h_{comb} is defined as the output δ_{cd} at time $t_n = n \cdot T$ when an impulse is applied to the system input F_d at time $t_m = m \cdot T$ [MacNeil et al., 1992]. Here, $n \cdot T$ and $m \cdot T$ represent integer multiples of the sampling time T .

The impulse response can be used to express the response of COMB to a generic input F_d :

$$\delta_{cd}(t_n) = T \sum_{k=-\infty}^{\infty} h_{comb}(t_n, t_k) F_d(t_k) \quad 8.1$$

This equation can be simplified by considering some properties of h_{comb} . Firstly, physical systems are generally causal, i.e., the output at time t_n only depends on past and current inputs but not on future inputs. Thus, $h_{comb}(t_n, t_m)$ is zero for $n < m$. Furthermore, the impulse response of COMB is likely to become zero after a finite number of samples. This means that $h_{comb}(t_n, t_m)$ becomes zero for all $n \geq m + M$, where M represents the finite memory of the system.

Assuming causality and finite memory, Equation (8.1) simplifies to:

$$\begin{aligned}
 \delta_{cd}(t_n) &= T \sum_{k=n-M}^n h_{comb}(t_n, t_k) F_d(t_k) \\
 &= \begin{bmatrix} T F_d(t_n) & \cdots & T F_d(t_{n-M+1}) \end{bmatrix} \begin{bmatrix} h_{comb}(t_n, t_n) \\ \vdots \\ h_{comb}(t_n, t_{n-M+1}) \end{bmatrix} \\
 &= \mathbf{F}_d^T(t_n) \mathbf{h}_{comb}(t_n). \tag{8.2}
 \end{aligned}$$

where $\mathbf{F}_d, h_{comb} \in \mathbb{R}^M$. To simplify the notation, the subscript of \mathbf{h}_{comb} will be omitted in the rest of the paper.

Our goal is to estimate the time-varying dynamics of COMB given measurements of F_d and δ_{cd} . As seen in Chapter 7, this can be done by using RLS-based methods. The following sections review the conventional RLS-based method developed in Chapter 7, focusing on its main drawbacks. Then, two novel regularized RLS-based methods are developed that do not suffer from the drawbacks of the conventional RLS-based method.

8.4 Conventional RLS-based method

As a first step, the conventional RLS-based method uses a RLS algorithm to estimate the impulse response h_{comb} . The impulse response is estimated at each time step as the optimal solution that minimizes the following cost function:

$$\hat{\mathbf{h}}(t_n) = \arg \min_{\mathbf{h} \in \mathbb{R}^M} V_\epsilon(\mathbf{h}, t_n) \tag{8.3}$$

where V_ϵ is a function of the prediction errors ϵ :

$$V_\epsilon(\mathbf{h}, t_n) = \sum_{k=n_0}^n \lambda^{n-k} \epsilon^2(\mathbf{h}, t_k) \tag{8.4}$$

$$\epsilon^2(\mathbf{h}, t_k) = \left[\mathbf{F}_d^T(t_k) \mathbf{h} - \delta_{cd}(t_k) \right]^2 \tag{8.5}$$

Here, n_0 is the initial time sample, and λ is a forgetting factor that gives less importance to samples occurred further in the past ($0 \ll \lambda < 1$). For the sake of clarity and without loss of generality, the initial time sample is assumed to be $n_0 = 1$.

The solution of the least-squares problem is given by:

$$\hat{\mathbf{h}}(t_n) = \mathbf{R}^{-1}(t_n) \mathbf{p}(t_n) \quad 8.6$$

where:

$$\mathbf{R}(t_n) := \sum_{k=1}^n \lambda^{n-k} \mathbf{F}_d(t_k) \mathbf{F}_d^T(t_k) \quad \in \mathbb{R}^{M \times M} \quad 8.7$$

$$\mathbf{p}(t_n) := \sum_{k=1}^n \lambda^{n-k} \mathbf{F}_d(t_k) \delta_{cd}(t_k) \quad \in \mathbb{R}^{M \times 1} \quad 8.8$$

Note that the solution in Equation (8.6) can only be computed if \mathbf{R} is invertible.

The least-squares solution in Equation (8.6) requires calculation of the inverse \mathbf{R}^{-1} at each time step. This is computationally expensive and hard to be done in applications with real-time constraints. However, a recursive algorithm can be applied to calculate the inverse. The matrix \mathbf{R} in Equation (8.7) can be rewritten as:

$$\mathbf{R}(t_n) = \lambda \mathbf{R}(t_{n-1}) + \mathbf{F}_d(t_n) \mathbf{F}_d^T(t_n), \quad \mathbf{R}(0) = \mathbf{R}_0 \quad 8.9$$

The matrix \mathbf{R} is initialized with a full-rank matrix \mathbf{R}_0 to ensure that \mathbf{R} is invertible during the initial time steps [Diniz, 2008]. Note however that the contribution of this initialization term on the solution becomes negligible after an initial transient [Diniz, 2008]. By applying the matrix inversion lemma:

$$(\mathbf{A} + \mathbf{BCD})^{-1} = \mathbf{A}^{-1} - \mathbf{A}^{-1} \mathbf{B} \left(\mathbf{D} \mathbf{A}^{-1} \mathbf{B} + \mathbf{C}^{-1} \right)^{-1} \mathbf{D} \mathbf{A}^{-1} \quad 8.10$$

we obtain:

$$\boldsymbol{\psi}(t_n) = \mathbf{R}^{-1}(t_{n-1}) \mathbf{F}_d(t_n) \quad 8.11$$

$$\mathbf{R}^{-1}(t_n) = \frac{1}{\lambda} \left[\mathbf{R}^{-1}(t_{n-1}) - \frac{\boldsymbol{\psi}(t_n) \boldsymbol{\psi}^T(t_n)}{\lambda + \boldsymbol{\psi}^T(t_n) \mathbf{F}_d(t_n)} \right] \quad 8.12$$

Table 8.1: Conventional RLS algorithm

INITIALIZE	$S(t_0) = S_0 \in \Re^{M \times M}$ $\mathbf{h}(t_0) = \mathbf{0}$
FOR $n \geq 1$ DO	$e(t_n) = \delta_{cd}(t_n) - \mathbf{F}_d^T(t_n) \mathbf{h}(t_{n-1})$ $\boldsymbol{\psi}(t_n) = S(t_{n-1})\mathbf{F}_d(t_n)$ $S(t_n) = \frac{1}{\lambda} \left[S(t_{n-1}) - \frac{\boldsymbol{\psi}(t_n)\boldsymbol{\psi}^T(t_n)}{\lambda + \boldsymbol{\psi}^T(t_n)\mathbf{F}_d(t_n)} \right]$ $\mathbf{h}(t_n) = \mathbf{h}(t_{n-1}) + e(t_n)S(t_n)\mathbf{F}_d(t_n)$

Thus, the inverse of \mathbf{R} at time t_n can be computed by only using the inverse at time t_{n-1} and current measurements of \mathbf{F}_d , without requiring actual computation of a matrix inverse.

Table 8.1 lists the main steps of the conventional RLS algorithm. The matrices \mathbf{S} and \mathbf{S}_0 denote the inverses of \mathbf{R} and \mathbf{R}_0 , respectively. The matrix \mathbf{S}_0 is commonly initialized with an identity matrix scaled by the inverse of the input signal power [Diniz, 2008].

8.4.1 Issues of conventional RLS algorithm

Unfortunately, the conventional solution in Equation (8.6) cannot be numerically computed if \mathbf{R} is rank-deficient or ill-conditioned. An insight into this issue can be obtained by using the Singular Value Decomposition (SVD) analysis. The SVD of \mathbf{R} is defined as [Ben-Israel and Greville, 2003]:

$$\mathbf{R}(t_n) = \mathbf{U}(t_n)\boldsymbol{\Sigma}(t_n)\mathbf{V}^T(t_n) \quad 8.13$$

where $\mathbf{U} = (\mathbf{u}_1, \dots, \mathbf{u}_M) \in \Re^{M \times M}$ and $\mathbf{V} = (\mathbf{v}_1, \dots, \mathbf{v}_M) \in \Re^{M \times M}$ are orthonormal matrices, and $\boldsymbol{\Sigma} \in \Re^{M \times M}$ is a diagonal matrix with non-negative diagonal elements σ_k appearing in non-increasing order. The vectors \mathbf{u}_k and \mathbf{v}_k are the left and right singular vectors of \mathbf{R} , respectively, and σ_k are the singular values.

By using the SVD, the inverse of \mathbf{R} can be expressed as:

$$\mathbf{R}^{-1}(t_n) = \mathbf{V}(t_n)\mathbf{\Sigma}^{-1}(t_n)\mathbf{U}^T(t_n) = \sum_{k=1}^M \frac{\mathbf{v}_k(t_n)\mathbf{u}_k^T(t_n)}{\sigma_k(t_n)} \quad 8.14$$

By substituting Equation (8.14) into Equation (8.6), the conventional RLS solution becomes:

$$\hat{\mathbf{h}}(t_n) = \left[\sum_{k=1}^M \frac{\mathbf{v}_k(t_n)\mathbf{u}_k^T(t_n)}{\sigma_k(t_n)} \right] \mathbf{p}(t_n) \quad 8.15$$

If \mathbf{R} is rank-deficient or ill-conditioned, some singular values σ_k are zero or approximately zero, respectively. If \mathbf{p} is contaminated by noise, divisions by approximately zero singular values could result in severe amplification of the noise. Note that the vector \mathbf{p} depends on measurements of the stick deflection δ_{cd} and is typically contaminated by an unknown signal due to remnant noise N , see Figure 8.1. This explains why the conventional RLS solution cannot be numerically computed if \mathbf{R} is rank-deficient or ill-conditioned.

According to Equation (8.7), the matrix \mathbf{R} depends on values of force disturbance F_d and forgetting factor λ . In studies for neuromuscular estimation, the force disturbance F_d is commonly chosen as a multisine signal due to its good properties in terms of signal-to-noise ratio and robustness to the noise [Schouten et al., 2008a]. Unfortunately, this choice leads to an ill-conditioned matrix \mathbf{R} . Thus, the conventional RLS-based approach cannot be used if the force disturbance is chosen as a multisine signal.

8.4.2 Solution adopted by the conventional RLS-based method: adding a pseudonoise

To overcome the ill-conditioning issue, the conventional RLS-based method uses a different force disturbance to yield a full-rank and well-conditioned \mathbf{R} . Specifically, F_d is designed as the sum of a multisine F_{ms} and a pseudonoise F_{pn} :

$$F_d(t_n) = F_{d,ms}(t_n) + F_{d,pn}(t_n) \quad 8.16$$

The pseudonoise component is chosen as a realization of a Gaussian white noise with standard deviation μ_{pn} and uncorrelated with the multisine F_{ms} .

With this choice of F_d , the matrix \mathbf{R} in Equation (8.7) becomes:

$$\mathbf{R}(t_n) = \sum_{k=1}^n \lambda^{n-k} [F_{d,ms}(t_k) + F_{d,pn}(t_k)] [F_{d,ms}(t_k) + F_{d,pn}(t_k)]^T \quad 8.17$$

where $F_{d,ms}$ and $F_{d,pn}$ are the multisine and the pseudonoise components of F_d , respectively. Since $F_{d,ms}$ is uncorrelated with $F_{d,pn}$, for large n Equation (8.17) can be approximated to [Diniz, 2008]:

$$\begin{aligned} \mathbf{R}(t_n) &\approx \frac{1}{1-\lambda} \mu_{pn}^2 \mathbf{I} + \sum_{k=1}^n \lambda^{n-k} F_{d,ms}(t_k) F_{d,ms}^T(t_k) \\ &= \frac{1}{1-\lambda} \mu_{pn}^2 \mathbf{I} + \mathbf{R}_{ms}(t_n) \end{aligned} \quad 8.18$$

where $\mathbf{I} \in \mathbb{R}^{M \times M}$ is the identity matrix, and $\mu_{pn}^2 \mathbf{I}$ is the autocorrelation matrix of F_{pn} . The singular values of \mathbf{R} become:

$$\sigma_i(t_n) = \frac{1}{1-\lambda} \mu_{pn}^2 + \sigma_{ms,i}(t_n), \quad i = 1, \dots, M \quad 8.19$$

where $\sigma_{ms,i}$ is the i -th singular value of \mathbf{R}_{ms} . It can be easily seen that $\sigma_i \approx \sigma_{ms,i}$ if $\sigma_{ms,i} \gg \mu_{pn}$, and $\sigma_i \approx \mu_{pn}^2 / (1-\lambda)$ if $\sigma_{ms,i} \ll \mu_{pn}$. Thus, μ_{pn} can be chosen such that all singular values of \mathbf{R} are different from zero and \mathbf{R} is well conditioned.

Unfortunately, the addition of the pseudonoise has several disadvantages. First, the power of F_d is spread over more frequencies than in the multisine signal, leading to small signal-to-noise ratio and low robustness to external noise [Schouten et al., 2008a]. Furthermore, the power spectrum of F_d cannot be easily shaped as for the multisine signals. This is crucial in experiments for identifying neuromuscular response, since the power spectrum of F_d must be shaped to satisfy certain requirements [Mugge et al., 2007].

8.5 Novel approaches: regularized RLS-based methods

This section presents two novel RLS-based approaches that allow use of multisine signals as force disturbances. These approaches apply regularization methods to overcome the ill-conditioning issue. Two different regularization techniques are investigated: the Truncated Singular Value Decomposition and the Tikhonov Regularization [Hansen, 1994; Hansen and O’Leary, 1993].

8.5.1 RLS algorithm with Truncated Singular Value Decomposition

Regularization with Truncated Singular Value Decomposition (TSVD) overcomes the ill-conditioning issue by cutting off the contribution of zero or tiny singular values of \mathbf{R} on the solution [Hansen, 1994]. The TSVD solution is given by:

$$\hat{\mathbf{h}}_{tsvd}(t_n) = \left[\sum_{k=1}^r \frac{v_k(t_n) \mathbf{u}_k^T(t_n)}{\sigma_k(t_n)} \right] \mathbf{p}(t_n) = \mathbf{R}_{tsvd}^{-1}(t_n) \mathbf{p}(t_n) \quad 8.20$$

where $r < M$, and \mathbf{R}_{tsvd} is the Truncated Singular Value Decomposition of \mathbf{R} . This solution clearly differs from the conventional solution of Equation (8.15) because it cuts off the singular values σ_k , $k > r$. If the matrix \mathbf{R} is ill-conditioned and $\sigma_k \approx 0$ for $k > r$, the solution in Equation (8.20) can still be computed because it does not involve divisions by these tiny singular values.

The crucial step for TSVD regularization is the selection of a suitable value for r . The parameter r should yield a fair trade-off between attenuation of the noise (small values of r) and good approximation of the actual impulse response \mathbf{h} (large values of r). If the singular values of \mathbf{R} are separated by a large gap, the parameter r can be easily determined such that $\sigma_r \ll \sigma_{r+1}$ and $\sigma_k \approx 0$ for $k > r$. However, in most cases the matrix \mathbf{R} presents singular values that gradually decay to zero. In such cases, great care must be paid in the selection of r .

A disadvantage of the solution in Equation (8.20) is that it requires calculation of \mathbf{R}_{tsvd} at each time step. This is computationally

expensive, since the TSVD of \mathbf{R} cannot be updated in a recursive way as the inverse operator [Fierro et al., 1999]. However, we derived an efficient way to calculate \mathbf{R}_{tsvd} by exploiting the fact that F_d is a periodic multisine signal. The main idea is to choose values of \mathbf{R}_0 in Equation (8.9) such that \mathbf{R} becomes periodic. Then, \mathbf{R}_{tsvd} can be pre-calculated over a period and these values can be used to obtain \mathbf{R}_{tsvd} at any time sample.

To find \mathbf{R}_0 that makes \mathbf{R} periodic, Equation (8.9) can be rewritten as follows:

$$\mathbf{R}(t_n) = \lambda^n \mathbf{R}_0 + \mathbf{R}_q(t_n) + \mathbf{R}_r(t_n) \quad 8.21$$

where:

$$\begin{aligned} \mathbf{R}_q(t_n) &= \sum_{k=1}^{n_q N} \lambda^{n-k} \mathbf{F}_d(t_k) \mathbf{F}_d^T(t_k) \\ \mathbf{R}_r(t_n) &= \sum_{k=n_q N+1}^{n_q N+n_r} \lambda^{n-k} \mathbf{F}_d(t_k) \mathbf{F}_d^T(t_k) \end{aligned} \quad 8.22$$

Here, N is the number of time samples within a period of F_d , and n_q and n_r are the quotient and the remainder after division of n by N , respectively.

Taking advantage of the periodicity of F_d , the matrices \mathbf{R}_q and \mathbf{R}_r can be rewritten in a more compact form. Defining the variable $\tilde{k} = k - n_q N$, the matrix \mathbf{R}_r becomes:

$$\mathbf{R}_r(t_n) = \sum_{\tilde{k}=1}^{n_r} \lambda^{n_r-\tilde{k}} \mathbf{F}_d(t_{\tilde{k}+n_q N}) \mathbf{F}_d^T(t_{\tilde{k}+n_q N}) \quad 8.23$$

Since F_d is periodic, $F_d(t_{\tilde{k}+n_q N}) = F_d(t_{\tilde{k}})$. Thus the matrix \mathbf{R}_r becomes:

$$\mathbf{R}_r(t_n) = \sum_{\tilde{k}=1}^{n_r} \lambda^{n_r-\tilde{k}} \mathbf{F}_d(t_{\tilde{k}}) \mathbf{F}_d^T(t_{\tilde{k}}) \quad 8.24$$

The matrix \mathbf{R}_r only depends on the remainder after division of n by N , thus it is periodic of period N .

Similar simplifications can be made for \mathbf{R}_q . Defining \mathbf{R}_N as the sum over one period:

$$\mathbf{R}_N = \sum_{k=1}^N \lambda^{N-k} \mathbf{F}_d(t_k) \mathbf{F}_d^T(t_k) \quad 8.25$$

then the matrix \mathbf{R}_q can be rewritten as:

$$\begin{aligned} \mathbf{R}_q(t_n) &= \lambda^{n_r} \left(1 + \dots + \lambda^{N(n_q-1)} \right) \mathbf{R}_N \\ &= \lambda^{n_r} \frac{1 - \lambda^{n_q N}}{1 - \lambda^N} \mathbf{R}_N \end{aligned} \quad 8.26$$

The matrix \mathbf{R}_q is not periodic since it depends on the number of completed periods n_q . This also holds for the term $\lambda^n \mathbf{R}_0$ in Equation (8.21). However, the sum of \mathbf{R}_q and $\lambda^n \mathbf{R}_0$ can be rewritten as:

$$\begin{aligned} \lambda^n \mathbf{R}_0 + \mathbf{R}_q(t_n) &= \lambda^{n_r+n_q N} \mathbf{R}_0 + \lambda^{n_r} \frac{1 - \lambda^{n_q N}}{1 - \lambda^N} \mathbf{R}_N \\ &= \lambda^{n_r} \frac{\lambda^{n_q N} (1 - \lambda^N) \mathbf{R}_0 + (1 - \lambda^{n_q N}) \mathbf{R}_N}{1 - \lambda^N} \end{aligned} \quad 8.27$$

Choosing \mathbf{R}_0 as:

$$\mathbf{R}_0 = \frac{1}{1 - \lambda^N} \mathbf{R}_N \quad 8.28$$

we obtain:

$$\lambda^n \mathbf{R}_0 + \mathbf{R}_q(t_n) = \frac{\lambda^{n_r}}{1 - \lambda^N} \mathbf{R}_N \quad 8.29$$

which only depends on the remainder after division n_r , thus it is periodic of period N . With this choice of \mathbf{R}_0 , the matrix \mathbf{R} in Equation (8.21) can be rewritten as:

$$\mathbf{R}(t_n) = \frac{\lambda^{n_r}}{1 - \lambda^N} \mathbf{R}_N + \sum_{k=1}^{n_r} \lambda^{n_r-k} \mathbf{F}_d(t_k) \mathbf{F}_d^T(t_k) \quad 8.30$$

which is also periodic of period N . This also holds for the TSVD of \mathbf{R} .

Table 8.2: RLS algorithm with TSVD regularization

STORE	$R_0 = \frac{1}{1-\lambda^N} R_N$ see Equation (8.25) $R(t_n) = \lambda R(t_{n-1}) + F_d(t_n) F_d^T(t_n) \quad n = 1, \dots, N$ $R_{tsvd}(t_n) = \text{TSVD}(R(t_n)) \quad n = 1, \dots, N$ $S_{tsvd}(t_n) = R_{tsvd}^{-1}(t_n) \quad n = 1, \dots, N$
INITIALIZE	$p(0) = 0$
FOR $n \geq 1$ DO	$p(t_n) = \lambda p(t_{n-1}) + \delta_{cd}(t_n)$ $\hat{h}_{tsvd}(t_n) = S_{tsvd}(t_{n_r}) p(t_n)$

Once R_{tsvd} is periodic, its value at a generic time t_n coincides with the value at time t_{n_r} , where $0 \leq n_r < N$. Thus, the solution in Equation (8.20) at a generic time t_n can be calculated by using R_{tsvd} at times t_{n_r} :

$$\hat{h}_{tsvd}(t_n) = R_{tsvd}^{-1}(t_{n_r}) p(t_n) \quad 8.31$$

The TSVD of R at time samples $n_r = 0, \dots, N-1$ can be pre-calculated and stored in memory. Then, the stored values can be used to estimate \hat{h}_{tsvd} at a generic time t_n only by performing a matrix multiplication. Table 8.2 summarizes the main steps of the resulting RLS algorithm with TSVD regularization.

Note that this approach can only be applied if F_d is a periodic signal. Different F_d signals would not allow a recursive update of the TSVD solution.

8.5.2 RLS algorithm with Tikhonov regularization

The rationale of Tikhonov regularization stems from the fact that ill-conditioned problems tend to provide solutions with large norms. Tikhonov regularization seeks to compute a useful approximation of h by penalizing estimates with large norms. This is achieved by

considering a different cost function than in Equation (8.3):

$$\hat{\mathbf{h}}(t_n) = \arg \min_{\mathbf{h} \in \mathbb{R}^M} V_\epsilon(\mathbf{h}, t_n) + V_{ti}(\mathbf{h}, t_n) \quad 8.32$$

As seen in Equation (8.4), the first term V_ϵ accounts for prediction errors ϵ between measured and predicted stick deflection δ_{cd} . The term V_{ti} is the Tikhonov regularization term [Tikhonov et al., 1995]:

$$V_{ti}(\mathbf{h}, t_n) = \|\mathbf{L}_{ti}^T(t_n) \mathbf{h}\|^2 = \mathbf{h}^T \mathbf{L}_{ti}(t_n) \mathbf{L}_{ti}^T(t_n) \mathbf{h} \quad 8.33$$

where $\|\cdot\|$ denotes the Euclidean norm, $\mathbf{L}_{ti} \in \mathbb{R}^{M \times p}$ and $p \leq M$. The matrix \mathbf{L}_{ti} penalizes solutions with large norms, skewing the least-squares solution towards vectors with small norms. Commonly \mathbf{L}_{ti} is chosen as a scaled identity matrix, or a suitable matrix that represents some known properties of the desired estimate [Reichel and Ye, 2009].

The solution of the minimum problem is given by:

$$\mathbf{h}_{ti}(t_n) = \mathbf{R}_{ti}^{-1}(t_n) \mathbf{p}(t_n) \quad 8.34$$

where:

$$\mathbf{R}_{ti}(t_n) = \mathbf{R}(t_n) + \mathbf{L}_{ti}(t_n) \mathbf{L}_{ti}^T(t_n) \quad 8.35$$

and the matrix \mathbf{R} is defined in Equation (8.7). It can be shown that \mathbf{h}_{ti} approximates the solution in Equation (8.15) by damping out the contribution of small singular values [Hansen, 1994; Paige and Saunders, 1981].

The solution in Equation (8.34) requires computation of the inverse of \mathbf{R}_{ti} , which is computationally expensive. However, we derived a procedure to recursively update the solution \mathbf{h}_{ti} . The matrix \mathbf{R}_{ti} can be rewritten in a recursive way:

$$\begin{aligned} \mathbf{R}_{ti}(t_n) &= \lambda \mathbf{R}_{ti}(t_{n-1}) + \mathbf{F}_d(t_n) \mathbf{F}_d^T(t_n) + \mathbf{L}_{ti}(t_n) \mathbf{L}_{ti}^T(t_n) \\ &\quad - \lambda \mathbf{L}_{ti}(t_{n-1}) \mathbf{L}_{ti}^T(t_{n-1}) \end{aligned} \quad 8.36$$

Since the subtraction of last two terms is a symmetric matrix $\in \mathbb{R}^{M \times M}$, it can be expressed as:

$$\mathbf{L}_{ti}(t_n) \mathbf{L}_{ti}^T(t_n) - \lambda \mathbf{L}_{ti}(t_{n-1}) \mathbf{L}_{ti}^T(t_{n-1}) = \Delta_L(t_n) \Delta_L^T(t_n) \quad 8.37$$

where $\Delta_L \in \Re^{M \times r}$ and r is the rank of L_{ti} . By substituting Equation (8.37) into Equation (8.36), we obtain:

$$R_{ti}(t_n) = \lambda R_{ti}(t_{n-1}) + \begin{bmatrix} F_d(t_n) & \Delta_L(t_n) \end{bmatrix} \begin{bmatrix} F_d^T(t_n) \\ \Delta_L^T(t_n) \end{bmatrix} \quad 8.38$$

By applying the matrix inverse lemma to compute the inverse of R_{ti} , we obtain:

$$\begin{aligned} \psi(t_n) &= R_{ti}^{-1}(t_{n-1}) \begin{bmatrix} F_d(t_n) & \Delta_L(t_n) \end{bmatrix} \\ R_{ti}^{-1}(t_n) &= \frac{1}{\lambda} R_{ti}^{-1}(t_{n-1}) \\ &\quad - \frac{1}{\lambda} \psi(t_n) \left(\lambda I + \begin{bmatrix} F_d^T(t_n) \\ \Delta_L^T(t_n) \end{bmatrix} \psi(t_n) \right)^{-1} \psi^T(t_n) \end{aligned} \quad 8.39$$

where $I \in \Re^{(r+1) \times (r+1)}$ is the identity matrix. Thus, the matrix R_{ti}^{-1} at time t_n can be calculated by using the matrix R_{ti}^{-1} at the previous time sample t_{n-1} and by inverting a matrix with dimensions $r+1$. If r is much smaller than the dimensions of R_{ti} , then using Equation (8.39) is more efficient than actually inverting R_{ti} .

To obtain a computationally efficient algorithm, our choice was to set the evolution of $L_{ti} L_{ti}^T$ as:

$$L_{ti}(t_n) L_{ti}^T(t_n) = \lambda L_{ti}(t_{n-1}) L_{ti}^T(t_{n-1}) + w(t_n) w^T(t_n) \quad 8.40$$

where $w \in \Re^M$. This choice yields a matrix $\Delta_L = w$ that has rank $r = 1$. Thus, the matrix inverse lemma only requires inverting a 2 by 2 matrix to compute the inverse of R_{ti} .

The evolution of $L_{ti} L_{ti}^T$ defines how much the term V_{ti} influences the cost function in Equation (8.32). Thus, it is worth investigating the evolution of $L_{ti} L_{ti}^T$ given by Equation (8.40). Equation (8.40) can be considered as the state representation of a discrete-time system whose state is $L_{ti} L_{ti}^T$, the dynamic matrix is λ , and the input is $w w^T$. The state evolution of this discrete-time system is given by:

$$L_{ti}(t_n) L_{ti}^T(t_n) = \lambda^n L_{ti}(t_0) L_{ti}^T(t_0) + \sum_{k=1}^n \lambda^{n-k} w(t_k) w^T(t_k) \quad 8.41$$

If w is chosen to be periodic of period P , the state evolution can be expressed as:

$$L_{ti}(t_n)L_{ti}^T(t_n) = \lambda^n L_{ti}(t_0)L_{ti}^T(t_0) + \lambda^{n_r} \frac{1 - \lambda^{n_q N}}{1 - \lambda^P} W_P + W_r(t_n) \quad 8.42$$

where n_q and n_r are the quotient and the remainder after division of n by P , respectively, and:

$$W_P = \sum_{k=1}^P \lambda^{P-k} w(t_k) w^T(t_k)$$

$$W_r(t_n) = \sum_{k=1}^{n_r} \lambda^{n_r-k} w(t_k) w^T(t_k) \quad 8.43$$

For a detailed proof see Equations 8.21 - 8.26. Since $\lambda < 1$, for large n it holds:

$$L_{ti}(t_n)L_{ti}^T(t_n) \approx \lambda^{n_r} \frac{1}{1 - \lambda^P} W_P + W_r(t_n) \quad 8.44$$

Thus, the matrix $L_{ti}L_{ti}^T$ equals $\frac{1}{1-\lambda} W_P$ at time samples where $n_q = 0$, i. e., at time samples t_n where n is an integer multiple of P . For different time samples, $L_{ti}L_{ti}^T$ assumes values given by Equation (8.44).

In our algorithm, w is set to:

$$w(t_n) = \sqrt{\frac{1 - \lambda^P}{\lambda^{P-k}}} \tilde{l}_k \quad 8.45$$

where \tilde{l}_k is the k -th column of a given matrix $\tilde{L} \in \mathbb{R}^{M \times P}$, k is a cycling index obtained as $k = 1 + \lfloor \frac{n-1}{P} \rfloor$, and $\lfloor \cdot \rfloor$ is the remainder after division. The resulting matrix W_P is:

$$W_P = (1 - \lambda^P) \sum_{k=1}^P \tilde{l}_k \tilde{l}_k^T = (1 - \lambda^P) \tilde{L} \tilde{L}^T \quad 8.46$$

which yields:

$$L_{ti}(t_n)L_{ti}^T(t_n) \approx \lambda^{n_r} \tilde{L} \tilde{L}^T + W_r(t_n) \quad 8.47$$

The main steps of the RLS algorithm with Tikhonov regularization are summarized in Table 8.3, where S_{ti} represents the inverse of R_{ti} .

Table 8.3: RLS algorithm with Tikhonov regularization.

INITIALIZE	$S_{ti}(t_0) = S_0 \in \Re^{M \times M}$ $h_{ti}(t_0) = \mathbf{0}$
FOR $n \geq 1$ DO	$w(t_n) = \sqrt{\frac{1-\lambda^P}{\lambda^{p-k}}} \tilde{l}_k$, see Equation (8.45) $e(t_n) = \delta_{cd}(t_n) - F_d^T(t_n) \hat{h}_{ti}(t_{n-1})$ $\psi(t_n) = S_{ti}(t_{n-1}) \begin{bmatrix} F_d(t_n) & w(t_n) \end{bmatrix}$ $Q^{-1}(t_n) = \left(\lambda I + \begin{bmatrix} F_d^T(t_n) \\ w^T(t_n) \end{bmatrix} \psi(t_n) \right)^{-1}$ $S_{ti}(t_n) = \frac{1}{\lambda} S_{ti}(t_{n-1})$ $\quad - \frac{1}{\lambda} \psi(t_n) Q^{-1}(t_n) \psi^T(t_n)$ $\hat{h}_{ti}(t_n) = \hat{h}_{ti}(t_{n-1}) + e(t_n) S_{ti}(t_n) F_d(t_n)$ $\quad - S_{ti}(t_n) w(t_n) w^T(t_n) \hat{h}_{ti}(t_{n-1})$

8.6 Conclusions

This chapter has provided the mathematical framework for two novel regularized RLS-based methods. The two methods are based on the Truncated Singular Value Decomposition and the Tikhonov regularization. Recursive implementation have been derived for the two regularized RLS-based methods. Future works will validate the two novel methods in simulation and in an experimental setup.

Methods for identifying time-varying neuromuscular response in multi-loop tasks

In the previous chapter, RLS-based methods were presented to estimate time-varying neuromuscular response in disturbance-rejection tasks. This chapter presents a RLS-based method to estimate time-varying responses to visual and force feedback during a compensatory tracking task. The method represents the pilot's responses with Finite Impulse Response filters and use a Recursive Least Squares algorithm with Tikhonov regularization to estimate the filter coefficients. The method was validated in a Monte-Carlo simulation study with different levels of remnant noise. With low levels of remnant noise, estimates were accurate and tracked the time-varying behavior of the simulated responses. On the other hand, estimates showed high variability in case of large remnant noise. Taken together, these findings suggest that the novel RLS-based method could be used to estimate time-varying pilot's responses in real human in-the-loop experiments.

The contents of this chapter are based on:

- | | |
|---------------------|---|
| Paper title | Identifying time-varying pilot's responses: a regularized Recursive Least-Squares algorithm |
| Authors | Olivari, M., Venrooij, J., Nieuwenhuizen, F. M., Pollini, L., and Bülthoff, H. H. |
| Published in | Proceedings of the AIAA Modeling and Simulation Technologies Conference, AIAA SciTech, San Diego, CA, January 2016, 1-15. |

9.1 Introduction

An understanding of adaptation of human control behavior is crucial to properly design a haptic aid. Human control behavior can be described by human dynamic responses to the external cues. In a compensatory tracking task with haptic aids, the external cues are the visual and haptic feedback. A quantitative insight into human responses to visual and haptic feedback can be obtained by using identification techniques.

There is a vast amount of literature on identification of human responses in compensatory tracking tasks, see Chapter 5. However, these methods assume that humans do not vary their responses during the identification period. Although this assumption can be met in experimental settings, humans are likely to change their responses in realistic control scenarios, due to human-related variables (e.g., fatigue, motivation, etc.) and to environmental factors (e.g., weather, ambient illumination, etc.) [McRuer]. Thus, methods are needed that can estimate time-varying human responses.

Little research on human manual control has focused on identifying time-varying responses to visual and haptic feedback. Parametric methods have been proposed to estimate motion and visual responses [Hess, 2011; Zaal and Sweet, 2011, 2012]. These methods use parametric models to represent human's responses and find parameter values that best fit the measured data. However, one must take care not to use too many parameters, as this may lead to inaccurate parameter estimation [Zaal and Sweet, 2012]. Unfortunately, multiple parameters are needed to describe the dynamic response to the haptic feedback [van Paassen et al., 2004; Schouten et al., 2008b], and therefore, parametric methods may be not appropriate for identifying such response.

Non-parametric estimates of time-varying dynamics can be obtained by using the Wavelet transform. Recent studies have attempted to use a method based on the Wavelet transform for estimating human visual, motion, and neuromuscular responses [Mulder et al., 2011b; Thompson et al., 2001; Zaal and Sweet, 2011]. However, the Wavelet transform was shown to be very sensitive to human

remnant noise and produced inaccurate results when applied to human data [Zaal and Sweet, 2011].

In Chapter 7 and Chapter 8, we developed RLS-based methods to estimate time-varying neuromuscular response in disturbance-rejection tasks. The methods approximate the neuromuscular response with a Finite Impulse Response (FIR) filter, and estimate the FIR coefficients by using Recursive Least Squares (RLS) algorithms. However, until now the RLS-based methods have only been applied to disturbance-rejection tasks, where no visual feedback is provided.

This chapter extends the RLS-based methods to simultaneously estimate human's responses to visual and force feedback. These responses are approximated with FIR filters, and a RLS algorithm with Tikhonov regularization is applied to simultaneously estimate the coefficients of the FIR filters. The novel method was validated in a Monte-Carlo simulation study.

The chapter is structured as follows. Section 9.2 presents a model of the control task considered in this chapter. Section 9.3 details the novel regularized RLS-based approach to simultaneously estimate visual and neuromuscular responses. After this, a Monte-Carlo simulation study is presented in Section 9.4 to investigate the robustness of the novel algorithm to increasing levels of remnant noise. Finally, conclusions are drawn.

9.2 Control task

This chapter focuses on a compensatory tracking task with haptic feedback [McRuer]. Figure 9.1 shows a model of the control task. The human operator controls the roll angle ϕ_{ce} of the controlled element H_{ce} by using the lateral deflection δ_{cd} of a control device. The task is to track a target trajectory ϕ_t by minimizing the tracking error e presented on a compensatory display. During the tracking task, the human operator is provided with a continuous haptic force F_{ha} . In addition, the control device is perturbed by a force disturbance F_d used for identification purposes. The total external force is $F_{ex} = F_{ha} + F_d$.

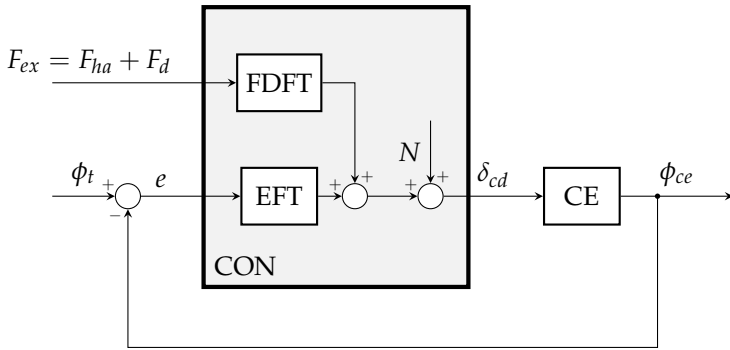


Figure 9.1: Compensatory tracking task.

Human control behavior in the compensatory tracking task can be described by quasi-linear models [McRuer]. Such models consist of linear dynamics that describe human's responses to all perceived external cues, and a remnant signal N that accounts for unmodeled non-linearities and noise. In the compensatory tracking task with haptic feedback, the human operator perceives two different cues, i.e., the visual tracking error e and the force feedback F_{ha} . The dynamic response to the tracking error is represented by the tracking error feedthrough (EFT), while the response to the force feedback is represented by so-called force disturbance feedthrough FDFT [Venrooij et al., 2013].

It is worth noting that EFT and FDFT include different components, such as neuromuscular dynamics (muscles, skin, and limb, a system for generating the muscle activation signal), visual response dynamics, and control device dynamics. A detailed model for EFT and FDFT can be found in a previous work [van Paassen et al., 2004]. Section A.2.4 gives an overview of the different components of the model.

9.3 Estimating time-varying human's responses

This section presents a RLS-based method to simultaneously estimate time-varying human's responses to visual error and force

feedback. The method represents human's responses with Finite Impulse Responses (FIR) filters, and uses a Recursive Least Squares algorithm with Tikhonov regularization to estimate the coefficients of FIR filters. Then, Fourier Transform is used to estimate the corresponding frequency responses.

Without loss of generality, the haptic feedback F_{ha} will be considered equal to zero for the purpose of developing the identification method. The method can be easily extended to the case of non-zero haptic feedback.

9.3.1 Impulse responses

Human control behavior in a compensatory tracking task can be represented by the multi-input single output system CON in Figure 9.1. The human's dynamic responses between the inputs F_d , e and the output δ_{cd} can be described by the corresponding impulse responses h_{F_dft} and h_{eft} . The impulse responses h_{F_dft} and h_{eft} can be used to express the human's response to generic input signals [Shmaliy, 2007]:

$$\delta_{cd}(t_n) = T \sum_{k=-\infty}^{\infty} \left[h_{eft}(t_n, t_k) e(t_k) + h_{F_dft}(t_n, t_k) F_d(t_k) \right] \quad 9.1$$

The previous equation has infinite number of terms. However, it can be simplified by considering physical properties of the human's responses in a compensatory tracking task. First, they can be assumed to be causal, thus $h_{eft}(t_n, t_m)$ and $h_{F_dft}(t_n, t_m)$ are zero for all $t_n < t_m$. Furthermore, human's impulse responses have finite memory, i.e., they become zero after finite time intervals. Assuming

causality and finite memory, Equation (9.1) simplifies to:

$$\begin{aligned}
 \delta_{cd}(t_n) &= T \sum_{k=n-M_e+1}^n h_{eft}(t_n, t_k) e(t_k) + T \sum_{k=n-M_F+1}^n h_{Fdft}(t_n, t_k) F_d(t_k) \\
 &= \begin{bmatrix} T e(t_n) & \dots & T e(t_{n-M_e+1}) \end{bmatrix} \begin{bmatrix} h_{e\delta}(t_n, t_n) \\ \vdots \\ h_{eft}(t_n, t_{n-M_e+1}) \end{bmatrix} \\
 &\quad + \begin{bmatrix} T F_d(t_n) & \dots & T F_d(t_{n-M_F+1}) \end{bmatrix} \begin{bmatrix} h_{Fdft}(t_n, t_n) \\ \vdots \\ h_{Fdft}(t_n, t_{n-M_F+1}) \end{bmatrix} \\
 &= e^T(t_n) \mathbf{h}_{eft}(t_n) + F_d^T(t_n) \mathbf{h}_{Fdft}(t_n). \tag{9.2}
 \end{aligned}$$

where M_e and M_F represent memory lengths of h_{eft} and h_{Fdft} , respectively. Combining the two impulse responses in a single vector \mathbf{h} , we obtain:

$$\delta_{cd}(t_n) = \begin{bmatrix} e^T(t_n) & F_d^T(t_n) \end{bmatrix} \begin{bmatrix} \mathbf{h}_{eft}(t_n) \\ \mathbf{h}_{Fdft}(t_n) \end{bmatrix} = \mathbf{u}^T(t_n) \mathbf{h}(t_n).$$

where \mathbf{u} contains the two input signals.

Our goal is to estimate the impulse response \mathbf{h} given measurements of e , F_d , and δ_{cd} . This is done by using a Recursive Least Squares (RLS) algorithm.

9.3.2 Recursive Least Squares algorithm

Three different RLS algorithms have been presented in Chapter 8 and Chapter 7 for estimating time-varying neuromuscular responses in single-loop tasks: the conventional RLS algorithm, the RLS algorithm with TSVD regularization, and the RLS algorithm with Tikhonov regularization. However, not all of these methods can be extended to multi-loop control tasks.

The conventional RLS algorithm requires that the input of the identified system must be persistently exciting. In single-input disturbance-rejection tasks, the input of the human model is the

disturbance force F_d . Since the commonly used multisine disturbance force was found not to be persistently exciting, a pseudonoise was added to F_d . In the compensatory tracking task in Figure 9.1, the input of the human model are the external force F_{ex} and the visual tracking error e . Although an additional pseudonoise could be added to F_{ex} , and additional pseudonoise on the tracking error e would excessively disturb the human operator and would make the control task too difficult.

The RLS algorithm with TSVD regularization can be used with multisine signals, without requiring the additional pseudonoise. However, the recursive implementation of TSVD requires a-priori knowledge of the input signals. This is not possible in the compensatory tracking task, since the tracking visual error e depends on human's control commands and cannot be known a-priori.

The RLS algorithm with Tikhonov regularization can be used with multisine signals, and does not require a-priori knowledge of the input signals. Thus, the RLS algorithm with Tikhonov regularization can be extended to a compensatory tracking task with haptic feedback.

The RLS algorithm with Tikhonov regularization estimates the impulse response \mathbf{h} at each time step as the least squares solution that minimizes the cost function V [Diniz, 2008; Zhou et al., 2008]:

$$\hat{\mathbf{h}}_{ti}(t_n) = \arg \min_{\mathbf{h} \in \mathbb{R}^M} V(\mathbf{h}, t_n) \quad 9.3$$

$$V(\mathbf{h}, t_n) = V_\epsilon(\mathbf{h}, t_n) + V_{ti}(\mathbf{h}, t_n) \quad 9.4$$

The first term V_ϵ accounts for the prediction errors ϵ between measured and predicted stick deflection δ_{cd} :

$$V_\epsilon(\mathbf{h}, t_n) = \sum_{k=1}^n \lambda^{n-k} \epsilon^2(t_k) \quad 9.5$$

$$\epsilon(t_k) = \delta_{cd}(t_k) - \mathbf{u}^T(t_k) \mathbf{h} \quad 9.6$$

where λ is a forgetting factor that weighs less the samples occurred further in the past ($0 \ll \lambda < 1$).

The second term V_{ti} is the Tikhonov regularization term:

$$V_{ti}(\mathbf{h}, t_n) = \|\mathbf{L}_{ti}^T(t_n) \mathbf{h}\|^2 = \mathbf{h}^T \mathbf{L}_{ti}(t_n) \mathbf{L}_{ti}^T(t_n) \mathbf{h} \quad 9.7$$

Table 9.1: RLS algorithm with Tikhonov regularization.

INITIALIZE	$S(t_0) = S_0 \in \mathbb{R}^{M \times M}$ $h(t_0) = \mathbf{0}$
FOR $n \geq 1$ DO	$w(t_n) = \sqrt{\frac{1-\lambda^p}{\lambda^{p-k}}} \tilde{\mathbf{l}}_k$, see Equation (8.45) $\epsilon(t_n) = \delta_{cd}(t_n) - \mathbf{u}^T(t_n) \hat{\mathbf{h}}(t_{n-1})$ $\boldsymbol{\psi}(t_n) = S(t_{n-1}) \begin{bmatrix} \mathbf{u}(t_n) & w(t_n) \end{bmatrix}$ $\mathbf{Q}^{-1}(t_n) = \left(\lambda \mathbf{I} + \begin{bmatrix} \mathbf{u}^T(t_n) \\ w^T(t_n) \end{bmatrix} \boldsymbol{\psi}(t_n) \right)^{-1}$ $S(t_n) = \frac{1}{\lambda} S(t_{n-1}) - \frac{1}{\lambda} \boldsymbol{\psi}(t_n) \mathbf{Q}^{-1}(t_n) \boldsymbol{\psi}^T(t_n)$ $\hat{\mathbf{h}}(t_n) = \hat{\mathbf{h}}(t_{n-1}) + \epsilon(t_n) S(t_n) \mathbf{u}(t_n)$ $\quad - S(t_n) w(t_n) w^T(t_n) \hat{\mathbf{h}}(t_{n-1})$

where $\|\cdot\|$ denotes the Euclidean norm, $L_{ti} \in \mathbb{R}^{M \times p}$ and $p \leq M$. Including the regularization term is beneficial when the problem of minimizing V_ϵ is ill-posed [Zhou et al., 2008]. The contribution of the regularization term on the cost function V depends on the matrix L_{ti} . A “large” $L_{ti} L_{ti}^T$ makes the Tikhonov regularization term dominant in the cost function V , skewing the minimum solution of V towards solutions with small norms. On the other hand, a “small” $L_{ti} L_{ti}^T$ places more weight on the prediction errors, and the minimum solution of V will be less biased towards solutions with small norms.

The minimum solution of V in Equation (9.3) is given by:

$$\hat{\mathbf{h}}(t_n) = \mathbf{R}_{ti}^{-1}(t_n) \mathbf{p}(t_n)$$

where:

$$\mathbf{R}_{ti}(t_n) = \mathbf{L}_{ti}(t_n)\mathbf{L}_{ti}^T(t_n) + \sum_{k=1}^n \lambda^{n-k} \mathbf{u}(t_k)\mathbf{u}^T(t_k) \quad 9.9$$

$$\mathbf{p}(t_n) = \sum_{k=1}^n \lambda^{n-k} \mathbf{u}(t_k) \delta_{cd}(t_k) \quad 9.10$$

The solution in Equation (9.8) requires calculation of the inverse of \mathbf{R} . However, the recursive algorithm developed in Chapter 8 can be used to avoid calculation of the matrix inverse at each time step. Table 9.1 lists the steps of the recursive algorithm.

9.4 A Monte-Carlo simulation study

A Monte-Carlo simulation study was performed to investigate robustness of the RLS method with Tikhonov regularization to different levels of remnant noise.

9.4.1 Control task

The compensatory tracking task in Figure 9.1 was simulated by using Simulink (The MathWorks, Inc.). The remnant noise N was generated as a Gaussian noise filtered by a third order filter [Zaal et al., 2009]:

$$H_N = K_n \frac{\omega_N^3}{(s + \omega_N)(s^2 + 2\epsilon_N \omega_N s + \omega_N^2)} \quad [-] \quad 9.11$$

where $\epsilon_N = 0.26$ and $\omega_N = 12.7$ rad/s. The value of K_N was scaled to obtain different ratios r_n between the variance σ_N^2 of the remnant signal and the variance $\sigma_{\delta_{cd}}^2$ of the stick deflection:

$$r_N = \frac{\sigma_N^2}{\sigma_{\delta_{cd}}^2} \quad 9.12$$

Time-varying dynamics were simulated for human's responses, based on dynamics estimated in a previous human-in-the-loop experiment [van Paassen et al., 2004]. In that experiment, participants

Table 9.2: Parameters for control device dynamics $H_{cd} = (m_{cd}s^2 + b_{cd}s + k_{cd})^{-1}$. The parameters are defined at 90 mm above the rotation axis.

	m_{cd} Kg	b_{cd} N s m ⁻¹	k_{cd} N m ⁻¹
$H_{cd,0}$	1.5	400.0	26.1
$H_{cd,1}$	4.0	400.0	26.1

Table 9.3: Pilot parameters identified with the control device dynamics in Table 9.2. The parameters are defined considering rotations and moments around the elbow rotation point.

	K_v -	τ_{v_L} s	τ_{v_l} s	Δt_v s	K_f rad ⁻¹	τ_{f_L} s	τ_{f_l} s	K_n rad ⁻¹	τ_{n_L} s
0	0.520	0.5	0.005	0.212	2.952	0.0	0.3	3.187	0.1
1	0.489	0.5	0.005	0.270	1.566	0.1	0.3	1.259	0.2

	τ_{n_l} s	Δt_n s	B_c $\frac{\text{Nm s}}{\text{rad}}$	K_c $\frac{\text{Nm}}{\text{rad}}$	K_{pec} $\frac{\text{Nm}}{\text{rad}}$	K_{sec} $\frac{\text{Nm}}{\text{rad}}$	B_m $\frac{\text{Nm s}}{\text{rad}}$	I Kg m ²
0	0.477	0.02	7.01	300	9.14	30	0.538	0.0417
1	0.273	0.02	7.01	300	9.14	30	0.538	0.0417

performed compensatory tracking tasks with different control device dynamics, i.e., $H_{cd,0}$ and $H_{cd,1}$ in Table 9.2. Then, human's responses were estimated by using the parametric model in Section A.2.4, resulting in the parameters values listed in Table 9.3. In our Monte-Carlo simulation study, two sets of human's responses $H_{e\delta,0}$, $H_{F\delta,0}$ and $H_{e\delta,1}$, $H_{F\delta,1}$ were calculated based on the parameters in Table 9.3. Then, time evolutions of human's responses and control device

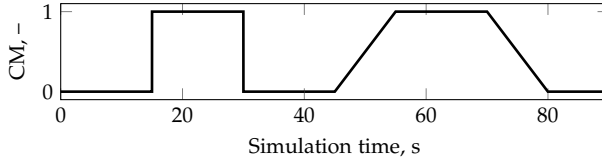


Figure 9.2: Time evolution of the control mode CM.

dynamics were chosen as:

$$H_{eft}(t_n) = (1 - \text{CM}(t_n)) H_{e\delta,0} + \text{CM}(t_n) H_{e\delta,1} \quad 9.13$$

$$H_{Fdf}(t_n) = (1 - \text{CM}(t_n)) H_{F\delta,0} + \text{CM}(t_n) H_{F\delta,1} \quad 9.14$$

$$H_{cd}(t_n) = (1 - \text{CM}(t_n)) H_{cd,0} + \text{CM}(t_n) H_{cd,1} \quad 9.15$$

where the Control Mode parameter (CM) varies between 0 and 1 as shown in Figure 9.2, to simulate abrupt and slow changes between the different dynamics.

The dynamics of the controlled element were time-invariant:

$$H_{ce} = \frac{2}{s(0.5s + 1)} \quad [\text{rad/rad}] \quad 9.16$$

9.4.2 Forcing functions

Estimation of two different human's responses requires two different external forcing functions to excite the system [van Lunteren, 1979]. In the compensatory tracking task in Figure 9.1, the target roll angle ϕ_t and the disturbance force F_d can be chosen as forcing functions. The two forcing functions were designed as multisine signals, since their properties can be controlled to obtain high signal-to-noise ratios [Schouten et al., 2008b]:

$$\phi_t(t_n) = \sum_{k=1}^{N_t} A_{t,k} \sin(f_{t,k} t_n + \psi_{t,k}) \quad 9.17$$

$$F_d(t_n) = \sum_{k=1}^{N_d} A_{d,k} \sin(f_{d,k} t_n + \psi_{d,k}) \quad 9.18$$

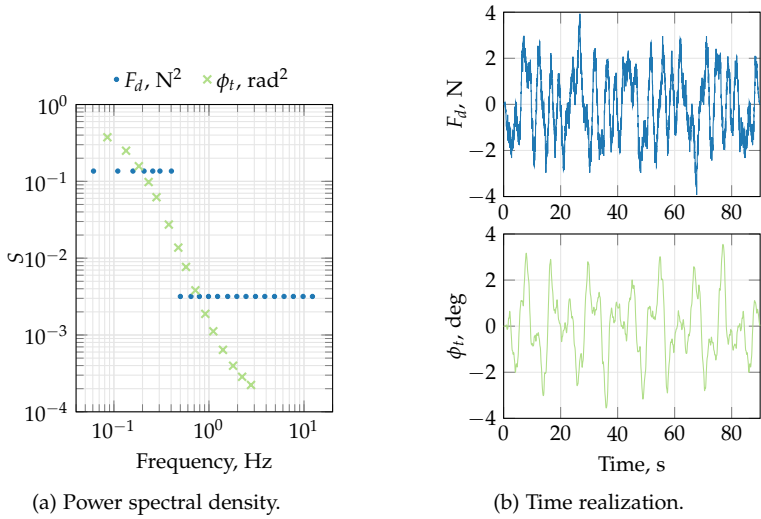


Figure 9.3: Target trajectory ϕ_t and disturbance force F_d .

The parameters of the multisines were chosen based on guidelines that are commonly used in human in-the-loop experiments [Abbink et al., 2011; Zaal et al., 2008]. Figure 9.3 shows Power Spectral Densities and time realizations of the designed forcing signals. The frequencies $f_{t,k}$, $f_{d,k}$ were chosen as integer multiples of the base frequency $f_0 = 1/81.92$ Hz, to yield an integer multiple of signal periods in the measurement window of 81.92 s. Different frequency points were assigned to ϕ_t and F_d , to distinguish their contribution on other signals in the control loop. To capture dynamical properties of visual and neuromuscular responses, the frequencies of ϕ_t were chosen in the range from 0.05 Hz up to 3 Hz, while the frequencies of F_d were in the range from 0.05 Hz up to 15 Hz [Abbink et al., 2011; Zaal et al., 2008].

Amplitudes and phases of the target signal ϕ_t were chosen to yield an unpredictable signal and to prevent crossover regression. The amplitudes $A_{t,k}$ were shaped according to the following filter

[Zaal et al., 2008]:

$$A_{t,k} = \left| \frac{(j2\pi f_k T_1 + 1)^2}{(j2\pi f_k T_2 + 2)^2} \right| \quad 9.19$$

where $T_1 = 0.1$ s and $T_2 = 0.8$ s. The phases $\psi_{t,k}$ were selected from a random set to yield a Gaussian distribution of the values of ϕ_t . The total power of the signal was set to 2 deg^2 .

The amplitudes $A_{d,k}$ of the disturbance force F_d were designed according to the Reduced Power Method [Mugge et al., 2007]. This method consists of applying full power and low frequencies and reduced power at higher frequencies, to enable identification of the neuromuscular response over a large frequency range without suppressing the reflexive activity. The signal contained full power up to 0.5 Hz, and a 5% fraction of that power at higher frequencies. The total power of F_d was set to 2 N^2 , not to disturb the human operator in the control task while still allowing for identification of neuromuscular response. The phases $\psi_{d,k}$ were randomized to generate an unpredictable signal, and a cresting technique was applied to minimize peaks in the signal realization [Pintelon and Schoukens, 2012].

9.4.3 Independent variables and data analysis

To test robustness of RLS-based method with Tikhonov regularization, different remnant levels r_N in Equation (9.12) were used:

$$r_N \in \{0, 0.01, 0.1\} \quad 9.20$$

For each remnant level, 100 different simulations were performed with different realizations of the Gaussian noise. The RLS-based method with Tikhonov regularization was then applied to the signals logged during each run. The parameters for the RLS algorithm were set as:

$$\lambda = 0.99 \quad 9.21$$

$$M_e = 2.56 \text{ s} \cdot 100 \text{ Hz} = 256 \quad 9.22$$

$$M_F = 256 \quad 9.23$$

$$L_{ti} = 10^{-5} I \quad 9.24$$

where I is the identity matrix. These parameters were chosen fairly arbitrarily based on previous studies on single-loop RLS-based algorithm and can probably be further optimized.

The RLS-based method with Tikhonov regularization provides estimates of human dynamic responses. To evaluate reliability of RLS estimates, the estimated frequency responses \hat{H} were compared to the simulated frequency responses H by calculating the averaged logarithmic squared error [Pintelon et al., 1994]:

$$\bar{E}(t_n) = \frac{1}{N_f} \sum_{f=f_{min}}^{f_{max}} E(f, t_n) \quad 9.25$$

where N_f is the total number of frequency points, and E is the logarithmic squared error:

$$E(f, t_n) = |\log \hat{H}(f, t_n) - \log H(f, t_n)|^2 \quad 9.26$$

9.4.4 Results

Figure 9.4 shows time evolutions of \bar{E} corresponding to H_{eft} and H_{Fdft} . Without remnant noise and with low level of remnant noise ($r_n = 0$ and $r_n = 0.01$, respectively), the errors presented similar time evolutions for both H_{eft} and H_{Fdft} . The errors were small when the dynamics were constant or changed slowly. After the abrupt dynamics changes ($t = 15$ s and $t = 30$ s), the errors significantly increased. However, they reached again a small steady state after almost 7 s. Note that the errors in H_{Fdft} estimates were larger than the errors in H_{eft} . This was because the power of the force disturbance was set small enough not to disturb pilots during the compensatory tracking task. With a force disturbance with higher power, smaller errors would be achieved.

With high level of remnant noise ($r_n = 0.1$), the errors in H_{Fdft} and H_{eft} estimates were large. Furthermore, the errors did not converge to small steady states after changes in pilot's dynamics.

To obtain a better insight into the evolution of the RLS-based estimates, Figure 9.5 and Figure 9.6 show H_{Fdft} and H_{eft} at different time points around the abrupt change at $t = 30$ s. The columns

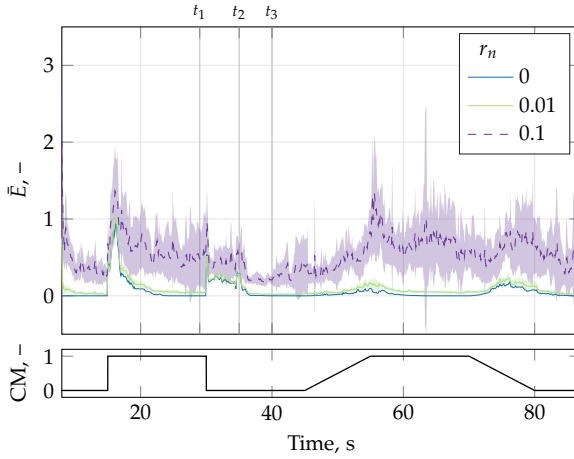
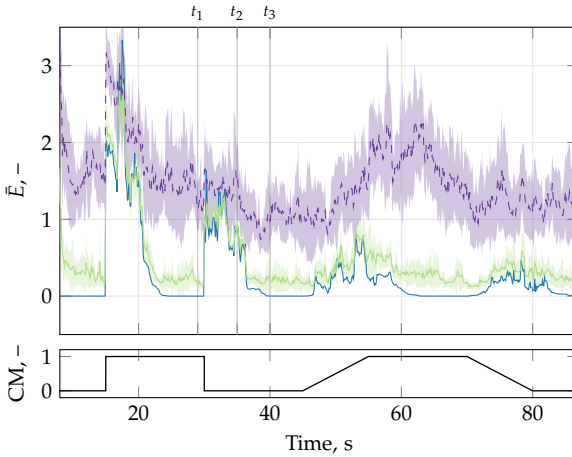
(a) H_{eff} .(b) H_{Fdft} .

Figure 9.4: Time evolution of the error \bar{E}_f . Lines and shades indicate means and standard deviations over different realizations of remnant noise.

correspond to different remnant levels, while the rows to different estimation times.

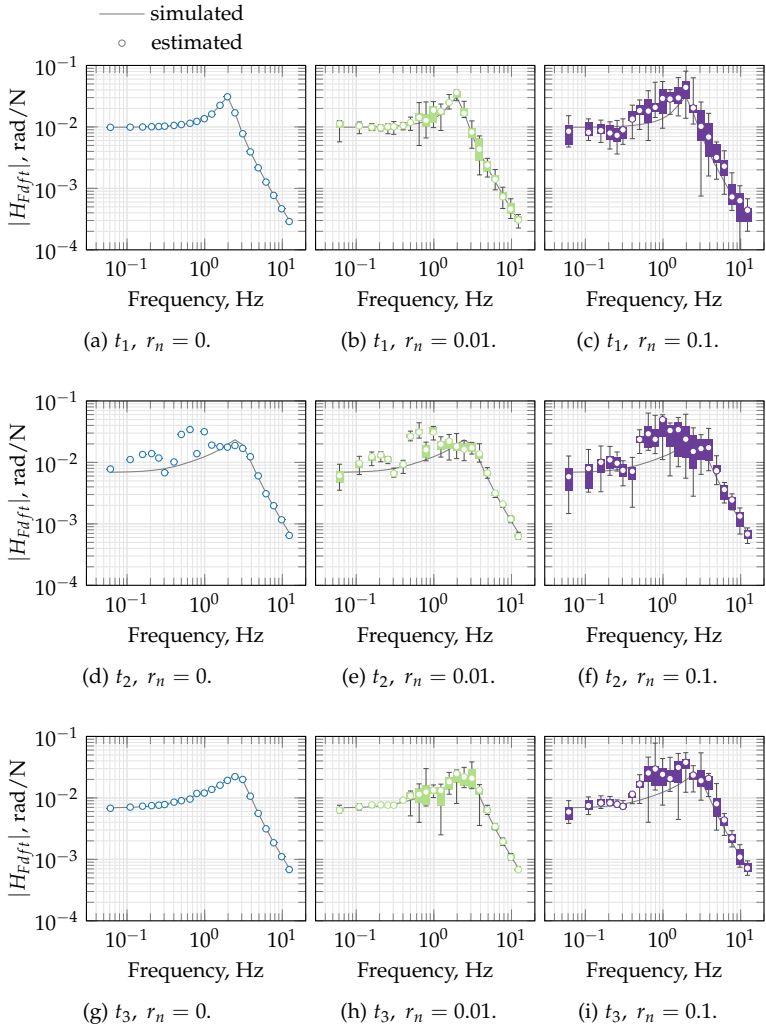


Figure 9.5: Time evolution of H_{Fdft} estimates. The circles represent mean values over different realizations of remnant noise, and the box-and-whisker plots indicate 25 and 75 percentiles (boxes) and minimum and maximum values (whiskers).

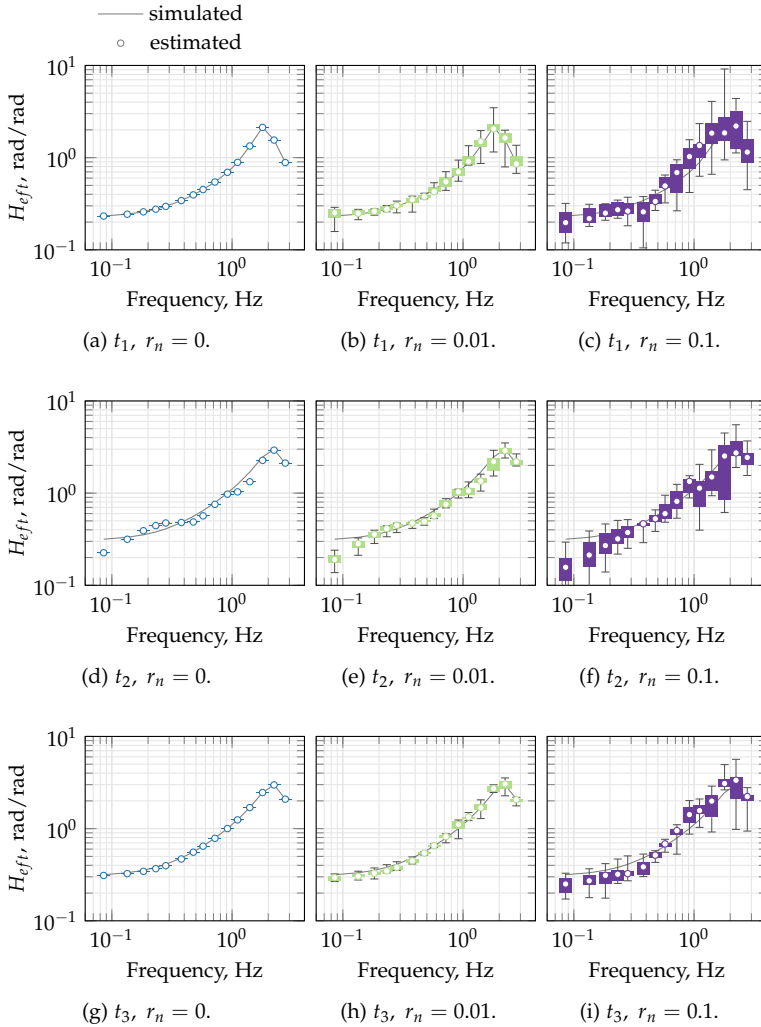


Figure 9.6: Time evolution of H_{eff} estimates. The circles represent mean values over different realizations of remnant noise, and the box-and-whisker plots indicate 25 and 75 percentiles (boxes) and minimum and maximum values (whiskers).

Similar trends were found for H_{eft} and H_{Fdf} estimates. Without remnant noise ($r_n = 0$), estimates of H_{eft} and H_{Fdf} well resembled the corresponding simulated dynamics before the abrupt change ($t_1 = 29$ s). After the abrupt changes the estimates differed from the two simulated dynamics ($t_2 = 35$ s). However, the estimates converged to the new dynamics at $t_3 = 40$ s.

A similar behavior was obtained with low level of remnant noise ($r_n = 0.01$). Mean values of the estimates resembled the simulated dynamics before and long after the abrupt change. Furthermore, small variability of the estimates was found over different noise realizations (small boxes and whiskers).

Unfortunately, accuracy of estimates degraded for high level of remnant noise ($r = 0.1$). Mean values of the estimates slightly differed from the simulated dynamics. Furthermore, a large variability of the estimates was found along different noise realizations.

9.5 Conclusions

This chapter has presented a method to estimate time-varying human's responses to visual and force feedback. The method describes human's responses with Finite Impulse Response filters and uses a Recursive Least Square algorithm with Tikhonov regularization to estimate the filters coefficients.

A set of Monte-Carlo simulations showed that the method provides accurate estimates of human's responses with low levels of remnant noise. The method was able to track slow changes in the simulated dynamics, while it required almost 10 s to converge to the new simulated dynamics after the abrupt changes. With high level of remnant noise, estimates presented high variability. However, the reason for this is probably a non optimal setting of the parameters for the RLS algorithm with Tikhonov regularization.

Although there are limitations for high levels of remnant noise, the RLS-based method provides a powerful tool for identifying time-varying human's responses to visual and haptic feedback. We are currently in the process of investigating how to optimize the RLS parameters to improve robustness to the remnant noise. Furthermore,

future works will explore the application of the RLS-based method to data measured during human-in-the-loop experiments.

Conclusions and recommendations

THE main goal of the thesis was:

Research goal

Increase the understanding of influence of haptic aids on pilot's performance and control behavior.

Three objectives were formulated toward the goal of this thesis. The first objective was to quantify effectiveness of haptic aids on pilot's performance and control effort in different control scenarios. Comparisons with input-mixing systems were of particular interest. The second objective was to evaluate influence of haptic aids on pilot's dynamic responses. To achieve this, novel methods were developed for estimating time-invariant pilot's responses during steering tasks. Finally, the third objective was to account for time-varying behavior of pilot's responses.

This chapter is structured as follows. First, conclusions obtained for the different chapters of the thesis are presented. Then, main contributions of this thesis are synthesized. Finally, some recommendations for future studies are given.

10.1 Quantifying effects of haptic feedback on human's performance

Overview of Chapter 2

Chapter 2 presented a quantitative comparison between haptic and input-mixing support systems. A human in-the-loop experiment was conducted where participants performed a compensatory tracking task with haptic and input-mixing aids. The haptic and input-mixing system were designed to be equivalent, i.e., to provide same control command without the pilot in-the-loop. From the pilot's point of view, the net effect of the input-mixing system was to augment controlled element dynamics making them easier to control. Pilot's performance and control effort were evaluated for the two support systems, and compared to a baseline condition without external aids.

Conclusions of Chapter 2

Haptic and input-mixing support systems allowed participants to improve their performances compared to the baseline condition, however the input-mixing system yielded better performance than the haptic aid. This indicates that participants found it easier to control the augmented dynamics, than controlling the original dynamics with the help of haptic feedback. Control effort was reduced by haptic and input-mixing aids in a similar way.

Main finding of Chapter 2

Haptic aids help human operators improve their performance compared to manual control, but they are outperformed by input-mixing systems.

Overview of Chapter 3

Although input-mixing systems yielded better performance than haptic aids, it is still poorly understood what happens in case of an expected event like a failure of the support system. An human in-the-loop experiment was performed to investigate this aspect. Participants performed a compensatory tracking task either with haptic aid or with an equivalent input-mixing support system. Failures of the support systems were simulated as total loss of support control action. Then, performance was evaluated before and after the failure, and contrasted to a baseline condition without external aids.

Conclusions of Chapter 3

After failures of both support systems, participants experienced a sudden decrease of performances. With input-mixing system, participants were not able to re-gain levels of performance similar to those obtained in the baseline condition. With haptic aids, participants were able to recover in a short time. Surprisingly, performances after recovering were similar to those just before the failure, which were better than those obtained during the baseline condition. This seems to show that haptic aids helped participants learn the control task.

Main finding of Chapter 3

Human operators recover quicker from failures of haptic aids than from failures of input-mixing systems.

Overview of Chapter 4

Chapter 4 presented an experiment to investigate effectiveness of haptic aids for learning purposes. Two groups of participants learned a compensatory tracking task either with (haptic group) or without haptic feedback (no-aid group). Then, all participants

performed some experimental trials without haptic feedback. Performances were evaluated and contrasted between the two groups.

Conclusions of Chapter 4

Results indicated that participants of the haptic group achieved steady performances after a small number of experimental trials. Furthermore, their performance did not worsen in the evaluation phase when the haptic feedback was switched off. On the other hand, the no-aid group needed a large number of trials to achieve similar performance as the haptic group.

Main finding of Chapter 4

Haptic aids help human operators learn a compensatory tracking task.

10.2 Identifying time-invariant human's responses

Overview of Chapter 5

In a compensatory tracking task with haptic aids, human behavior can be described by the visual and the neuromuscular responses. To estimate these responses, identification methods can be applied. We proved that the commonly used CS method was shown to be biased when a non-interference hypothesis is not fulfilled. To overcome this issue, two novel methods were developed that are unbiased even when the non-interference hypothesis is not fulfilled: the ARX and CS-ML methods. The two novel methods were validated in a set of Monte-Carlo simulations and in a human in-the-loop experiment.

Conclusions of Chapter 5

In the simulation study, the CS method provided biased estimates of the neuromuscular response. On the other hand, the estimates of ARX and CS-ML methods resembled the simulated responses. In

the experiment, the two novel methods provided similar estimates, while the CS method showed similar bias obtained in the simulation study. These findings indicate that ARX and CS-ML indeed provide reliable estimates even when the CS method provides biased estimates.

Main finding of Chapter 5

The commonly used CS method provides biased estimates of neuromuscular response when the non-interference hypothesis is not fulfilled. On the other hand, the novel ARX and CS-ML methods provide unbiased estimates.

Overview of Chapter 6

The novel ARX and CS-ML methods were applied to experimental data obtained in compensatory tracking tasks with different haptic aids. Two haptic aids were designed according to different approaches: the Direct Haptic Aid (DHA) and Indirect Haptic Aid (IHA) methods. The two approaches provide haptic information in opposite ways and require humans to adopt different dynamic responses.

Conclusions of Chapter 6

Participants significantly adapted their neuromuscular responses to fully exploit DHA and IHA systems. With DHA, participants adopted compliant neuromuscular settings to actively follow the haptic feedback, whereas participants were stiffer with IHA as this approach requires counteracting the force feedback.

Main finding of Chapter 6

Haptic feedback has a strong influence on neuromuscular and visual dynamic responses.

10.3 Methods for identifying time-varying human's responses

Overview of Chapter 7

The third objective of the thesis was to account for time-varying behavior of human's dynamic responses. A novel method RLS-based method was developed to identify time-varying neuromuscular responses. The method was initially applied in disturbance-rejection tasks, where humans can be modelled as single-input systems. The method approximates the neuromuscular response with a Finite Impulse Response (FIR) filter and estimate the FIR parameters at each time step by using a Recursive Least Squares (RLS) algorithm. The reliability and robustness of the method were investigated by using different sets of Monte-Carlo simulations. Then, the RLS-based was applied to data obtained from experimental measurements.

Conclusions of Chapter 7

In a first set of Monte-Carlo simulations, the RLS-based method allowed a fast tracking of ramp neuromuscular variations, whereas it gradually converged to the new neuromuscular dynamics after instantaneous changes. Furthermore, the RLS-based method was shown to be robust to high levels of remnant noise on a broad range of frequencies. Only at high frequencies, estimates were not accurate. A second set of Monte-Carlo simulations provided values for RLS-based parameters that gave the best compromise between robustness to the noise and converging rate of the estimates. These values were used to apply the RLS-based method to experimental data. Experimental results showed that the RLS-based estimates accurately tracked time-varying neuromuscular dynamics. However, estimates showed high variability at low and high frequencies, indicating that the RLS-based method was sensitive to relatively high levels of remnant noise.

Main finding of Chapter 7

The novel RLS-based method can track time-varying behavior of neuromuscular dynamics in disturbance-rejection tasks. However, when applied to experimental data, RLS-based estimates are sensitive to external noise at low and high frequencies.

Overview of Chapter 8

The RLS-based method requires an additional pseudonoise signal to be added as a force disturbance on the control device. However, this may be the cause of the poor robustness to noise of the RLS-based method. To improve robustness to noise, two novel RLS-based methods were developed. The novel methods combine a RLS algorithm with two regularization methods: the Truncated Singular Value Decomposition and the Tikhonov regularization. The mathematical framework of the regularized RLS-based methods was described, and recursive implementations were derived.

Conclusions of Chapter 8

The regularized RLS-based methods can estimate time-varying neuromuscular dynamics without requiring an additional pseudonoise signal. This improves the robustness to external noise.

Main finding of Chapter 8

A mathematical framework is provided for regularized RLS-based methods.

Overview of Chapter 9

The RLS-based method with Tikhonov regularization was extended to estimate visual and neuromuscular responses in a compensatory

tracking task. Pilot's visual and neuromuscular responses are approximated with FIR filters, and a RLS algorithm with Tikhonov regularization is used to simultaneously estimate the FIR filters coefficients. A Monte-Carlo simulation study was performed to validate the method and to test robustness to different levels of remnant noise.

Conclusions of Chapter 9

With low levels of remnant noise, the RLS-based method with Tikhonov regularization tracked slow changes in pilot's dynamic responses, whereas it needed almost 10 s to converge to the new simulated dynamics after the instantaneous change. However, high levels of remnant noise resulted in high variability of estimates. This was probably due to non optimal settings of the parameters for the algorithm.

Main finding of Chapter 9

The novel RLS-based method with Tikhonov regularization can be used to simultaneously estimate visual and neuromuscular responses. A further investigation is needed to find an optimal set of parameters that would improve robustness to remnant noise.

10.4 Main contributions

The results obtained throughout the thesis can be synthesized in three main contributions:

- Haptic aids help humans perform a control task while still keeping the human operator in-the-loop. Human operators quickly get acquainted with the haptic feedback and learn how to exploit it to improve performances. Although haptic aids generally yield worse performance compared to input-mixing

systems in nominal conditions, they improve human's skills in recovering from possible failures of the support system.

- The commonly used CS method for identifying pilot's responses introduces a bias in the estimate of neuromuscular response when the non-interference hypothesis is not fulfilled. The novel ARX and CS-ML methods overcome this issue and provide reliable estimates even when the CS method fails. By applying ARX and CS-ML to compensatory tracking tasks with different haptic aids, human operators were found to largely adapt their responses to different types of haptic feedback.
- The RLS-based methods successfully estimated time-varying neuromuscular dynamics in disturbance-rejection tasks. In compensatory tracking tasks, the methods showed high variability in case of large remnant noise. However, parameters of the RLS-based method could be further optimized to improve robustness to noise.

10.5 Recommendations

In our view the results of this thesis are an excellent initial step toward a human-centered designed of haptic aids. However, further research should be undertaken in the following areas:

- In this thesis, haptic aids were designed for a compensatory tracking task. Even though such task allows for studying elementary pilot control behavior, it does not account for the complexity of a realistic control scenario. Further work needs to be carried out to establish whether beneficial effect of haptic aids also apply to realistic control scenarios.
- The ARX, CS-ML, and RLS-based methods were developed to estimate pilot's visual and neuromuscular in a compensatory tracking task. In realistic control scenarios, more complex models are required to capture the simultaneous response to multiple external cues. Future studies should be directed at

evaluating whether the identification methods can be extended to such complex scenarios.

- The ARX, CS-ML, and RLS-based methods require a force disturbance on the control device to allow identification of neuromuscular response. However, use of a continuous force disturbance would disturb human operators in realistic control scenarios. The prospect of being able to estimate the neuromuscular response without using a force disturbance, serves as a continuous stimulus for future research.

Bibliography

- Abbink, D. A., *Neuromuscular analysis of haptic gas pedal feedback during car following*, Ph.D. thesis, TU Delft, Delft University of Technology, Faculty of Mechanical Maritime and Materials Engineering, 2006.
- Abbink, D. A., "Task instruction: the largest influence on human operator motion control dynamics," *Proceedings of the Second Joint EuroHaptics Conference and Symposium on Haptic Interfaces for Virtual Environment and Teleoperator Systems (WHC'07)*, pp. 206 – 211, IEEE, Mar. 2007, doi:10.1109/whc.2007.108.
- Abbink, D. A., Boer, E. R., and Mulder, M., "Motivation for continuous haptic gas pedal feedback to support car following," *Proceedings of the IEEE Intelligent Vehicles Symposium*, pp. 283–290, IEEE, Jun. 2008, doi:10.1109/IVS.2008.4621325.
- Abbink, D. A. and Mulder, M., "Exploring the dimensions of haptic feedback support in manual control," *Journal of Computing and Information Science in Engineering*, vol. 9, no. 1, pp. 0110061–0110069, 2009, doi:10.1115/1.3072902.
- Abbink, D. A. and Mulder, M., "Neuromuscular analysis as a guideline in designing shared control," *Advances in Haptics*, pp. 501–514, 2010, doi:10.5772/8696.

- Abbink, D. A., Mulder, M., and Boer, E. R., "Haptic shared control: smoothly shifting control authority?" *Cognition, Technology and Work*, vol. 14, no. 1, pp. 19–28, Nov. 2012, doi:10.1007/s10111-011-0192-5.
- Abbink, D. A., Mulder, M., Van der Helm, F. C. T., and Boer, E. R., "Measuring neuromuscular control dynamics during car following with continuous haptic feedback," *IEEE Transactions on Systems, Man, and Cybernetics, Part B: Cybernetics*, vol. 41, no. 5, pp. 1239–1249, 2011, doi:10.1109/TSMCB.2011.2120606.
- Abildgaard, M. and von Grünhagen, W., "Demonstration of an active sidestick in the DLR Flying Helicopter Simulator (FHS)," *Proceedings of the European Rotorcraft Forum (ERF)*, Oct. 2008.
- Alaimo, S., Pollini, L., and Bülthoff, H. H., "Admittance-based bilateral teleoperation with time delay for an unmanned aerial vehicle involved in an obstacle avoidance task," *AIAA Modeling and Simulation Technologies Conference*, also AIAA Paper 2011-6243, pp. 1–19, Aug. 2011a, doi:10.2514/6.2011-6243.
- Alaimo, S. M. C., Pollini, L., Bresciani, J. P., and Bulthoff, H. H., "A comparison of direct and indirect haptic aiding for remotely piloted vehicles," *Proceedings of the IEEE 19th International Symposium in Robot and Human Interactive Communication (RO-MAN)*, pp. 506 – 512, IEEE, Sep. 2010, doi:10.1109/roman.2010.5598647.
- Alaimo, S. M. C., Pollini, L., Bresciani, J.-P., and Bülthoff, H. H., "Experiments of direct and indirect haptic aiding for remotely piloted vehicles with a mixed wind gust rejection/obstacle avoidance task," *Proceedings of the AIAA Modeling and Simulation Technologies Conference*, pp. 1–18, Aug. 2011b, doi:10.2514/6.2011-6242, also AIAA Paper 2011-6242.
- Bainbridge, L., "Ironies of automation," *Automatica*, vol. 19, no. 6, pp. 775–779, Nov. 1983, doi:10.1016/0005-1098(83)90046-8.
- Balderas Silva, D., *Time-varying identification of human properties using the wavelet analysis*, Master thesis, TU Delft, Delft University

- of Technology, Faculty of Mechanical, Maritime and Materials Engineering, 2009.
- Ben-Israel, A. and Greville, T. N., *Generalized Inverses: Theory and Applications*, vol. 15, Springer Science & Business Media, 2003.
- Billings, C. E., "Human-centered aircraft automation: a concept and guidelines," NASA/TM-103885, NASA, Aug. 1991.
- Billings, C. E., *Aviation automation : the search for a human-centered approach*, CRC Press, 1st edn., 1997.
- Brandt, T., Sattel, T., and Bohm, M., "Combining haptic human-machine interaction with predictive path planning for lane-keeping and collision avoidance systems," *Proceedings of the IEEE Intelligent Vehicles Symposium*, pp. 582–587, IEEE, Jun. 2007, doi: 10.1109/IVS.2007.4290178.
- Cousineau, D., "Confidence intervals in within-subject designs: A simpler solution to Loftus and Masson's method," *Tutorials in Quantitative Methods for Psychology*, vol. 1, no. 1, pp. 42–45, 2005.
- Damveld, H. J., Abbink, D. A., Mulder, M., Mulder, M., van Paassen, M. M., van der Helm, F. C. T., and Hosman, R. J. A. W., "Identification of the feedback component of the neuromuscular system in a pitch control task," *Proceedings of the AIAA Guidance, Navigation, and Control Conference*, pp. 1–22, AIAA, Aug. 2010, doi:10.2514/6.2010-7915, also AIAA Paper 2010-7915.
- Damveld, H. J., Abbink, D. A., Mulder, M., Mulder, M., Van Paassen, M. M., Van der Helm, F. C. T., and Hosman, R. J. A. W., "Measuring the contribution of the neuromuscular system during a pitch control task," *Proceedings of the AIAA Modeling and Simulation Technologies Conference*, pp. 10–13, AIAA, Aug. 2009, doi: 10.2514/6.2009-5824, also AIAA Paper 2009-5824.
- Diniz, P. S. R., *Adaptive Filtering - Algorithms and Practical Implementation*, Springer, 2008.

- Doehler, H.-U., Lüken, T., and Lantzsch, R., "Allflight: a full scale enhanced and synthetic vision sensor suite for helicopter applications," *SPIE Defense, Security, and Sensing*, pp. 1–11, International Society for Optics and Photonics, Apr. 2009, doi:10.1117/12.818454.
- Drop, F. M., Pool, D. M., Damveld, H. J., van Paassen, M. M., and Mulder, M., "Identification of the feedforward component in manual control with predictable target signals," *IEEE Transactions on Cybernetics*, vol. 43, no. 6, pp. 1936–1949, 2013, doi:10.1109/TSMCB.2012.2235829.
- Endsley, M. R., "Toward a theory of situation awareness in dynamic systems," *Human Factors: The Journal of the Human Factors and Ergonomics Society*, vol. 37, no. 1, pp. 32–64, Mar. 1995, doi:10.1518/001872095779049543.
- Endsley, M. R. and Kiris, E. O., "The out-of-the-loop performance problem and level of control in automation," *Human Factors: The Journal of the Human Factors and Ergonomics Society*, vol. 37, no. 2, pp. 381–394, Jun. 1995, doi:10.1518/001872095779064555.
- Feygin, D., Keehner, M., and Tendick, R., "Haptic guidance: Experimental evaluation of a haptic training method for a perceptual motor skill," *Proceedings of the 10th Symposium on Haptic Interfaces for Virtual Environment and Teleoperator Systems*, pp. 40–47, IEEE, Mar. 2002, doi:10.1109/HAPTIC.2002.998939.
- Field, A., *Discovering Statistics Using IBM SPSS Statistics*, Sage, 2013.
- Fierro, R. D., Hansen, P. C., and Hansen, P. S. K., "UTV tools: Matlab templates for rank-revealing utv decompositions," *Numerical Algorithms*, vol. 20, no. 2-3, pp. 165–194, Aug. 1999, doi:10.1023/A:1019112103049.
- Flemisch, F. O., Adams, C. A., Conway, S. R., Goodrich, K. H., Palmer, M. T., and Schutte, P. C., "The H-metaphor as a guideline for vehicle automation and interaction," NASA/TM-2003-212672, NASA, Aug. 2003.

- Franklin, M. F., Denes, J., and Keedwell, A. D., "Latin squares: New developments in the theory and applications," *Applied Statistics*, vol. 41, no. 3, p. 601, 1992, doi:10.2307/2348094.
- Goodrich, K., Schutte, P., and Williams, R., "Haptic-multimodal flight control system update," *Proceedings of 11th AIAA Aviation Technology, Integration, and Operations (ATIO) Conference*, also AIAA Paper 2011-6984, pp. 1-17, AIAA, Sep. 2011, doi: 10.2514/6.2011-6984.
- Goodrich, K., Schutte, P. C., and Williams, R. A., "Piloted evaluation of the H-mode, a variable autonomy control system, in motion-based simulation," *Proceedings of the AIAA Atmospheric Flight Mechanics Conference and Exhibit*, pp. 1-15, AIAA, Aug. 2008, doi:10.2514/6.2008-6554, also AIAA Paper 2008-6554.
- Griffiths, P. G. and Gillespie, R. B., "Sharing control between humans and automation using haptic interface: Primary and secondary task performance benefits," *Human Factors*, vol. 47, no. 3, pp. 574-590, Oct. 2005, doi:10.1518/001872005774859944.
- Hansen, P. C., "Regularization tools: A Matlab package for analysis and solution of discrete ill-posed problems," *Numerical Algorithms*, vol. 6, no. 1, pp. 1-35, 1994, doi:10.1007/bf02149761.
- Hansen, P. C. and O'Leary, D. P., "The use of the L-curve in the regularization of discrete ill-posed problems," *SIAM Journal on Scientific Computing*, vol. 14, no. 6, pp. 1487-1503, 1993, doi:10.1137/0914086.
- Hasstrudi-Zaad, K. and Salcudean, S. E., "Transparency in time-delayed systems and the effect of local force feedback for transparent teleoperation," *IEEE Transactions on Robotics and Automation*, vol. 18, no. 1, pp. 108-114, Feb. 2002, doi:10.1109/70.988981.
- van der Helm, F. C., Schouten, A. C., de Vlugt, E., and Brouwn, G. G., "Identification of intrinsic and reflexive components of human arm dynamics during postural control," *Journal of Neuroscience Methods*, vol. 119, no. 1, pp. 1-14, Sep. 2002, doi:10.1016/s0165-0270(02)00147-4.

- Hess, R. A., "Pursuit tracking and higher levels of skill development in the human pilot," *IEEE Transactions on Systems, Man and Cybernetics*, vol. 11, no. 4, pp. 262–273, 1981, doi:10.1109/TSMC.1981.4308673.
- Hess, R. A., "Modeling the effects of display quality upon human pilot dynamics and perceived vehicle handling qualities," *IEEE Transactions on Systems, Man, and Cybernetics*, vol. 25, no. 2, pp. 338–344, 1995, doi:10.1109/21.364831.
- Hess, R. A., "A preliminary study of human pilot dynamics in the control of time-varying systems," *Proceedings of the AIAA Modelling and Simulation Technologies Conference*, AIAA, 2011, doi: 10.2514/6.2011-6554, also AIAA Paper 2011-6554.
- Honing, V., Gibo, T. L., Kuiper, R. J., and Abbink, D. A., "Training with haptic shared control to learn a slow dynamic system," *Proceedings of the IEEE International Conference on Systems, Man and Cybernetics (SMC)*, pp. 3126–3131, IEEE, Oct. 2014, doi: 10.1109/SMC.2014.6974408.
- Jenkins, G. M. and Watts, D. G., *Spectral Analysis and its Applications*, Holden-Day, 1969.
- Johnston, D. E. and McRuer, D. T., "Investigation of limb-side stick dynamic interaction with roll control," *Journal of Guidance, Control, and Dynamics*, vol. 10, no. 2, pp. 178–186, Mar. 1987, doi:10.2514/3.20200.
- Kaber, D. B. and Endsley, M. R., "Out-of-the-loop performance problems and the use of intermediate levels of automation for improved control system functioning and safety," *Process Safety Progress*, vol. 16, no. 3, pp. 126–131, 1997, doi:10.1002/prs.680160304.
- Kaber, D. B. and Endsley, M. R., "The effects of level of automation and adaptive automation on human performance, situation awareness and workload in a dynamic control task," *Theoretical Issues in Ergonomics Science*, vol. 5, no. 2, pp. 113–153, 2004, doi:10.1080/1463922021000054335.

- Katzourakis, D. I., Abbink, D. A., Happee, R., and Holweg, E., "Steering force feedback for human-machine-interface automotive experiments," *IEEE Transactions on Instrumentation and Measurement*, vol. 60, no. 1, pp. 32–43, 2011, doi:10.1109/tim.2010.2065550.
- Katzourakis, D. I., Abbink, D. A., Velenis, E., Holweg, E., and Happee, R., "Driver's arms' time-variant neuromuscular admittance during real car test-track driving," *IEEE Transactions on Instrumentation and Measurement*, vol. 63, no. 1, pp. 221–230, 2014, doi:10.1109/tim.2013.2277610.
- Kirsch, R. F. and Kearney, R. E., "Identification of time-varying stiffness dynamics of the human ankle joint during an imposed movement," *Experimental Brain Research*, vol. 114, no. 1, pp. 71–85, 1997, doi:10.1007/pl00005625.
- Lam, T., Mulder, M., and Van Paassen, M. M. R., "Haptic feedback for UAV tele-operation-force offset and spring load modification," *Proceedings of the IEEE International Conference on Systems, Man and Cybernetics (SMC)*, pp. 1618–1623, IEEE, Oct. 2006, doi:10.1109/ICSMC.2006.384950.
- Lam, T. M., Boschloo, H. W., Mulder, M., and Van Paassen, M. M., "Artificial force field for haptic feedback in UAV teleoperation," *IEEE Transactions on Systems, Man and Cybernetics, Part A: Systems and Humans*, vol. 39, no. 6, pp. 1316–1330, 2009, doi:10.1109/TSMCA.2009.2028239.
- Lam, T. M., Mulder, M., and van Paassen, M. M. R., "Haptic interface for UAV collision avoidance," *The International Journal of Aviation Psychology*, vol. 17, no. 2, pp. 167–195, Apr. 2007, doi:10.1080/10508410701328649.
- Lasschuit, J., Lam, T., Mulder, M., Van Paassen, M., and Abbink, D., "Measuring and modeling neuromuscular system dynamics for haptic interface design," *Proceedings of the AIAA modeling and simulation technologies conference and exhibit*, pp. 18–21, AIAA, Aug. 2008, doi:10.2514/6.2008-6543, also AIAA Paper 2008-6543.

- Lataire, J., Pintelon, R., and Louarroudi, E., "Non-parametric estimate of the system function of a time-varying system," *Automatica*, vol. 48, no. 4, pp. 666–672, Apr. 2012, doi:10.1016/j.automatica.2012.01.013.
- Ljung, L., *System Identification: Theory for the User*, 2nd edn., ????
- Lortie, M. and Kearney, R. E., "Identification of physiological systems: Estimation of linear timevarying dynamics with non-white inputs and noisy outputs," *Medical & Biological Engineering & Computing*, vol. 39, no. 3, pp. 381–390, May 2001, doi:10.1007/bf02345295.
- Ludvig, D. and Perreault, E. J., "Interpretation of non-parametric estimates of time-varying systems," *Proceedings of the IEEE American Control Conference (ACC)*, pp. 2701–2706, IEEE, Jun. 2012, doi:10.1109/acc.2012.6315221.
- Ludvig, D., Visser, T. S., Giesbrecht, H., and Kearney, R. E., "Identification of time-varying intrinsic and reflex joint stiffness," *IEEE Transactions on Biomedical Engineering*, vol. 58, no. 6, pp. 1715–1723, Feb. 2011, doi:10.1109/TBME.2011.2113184.
- van Lunteren, A., *Identification of human operator describing function models with one or two inputs in closed loop systems*, Ph.D. thesis, TU Delft, Delft University of Technology, Faculty of Mechanical, Maritime and Materials Engineering, 1979.
- MacNeil, J. B., Kearney, R. E., and Hunter, I. W., "Identification of time-varying biological systems from ensemble data (joint dynamics application)," *IEEE Transactions on Biomedical Engineering*, vol. 39, no. 12, pp. 1213–1225, 1992, doi:10.1109/10.184697.
- McRuer, D. T., "Human pilot dynamics in compensatory systems: Theory, models and experiments with controlled element and forcing function variations," Tech. rep., Air Force Flight Dynamics Laboratory, ????
- McRuer, D. T. and Jex, H. R., "A review of quasi-linear pilot models," *IEEE Transactions on Human Factors in Electronics*, vol. HFE-8, no. 3, pp. 231–249, Sep. 1967, doi:10.1109/THFE.1967.234304.

- McRuer, D. T. and Krendel, E. S., "Mathematical models of human pilot behavior," Tech. rep., NTIS, ????
- McRuer, D. T. and Weir, D. H., "Theory of manual vehicular control," *Ergonomics*, vol. 12, no. 4, pp. 599–633, Jul. 1969, doi:10.1080/00140136908931082.
- Morris, D., Tan, H., Barbagli, F., Chang, T., and Salisbury, K., "Haptic feedback enhances force skill learning," *Proceedings of the Second Joint EuroHaptics Conference and Symposium on Haptic Interfaces for Virtual Environment and Teleoperator Systems (WHC)*, pp. 21–26, IEEE, Mar. 2007, doi:10.1109/WHC.2007.65.
- Mugge, W., Abbink, D. A., and van der Helm, F. C., "Reduced power method: how to evoke low-bandwidth behaviour while estimating full-bandwidth dynamics," *Proceedings of the IEEE 10th International Conference on Rehabilitation Robotics (ICORR)*, pp. 575–581, IEEE, Jun. 2007, doi:10.1109/ICORR.2007.4428483.
- Mugge, W., Abbink, D. A., Schouten, A. C., Dewald, J. P., and van der Helm, F. C., "A rigorous model of reflex function indicates that position and force feedback are flexibly tuned to position and force tasks," *Experimental brain research*, vol. 200, no. 3-4, pp. 325–340, 2010, doi:10.1007/s00221-009-1985-0.
- Mulder, M., *Haptic gas pedal feedback for active car-following support*, Ph.D. thesis, TU Delft, Delft University of Technology, Faculty of Mechanical Maritime and Materials Engineering, 2007.
- Mulder, M., Abbink, D. A., and Boer, E. R., "The effect of haptic guidance on curve negotiation behavior of young, experienced drivers," *Proceedings of the IEEE International Conference on Systems, Man and Cybernetics (SMC)*, pp. 804–809, IEEE, Oct. 2008a, doi:10.1109/ICSMC.2008.4811377.
- Mulder, M., Abbink, D. A., and Boer, E. R., "Sharing control with haptics seamless driver support from manual to automatic control," *Human Factors: The Journal of the Human Factors and Ergonomics Society*, vol. 54, no. 5, pp. 786–798, 2012, doi:10.1177/0018720812443984.

- Mulder, M., Abbink, D. A., Van Paassen, M. M., and Mulder, M., "Design of a haptic gas pedal for active car-following support," *IEEE Transactions on Intelligent Transportation Systems*, vol. 12, no. 1, pp. 268–279, 2011a, doi:10.1109/TITS.2010.2091407.
- Mulder, M., Mulder, M., van Paassen, M. M., and Abbink, D. A., "Haptic gas pedal feedback," *Ergonomics*, vol. 51, no. 11, pp. 1710–1720, Oct. 2008b, doi:10.1080/00140130802331583.
- Mulder, M., Verspecht, T., Abbink, D. A., Van Paassen, M. M., Balderas, S., David, C., Schouten, A., De Vlugt, E., and Mulder, M., "Identification of time variant neuromuscular admittance using wavelets," *Proceedings of the IEEE International Conference on Systems, Man, and Cybernetics (SMC)*, pp. 1474–1480, IEEE, Oct. 2011b, doi:10.1109/ICSMC.2011.6083879.
- Nieuwenhuizen, F. M., Zaal, P. M. T., Mulder, M., Van Paassen, M. M., and Mulder, J. A., "Modeling human multichannel perception and control using linear time-invariant models," *Journal of Guidance, Control, and Dynamics*, vol. 31, no. 4, pp. 999–1013, Jul./Aug. 2008, doi:10.2514/1.32307.
- Norman, D. A., "The problem of automation: inappropriate feedback and interaction, not over-automation," *Philosophical Transactions of the Royal Society of London B: Biological Sciences*, vol. 327, no. 1241, pp. 585–593, 1990, doi:10.1098/rstb.1990.0101.
- NTSB, "Review of U.S. civile aviation accidents: calendar year 2010," NTSB/ARA-12/01, National Transportation Safety Board, Oct. 2012.
- O' Malley, M. K., Gupta, A., Gen, M., and Li, Y., "Shared control in haptic systems for performance enhancement and training," *Journal of Dynamic Systems, Measurement, and Control*, vol. 128, no. 1, pp. 75–85, Mar. 2006, doi:10.1115/1.2168160.
- van Paassen, M. M., *Biophysics in aircraft control, a model of the neuromuscular system of the pilot's arm*, Ph.D. thesis, TU Delft, Delft University of Technology, Faculty of Aerospace Engineering, 1994.

- van Paassen, M. M., Van Der Vaart, J. C., and Mulder, J. A., "Model of the neuromuscular dynamics of the human pilot's arm," *Journal of Aircraft*, vol. 41, no. 6, pp. 1482–1490, 2004, doi:10.2514/1.14434.
- Paige, C. C. and Saunders, M. A., "Towards a generalized singular value decomposition," *SIAM Journal on Numerical Analysis*, vol. 18, no. 3, pp. 398–405, 1981, doi:10.1137/0718026.
- Paleologu, C., Benesty, J., and Ciochina, S., "A robust variable forgetting factor Recursive Least-Squares algorithm for system identification," *IEEE Signal Processing Letters*, vol. 15, pp. 597–600, 2008, doi:10.1109/lsp.2008.2001559.
- Parker, N. R., Salcudean, S. E., and Lawrence, P. D., "Application of force feedback to heavy duty hydraulic machines," *Proceedings of the IEEE International Conference on Robotics and Automation*, pp. 375–381, IEEE, May 1993, doi:10.2514/6.2011-6984.
- Pintelon, R., Guillaume, P., Rolain, Y., Schoukens, J., and van Hamme, H., "Parametric identification of transfer functions in the frequency domain—a survey," *IEEE Transactions on Automatic Control*, vol. 39, no. 11, pp. 2245–2260, Nov. 1994, doi:10.1109/9.333769.
- Pintelon, R. and Schoukens, J., *System Identification: a Frequency Domain Approach*, Wiley-IEEE Press, 2nd edn., 2012.
- Pollini, L., Razzanelli, M., Olivari, M., Brandimarti, A., Maimeri, M., Pazzaglia, P., Pittiglio, G., Nuti, R., Innocenti, M., and Bulthoff, H. H., "Design, realization and experimental evaluation of a haptic stick for shared control studies," *Proceedings of the IFAC Symposium on Analysis, Design, and Evaluation of Human-Machine Systems(HMS)*, pp. 1–6, Aug. 2016.
- Pool, D. M., Mulder, M., Van Paassen, M. M., and Van Der Vaart, J. C., "Effects of peripheral visual and physical motion cues in roll-axis tracking tasks," *Journal of Guidance, Control, and Dynamics*, vol. 31, no. 6, pp. 1608–1622, Nov. 2008, doi:10.2514/1.36334.
- Pool, D. M., T. Zaal, P. M., Damveld, H. J., Van Paassen, M. M., Van der Vaart, J. C., and Mulder, M., "Modeling wide-frequency-range pilot equalization for control of aircraft pitch dynamics,"

- Journal of Guidance, Control, and Dynamics*, vol. 34, no. 5, pp. 1529–1542, Sep. 2011, doi:10.2514/1.53315.
- Pritchett, A. R., “Reviewing the role of cockpit alerting systems,” *Human Factors in Aerospace Safety*, vol. 1, no. 1, pp. 5–38, 2001.
- Profumo, L., Pollini, L., and Abbink, D. A., “Direct and indirect haptic aiding for curve negotiation,” *Proceedings of the IEEE International Conference on System, Man and Cybernetics (SMC)*, pp. 1846–1852, IEEE, Oct. 2013, doi:10.1109/SMC.2013.318.
- Reichel, L. and Ye, Q., “Simple square smoothing regularization operators,” *Electronic Transactions on Numerical Analysis*, vol. 33, pp. 63–83, Jan. 2009, doi:10.1.1.418.5500.
- Rosen, J., Hannaford, B., MacFarlane, M., and Sinanan, M., “Force controlled and teleoperated endoscopic grasper for minimally invasive surgery - experimental performance evaluation,” *IEEE Transactions on Biomedical Engineering*, vol. 46, no. 10, pp. 1212–1221, 1999, doi:10.1109/10.790498.
- Schouten, A. C., de Vlugt, E., and van der Helm, F. C. T., “Design of perturbation signals for the estimation of proprioceptive reflexes,” *IEEE Transactions on Biomedical Engineering*, vol. 55, no. 5, pp. 1612–1619, 2008a, doi:10.1109/TBME.2007.912432.
- Schouten, A. C., de Vlugt, E., van Hilten, B. J. J., and van der Helm, F. C. T., “Quantifying proprioceptive reflexes during position control of the human arm,” *IEEE Transactions on Biomedical Engineering*, vol. 55, no. 1, pp. 311–321, Jan. 2008b, doi:10.1109/TBME.2007.899298.
- Schutte, P. C., Goodrich, K. H., Cox, D. E., Jackson, B., Palmer, M. T., Pope, A. T., Schlecht, R. W., Tedjojuwono, K. K., Trujillo, A. C., Williams, R. A., Kinney, J. B., and Barry, J. S. J., “The naturalistic flight deck system: an integrated system concept for improved single-pilot operations,” NASA/TM-2007-215090, NASA Langley Research Center, Dec. 2007.

- Shmaliy, Y., *Continuous-Time Systems*, Springer Netherlands, 2007, doi:10.1007/978-1-4020-6272-8.
- Smisek, J., Paassen, R. M. v., and Schiele, A., "Naturally-transitioning rate-to-force controller robust to time delay by model-mediated teleoperation," *Proceedings of the IEEE International Conference on Systems, Man, and Cybernetics (SMC)*, pp. 3066–3071, IEEE, Oct. 2015, doi:10.1109/SMC.2015.533.
- de Stigter, S., Mulder, M., and van Paassen, M. M., "Design and evaluation of a haptic flight director," *Journal of Guidance, Control, and Dynamics*, vol. 30, no. 1, pp. 35–46, Jan. 2007, doi:10.2514/1.20593.
- Tada, S. and Wada, T., "Effect of skill development of haptic shared control in backward parking assist," *Proceedings of the IEEE International Conference on Vehicular Electronics and Safety*, pp. 164–169, IEEE, Nov. 2015, doi:10.1109/ICVES.2015.7396912.
- Thompson, P., Bachelder, E., Klyde, D., Harris, C., and Brenner, M., "Wavelet-based techniques for improved on-line systems identification," *Proceedings of the USAF Developmental Test and Evaluation Summit*, AIAA, Nov. 2004, doi:10.2514/6.2004-6838, also AIAA paper 2004-6838.
- Thompson, P. M., Klyde, D. H., and Brenner, M., "Wavelet-based time-varying human operator models," *Proceedings of the AIAA Atmospheric Flight Mechanics Conference and Exhibit*, AIAA, Aug. 2001, doi:10.2514/6.2001-4009, also AIAA paper 2001-4009.
- Tikhonov, A. N., Goncharsky, A. V., Stepanov, V. V., and Yagola, A. G., "Numerical methods for the approximate solution of ill-posed problems on compact sets," *Numerical Methods for the Solution of Ill-Posed Problems*, pp. 65–79, Springer Science Business Media, 1995, doi:10.1007/978-94-015-8480-7-3.
- Vahidi, A., Stefanopoulou, A., and Peng, H., "Recursive least squares with forgetting for online estimation of vehicle mass and road grade: Theory and experiments," *Vehicle System Dynamics*, vol. 43, no. 1, pp. 31–55, Jan. 2005, doi:10.1080/00423110412331290446.

- Venrooij, J., Abbink, D. A., Mulder, M., and van Paassen, M. M., "A method to measure the relationship between biodynamic feedthrough and neuromuscular admittance," *IEEE Transactions on Systems, Man, and Cybernetics, Part B: Cybernetics*, vol. 41, no. 4, pp. 1158–1169, Aug. 2011, doi:10.1109/tsmcb.2011.2112347.
- Venrooij, J., Mulder, M., Abbink, D. A., Van Paassen, M. M., Van Der Helm, F. C., and Bülthoff, H. H., "A new view on biodynamic feedthrough analysis: Unifying the effects on forces and positions," *IEEE Transactions on Cybernetics*, vol. 43, no. 1, pp. 129–142, 2013, doi:10.1109/TSMCB.2012.2200972.
- Venrooij, J., van Paassen, M. M., Mulder, M., Abbink, D. A., Mulder, M., van der Helm, F. C. T., and Bülthoff, H. H., "A framework for biodynamic feedthrough analysis - part I: Theoretical foundations," *IEEE Transactions on Cybernetics*, vol. 44, no. 9, pp. 1686–1698, 2014, doi:10.1109/TCYB.2014.2311043.
- Wellstead, P. E., "Non-parametric methods of system identification," *Automatica*, vol. 17, no. 1, pp. 55–69, Jan. 1981, doi:10.1016/0005-1098(81)90084-4.
- Wickens, C. D., "Situation awareness: Review of Mica Endsley's 1995 articles on situation awareness theory and measurement," *Human Factors: The Journal of the Human Factors and Ergonomics Society*, vol. 50, no. 3, pp. 397–403, 2008, doi:10.1518/001872008X288420.
- Wickens, C. D., Mavor, A. S., Parasuraman, R., and McGee, J. P., *The future of air traffic control: Human operators and automation*, National Academies Press, 1st edn., 1998, doi:10.17226/6018.
- Yokokohji, Y., Hollis, R. L., Kanade, T., Henmi, K., and Yoshikawa, T., "Toward machine mediated training of motor skills. skill transfer from human to human via virtual environment," *Proceedings of the 5th IEEE International Workshop on Robot and Human Communication*, pp. 32–37, IEEE, Nov. 1996, doi:10.1109/ROMAN.1996.568646.

- Zaal, P., Pool, D., Mulder, M., and van Paassen, M. M., "New types of target inputs for multi-modal pilot model identification," *Proceedings of the AIAA Modeling and Simulation Technologies Conference and Exhibit*, pp. 1–17, AIAA, Aug. 2008, doi:10.2514/6.2008-7106, also AIAA Paper 2008-7106.
- Zaal, P. M. T., Pool, D. M., and Van Paassen, M. M., "Multimodal pilot control behavior in combined target-following disturbance-rejection tasks," *Journal of Guidance, Control, and Dynamics*, vol. 32, no. 5, pp. 1418–1428, Aug. 2009, doi:10.2514/6.2009-6027.
- Zaal, P. M. T. and Sweet, B. T., "Estimation of time-varying pilot model parameters," *Proceedings of the AIAA Modeling and Simulation Technologies Conference*, pp. 1–17, AIAA, Aug. 2011, doi: 10.2514/6.2011-6474, also AIAA Paper 2011-6474.
- Zaal, P. M. T. and Sweet, B. T., "Identification of time-varying pilot control behavior in multi-axis control tasks," *Proceedings of the AIAA Modeling and Simulation Technologies Conference*, pp. 1–20, AIAA, Aug. 2012, doi:10.2514/6.2012-4793, also AIAA Paper 2012-4793.
- Zhou, N., Trudnowski, D. J., Pierre, J. W., and Mittelstadt, W. A., "Electromechanical mode online estimation using regularized robust RLS methods," *IEEE Transactions on Power Systems*, vol. 23, no. 4, pp. 1670–1680, Nov. 2008, doi:10.1109/TPWRS.2008.2002173.

Appendices

Modelling of pilot's dynamic responses

DIFFERENT pilot models have been used throughout this thesis. This appendix reviews all the used models, focusing on their differences and similarities. Throughout this appendix, the notation H_{block} denotes the transfer function of BLOCK.

A.1 Single-input pilot model for a compensatory tracking task

In a compensatory tracking task, the human control behavior can be modelled by a single-input dynamic system CON as shown in Figure A.1. The dynamics of CON describe how the human operator HO moves the control device CD based on the tracking error e . The stick deflection δ_{cd} is the control command for the controlled element CE. The dynamics of CON are assumed linear, and the remnant N accounts for unmodelled non-linearities. Note that CON includes dynamics of the human operator and control device.

This model was considered in Chapter 2, Chapter 3, and Chapter 4.

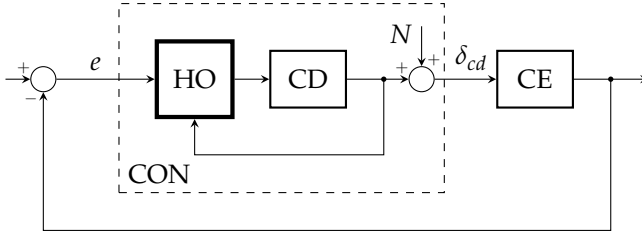


Figure A.1: Compensatory tracking task.

A.2 Multi-input pilot models for a compensatory tracking task

When haptic aids are employed and tactile information is provided on the control device, the tactile perception channel needs to be modelled as an additional input to the human operator model. In literature, different models have been developed that account for the tactile input. This section reviews the models used in this thesis.

A.2.1 Non-parametric model with admittance and visual response

A multi-loop human model with the tactile feedback as input is shown Figure A.2 [Abbink et al., 2011; Damveld et al., 2010; van Paassen, 1994]. The human operator HO is described by two control loops, the outer describing the visual response VIS, whereas the inner loop describes the neuromuscular response. The neuromuscular response is represented by the inverse of the arm admittance ADM, defined as the dynamic relationship between the force acting on the arm and the position of the arm [Abbink et al., 2011]. Both the visual and neuromuscular systems contribute to the total human force F_{ho} . The visual and the neuromuscular responses are assumed to be linear and time-invariant. Nonlinearities in human responses are accounted for by the remnant signal N [McRuer and Jex, 1967].

Figure A.2 shows that CON includes dynamics of ADM, VIS, and CD. The relationship between the corresponding transfer functions

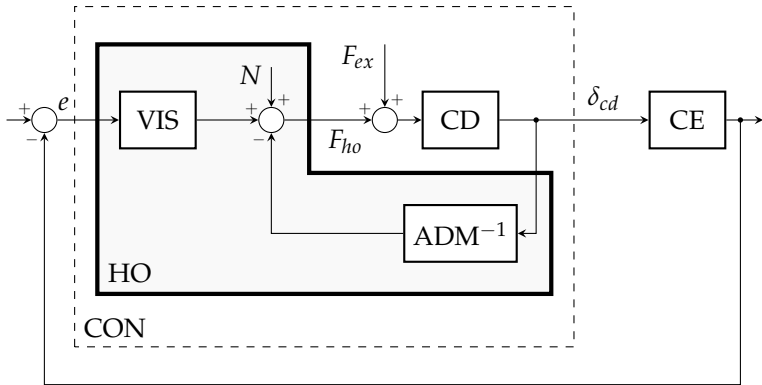


Figure A.2: Human operator model with admittance ADM and visual response VIS.

H_{con} and H_{adm} , H_{vis} , H_{cd} can be found by using block diagram algebra:

$$H_{con} = H_{vis} \frac{H_{cd} H_{adm}}{H_{adm} + H_{cd}} \quad \text{A.1}$$

The human operator model in Figure A.2 was considered in Chapter 5 and Chapter 6.

A.2.2 Non-parametric model with force and error feedthroughs

Figure A.3 shows a slightly different pilot model from Figure A.2. The human operator model has the visual error e and the external force F_{ex} as inputs, and δ_{cd} as output. Thus, the human operator is described by the dynamic responses from e to δ_{cd} (error feedthrough EFT) and from F_{ex} to δ_{cd} (force disturbance feedthrough FDFT). Note that error and force feedthroughs include the dynamics of the control device.

Relationships between the transfer functions corresponding to the models in Figure A.2 and Figure A.3 can be obtained by applying

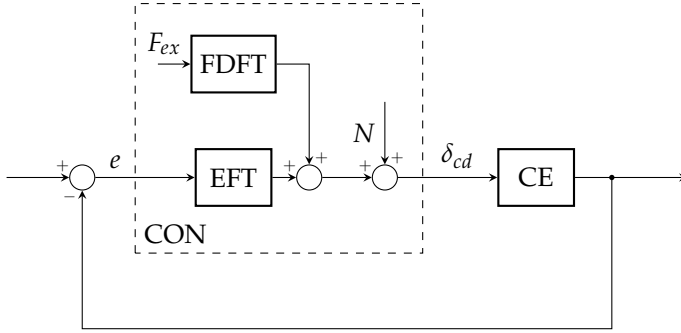


Figure A.3: Pilot model with force feedthrough FDFT and error feedthrough EFT.

block diagram algebra:

$$H_{Fdft} = \frac{H_{cd}H_{adm}}{H_{adm} + H_{cd}} \quad \text{A.2}$$

$$H_{eft} = H_{vis} \frac{H_{cd}H_{adm}}{H_{adm} + H_{cd}} = H_{con} \quad \text{A.3}$$

This model was used in Chapter 9.

A.2.3 Parametric model - Schouten et al. [2008b]

This thesis performed sets of Monte-Carlo simulations that simulated time-varying neuromuscular responses. To simulate the time-varying response, parametric models were used and the parameters were varied between different sets provided by previous studies.

Figure A.4 shows a parametric model for the human operator model in Figure A.2. The block SKIN represents the visco-elasticity of the arm contact with the control device, generated by the skin of the hand. The block INT describes the intrinsic arm dynamics, which include the lumped mass of hand, lower arm, and upper arm, together with the contractile and elastic components of antagonistic muscles. The contractile components are activated by the efferent neurons ACT. The muscle spindle sensory system is represented by the reflexive dynamics REFL. The equalization dynamics EQ

block diagram algebra, we obtain:

$$H_{arm} = \frac{H_{int}}{1 + H_{act}H_{int}H_{refl}} \quad \text{A.4}$$

$$H_{adm} = H_{arm} + \frac{1}{H_{skin}} \quad \text{A.5}$$

$$H_{vis} = -H_{eq} \frac{H_{skin}H_{int}H_{act}}{1 + H_{int}H_{refl}H_{act} - H_{skin}H_{int}} \quad \text{A.6}$$

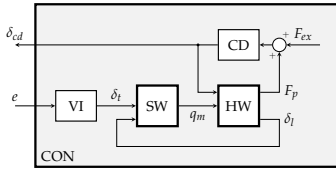
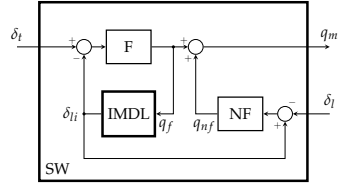
This model was used in Chapter 7 and Chapter 8 to describe human behavior disturbance-rejection tasks. In these tasks, humans are asked to oppose or to be compliant with a force disturbance F_d presented on the control device. Since no visual cues are provided to the humans, the signal u_{cns} can be considered negligible.

A.2.4 Parametric model - van Paassen et al. [2004]

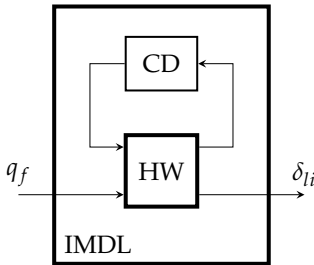
Figure A.5 shows a parametric model for the human operator model in Figure A.3. The model represents the human operator by the visual (VI) and the arm neuromuscular system (SW, HW), see Figure A.5a. The visual system VI generates a target trajectory δ_t for the neuromuscular system based on the tracking error e . The neuromuscular system includes two components: the neuromuscular software SW and the neuromuscular hardware HW. The neuromuscular software SW generates the activation signal q_m that makes the limb position δ_l of the neuromuscular hardware HW follow the desired trajectory δ_t .

The activation signal q_m is generated as the sum of two activation signals, q_f and q_n , see Figure A.5b. The signal q_f is generated by a closed control loop (F, IMDL) that ensures the limb position δ_{li} of an internal model IMDL to follow the desired trajectory δ_t . The internal model IMDL represents an internal representation of the neuromuscular hardware and the control device, see Figure A.5c. The signal q_{nf} is a feedback control action filtered by NF that corrects for differences between internal and actual limb position.

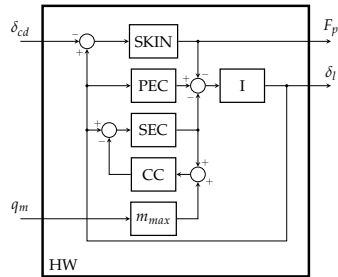
The neuromuscular hardware HW represents all the passive components of the limb, see Figure A.5d. It includes the skin SKIN,

(a) Block diagram of H_{con} .

(b) Block diagram of neuromuscular software SW.



(c) Block diagram of internal model IM.



(d) Block diagram of neuromuscular hardware HW.

Transfer function	Description
$H_{vi} = K_v \frac{1+\tau_{vi}s}{1+\tau_{vi}s} e^{-\Delta t_v}$	Visual response
$H_f = K_f \frac{1+\tau_{fi}s}{1+\tau_{fi}s}$	Internal model filter
$H_{nf} = K_n \frac{1+\tau_{ni}s}{1+\tau_{ni}s} e^{-\Delta t_n}$	Neural feedback filter
$H_{cd} = \frac{1}{m_{cd}s^2 + b_{cd}s + k_{cd}}$	Control device
$H_{skin} = B_c s + K_c$	Skin
$H_{pec} = -K_{pec}$	Parallel elastic component
$H_{sec} = K_{sec}$	Series elastic component
$H_{cc} = \frac{1}{b_n s}$	Contractile component
$H_I = \frac{1}{I_a s^2}$	Inertia of the arm

(e) Block dynamics.

Figure A.5: Parametric model for the human operator model in Figure A.3.

the mass inertia I , the contractile components CC of the muscles, and the muscles elastic properties SEC , PEC .

Relationships between the transfer functions of the blocks in Figure A.5 and the error and force feedtroughs in Figure A.3 can be found in van Paassen [1994]. The model in Figure A.5 was used in Chapter 9.

List of my publications

Journal publications

Olivari, M., Geluardi, S., Venrooij, J., Nieuwenhuizen, F. M., Pollini, L., and Bulthoff, H. H., "Identifying time-varying neuromuscular response: Regularized recursive least-squares algorithms," *IEEE Transactions on Cybernetics*, 2016, **in preparation**.

Geluardi, S., Venrooij, J., **Olivari, M.**, Pollini, L., and Bulthoff, H. H., "Validation of augmented civil helicopters in the MPI cybermotion simulator," *Journal of Guidance, Control, and Dynamics*, 2016, **in preparation**.

Olivari, M., Nieuwenhuizen, F. M., Bühlhoff, H. H., and Pollini, L., "Pilot adaptation to different classes of haptic aids in tracking tasks," *Journal of Guidance, Control, and Dynamics*, vol. 37, no. 6, pp. 1741–1753, Nov./Dec. 2014c, doi:10.2514/1.G000534.

Olivari, M., Nieuwenhuizen, F. M., Venrooij, J., Bühlhoff, H. H., and Pollini, L., "Methods for multiloop identification of visual and neuromuscular pilot responses," *IEEE Transactions on Cybernetics*, vol. 45, no. 12, pp. 2780–2792, Dec. 2015c, doi:10.1109/TCYB.2014.2384525.

Conference publications

- Symeonidou, E.-R., **Olivari, M.**, Bülthoff, H. H., Venrooij, J., and L., Chuang L. L., "EEG oscillatory modulations (10-12 hz) discriminate for voluntary motor control and limb movement," *46th Annual Meeting of the Society for Neuroscience (SfN)*, Nov. 2016, **submitted**.
- D'Intino, G., **Olivari, M.**, Venrooij, J., Bülthoff, H. H., and Pollini, L., "Evaluation of haptic support system for training purposes in a tracking task," *Proceedings of the IEEE international Conference on Systems, Man and Cybernetics (SMC)*, pp. 1–6, Institute of electrical and electronics engineers (IEEE), Oct. 2016, **accepted**.
- Pollini, L., Razzanelli, M., **Olivari, M.**, Brandimarti, A., Maimeri, M., Pazzaglia, M., Pittiglio, G., Nuti, R., Innocenti, M., and Bülthoff, H., "Design, realization and experimental evaluation of a haptic stick for shared control studies," *Proceedings of the 13th IFAC/IFIP/IFORS/IEA Symposium on Analysis, Design, and Evaluation of Human-Machine Systems*, pp. 1–6, International Federation of Automatic Control (IFAC), Aug./Sep. 2016, **accepted**.
- Venrooij, J., **Olivari, M.**, and Bülthoff, H., "Biodynamic feed-through: Current status and open issues," *Proceedings of the 13th IFAC/IFIP/IFORS/IEA Symposium on Analysis, Design, and Evaluation of Human-Machine Systems*, pp. 1–6, International Federation of Automatic Control (IFAC), Aug./Sep. 2016, **accepted**.
- Picardi, G., Geluardi, S., **Olivari, M.**, Pollini, L., Innocenti, M., and Bülthoff, H. H., " \mathcal{L}_1 -based model following control of an identified helicopter model in hover," *Proceedings of the American Helicopter Society 72th Annual Forum*, pp. 1–8, May 2016.
- Olivari, M.**, Venrooij, J., Nieuwenhuizen, F. M., Pollini, L., and Bülthoff, H. H., "Identifying time-varying pilot responses: a regularized recursive least-squares algorithm," *Proceedings of the AIAA Modeling and Simulation Technologies Conference*, also AIAA paper 2016-1182, pp. 1–15, American Institute of Aeronautics and Astronautics (AIAA), Jan. 2016, doi:10.2514/6.2016-1182.

- Maimeri, M., **Olivari, M.**, Bühlhoff, H., and Pollini, L., "On effects of failures in haptic and automated pilot support systems," *Proceedings of the AIAA Modeling and Simulation Technologies Conference*, also AIAA paper 2016-1181, pp. 1–12, American Institute of Aeronautics and Astronautics (AIAA), Jan. 2016, doi: 10.2514/6.2016-1181.
- Olivari, M.**, Nieuwenhuizen, F. M., Bühlhoff, H. H., and Pollini, L., "Identifying time-varying neuromuscular response: A recursive least-squares algorithm with pseudoinverse," *Proceedings of the IEEE international Conference on Systems, Man and Cybernetics (SMC)*, pp. 1–7, Institute of electrical and electronics engineers (IEEE), Oct. 2015a, doi:10.1109/smc.2015.535.
- Symeonidou, E.-R., **Olivari, M.**, Bühlhoff, H. H., and L., Chuang L. L., "Direct haptic feedback benefits control performance during steering," *Proceedings of 57th Conference of Experimental Psychologists (TeaP)*, Mar. 2015.
- Olivari, M.**, Nieuwenhuizen, F. M., Bühlhoff, H. H., and Pollini, L., "Identifying time-varying neuromuscular response: Experimental evaluation of a rls-based algorithm," *Proceedings of the AIAA Modeling and Simulation Technologies Conference*, also AIAA paper 2015-0658, pp. 3573–3578, American Institute of Aeronautics and Astronautics (AIAA), Jan. 2015b, doi:10.2514/6.2015-0658.
- Olivari, M.**, Nieuwenhuizen, F. M., Bühlhoff, H. H., and Pollini, L., "Identifying Time-varying Neuromuscular System with a Recursive Least-squares Algorithm: a Monte-Carlo Simulation Study," *Proceedings of the IEEE international Conference on Systems, Man and Cybernetics (SMC)*, pp. 3573–3578, Institute of electrical and electronics engineers (IEEE), Oct. 2014b, doi:10.1109/SMC.2014.6974484.
- Gerboni, C. A., Geluardi, S., **Olivari, M.**, Nieuwenhuizen, F. M., Bühlhoff, H. H., and Pollini, L., "Development of a 6 dof nonlinear helicopter model for the mpi cybermotion simulator," *Proceedings of the 40th European Rotorcraft Forum (ERF)*, pp. 615–626, Royal Aeronautical Society, Oct. 2014.

- Symeonidou, E.-R., **Olivari, M.**, Bülthoff, H. H., and L., Chuang L. L., "The role of direct haptic feedback in a compensatory tracking task," *Proceedings of 12th Biannual Conference of the German Cognitive Science Society (KogWis)*, Sep. 2014a.
- Symeonidou, E.-R., **Olivari, M.**, Bülthoff, H. H., and L., Chuang L. L., "The role of direct haptic feedback in a compensatory tracking task," *Proceedings of 6th International Conference on Brain and Cognitive Engineering (BCE)*, Jun. 2014b.
- Olivari, M.**, Nieuwenhuizen, F. M., Bülthoff, H. H., and Pollini, L., "An experimental comparison of haptic and automated pilot support systems," *Proceedings of the AIAA Modeling and Simulation Technologies Conference*, also AIAA paper 2014-0809, pp. 1–11, American Institute of Aeronautics and Astronautics (AIAA), Jan. 2014a, doi:10.2514/6.2014-0809.
- Olivari, M.**, Nieuwenhuizen, F. M., Venrooij, J., Bülthoff, H. H., and Pollini, L., "Multi-loop pilot behaviour identification in response to simultaneous visual and haptic stimuli," *Proceedings of the AIAA Modeling and Simulation Technologies Conference*, also AIAA paper 2012-4795, pp. 1–23, American Institute of Aeronautics and Astronautics (AIAA), Aug. 2012, doi:10.2514/6.2012-4795.

Curriculum Vitae

Mario Olivari received the M.Sc. degree in automation engineering (*cum laude*) from the University of Pisa, Pisa, Italy, in October 2012, for his work on the identification of pilot control behavior in a closed-loop control task with haptic aids. Currently, he is a Ph.D student in the context of a collaborative project between the Department of Human Perception, Cognition and Action at the Max Planck Institute for Biological Cybernetics, Tübingen, Germany, and the Faculty of Automation Engineering at the University of Pisa.



His research interests include haptic guidance systems, pilot identification and the modelling of the neuromuscular system.

